# Multiple Scale Landscape Pattern Index Interpretation for the Persistent Monitoring of Land-Cover and Land-Use

by

Alvin J. Spivey

B.S. Rochester Institute of Technology, 2004

A dissertation submitted in partial fulfillment of the
requirements for the degree of Doctor of Philosophy
in the Chester F. Carlson Center for Imaging Science
Rochester Institute of Technology

May 01, 2011

Signature of the Author _____

Accepted by _____
 Coordinator, Ph.D. Degree Program                         Date

CHESTER F. CARLSON CENTER FOR IMAGING SCIENCE

ROCHESTER INSTITUTE OF TECHNOLOGY

ROCHESTER, NEW YORK

<u>CERTIFICATE OF APPROVAL</u>

---

Ph.D. DEGREE DISSERTATION

---

The Ph.D. Degree Dissertation of Alvin J. Spivey
has been examined and approved by the
dissertation committee as satisfactory for the
dissertation required for the
Ph.D. degree in Imaging Science

_____
Dr. Anthony Vodacek, Dissertation Advisor

_____
Dr. John Schott

_____
Dr. Carl Salvaggio

_____
Dr. Emmett Ientilucci

_____
Dr. Karl Korfmacher

_____
Date

DISSERTATION RELEASE PERMISSION

ROCHESTER INSTITUTE OF TECHNOLOGY

CHESTER F. CARLSON CENTER FOR IMAGING SCIENCE

Title of Dissertation:

**Multiple Scale Landscape Pattern Index Interpretation for the**

**Persistent Monitoring of Land-Cover and Land-Use**

I, Alvin J. Spivey, hereby grant permission to Wallace Memorial Library of R.I.T. to reproduce my thesis in whole or in part. Any reproduction will not be for commercial use or profit.

Signature _____

Date

## Abstract

Mapping land-cover land-use change (LCLUC) over regional and continental scales, and long time scales (years and decades), can be accomplished using thematically identified classification maps of a landscape—a LCLU class map. Observations of a landscape's LCLU class map pattern can indicate the most relevant process, like hydrologic or ecologic function, causing landscape scale environmental change. Quantified as Landscape Pattern Metrics (LPM), emergent landscape patterns act as Landscape Indicators (LI) when physically interpreted. The common mathematical approach to quantifying observed landscape scale pattern is to have LPM measure how connected a class exists within the landscape, through nonlinear local kernel operations of edges and gradients in class maps. Commonly applied kernel-based LPM that consistently reveal causal processes are *Dominance*, *Contagion*, and *Fractal Dimension*. These kernel-based LPM can be difficult to interpret. The emphasis on an image pixel's edge by gradient operations and dependence on an image pixel's existence according to classification accuracy limit the interpretation of LPM. For example, the *Dominance* and *Contagion* kernel-based LPM very similarly measure how connected a landscape is. Because of this, their reported edge measurements of connected pattern correlate strongly, making their results ambiguous. Additionally, each of these kernel-based LPM are unscalable when comparing class maps from separate imaging system sensor scenarios that change the image pixel's edge position (*i.e.* changes in landscape extent, changes in pixel size, changes in orientation, etc), and can only interpret landscape pattern as accurately as the LCLU map classification will allow. This dissertation discusses the reliability of common LPM in light of imaging system effects such as: algorithm classification likelihoods, LCLU classification accuracy due to random image sensor noise, and image scale. A description of an approach to generating well behaved LPM through a Fourier system analysis of the entire class map, or any subset of the class map (*e.g.* the watershed) is the focus of this work. The Fourier approach provides four improvements for LPM. First, the approach reduces any correlation between metrics by developing them within an independent (*i.e.* orthogonal) Fourier vector space; a Fourier vector space that includes relevant physically representative parameters (*i.e.* between class Euclidean distance). Second, accounting for LCLU classification accuracy the LPM measurement precision and measurement accuracy are reported. Third, the mathematics of this approach makes it possible to compare image data captured at separate pixel resolutions or even from separate landscape scenes. Fourth, Fourier interpreted landscape pattern measurement can be a measure of the entire landscape shape, of individual landscape cover change, or as exchanges between class map subsets by operating on the entire class map, subset of class map, or separate subsets of class map[s] respectively. These LCLUC LPM are examined along the 1991-1992 and 2000-2001 records of National Land Cover Database Landsat data products. Those LPM results are used in a predictive fecal coliform model at the South Carolina watershed level in the context of past (validation study) change. Finally, the proposed LPM ability to be used as ecologically relevant environmental indicators is tested by correlating metrics with other, well known LI that consistently reveal causal processes in the literature.

# Acknowledgements

Being here for so long, I've had the chance to pass out a few signed theses and dissertations belonging to other graduates. Every time I put one into a hand, the page turned to most was the dedication. While flipping past the committee signature page and abstract Cindy Schultz once noted, "...that's the only thing people ever read anyways." So, if anything, I better get this part right.

No matter how long it's been, where we are or what may have happened the last time we spoke. If you ever think of me, find that you're within stomping grounds or just want to see what's going on, contact me. I've been here for way too long, and not long enough. You people have become more than friends, acquaintances, mentors, teachers, peers, advisers, etc.—you've become family. Family I didn't have much choice in the making of, but family nonetheless. An indelible experience. Welcome to the Spivey household.

And now for the requisite list of names whom will never be forgotten, thanks to: my advisor, Dr. Anthony Vodacek and family, you've been stepping up for me from the beginning and the fam wrapped around me through the end, let's keep going; committee member Dr. John Schott, whom without the imprint of his palm along the backside of my head and the imprint of his steady guidance in this work, I would have never left the program in success; committee member, mentor and friend Dr. Carl Salvaggio, who plucked me from obscurity and continues to bring me out of it; committee member Dr. Emmett Ientilucci, who has been an endless source of academic inspiration and awe, and whose patience I have learned to appreciate most; and committee member Dr. Karl Korfmacher, the renegade GIS expert that broke my sanity for the better; GIS specialists and friend Nina Raqueño, who sat through many frustrating ArcGIS e-mails; confidant, friend and the man whom I am eternally indebted to, Dr. Jon Arney; the most inviting woman alive whose shoulders couldn't be softer, Dr. Maria Helguera; Coach Joe Pow, Erin Ontiveros, May 'not Arsenovic' Casterline, Dr. Roger Easton, Dr. Jeff Pelz, Mrs. Sue Chan, Cindy Schultz, and Sara Paul.

A fact both upsetting and inspiring, I've spent literally over a third of my life at the Center for Imaging Science. If these are the relationships, friendships, and memories awarded in one decade of living together I look forward to the next six. Thank you, thank you, thank you all.

*This dissertation is dedicated to the women who always stood at my side, and the man who held them up. Thank you Grandma Carrie, my mom Carin Spivey, the boss Kutosha Williams, 'Aunty-so-fine' Synitra Scott and the formidable Roosevelt Spivey.*

# Contents

# List of Figures

# List of Tables

# Chapter 1

# Introduction

Traditional approaches to detecting human impacts on rivers include chemical, biotic, hydrologic, and physical habitat assessment. Most notable are the water chemistry and biotic indices developed along community and regional scale monitoring programs. These programs typically monitor water quality attributes such as water clarity, temperature, and conductivity; or are biotic surveys of aquatic invertebrates, algae, plankton, and vascular plants. Using traditional hydrological indices, instream flow, methods reduce the riparian system to a series of pipes and drains where comparisons between contemporary and historic flows, methods based on hydraulic geometry, and instream habitat assessment are recorded to describe potential ecological efficacy. Sediment sequence and composition, soil and sediment erosion, stream flow, stream channel morphology, stream sediment storage and load, surface water quality, and hydrology of floodplains and wetlands are several of the traditional geoindicators used in physical habitat monitoring [Gergel et al., 2002]. Still, in all of their attention to detail neither of these indicators are a direct measure of human influence, consider the effects of upland land-use on riverine systems, or are directly connected to an effect of its cause. They are strictly local in interpretation, and can be application (*e.g.* region, watershed, catchment, *etc.*) specific.

These traditional river indicator campaigns tend to be totally biologic or geologic in construction. However, biological activity has not been well linked with river-bed shape, making it difficult to interpret one type of indicator from another [Maddock, 1993]. An answer to connecting the separate biologic and geologic perspectives for interpreting causal environmental relationships can be found in Landscape Ecology. The science of Landscape Ecology employs landscape scale indicators that have a strong correlation with traditional riparian indicators, particularly for water chemistry indicators. These landscape scale indicators form a more complete picture of the watershed due to terrestrial effects, including human influences.

In Landscape Ecology, the entire surface of the Earth is considered to be a living organism. Where, a map of categorized surfaces (*e.g.* satellite derived land-cover land-use (LCLU) classification maps, or census data) are a snap shot of biotic activity. Shape characteristics of an individual class *patch* and interrelationships between class shapes are an indication of current and potential biotic health. Where, for a given LCLU class type, any set of contiguous pixels are referred to as a patch.

Multiple landscape level indices of biotic health have been proposed; mostly concerning coverage percentage, statistical moments, entropy, fractal dimension, and spatial characteristics (*e.g.*

physical extent of class coverage, distance from nearest body of water, *etc.*) to name a few. A significant amount of theory used in interpreting these landscape indices is borrowed from the science of population dynamics. Where nine factors of population (or patch) influence and existence are used for population dynamics index interpretation [Akcakaya et al., 1999]:

- Degree of isolation (distance to nearest neighbor, and mainland)

- Length of isolation (time)

- Relative size of class patch (larger coverage area usually facilitates greater activity)

- Climate (tropical versus arctic, humid versus arid, *etc.*)

- Location relative to ocean currents (influences nutrient, fish, bird, and seed flow patterns)

- Initial plant and animal composition if previously attached to a larger land mass (*e.g.*, marsupials, primates, *etc.*)

- During initial contact: the relationship between the pairing classes (if always isolated)

- Serendipity (the impacts of chance arrivals)

- Human activity

Three landscape indices have consistently shown a high correlation to biotic health. As indicators of watershed integrity, biotic integrity and diversity, and landscape stability and resilience: the Environmental Protection Agency (EPA) has identified entropic measures of *Dominance* and *Contagion*, as well as the statistical measure of *Fractal Dimension*. However, these three indices of *Dominance*, *Contagion*, and *Fractal Dimension* suffer from a nonlinear dependence on imaging system resolvability. Also, a strong correlation between *Dominance* and *Contagion* indices make it difficult to understand which population dynamics factor is effecting index variability.

Now, consider the measure of landscape level indices as a nonlinear operator on any imaging system derived landscape product. From a systems perspective, each map of the landscape is ideally effected by only the imaging system's capture method. These imaging system effects are functions of observed spatial scale. Where for a satellite derived LCLU map, imaging system spatial scale effects are completely dependent on sensor pixel size and sensor observation height. Landscape Ecology's respective parameters of spatial scale are grain size and extent. The nonlinear effects of these operators (scale effects) limit the interpretation of landscape indices for LCLU maps of different spatial scales.

Spatially, the imaging system scale effects are introduced as a series of summations (see Figure 1.1). The relationship between a spatially varying lower resolution function $f'[x]$ and a spatially varying higher resolution function $f[x]$ using pixel element $h[\frac{x}{d}]$ is $f'[x] \equiv f[x] * h\left[\frac{x}{d}\right] = \int_{\alpha} f[\alpha] \cdot h[\frac{\alpha-x}{d}]\partial\alpha$—here, $d$ is the pixel width and $*$ is the convolution operator. The summation makes it difficult to compare one pixel from a lower resolution image $f'[x]$ and its higher resolution component positions in $f[x]$. Interpreting any pixel-based operation done on multiple resolution images would be even more difficult. However, when interpreting the observed landscape along its spatial frequency, scale effects are introduced as a single summation, smoothly varying, windowed function of bandwidth (see Figure 1.2). The relationship between a lower resolution's spatial frequency $F'[\xi]$ and a higher resolution's spatial frequency $F[\xi]$ with pixel spatial frequency response

function (*i.e.* bandwidth) $d \cdot H[d \cdot \xi]$ is $F'[\xi] \equiv F[\xi] \cdot d \cdot H[d \cdot \xi]$—again, $d$ is the pixel width. Developing and interpreting indices along the observed landscape's spatial frequency provides clarity about system scale effects. Analysis of spatial frequency is done using the Fourier transform.
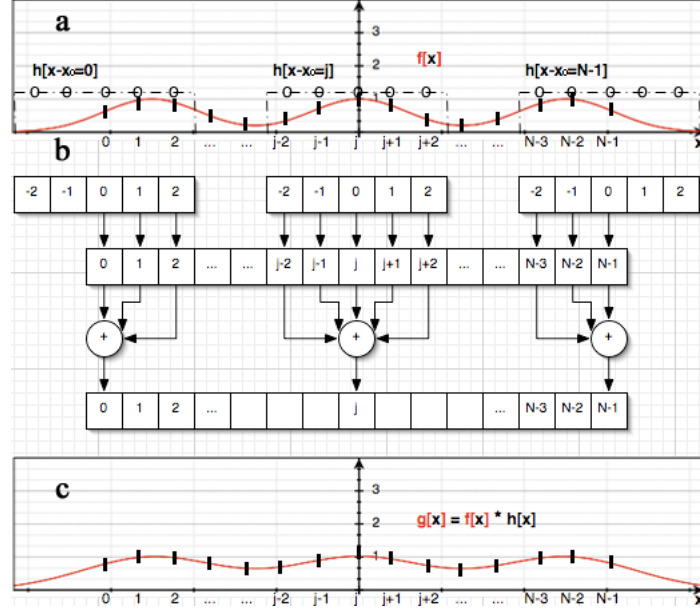


Figure 1.1: The spatial convolution operation for a detector sampled function. Pixel element $h[x - x_0]$ is a sample across the function $f[x]$ at every position $x_0$, for all of the $N$ pixel positions in the scene. Shown in **a** are the areas sampled for $h[x]$ at positions $x = 0, j$ and $N - 1$; where a sample is a simple average of the values contained within $h[x]$. **b** shows this process graphically with "+" as the average, and the resultant convolution $g[x]$ is shown in **c**.

Three indices are proposed to take advantage of this bandwidth interpretation: the Fourier Metric of Proportion (FMP), the Fourier Metric of Fragmentation (FMF), and the least squares Fourier transform (lsFT) method for fractal dimension. Each of these indices are developed, and interpreted within the Fourier transform's spatial frequency domain.

As a measure of landscape composition, FMP reveals how evenly distributed each class patch is across the landscape. A single LCLU class dominating landscape cover may be interpreted as aggressive biotic activity, whereas an evenly distributed landscape LCLU would hold greater class diversity. FMF measures landscape spatial configuration, or the nature of movement between classes. Fractal dimension is an indication of LCLU influence and occupancy across a landscape. A new approach to fractal dimension estimation analysis is presented, and reveals the lsFT method to report a relatively more accurate measure of statistically self-similar fractals. These self-similar fractals are the types of fractal found in landscape patterns [Mandelbrot, 1977].

Chapter 2 discusses the objectives, and directly identifies each goal of this research effort. Chapter 3 serves as a general introduction to the field of Landscape Ecology. Chapter 3 also covers the elementary theory for the practice of Landscape Ecology, the considered Landscape Indicators

3
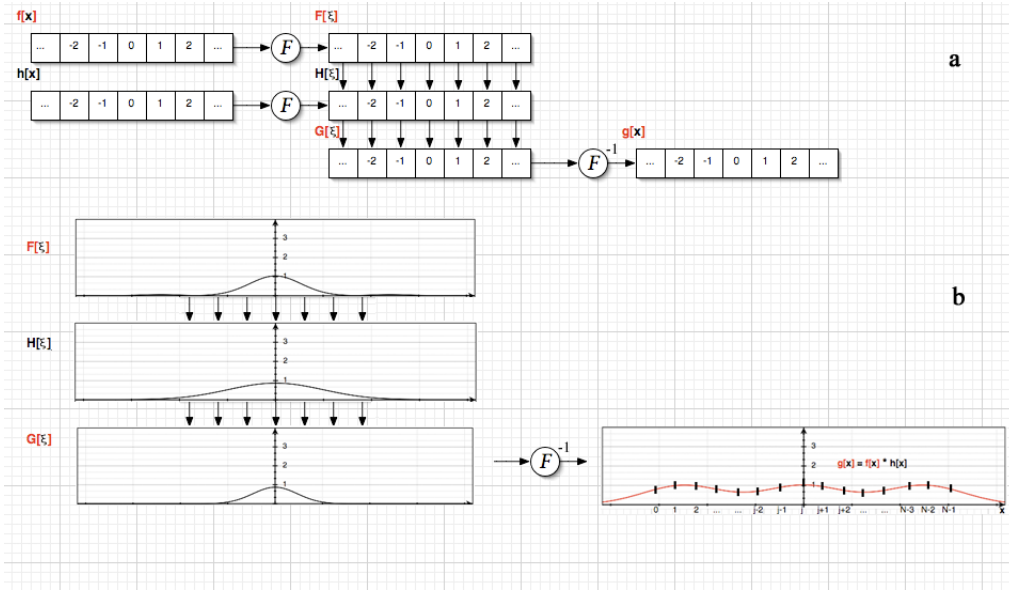
Figure 1.2: The Fourier convolution operation. After being transformed into the Fourier domain, convolution is a simple multiplication between the representative signal $F[\xi]$ and representative pixel element $H[\xi]$. When the resultant product $G[\xi]$ is transformed back into a spatial signal, the expected result $g[x]$ is found. **a** shows this graphically, and **b** plots this process. No matter what spatial resolution window $H[\xi]$ is used the relationship between higher and lower spatial frequencies are always the same (as indicated by the arrows in **a**), and so are easy to compare between multiple resolution images. Both plots $g[x]$ here, and $g[x]$ in Figure 1.1 are the same.

(LI), and appropriate background in Fourier system analysis for the discussion of proposed LI in a Fourier vector space. The approach of each of these Fourier metrics is discussed in Chapter 4, where the concept and theory of each of these Fourier-based LI are considered. Chapter 5 reveals preliminary results of each proposed indicator, and makes a comparison between current and proposed LI. Chapter 6 compares the Fourier-based metrics against traditional Landscape Pattern Metrics (LPM) popular in the literature. This comparison reveals how unique the Fourier-based metrics are. The relevance of these metrics are then determined for fecal-coliform prediction in Chapter 7. Also, a 1991-1992 training and 2000-2001 testing model validation study of South Carolina watersheds is analyzed. Finally, Chapter 8 provides an overview of this work by summarizing each of the preceding chapters.

# Chapter 2

# Objectives

This dissertation develops a systems approach to understanding the long-term effects spatially revealed landscape function have on their environment. The question asked when monitoring landscape function using different types of sensors is, "how to consistently report the change in landscape function pattern, that is ecologically relevant?" The objectives of this proposed work are to increase the reliability of multiple sensor scale Landscape Pattern Metric (LPM) comparisons, as Landscape Indicators (LI), by developing and applying a Fourier systems analysis approach for LPM. Here, LPM quantitatively describe spatially revealed landscape function change, while LI describe spatially revealed and ecologically relevant landscape function. This approach operates on whole images of a class map or image subsets of class map to understand what process(es) encourage the patterns seen across a landscape, independent of the image capture method. The metrics derived this way have advantages over metrics found from traditional local kernel-based edge and gradient operators by eliminating the statistical dependence between LPM, and resolving issues of scalability. The hypothesis: by incorporating information from larger regions of class map, the proposed metrics will be more sensitive to large scale, but subtle land-cover land-use (LCLU) change.

My research goals are to:

1. **Reduce correlation between metrics by developing them under an uncommon (*i.e.* orthogonal), physically representative Fourier vector space.** Each pixel element in the Fourier vector space is spatially independent from one another. This is granted by the orthogonal sinusoidal basis that composes the Fourier Transform operator. Additionally, the Fourier vector can be separated into independent image parameters of magnitude and phase. Combinations of these individual LCLU class magnitude and phase independent parameters prevent metric ambiguity due to the measurement-operator bias. This makes LPM correlation analysis clear when interpreting whether the prescribed relationship is due to the mathematics used to observe the pattern, the image scale (*i.e.* image pixel resolution), or the process being observed.

2. **Relieve misunderstandings between measurement precision and measurement accuracy when reporting LPM from satellite imagery.** How well behaved any LPM might be versus how relevant the LPM is to an observed process are concerns of measurement precision versus measurement accuracy. Including the effects of LCLU map algorithm

classification likelihood, the ability of each metric to consistently report change to within some degree of confidence is evaluated.

3. **Compare image landscape pattern captured under separate image scenarios, along with a statistical measure of confidence.** Expressed as error bounds each metric reports its dependence on the accuracy of the LCLU classification algorithm, LCLU classification due to random image sensor noise, and LCLU classification due to image scale.

4. **Interpret landscape pattern measurement spatially: measuring the entire landscape shape (*i.e.* entire class map), or individual landscape cover interactions (*i.e.* subset of class map, or exchanges between class map subsets).** All of the metrics proposed in this dissertation report local information of landscape change using global parameters of the LCLU map. This global operation along with the ability to locally interpret LCLU class map provide Fourier LPM the flexibility to be applied to any combination of LCLU classes.

# Chapter 3

# Background

## 3.1 Landscape Ecology

German Geographer Carl Troll published a paper titled, *"Aerial Photography and Ecological Studies of the Earth"* where he considered the entire landscape, so the totality of species within an area, to study interactions between environment and vegetation [Troll, 1939]. This was not, and is not, the typical approach to case studies within Ecology—usually ecological investigations simplify their questions by handling a single, homogenous species (*e.g.* camphor tree, lions, wheat, red imported fire ant). This change in philosophy of approach is portrayed in Ingegnoli's 2002 ecotissue[1] model, shown in Figure 3.1. Beginning nearly fifty years later, applications of Troll's landscape level analysis, emphasizing the significance of spatial pattern and scale on ecology across landscapes, began to arise [Baker and Cai, 1992, Gustafson and Parker, 1992, Haines-Young and Chopping, 1996, Krummel et al., 1987, O'Neill et al., 1988, Romme and Knight, 2004, Turner, 1989, Wickham and Norton, 1994]. Dubbed Landscape Ecology, the study of spatial variation in landscapes at a variety of scales has seen much of its activity in the manufacturing of simple spatial metrics for change in scale and pattern, and the theoretical limitations of this approach [IAL, 2007]. With the advent of MacArthur and Wilson's 1967 theory of Island Biogeography [MacArthur and Wilson, 1967] and Levins' [1969] Metapopulation model, a mathematical framework for understanding heterogeneous landscapes using land-cover land-use (LCLU) maps from labeled satellite imagery had been developed. An example of these labeled (*i.e.* classification) maps can be seen in Figure 3.2. Predominantly due to the work of Turner, Gardner, and O'Neill, Landscape Ecology's questions of pattern and scale have been treated by applying landscape pattern metrics[2] (LPM) to classification maps on each LCLU class, or contiguous pixels of a given classification, known as an ecological patch[3]: these metrics being measures of entropy, fractal dimension, regression schemes, moments, etc. [Crews-Meyer, 2006, Turner and Gardner, 2001].

---

[1]Ingegnoli [2002]'s ecotissue separates the ecological landscape into connected macroecologic and microecologic subdivisions.

[2]Quantitatively described, spatially revealed, landscape change.

[3]The smallest contiguous unit of a LCLU class.
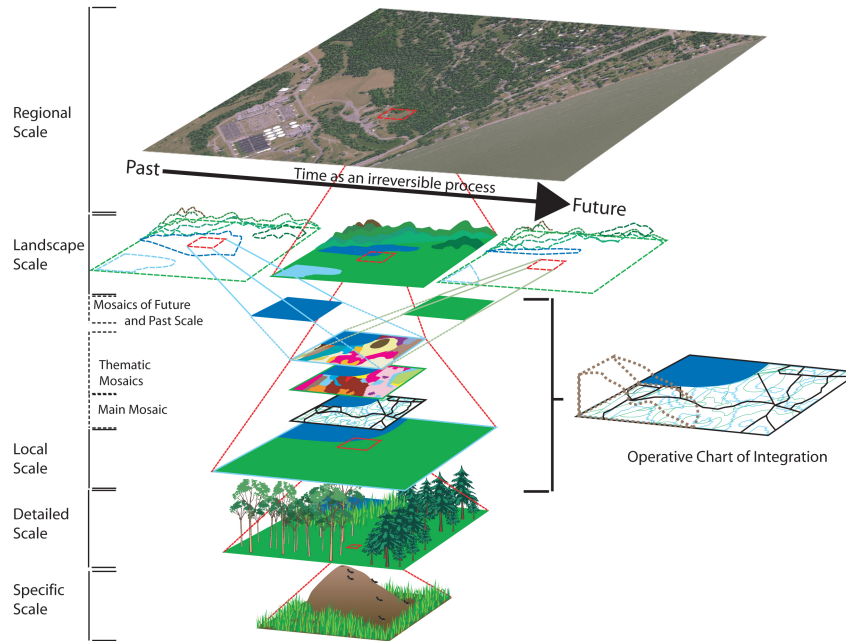
Figure 3.1: The ecotissue model. The basic mosaic is generally the vegetation one where the complex structure of a landscape is integrated over diverse components: temporal, spatial, and thematic. The integration at each stage are intrinsic, meaning every level of the ecotissue model must follow the population dynamics derived from the intrinsic characters at that level of life organization [Ingegnoli, 2002].

### 3.1.1 Elementary Theory of Landscape Ecology

**Island Biogeography**

MacArthur and Wilson's [1967] theory of Island Biogeography, while developed separately from Landscape Ecology, gives credence to Troll's focus on the consequences of landscape heterogeneity by considering any isolated species to be an island unto itself. For instance, mountains surrounded by desert, or an isolated lake in the middle of dry land. The existence of these confined objects is then dependent on two factors: the size of the object, and its proximity to objects that would compromise its existence. So, according to Island Biogeography at the landscape level, any evidence of an individual object's size, and proximity to other objects within an area is indicative of the potential health of that object. Example ecological patches are shown for the emboldened blue LCLU patch (*i.e.* object) in Figure 3.2 of a general water land cover, and the emboldened red LCLU patch of general mixed vegetation/soil land cover). Figure 3.3 below show these Island Biogeography concepts.
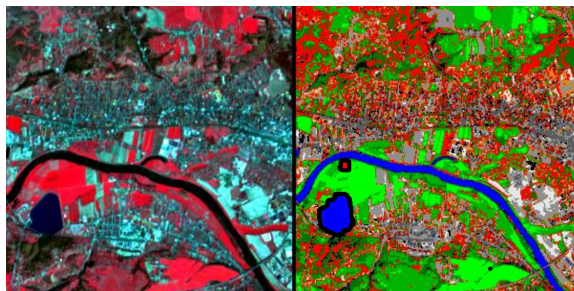
Figure 3.2: A land-cover land-use (LCLU) classification map of Dresden, Germany acquired by the SPOT-3 sensor (22 April 1995). The left image presents surface reflectance after atmospheric correction (RGB=SPOT bands 3/2/1, NIR/Red/Green), and the right image shows the results of the automatic spectral reflectance classification. The map legend goes as: dark to bright green—different vegetation covers; blue—water; brown—bare soil; grey—asphalt, dark sand/soil; white—bright sand/soil; red—mixed vegetation/soil; yellow—sun-flower rape while blooming [ATC, 2007]. Examples of ecological patches are shown by the emboldened blue, water class and emboldened red, mixed vegetation/soil class ecological patches in the spectrally labeled (right-side) image of Dresden.

**Metapopulation**

MacArthur and Wilson's theory of Island Biogeography interprets the potential survival of: a single object, two objects of the same type, and two objects of a different type within a landscape. Each object is a LCLU patch. Levins' Metapopulation model explains how the existence and interaction of these LCLU patches can be represented. The better or more realistic model of species fragmentation—how each LCLU patch is worn away or grows—would be stochastic, but Levins modeled within-species island aggregation, and invasive-species succession deterministically. Using a satellite derived LCLU map as an object process model of either existence or nonexistence in a landscape has consistently given an accurate description of ecological exchange [Gaggiotti and Hanski, 2004, Hanski, 2002, Hanski et al., 2004, Ovaskainen and Hanski, 2004, Singer and Hanski, 2004, Wahlberg et al., 2004, Wiegand et al., 2003]. Levins described Metapopulation as, "a population of populations which go extinct locally and recolonize." The mathematical expression is:

$$\frac{\partial p}{\partial t} = m \cdot p \cdot (1 - N) - \varepsilon \cdot p \tag{3.1}$$

where $p$ is the proportion (fraction) of population centers (*e.g.* LCLU patches), $m$ is the migration (colonization) rate, $\varepsilon$ is the rate at which local populations go extinct, and $N$ is the total number in the population. The existence or nonexistence of a classified pixel, like the ones of a LCLU map in Figure 3.2, is then sufficient to accurately model ecological processes.
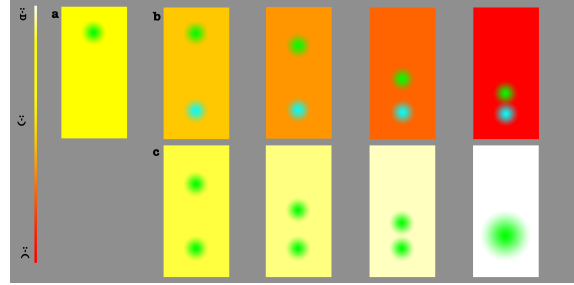
Figure 3.3: The legend for Island Biogeography concepts is located on the far left. The legend goes from a hazardous object state of existence (red), to a neutral state (yellow), and an optimal state (white). In example **a**, the single localized object is at a neutral state of existence. However in the **b** and **c** examples, introducing a second object affects the original object's existence. For **b**, the distance between separate objects (green ball vs. cyan ball) is directly proportional to the green object's existence. Here, cyan identifies the predator and green identifies the prey. For **c**, the distance between similar but separate objects (green ball vs. green ball) is inversely proportional to the green object's increased support and state of existence. The closer similar groups are to each other, the more likely they are to join as one group, which increases preservation. Note: that for any object (green or cyan), the farther away from the center of the ball, the lower the object's likelihood of existence. This is a stochastic (Gaussian) representation of species interaction.

## 3.2 Landscape Pattern Metrics (LPM)

With this new synoptic ecological focus on heterogeneous structure, and a simple but sufficient model of heterogeneous structure dynamics, the utility of remote sensing classification maps becomes obvious. Using the LCLU classification map, LPM have evolved and have been used to quantify aspects of spatial pattern, correlating them to ecological processes [Baker and Cai, 1992, Frohn, 1998, McGarigal and Marks, 1994, O'Neill et al., 1988, Ritters et al., 1995, Turner and Gardner, 2001]—correlated spatial metrics are then interpreted as landscape indicators (LI) of ecological processes. Of that evolution, three metrics have consistently shown a correlation between pattern and process. *Dominance*, *Contagion*, and *Fractal Dimension* are LPM that have been proposed by the Environmental Protection Agency (EPA) Environmental Monitoring and Assessment Program (EMAP) [Agency, 1994] to act as *watershed integrity and diversity* indicators, *landscape stabillity and resilience* indicators, and *biotic integrity and diversity* indicators.

As an example of such an indication of landscape level influence: in an upland catchment of the Calado floodplain along the Amazon, Williams et al. [1997] and Williams and Melack [1997] found large increases in solute mobilization from the upper soil horizons after cutting and burning catchments. Nutrient ratios in streams were altered from a nitrogen-to-phosphorus ratio of 120:1 before deforestation, to a ratio of 33:1 after deforestation [Gergel et al., 2002]. The variability in Calado floodplain catchment nitrogen-to-phosphorus water chemistry was inversely correlated to the 80% change in *presence of forest land-cover* [Williams and Melack, 1997]. *Presence of forest land-cover* is a landscape pattern metric. Williams and Melack observed a direct temporal connection between the stream water chemistry *process*, and the change in landscape *Presence of*

*forest land-cover* LPM *pattern.* Nitrogen-to-phosphorous temporal variability, *caused* by cutting and burning catchments, could be explained to within 80% confidence by LPM. Very encouraging for Landscape Ecology. This approach to LPM landscape analysis is shown in Figure 3.4, and additional examples of landscape indicators are shown in Table 3.1.
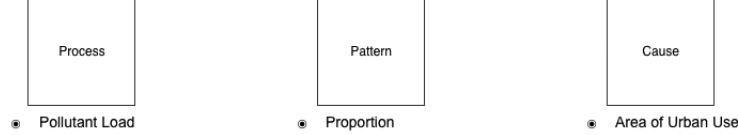


Figure 3.4: The LPM approach to landscape analysis. When using LPM the process being observed must first be defined. After having defined the process being observed, expected process relevant patterns can be used to determine an environmental cause. In the bullets, at every level of analysis, a general description for identifying the cause behind some pollutant loading process is shown using the proportion LPM.

## 3.2.1   Dominance

The measure of landscape class *Proportion* $p_j$ used by Williams and Melack is the fraction of class $j$ occupying the landscape.

$$p_j \equiv \frac{n_j}{N} = \frac{\text{the total number of cells (pixels) of class } j}{\text{the total number of cells (pixels) in the landscape (image)}} \quad (3.2)$$

It is a simple metric, but a metric that correlates most with ecological function [Turner and Gardner, 2001].

A metric of greater complexity, that describes the relative variability in *Proportion* across the landscape, is *Dominance*. *Dominance* measures the equality of LCLU class proportion on the landscape [O'Neill et al., 1988]. The *Dominance* equation is shown in Equation 3.3 where $S$ is the number of classes in the scene, and $p_j$ is the proportion of the $j^{th}$ class of all $S$ classes. Values of $d$ range between 0 and 1. Values near 1 describe a landscape dominated by few classes, while values near 0 describe the proportions of each class being nearly equal. By a units analysis, the *Dominance* $S$-normalization constrains the metric $0 \leq d \leq 1$, and in turn allows comparisons between multiple scenes of variable class amounts. The $p_j$ $N$-normalization allows $d$ results to be compared to registered images with or without the same pixel physical area.

The relative distribution of patches across a landscape is a description of the terrain's ecological navigability. Small patches across a landscape are interpreted as stepping-stones for LCLU patch movement, and would have a low *Dominance* value. Additionally, a network of small patches provide different and supplemental ecological benefits as opposed to a network of large patches (see [Dramstad, 1996]). An example of trends seen using *Dominance* is given in Figure 3.5.

$$d \equiv \frac{\ln(S) + \sum_{j=1}^{S} p_j \cdot \ln(p_j)}{\ln(S)} \quad (3.3)$$

Table 3.1: Landscape Indicators for Monitoring Riverine Ecosystems [Gergel et al., 2002].

| Landscape Indicator | Scale of Measurement | Riverine Component |
|---|---|---|
| Amount of urban land cover distance to stream | Catchment | N, P Osborne and Wiley [1988] |
| % Forest cover, % Agriculture | Catchment | Pb, Cl$^-$ Detenbeck et al. [1993] |
| % Land use from annual agricultural census | Catchment | N, P Johnes et al. [1996] |
| % Nonforest | Catchment | N Sponseller et al. [2001] |
| % Cover, row crop agriculture and wetlands | Catchment | Woody debris Richards et al. [1996] |
| Forest (positively correlated) and agriculture (negatively correlated) | Catchment | Fish communities Wang et al. [1998] |
| % Impervious surface | Catchment | Increase in bankfull discharge and surface runoff Arnold and Gibbons [1996] |
| % Impervious surface | Catchment | Channel widening Booth and Jackson [1997], Dunne and Leopold [1978] |
| % Impervious surface | Catchment | Fish diversity Klein [1979], Schueler and Galli [1992] |
| % Impervious surface | Catchment | Insect/Invertebrate diversity Klein [1979] |
| Agriculture | Catchment and nearshore scales | NO$_3^-$+NO$_2^-$, alkalinity, total dissolved solids Johnson et al. [1997] |
| % Wetlands | Catchment and riparian zone | Dissolved organic carbon Gergel et al. [1999] |
| % Forest | A variety of scales from riparian zone through catchment | Fish and invertebrate diversity Har [1998] |
| Average buffer width, average frequency of gaps | Riparian | Material discharge (theoretical) Weller et al. [1998] |
| % Improved riparian zone | Riparian | Base cations, alkalinity Cresser et al. [2000] |
| Land Use | Nearshore | Nutrients Johnson et al. [1997] |
| % Nonforest | Riparian | Macroinvertebrate density Sponseller et al. [2001] |
| % Land Cover, Land Use | Riparian | Sediment Richards et al. [1996] |
| Length of nonforest along riparian zone | Riparian | Fish abundance Jones et al. [1999] |

### 3.2.2  Contagion

*Probability of Adjacency* $q_{i,j}$ is the probability that a pixel of class $i$ is horizontally or vertically adjacent to a pixel of class $j$. The landscape metric $q_{i,j}$ is normalized by the total number of adjacencies in class $j$, constraining the metric between $0 \leq q_{i,j} \leq 1$.
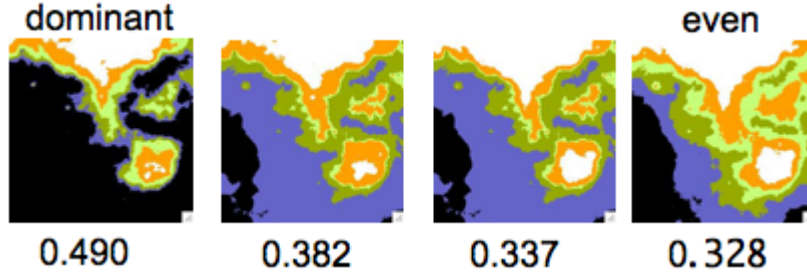
Figure 3.5: Using Gardner's **Rule** program four landscapes were generated, and are shown above. In the leftmost landscape, at a *Dominance* value of 0.490, the black class holds the largest proportion in the scene. The rightmost landscape, at a *Dominance* value of 0.328, has class proportions of 20% for each. The *Dominance* value follows the trend of landscape distribution, as from left-to-right the landscape becomes equally divided.

$$q_{i,j} \equiv \frac{n_{i,j}}{n_j} = \frac{\text{the number of adjacencies between cells (pixels) of classes } i \text{ and } j}{\text{the total number of adjacencies for class } j} \qquad (3.4)$$

When interpreting, low values reveal low adjacency, and high values reveal high adjacency. For $q_{i,j}$ values of one LCLU (where $i = j$) low values describe small, isolated, and dispersed landscape patches; while high values describe highly aggregated, clumpy patches. Due to the normalization across class $j$ adjacencies, comparisons between multiple scenes of variable class amounts but with the same physical dimensions are allowed. The metric can only be interpreted as a measure of relative class adjacency when compared in scenes of different physical dimensions, since there is no normalization of a parameter that refers to the entire scene (*e.g.* the scene wide $N$-normalization in $p_j$).

Providing an increase in sensitivity to $q_{i,j}$—a LOG-amplified measure of classes distributing themselves, through adjacencies—*Contagion* too reveals the overall degree of clumping in the landscape. *Contagion* in Equation 3.5, is constrained between $0 \leq Contagion \leq 1$ and accounts for each edge across the left- and right- horizontal, or top and bottom vertical between class edge pixel through normalizing by twice the number of classes. The description of high or low pattern adjacency and the degree of clumping is the same as for $q_{i,j}$.

The *Contagion* metric is inversely related to the amount of clumping or fragmentation of patches on a landscape [O'Neill et al., 1988]. Within the literature, a metric of fragmentation has been used to monitor ecosystem processes as varied as vegetation dispersal to animal movements [Agency, 1994, 1996, Graham et al., 1991, Gustafson and Parker, 1992, Li and Reynolds, 1993, Turner, 1989, 1990a,b, Turner et al., 1989]. Discontinuities of species coverage, or speciation as indicated by *Contagion*, would lead to the extinction of that species given Island Biogeography. The inverse *Contagion*-to-fragmentation relationship is shown in Figure 3.6 for the projected fragmentation and destruction of the Great Ape Habitat of Central Africa. More about how this metric measures fragmentation can be found in Frohn's *Remote Sensing for Landscape Ecology* [Frohn, 1998].

13
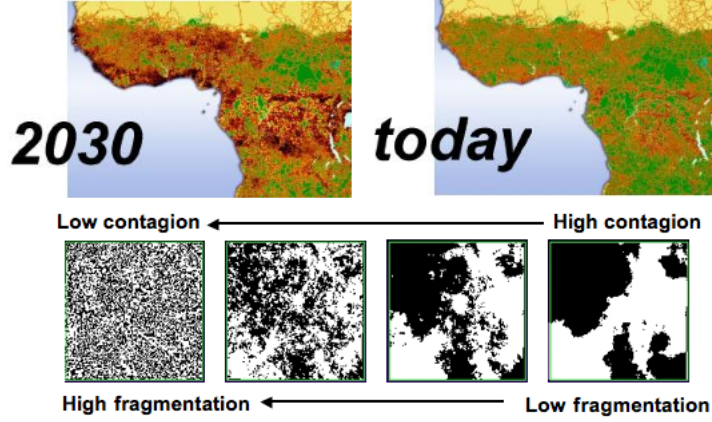
Figure 3.6: On the top, fragmentation and destruction of the Great Ape habitat in Central Africa, from the Global Methodology for Mapping Human Impacts on the Biosphere (GLOBIO) and Great Apes Survival Program (GRASP) projects is shown [GLO, 2001]. On the bottom, the *Contagion*-fragmentation relationship is shown for a single classified species, modeled as a binary image.

$$
\begin{aligned}
Contagion \quad &\equiv \quad \frac{2\ln\left(S\right) + \sum_{i=1}^{S} \sum_{j=1}^{S} \left(p_j \cdot q_{i,j}\right) \cdot \ln\left(p_j \cdot q_{i,j}\right)}{2\ln\left(S\right)} \\
&= \quad \frac{2\ln\left(S\right) + \sum_{i=1}^{S} \sum_{j=1}^{S} \left(\frac{n_{i,j}}{N}\right) \cdot \ln\left(\frac{n_{i,j}}{N}\right)}{2\ln\left(S\right)}
\end{aligned} \tag{3.5}
$$

### 3.2.3 Fractal Dimension

*Fractal Dimension* [De Cola, 1989, Krummel et al., 1987, O'Neill et al., 1988, Turner and Ruscher, 1988] is a metric of shape complexity across the landscape—useful in monitoring the influence of current and potential landscape LCLU. Figure 3.7 shows how human activity on the landscape tends to be identifiable by simple and rectilinear shapes while a more natural landscape is often identified by landscape structure that is not so well defined. This description of spatial signature is one example of the spatial relevance of *Fractal Dimension*. *Fractal Dimension* serves to:

1. Describe trends in ecological navigability:

   - As LCLU dimension increases so does its existence across the landscape (see Figure 3.8) and integer dimensions tend to be well connected encouraging ecological exchange, unlike non-integer dimensions.

2. Identify spatial signatures:

14

- Every LCLU process has a characteristic fractal dimension at their ecological equilibrium[4].

3. Report potential available resources:

  - LCLU with similar dimension tend to exchange landscape cover.

[Milne, 1991b].

The *Fractal Dimension* metric in Equation 3.7 first separates the LCLU map into its patches. For each patch: $P$ is the respective patch perimeter of edges, $A$ is the respecive patch area, and $k$ is a constant of proportionality. A power relationship between pixel perimeter $P$ and pixel area $A$ can be expressed as:

$$P = k \cdot A^{\frac{D}{2}} \tag{3.6}$$

with some constant of proportionality $k$. Equation 3.6 is only scale invariant for true fractals, and $k$ is only known for geometric equilateral shapes ($k = 4$ for squares) and true fractals. How true fractals are defined is discussed in Section 3.2.4.

In an image, the *Fractal Dimension* value is between 0 (with simple shapes) and 2 (for most complex shapes) like those shown in Figure 3.8, which can be solved as:

$$
\begin{aligned}
\ln\left[P\right] &= \ln\left[k \cdot A^{\frac{D}{2}}\right] \\
\ln\left[P\right] &= \ln\left[k\right] + \ln\left[A^{\frac{D}{2}}\right] \\
\ln\left[P\right] &= \ln\left[k\right] + \left[\frac{D}{2}\right] \cdot \ln\left[A\right] \\
D &= 2 \cdot \frac{\ln\left[P\right] - \ln\left[k\right]}{\ln\left[A\right]}
\end{aligned}
\tag{3.7}
$$

Unless the constant of proportionality $k$ is known, there are two unknowns in Linear Equation 3.7. Linear regression solves for the unknown $\ln\left[k\right]$ by determining the $y$-intercept. More about how this metric is a measure of LCLU complexity and potential LCLU occupancy can be found in Frohn's text, *Remote Sensing for Landscape Ecology* [Frohn, 1998] and Milne's article, "Lessons from Applying Fractal Models to Landscape Patterns" [Milne, 1991b] respectively.

### 3.2.4  Limitations

Each of these metrics are strong measures for interpreting landscape ecology, but there are shortcomings. What are shared between each landscape pattern metric are their image edge detection by kernel-based operation, and precarious scalability. This focus on spatial edge pixel creates problems:

---

[4]Using the Barnsley [1988] shadow theorem as his premise, Milne [1991b] suggests that individual patterns made by some process creates a complete coverage, or shadow, on the landscape. Organisms that live long enough to integrate in this way, perceive the landscape as more homogeneous than is apparent in an instantaneous representation of the pattern. This eventual integration is a specie's ecological equilibrium.
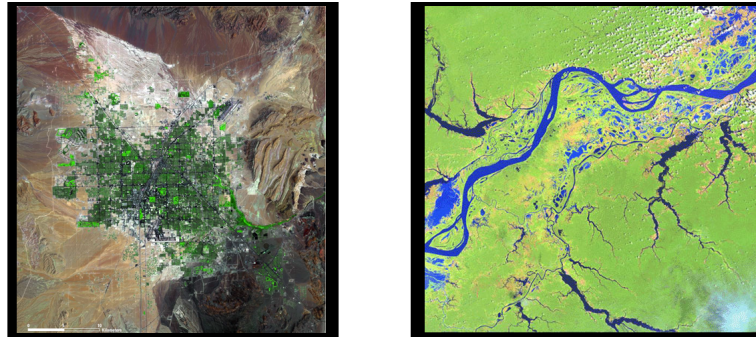
Figure 3.7: On the left is a Landsat image of Las Vegas, Nevada path 39, row 35 taken on August 3, 1984. On the right is a Landsat image of Amazon, Brazil path 224, row 60 taken November 3, 2000. The urban sprawl of Las Vegas has a quickly identifiable rectilinear structure that is characteristic of developed areas of the earth. Brazil's Amazon on the other hand, holds no real rectilinear shape, but a characteristic fractal structure—as would be expected in natural landscapes. This fractal structure of natural landscapes is seen especially along the Amazon river coastline.



Figure 3.8: From left to right an increase of Fractal Dimension is shown. With each additional degree of complexity, the shape is developed from a simple one-dimensional line to a two-dimensional triangle. These middle fractal shapes are what would be expected along the perimeter of natural landscapes [Vassallo, 2007].

1. the measured spatial edge is hard to define and can cause LPM to behave unpredictably across scales;

2. in the cases of *Dominance* and *Contagion*, a logarithmic measure of only pixel edge have no physical spatial interpretation;

3. by monitoring an entire image's edge pixels alone landscape pattern metrics are limited to only report ecological change between adjacent classes [O'Neill et al., 1999];

4. and completely relying on edge measurement hamper LPM diversity.

Landscape Ecology edge detection methods are not defined as every possible edge pixel, but only include a patch's horizontal or vertical edge pixels [Gergel and Turner, 2003]. The typical rule for defining what is a patch is referred to as the *nearest-neighbor rule* (see Figure 3.9). Where for a given class pixel, the *nearest-neighbor rule* makes any horizontally or vertically neighboring pixel of the same class part of an individual patch. In this rule pixels along the diagonal would not be included as LCLU patch. To change LPM results, making them better reflect a particular process, the rule can be more generalized to include diagonal parts. The generalizations of the

*nearest-neighbor rule* are shown in Figure 3.9 as *next-nearest- neighbor* and *third-nearest-neighbor* rules. Patch edges are then defined as the contiguous patch edge pixels after nearest-neighborhood classification.

When the method of edge measurement changes from rule to rule so do the accuracy of landscape pattern metrics that depend on their edge information. This is not a previously unknown source of error. To prevent confusion, Turner and Gardner [2001] suggests authors report which nearest-neighbor method has been used. What has not been addressed is the nearest-neighbor method's effect on measurement error. As the size of these nearest-neighbor methods decrease, so does the average sampling accuracy. This source of error has not been addressed and is camera resolution dependent.
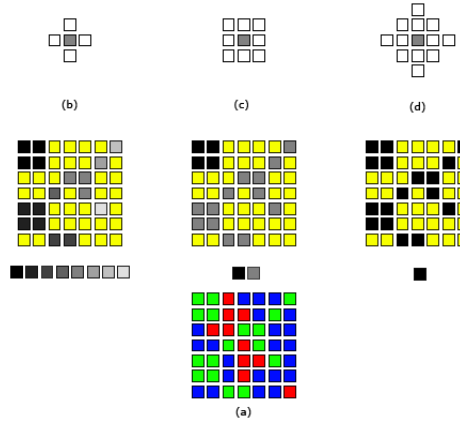


Figure 3.9: Three major neighborhood rules: nearest-neighbor (b), next-nearest-neighbor (c), and third-nearest-neighbor (d) [Gergel and Turner, 2003]. An example landscape class map is shown in (a). The resulting neighborhood rule number for green class patches, and color key are shown in shades of gray under their respective kernel rules. For this example the nearest-neighbor rule produces eight separate green class patches, the next-nearest-neighbor rule produces two separate green class patches, and the third-nearest-neighbor rule produces one green class patch.

A study of the literature shows that landscape patterns are known to nonlinearly change when the spatial resolution of the satellite camera changes. Understanding this, O'Neill found that LPM are fairly consistent, given different scales of spatial resolution [O'Neill et al., 1988]. However, all landscape analysis has not shown consistency between LPM and spatial resolution change [O'Neill et al., 1988]. Wu et al. [2002] studied nineteen LPM and found that only six of the metrics were scaleable from one camera resolution to another. Even more scalable LPM were found by Wu [2004], when he included within class patterns and landscape patterns. Examples of these metrics include *Number of Patches*, *Total Edge*, and *Landscape Shape Index* (see Appendix A). The *Dominance*, *Fractal Dimension*, and *Contagion* metrics are not in this list of scaleable metrics, but Wu et al. [2002] points out that they are useful because of their strong relation to ecological patches. This relationship could be stronger by eliminating any dependence on the image capture method.

LPM must not only be independent of the image capture method (*i.e.* the imaging system), but they should also be *unbiased* measurements of ecologically relevant LCLU activity. Metapopluation models and Island Biogeography theory have LCLU patches obtaining an increasing nonlinear influence on its environment as it increases in size and as distances between other LCLU patches become shorter. *Contagion* and *Dominance* incorporate a notion of LCLU size dependence in their calculation through a measure of patch *proportion* information entropy:

$$\text{Information Entropy} \quad : \quad I\left(\mathbf{X}\right) = \ln\left(\frac{1}{p\left(x_i\right)}\right) = -\ln\left(p\left(x_i\right)\right) \tag{3.8}$$

In Equation 3.8, $p\left(x_i\right)$ can be exchanged for $p_j \cdot q_{i,j}$ or $p_j$ to respectively represent *Contagion* and *Dominance* size weighting coefficients. These size weighting coefficients report a contrary relationship to LCLU size influences than the theory supposes. Figure 3.10 shows how the metrics report a decrease in LCLU patch influence as there is an increase in LCLU patch size. Also, the weightings are similar to exponential—as understood by theory and observation—but trend in a different direction than theory; a reflected, inverse exponential direction. More obviously, *Contagion* and *Dominance* measurements are most misleading by completely ignoring the influence of a physical distance between LCLU patches.
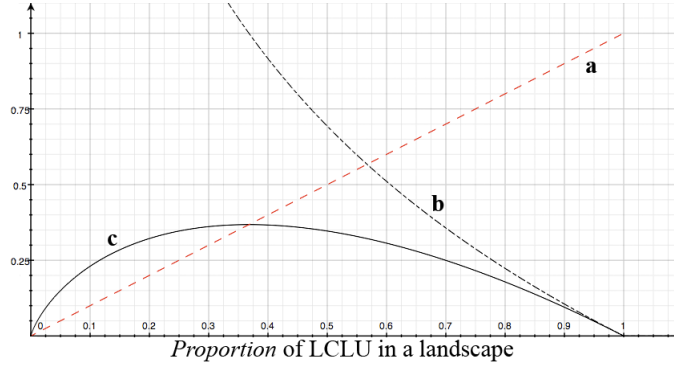


Figure 3.10: Weighting coefficient schema for *Contagion* and *Dominance* measurements. For **a**, the *proportion* model of LCLU size is shown as a red dashed line, and increases directly as LCLU size increases. It is an unbiased measurement of LCLU size. The **b** LCLU size weighting coefficients decrease LCLU significance as LCLU size increase. This is opposite from observations and theory of LCLU population dynamics. The result of applying these coefficients are shown in **c**. **c** is a biased measurement of LCLU activity.

For an example of how *Contagion* average information entropy has no measure of distance, see Figure 3.11. Figure 3.11 shows the contribution of information entropy for each LCLU class edge pixel. *Contagion* reports the average information entropy in LCLU class edge, ignoring where in the scene that edge information exists or how much influence a LCLU patch has on its surrounds. A measure of *Dominance* for Figure 3.11 would be the same at every step, again reporting a misleading measure of the physics as understood by Landscape Ecology theory and observation. A LPM should increase LCLU patch influence as the distance between LCLU patches decreases.

18
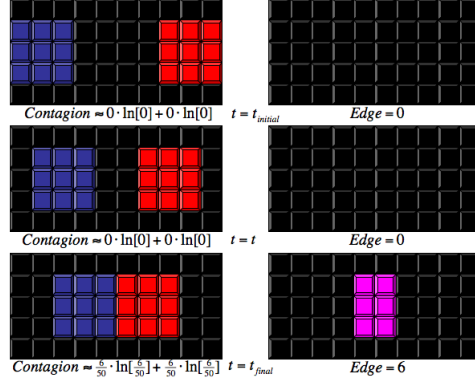
Figure 3.11: Measurement of *Contagion's* edge information entropy in a LCLU map. The average information for image edge pixel is measured using *Contagion* metric. The red and blue, two class, LCLU map in the left column goes from the two classes being initially far apart ($t = t_{initial}$) to finally near (at $t = t_{final}$). As they come closer together over time $t$, there is no change in the number of edge pixels or the *Contagion* value. This does not correspond to LCLU theory (see Section 3.1.1)

Lastly, each landscape pattern metric has an expression of edges or edge related phenomena, like area, in their calculation. This makes the diversity of information relayed by these metrics slim. A well-known example of this is in the relationship between *Contagion* and *Dominance*, as shown in Figure 3.12 [Frohn, 1998]. This dissertation work presents a physical approach to landscape pattern metric generation that relieve these imaging system and metric operator dependent errors.
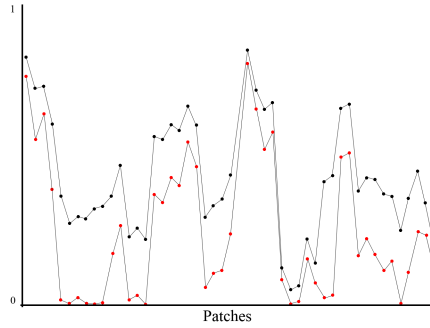


Figure 3.12: The correlation between *Dominance* (top) and *Contagion* (bottom) for patches on a sequoia landscape [Frohn, 1998].

19

**Fractal Dimension Estimation**

The *Fractal Dimension* is considerably more abstract than either of the *Contagion* or *Dominance* LPM. So, before going into the background of how to approach understanding these LPM imaging system dependencies, an entire section is devoted to the most complicated LPM considered in this work. While we have already introduced the mathematical expression of Landscape Ecology's *Fractal Dimension* (see Section 3.2.3) and the previously discussed arguments on kernel-based LPM limitations still apply, a clear approach to how to test for reliable fractal measurements is presented here. First, an introduction to what fractals are and then a discussion on how to consistently measure them.

The best reference for a conversation on fractals can be found in Liebovich's text, *Fractals and Chaos Simplified for the Life Sciences* [Liebovitch, 1998]. For fractals in Landscape Ecology, Milne gives a clear description on how to interpret their results in Chapter 8 of *Landscape Ecology* [Burel and Baury, 2003].

We see in Figure 3.13, that when a non-fractal LCLU patch is magnified no new features are revealed. However, as a fractal LCLU patch is magnified increasingly finer features are revealed. The shapes of the smaller features are similar to the shapes of the larger features in this particular fractal's magnification. The property that defines this fractal characteristic is called self-similarity.
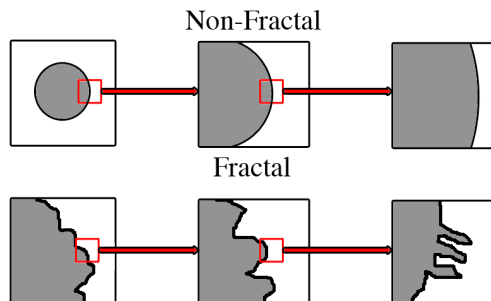


Figure 3.13: Definition of a fractal patch. Non-fractal patches reveal no new features when magnified. When fractal patches are magnified, they reveal similar shapes of the larger patch.

Half the size of the smallest feature in a non-fractal patch is called its characteristic scale. When we measure the patch length and area in a spatial resolution that is lower than this characteristic scale, all of the non-fractal patch features are included. This means the non-fractal patch information is completely represented. Any length or area measurement made that is larger this characteristic scale spatial resolution is correct.

On the other hand, a fractal patch has multiple characteristic scales. Multiple characteristic scales that introduce features over a broad range of sizes. As we measure patch length or area at higher spatial resolutions we include more of the fractal patch's finer features. Inextricably, the resolution used when measuring fractal patches effects any measure of patch length and area since the characteristic scale is variable. Figure 3.14 show both a non-fractal, and fractal pattern at multiple scales.

For self-similar fractals, features at one spatial resolution are related to features at another

Non-Fractal

size of features

1cm —

1 characteristic scale

Fractal

size of features

2 cm ——
1 cm —
.5 cm –
.25cm -

many different scales
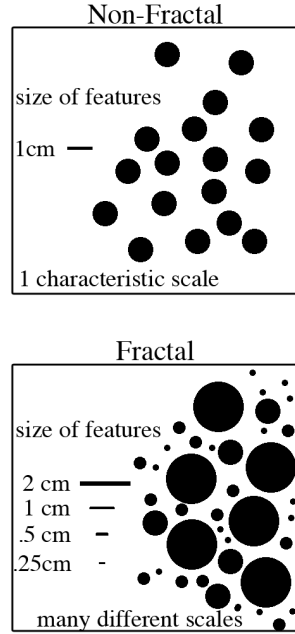
Figure 3.14: Characteristic non-fractal and fractal patches. Non-fractal patches have a singular characteristic scale. Fractal patches have many different scales.

spatial resolution. The smaller features are smaller copies of the larger features. This makes patch lengths measured at a higher spatial resolution longer as finer features are included. How measured properties like length and area depend on the spatial resolution used to observe the fractal is called the scaling relationship. Using Fractal Dimension provides a quantitative measure of scaling by revealing how many new self-similar pieces of a patch are revealed as it is viewed at increasingly higher spatial resolution.

Since LPM are used as correlated Landscape Indicators, landscape analysis of fractal measurements is more interested in precision (consistency) rather than accuracy. Each fractal measurement is normalized by the maximum fractal value possible before being correlated to a process. What precision and accuracy are for LPM is discussed in Section 3.3.2. But until then, understand that a measure of Fractal Dimension that is incorrect, though consistently so, is the acceptable goal for Fractal Dimension LPM here.

One of the most popular applications of fractal models is to obtain consistent records of Fractal Dimension estimates as a measure of resource density [Milne, 1991a, 1992, 1997, Morse et al., 1985, Shorrocks et al., 1991]. If there are 10 LCLU patches of dimension 10, or 100 patches of dimension 1 a landscape of dimension 100 could hold those and any other factor combinations of LCLU patch dimension (*e.g.* 2:50, 4:25, etc.). Understanding this, If a LCLU has a characteristic fractal dimension (*i.e. ecological equilibrium*) which landscapes would be amenable to that LCLU progression or recession could be predicted quantitatively [Burel and Baury, 2003, Liu and Cameron, 2001,

Rychener et al., 2004]. These applications of landscape pattern fractal models continue to extend one into the other. Though, the appropriate measurement of fractals and *fractal-like* patches in an image have remained an elusive task.

When Castelnovo et al. [2002], Saloma and Narisma [1995] recorded the effects of using multiple sampling scenarios for estimating Fractal Dimension, they found the sampling error magnitude was a significant source of statistical error. An error that was very dependent on the fractal pattern being measured. Huang et al. [1994] and Leduc et al. [1994] also varied the number of fractal patch data points being measured, but unlike Castelnovo, Saloma and Narisma they included quantization error. After observing quantization error on the measurement of Fractal Dimension Huang concludes that quantization error due to imaging system *radiometric* resolution limits the precision of measured Fractal Dimension rather than accuracy (*i.e.* the results are erratic)— especially when estimating types of fractal patterns with small fractal dimensions. Kolibal and Monde [1998] complete the imaging system perspective by evaluating Fractal Dimension measurements under the existence of random noise, and found the significance of random noise is dependent on which Fractal Dimension LPM is used. And still, Kolibal and Monde [1998] found the measured accuracy and precision depend on what fractal pattern is being observed.

To get away from measurements dependent on the fractal pattern being observed, and to understand the effects an imaging system has on Fractal Dimension measurement, Fractal Dimension measurements should be separated into two categories: inherent and apparent fractal property. Separating fractal analysis into the *inherent* and *apparent* fractal properties clarifies the results of these tests. Inherent fractal properties include the characteristics of a fractal discussed before: characteristic scale, and self-similarity. The limitations to measuring these inherent characteristics can be found by measuring a self-similar fractal with an increasing number of characteristic scales. The ability of a LPM to measure Fractal Dimension as characteristic scales are removed effects the LPM ability to measure Fractal Dimension captured by any imaging system. Just by observing a fractal, resolution limited imaging systems decrease the number of characteristic scales. Apparent fractal properties are the ways resolution limited imaging systems decrease characteristic scales: spatial resolution, sampling resolution, and radiometric resolution.

The system error varied for analysis in this dissertation work, to measure the least squares Fourier transform method (*lsFT*) Fractal Dimension against relevant Fractal Dimension LPM, and references for their previously made observations are:

1. Inherent fractal property

    - fractal resolution [Brewer and Girolamo, 2006]

2. Apparent fractal property:

    - spatial resolution [Castelnovo et al., 2002, Saloma and Narisma, 1995]
    - sampling resolution [Castelnovo et al., 2002, Huang et al., 1994, Saloma and Narisma, 1995]
    - radiometric resolution as random noise [Kolibal and Monde, 1998]

## 3.3 Systems Analysis

Every image reveals information about its scene. For satellite imagery that information is revealed as horizontal and vertical landscape spatial variability; information that is characteristic for a

particular set of spectral wavelengths, individual spectral wavelength, or some other radiometric parameter. The satellite image is a representative signal of the landscape, and like all signals it can be represented in many ways. For instance, a voltage signal $\hat{v}[t]$ can be represented as a function of time $t$ using the function $\hat{v}[t] = 2 \cdot \cos[2\pi \cdot 10 \cdot t] \cdot V$, with $t$ being measured in seconds and $V$ the voltage amplification. Since $2 \cdot \cos[2\pi \cdot 10 \cdot t] = 2 \cdot \frac{e^{-2\pi \cdot 10 \cdot t} + e^{2\pi \cdot 10 \cdot t}}{2}$ by trigonometry, the same voltage information is equally well represented using the sinusoid's two $10[hz]$ exponential temporal frequency $\nu$ components, in the form $\hat{V}[\nu] = (\delta[\nu - 10] + \delta[\nu + 10]) \cdot V$. $\hat{V}[\nu]$ is the Fourier representation of $\hat{v}[t]$. The Fourier transform is an operator that changes any time-dependent function like $\hat{v}[t]$ and reexpresses it as an equivalent frequency-dependent function like $\hat{V}[\nu]$. While each signal is a representation of the voltage $V$, they are interpreted within separate coordinate systems (domains) of time (seconds) and frequency (hertz) [Easton, 2005, Gaskill, 1978, Hecht, 1987, Ozaktas et al., 2001].

The image being a two-dimensional signal of landscape spatial variability, a two-dimensional Fourier Transform would produce an analogous two-dimensional spatial frequency representation— revealing different ways of interpreting scene phenomena. Understanding an image as a parameter driven representation of the landscape that can be transformed[5] to reveal information is the Systems Perspective. Figure 3.15 shows examples of image signal transformations and their resulting representations.
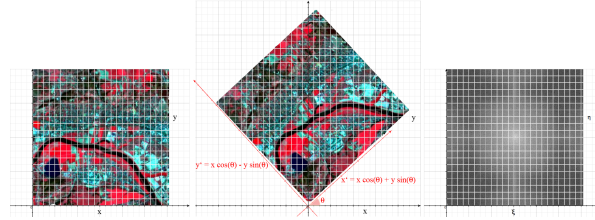


Figure 3.15: From left to right, each image reveals a different representation of the SPOT-3 sensor satellite image of Dresden, Germany (see fig. 3.2): the original radiometric product, the original radiometric product rotated $45^o$, and the log-scaled spatial frequency of the original radiometric product.

A system comprises a rule or set of rules that map an input signal $f$ to an output signal $g$. These rules are called system operators and may alter[6] the input image signal. Alter is being used here as a transformation whose operation removes information from an input signal. A pattern recognition system whose inputs are images, and outputs are labels of recognized images, alters the input image signal. It is impossible to retrieve the original image information from a system operator like this. These types of system operators are referred to as being not invertible. The system model and some example imaging system operators are shown in Figure 3.16.

Not being aware of the effects imaging system operators like these have on LPM, compromises LPM analysis. Figure 3.17 shows the imaging system operators that bias the Landscape Ecology LPM approach to landscape analysis. While the effects caused by imaging system transformations can be corrected for, the effects of imaging system alterations are permanent. To prevent incorrect

---

[5]A reversible operation.

[6]An irreversible operation.
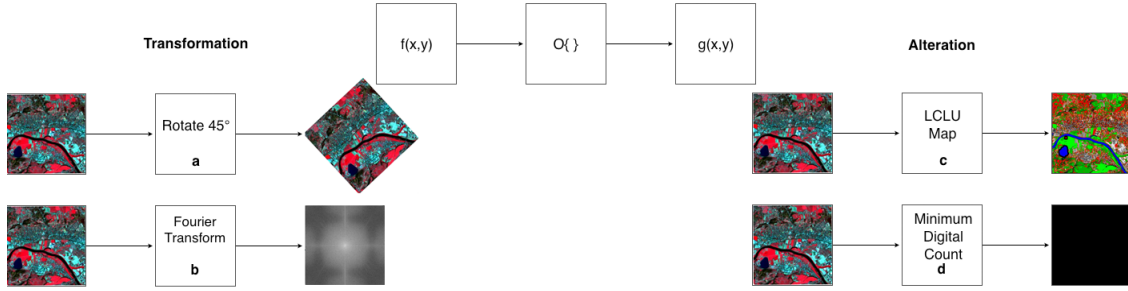
Figure 3.16: Examples of imaging system operations $O\{\}$ on the input SPOT-3 sensor, image signal of Dresden, Germany $f[x, y]$ and their respective output image signals $g[x, y]$. Imaging system **a** rotates the image signal by $45^o$, imaging system **b** takes the Fourier transformation of the image, imaging system **c** is a pattern recognition imaging system that alters the image and labels spectrally separable areas, and imaging system **d** alters the image by a threshold that returns the minimum image signal digital count value.

LPM interpretation due to imaging system alterations, a general measure of confidence can be recorded along with reported LPM. When understood as variable Fourier sampling, LCLU spatial resolution is an invertible imaging system transformation. For the imaging system alterations LCLU spectral and radiometric resolution, their effects can be measured through the precision and accuracy of classification decisions made.
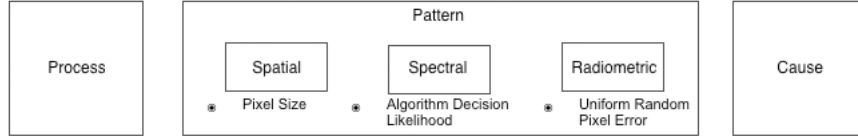


Figure 3.17: The effect an imaging system has on the LPM approach to landscape analysis. When interpreting landscape pattern, an imaging system's spatial, spectral, and radiometric parameters influence observations. In the bullets, at the pattern level of analysis, a description of these imaging system parameters is given.

### 3.3.1 Sampling Theory

Satellite sampling position and sampling area limit the interpretation of LCLU maps. These two spatial parameters alter the image signal, but information is recoverable under certain conditions. In sampling theory, the case for perfect signal (*i.e.* entire landscape) sampling and reconstruction is described by Whittaker-Shannon's sampling theorem [Easton, 2005]. The theorem for an infinite length, one-dimensional landscape line-scan image signal $f[x]$ can be extended to any multidimensional, full extent landscape case $f[x, y, z, t, \lambda]$:

1. Samples of $f[x]$ are generated by multiplying by a COMB function composed of unit-area

24

Dirac delta functions separated by intervals of width $\Delta x$. The mathematics used in this model will be explained later, but in Figure 3.18 this ideal detector array model of equally spaced samples is shown.
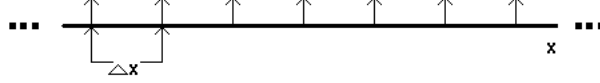


Figure 3.18: One-dimensional sampling array composed of a series of infinitesimal support and finite area Dirac delta functions separated by intervals $\Delta x$.

2. If the width $\epsilon$ of the smallest object being observed in the landscape $f[x]$ is larger than twice the sampling interval (*i.e.* $\epsilon > 2 \cdot \Delta x$), then $f[x]$ can be recovered perfectly from the complete (infinite) set of samples obtained at intervals $n \cdot \Delta x$ ($-\infty \leq n \leq +\infty$) along the detector array in Figure 3.18.

3. $f[x]$ is recovered from $f[n \cdot \Delta x]$ through an interpolating method that estimates the intermediary signal between samples using each of the infinitesimal samples, while putting emphasis on samples closest each other. This ideal interpolant is the SINC function, and is given by:

$$f[x] = \sum_{n=-\infty}^{+\infty} f[n \cdot \Delta x]\, \text{SINC}\left[\frac{x - n \cdot \Delta x \cdot \epsilon}{\epsilon}\right] \tag{3.9}$$

An example of the SINC interpolant and a comparison with common interpolants is shown in Figure 3.19. In this example, each interpolant reconstructs the signal, but only the SINC interpolator accurately reconstructs the signal.

These conditions, however, are unrealistic for any real imaging system or experimental design:

1. It is not possible to sample the amplitude of $f[x]$ exactly at any sampling location. Instead, each sample location is an average across the area of the detector element $d$. Figure 3.20 shows this realistic sampling array.

2. It is impossible to infinitely sample the landscape $f[x]$ to obtain perfect reconstruction of the landscape signal. While in some cases the smallest element of interest $\epsilon$ may be recoverable (*i.e.* $\epsilon > 2 \cdot \Delta x$), no imaging system captures the entire extent of a landscape.

3. Reconstruction of any function requires filtering by an infinite-length bipolar SINC-function interpolator. In reality, a filter can not have infinite length.

Given these limitations, realistic interpretation across image scale is done by considering the spatial frequency bandpass (*i.e.* spatial frequency window) of the sampling array (*i.e.* detector). As the detector element width $d$ gets larger and the signal decreases resolvability fewer spatial frequencies are passed, the spatial frequency window size decreases, and measurement accuracy
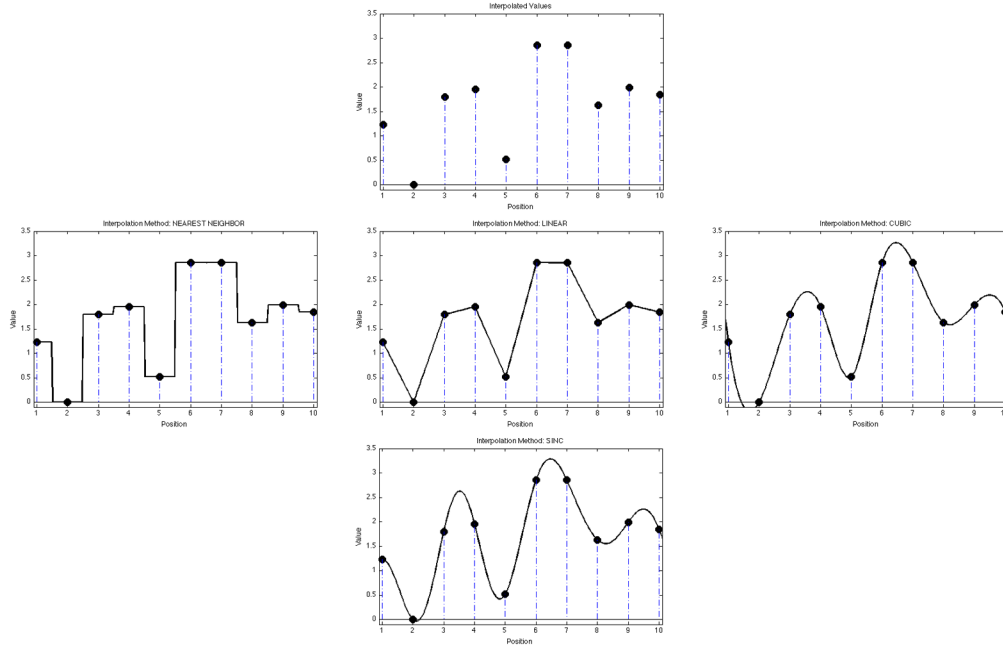
Figure 3.19: One-dimensional interpolants. Each interpolant is labeled above their respective reconstructions, and include: Nearest-Neighbor, Linear, Cubic, and SINC. Notice how the interpolations become increasingly smooth and approach the SINC interpolated reconstruction.
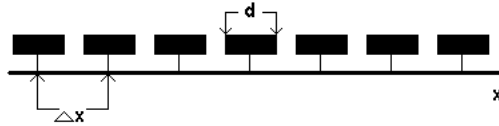


Figure 3.20: One-dimensional sampling array composed of rectangular elements of width $d$ separated by intervals $\Delta x$.

decreases. These decreases in pixel measure confidence are quantifiable. The relationship between a spatially varying lower resolution function $f'[x]$ and a spatially varying higher resolution function $f[x]$ using detector element $h[\frac{x}{d}]$ is $f'[x] \equiv f[x] * h\left[\frac{x}{d}\right] = \int_\alpha f[\alpha] \cdot h[\frac{\alpha - x}{d}]\partial\alpha$. When interpreting the observed landscape along its spatial frequency, scale effects are introduced as a smoothly varying, windowed, function of bandwidth. The relationship between a lower resolution's spatial frequency $F'[\xi]$ and a higher resolution's spatial frequency $F[\xi]$ with detector spatial frequency response function (*i.e.* bandwidth) $d \cdot H[d \cdot \xi]$ is $F'[\xi] \equiv F[\xi] \cdot d \cdot H[d \cdot \xi]$. Within the spatial frequency window, so for reasonably unaliased frequencies, the trend of representative energy $\int \mid f'[x] \mid^2 \partial x$ from one detector resolution to another describes a decrease of effective image signal energy as the detector size increases. This decreasing trend significantly effects any following image operation,

26

especially in the case of landscape pattern metrics [O'Neill et al., 1988, Wu, 2004, Wu et al., 2002], and is shown for some example LCLU images in Figure 3.21.
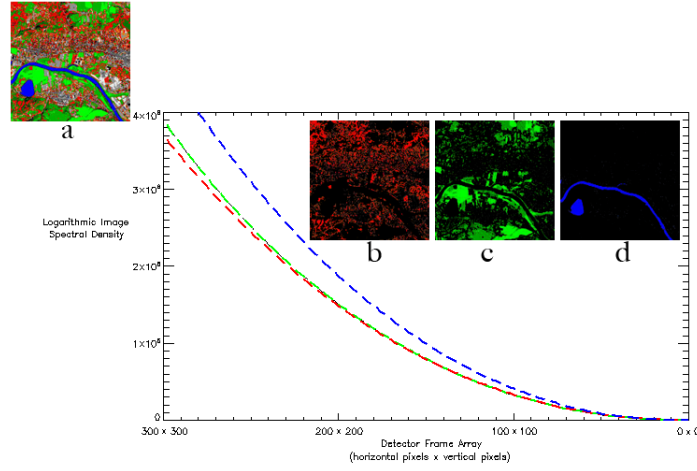


Figure 3.21: Decreases in image spatial frequency density as pixel size increases. Keeping the imaging system height and orientation constant over a scene: as pixel size $d$ increases, less pixels can fit within a frame array and image resolution decreases. Using the labeled SPOT-3 sensor image signal of Dresden, Germany **a** (see Figure 3.2) the log-scaled spatial frequency energy $\log \left[ \int \mid f'[x; d] \mid^2 \partial x \right]$ for each detector frame array is reported. While the general trend is the same, the mixed vegetation/soil land cover **b**, the different vegetation land cover **c**, and the water land cover **d** each have separate trends. LCLU trends across image scales are scene dependent.

### 3.3.2   Precision and Accuracy

Within each of the system operations, every observation of $f[x]$ can be affected by noise; where observations $\hat{f}[x]$ with error are modeled as $\hat{f}[x] = a \cdot f[x] + c$. The effects of system operator noise, either multiplicative $a$ or additive $c$, are quantifiable. By measuring how far away observations $\hat{f}[x]$ are from expectations $f[x]$, system operator accuracy can be reported. With accuracy defined as the closer the model $\hat{f}[x]$ is to the expectation $f[x]$. A measure of confidence in how consistently well an observation's accuracy is measured is what is known as precision. An example of these errors are shown in Figure 3.22.

One measure of confidence in what a system operation is reporting would be variance. When looking across each point $i$ of the observation $\hat{f}[x_i]$, the magnitude of any error from the expected observation $f[x_i]$ would be the deviation. When the deviation is different at any point $i$, the average model deviation, or variance, can be reported. The closer each individual deviation's magnitude $\mid f[x_i] - \hat{f}[x_i] \mid$ is to 0, the more precise. A measure of confidence that satisfies measuring typical observation deviation from what is expected is the residual sum of squares ($RSS$). $RSS$ is shown in Equation 3.10 using the observed multiplicative deviation $\bar{a}$ and the observed additive deviation $\bar{c}$.
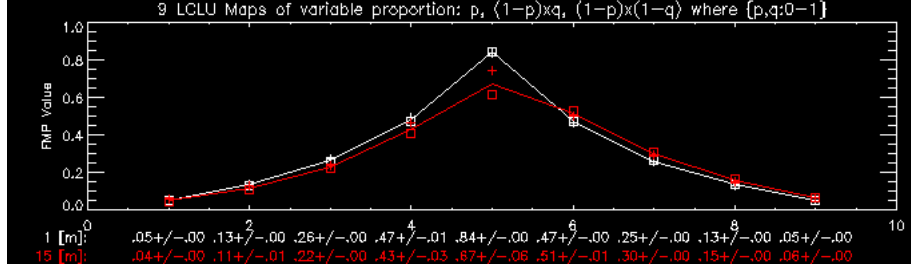
Figure 3.22: A plot of FMP values for nine separate LCLU maps at $1[m]$ and $15[m]$ spatial resolutions. The white $1[m]$ spatial resolution values are the real (accurate) values of FMP for these LCLU maps. The upper and lower bound of the uncertainty are $+$ and $\boxdot$, respectively. As shown in the white text below the plot, all the $1[m]$ FMP values have perfect precision, $\pm 0.00[units]$ uncertainty. Inaccuracies can be seen in the red $15[m]$ spatial resolution values, where images 1 and 9 have perfect precision $\pm 0.00[units]$ with $0.01[units]$ inaccuracy. For image 6, the precision error is $\pm 0.01[units]$, with $0.04[units]$ inaccuracy at $15[m]$ resolution.

$$RSS = \sum_{i=1}^{N}(f[x_i] - \hat{f}[x_i])^2 = \sum_{i=1}^{N}(f[x_i] - (\bar{a} \cdot f[x_i] + \bar{c}))^2; \qquad (3.10)$$

$$\bar{a} = \frac{\sum_{i=1}^{N}\hat{f}[x_i] \cdot f[x_i] - N\overline{\hat{f}[x_i]} \cdot \overline{f[x_i]}}{\sum_{i=1}^{N}(\hat{f}[x_i])^2 - N(\overline{\hat{f}[x_i]})^2},$$

$$\bar{c} = \overline{f[x_i]} - \bar{a}\overline{\hat{f}[x_i]}$$

Each measure of difference at observation $i$ is correlated, so equation 3.10's step 1 linear difference at each observation point $(f[x_i] - \hat{f}[x_i])$ is mathematically allowed. For multiple uncorrelated observations, $RSS$ adds the deviations in quadrature $\sum_{i=1}^{n}(f[x_i] - \hat{f}[x_i])^2$. In practice, when reporting confidence of multiple system operators—for total system noise $n_t$, and assuming the observed noise is 0 on average—expected deviation of the complete system of uncorrelated system operators do tend to add in quadrature as well [Schott, 2007]:

$$\sigma_t^2 = \sigma_t^2[\sigma_1 + \sigma_2 + \ldots] = \sigma_1^2 + \sigma_2^2 + \ldots = RSS_1^2 + RSS_2^2 + \ldots \qquad (3.11)$$

At every stage, in any level, a measure of error can be reported—$\sigma_i$. The total system measure of confidence $\sigma_t^2$ is the quadratic sum of each operator error. The quadratic sum of each system operator's residuals is correct for a series of system operators, however the total system measure of confidence from the product of two systems is called the joint variance, and shown in Equation 3.12.

$$\sigma_t^2 = \sigma_t^2[\sigma_i \cdot \sigma_j] = \sigma_i^2 \cdot \overline{f[x_j]}^2 + \sigma_j^2 \cdot \overline{f[x_i]}^2 + \sigma_i^2 \cdot \sigma_j^2 \qquad (3.12)$$

The LPM approach presented here includes precision estimates from each metric and the LCLU map. The considered LCLU map confidence estimates are:

Spatial Confidence [Schott, 2007]

- Resolution: $GSS$, $EIFOV$, or $GIFOV$
- Registration: $\Delta x$, $\Delta y$

Spectral and Radiometric Confidence [Schott, 2007]

- LCLU map class likelihoods: target detection false negatives (see, Figure 3.24)

Background for LPM accuracy across multiple sensor scales and the precision of spectral and radiometric observations are discussed in the **Sensor Scale Spectral Density Analysis** and **Receiver Operating Characteristics** subsections below.

### Sensor Scale Spectral Density Analysis

For this model, assume a one-dimensional sampling array constructed of identical rectangular elements of width $d$ centered at integer multiples of the sampling interval $\Delta x$, as is shown in Figure 3.23 and described for one of those detector elements in Equation 3.13. The measured output signal at a sample is proportional to the integral of the input signal over the surface of the identical detector. The signal evaluated at the element of the sample array is a function of $x$, and $x'$ is the sampled domain of the continuous function $x$.
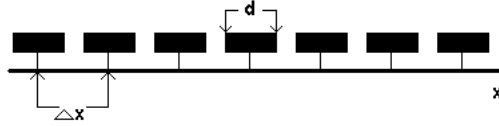


Figure 3.23: One-dimensional sampling array composed of rectangular elements of width $d$ separated by intervals $\Delta x$.

$$\frac{1}{d} \int_{x=\frac{-d}{2}}^{x=\frac{d}{2}} f[x] \partial x = \int_{x=-\infty}^{x=\infty} f[x] \cdot \frac{1}{d} \text{RECT} \left[\frac{x}{d}\right] \partial x \tag{3.13}$$

This integral evaluates the average value of $f[x]$ across the detector surface area $d$. The amplitude of the signal measured by a similar detector located at position $x = n_0 \cdot \Delta x$ along the detector array, is obtained by translating the coordinate $x$ to the position some integer number $n_0$ of detector widths $\Delta x$ away. Equation 3.14 shows the detector array sampling function equation for a single detector at position $n_0$.

$$\frac{1}{d} \int_{x=n_0\Delta x - \frac{d}{2}}^{x=n_0\Delta x + \frac{d}{2}} f[x] \partial x = \int_{x=-\infty}^{x=\infty} f[x] \cdot \frac{1}{d} \text{RECT} \left[\frac{x - n_0\Delta x}{d}\right] \partial x \tag{3.14}$$

Equation 3.14 describes a single detector sample of the input function $f[x]$, but can be generalized for the detector samples at every location along the detector array. This is done in Equation 3.15 by varying integer position $n_0$ to every integer value $n$, and placing the weighting of the detector response at its respective detector sampling position $\delta[\frac{x'-n\Delta x}{d}]$ where the sampled position $x = x'$.

$$
\begin{aligned}
\sum_{n=-\infty}^{+\infty} \frac{1}{d} \int_{x=n\Delta x-\frac{d}{2}}^{x=n\Delta x+\frac{d}{2}} f[x]\partial x &= \sum_{n=-\infty}^{+\infty} \int_{x=-\infty}^{x=\infty} f[x] \cdot \frac{1}{d} \int_{x'=-\infty}^{x'=\infty} \text{RECT}\left[\frac{x-n\Delta x}{d}\right] \cdot \delta\left[\frac{x'-n\Delta x}{d}\right] \partial x'\partial x \\
&= \sum_{n=-\infty}^{+\infty} \int_{x'=-\infty}^{x'=\infty} \int_{x=-\infty}^{x=\infty} f[x] \cdot \frac{1}{d} \text{RECT}\left[\frac{x-x'}{d}\right] \partial x \cdot \delta\left[\frac{x'-n\Delta x}{d}\right] \partial x' \\
&= \sum_{n=-\infty}^{+\infty} \int_{x'=-\infty}^{x'=\infty} \int_{x=-\infty}^{x=\infty} f[x] \cdot \frac{1}{d} \text{RECT}\left[\frac{x-x'}{d}\right] \partial x \cdot d \cdot \delta\left[x'-n\Delta x\right] \partial x' \\
&= \sum_{n=-\infty}^{+\infty} \int_{x'=-\infty}^{x'=\infty} f[x'] \star \text{RECT}\left[\frac{x'}{d}\right] \cdot \delta\left[x'-n\Delta x\right] \partial x' \qquad (3.15)
\end{aligned}
$$

where $\star$ is the correlation operator

The integral property of the delta function was used in the first step of equation 3.15, the linearity of the summation operator and the sifting theorem of the Dirac delta function were used in the second step, and the Dirac Delta scaling property was used in the third. Equation 3.15 is the mathematical equation for the sampled function obtained by integrating a continuous signal over an array of identical rectangular detectors of width $d$. This means that the realistically sampled signal is obtained by correlating the continuous input signal by the detector response function, and then sampling that intermediate signal at the centers of each detector.

As mentioned before, the smooth, continuous trend in figure 3.21 represents image spectral density for variable pixel detector sizes. Image spectral density which can be mathematically expressed as the observation's summed squared vector magnitude $\int |f[x]|^2$, has equivalent spatial and spectral representations:

$$
\int_{-\infty}^{\infty} |\hat{f}[x]|^2 \partial x = \int_{-\infty}^{\infty} |\hat{F}[\xi]|^2 \partial \xi,
$$

where,

$$
\begin{aligned}
\hat{f}[x] &= \sum_{n=-\infty}^{+\infty} \int_{x'=-\infty}^{x'=\infty} \int_{x'=-\infty}^{x'=\infty} f[x'] \star \text{RECT}\left[\frac{x'}{d}\right] \cdot \delta\left[x'-n\Delta x\right] \partial x' \\
&= \sum_{n=-\infty}^{+\infty} \int_{x'=-\infty}^{x'=\infty} \int_{x'=-\infty}^{x'=\infty} \int_{\xi=-\infty}^{\xi=\infty} F[\xi] \cdot \text{SINC}\left[d \cdot \xi\right] * \frac{1}{d} \cdot e^{-\imath 2\pi n\Delta x\xi} \cdot e^{+\imath 2\pi x'\xi} \partial \xi \partial x'
\end{aligned}
$$

$$(3.16)$$

Equation 3.16 shows the Fourier expansion of $\hat{f}[x]$. As the spectral window of that expansion $\text{SINC}\left[d \cdot \xi\right]$ expands, the detector size increases, image-wide resolution decreases, and the spectral

density is effected by $\frac{1}{d}$. these effects are reflected in the smooth continuous trend of image spectral density.

**Receiver Operating Characteristics**

In this subsection, a brief introduction to the concepts of target detection is made for the accurate detection of LCLU map classification. An expansive introduction and multiple recipes for assigning pixels to a thematic class can be found in Schott [2007] Chapter 9.2, *Image Classification*. Additionally, Fawcett [2004] provides a general introduction to receiver operator characteristics theory for research scientists and engineers.

For this discussion on LCLU map uncertainty, only receiver operating characteristics (ROC) curve confidence parameters are used. These parameters assume reference data is available, and describe four pixel classification situations that may be observed:

1. **True Positive:** A pixel assumed to belong to class $i$, does belong to class $i$.

2. **True Negative:** A pixel assumed not to belong to class $i$, does not belong to class $i$.

3. **False Positive:** A pixel assumed to belong to class $i$, does not belong to class $i$.

4. **False Negative:** A pixel assumed not to belong to class $i$, does belong to class $i$.

Typically, reference data is an original source image of known LCLU class. Every pixel in this image is compared to every pixel of the estimated LCLU map for ROC analysis. Hopefully, True Positives and True Negatives are maximized, while False Positives and False Negatives are minimized.

For pattern recognition systems without original source imagery, the reference data are any class likelihood estimates used for pixel classification. These likelihoods are produced by Bayesian supervised classification methods (see [Schott, 2007]). In supervised classification the user identifies the type and number of LCLU classes in the scene; unlike with unsupervised classification methods that develop decisions ad hoc without user intervention. Only the supervised classification method accuracy will be addressed here.

As an example, Gaussian Maximum Likelihood (GML) supervised classification of satellite imagery assigns normally distributed likelihoods to each pixel, according to the brightness value of a pixel's digital count:

$$
\begin{aligned}
p_{DC|j} &= \frac{1}{\sqrt{2\pi\sigma_j^2}} e^{-\frac{(DC - \overline{DC_j})^2}{2\sigma_j^2}}; \\
\overline{DC_j} &= \frac{\sum_{q=1}^{Q} DC_{j,q}}{Q}, \\
\sigma_j^2 &= \frac{\sum_{q=1}^{Q} \left( DC_{j,q} - \overline{DC_j} \right)^2}{Q-1}.
\end{aligned}
\tag{3.17}
$$

The GML model class $j$ average digital count $\overline{DC_j}$ and class $j$ digital count variance $\sigma_j^2$ are taken from a sample of $q = 1, 2, \ldots, Q-1, Q$ satellite image pixels that best represent the interested

class. This is done for every LCLU class, and are conditional probabilities. Called conditional probability $p_{DC|j}$, because it describes the probability of a digital count $DC$ occurring, on the condition that it is in class $j$. These conditional probabilities are compared against each other using pixel proportion, $p_j$, to find the most likely LCLU class assignment, $p_j \cdot p_{DC|j}$, for each pixel brightness (see, Figure 3.24).
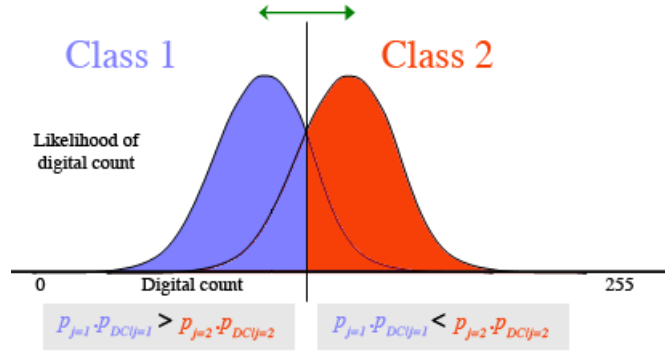


Figure 3.24: Two class conditional likelihood distribution. When the blue Class 1 Gaussian likelihood of digital count $p_1 \cdot p_{DC|1}$ is greater than the red Class 2 Gaussian likelihood of digital count $p_2 \cdot p_{DC|2}$, the respective digital count is to Class 1. The digital count is assigned to the red Class 2 Gaussian likelihood when it is the maximum likelihood. The vertical decision threshold for this model occurs where blue Class 1 and red Class 2 likelihoods are the same.

By allowing model parameters to vary in time (*i.e.* $\overline{DC_j}[t]$ and $\sigma_j^2[t]$) , this supervised classification method becomes a population dynamics model for LCLU class spatial existence. Similar to Metapopulation process models (see Section 3.1.1). LCLU class likelihoods $p_{DC|j}$ go from least likely to exist $p_{DC|j} \approx 0$, to most likely to exist $p_{DC|j} \approx 1$ in an individual class. The GML likelihood of LCLU existence varies exponentially in space, as do Metapopulation models. This means that these class likelihoods have a potentially accurate spatial interpretation. The GML discrimination metric has pixel digital counts $DC$ that are most likely for class $j$, at the average digital count value $\overline{DC_j}[t]$, and each GML class likelihood decreases away from each class average Digital Count value $\overline{DC_j}[t]$, according to the digital count variance $\approx e^{-\sigma_j^{-2}[t]}$. Contiguous patches are most likely unmixed pixels and have high values of likelihoods. Small patches and patch edges would most likely be mixed pixels and have the least likely class likelihood values.

In the LPM presented here uncertainty in a pixels' class likelihood will have degrees of uncertainty. The lower bound LCLU pixels have likelihoods of class $j$ True Positive pixels $TP$, the upper bound LCLU pixels have likelihoods of class $j$ True Positive and False Negative pixels $TP + FN$, and the observed LCLU pixels have likelihoods of class $j$ pixels between the two bounds, $TP + \frac{FN}{2}$. Three, two-class, GML prediction scenarios with uncertainty assignments are shown in Figure 3.25. LPM are applied to each map of class $j$ pixels associated with the Lower Bound, Upper Bound, and Observed uncertainties to produce Lower Bound, Upper Bound, and Observed LPM values.
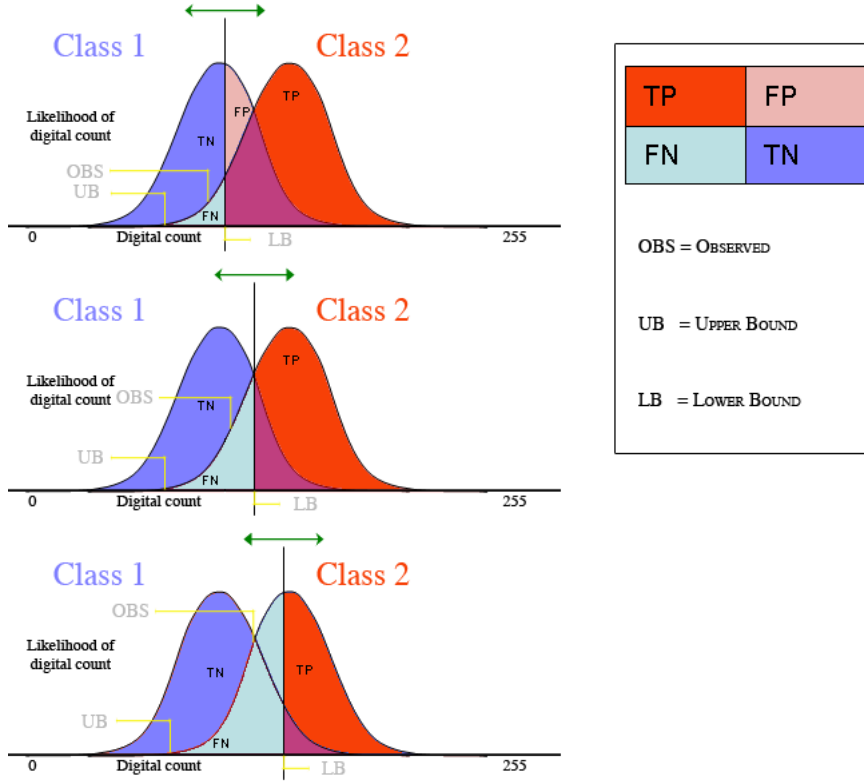
Figure 3.25: Statistical pattern recognition measures of confidence for the red Class 2 decision. For each class decision, the uncertainty assignments lower bound (LB), upper bound (UB), and observed (OBS) are shown by the yellow arrows. Each ROC likelihood is labeled as True Positive (TP), True Negative (TN), False Positive (FP), and False Negative (FN). The ROC legend is boxed on the right. Notice how the observed likelihood for Class 2, assigned at $TP + \frac{FN}{2}$, is at the statistical average of the False Negative parameter.

## 3.4 Fourier

In Section 3.1 we obtained a workable knowledge of Landscape Ecology theory. Emphasizing the concepts concerning whole map analysis using LCLU shape characteristics. Section 3.2 reviewed relevant LCLU landscape pattern metrics, as well as what they attempt to measure and the potential limitations of their approach. And, Section 3.3 discussed the systems based approach, and the system operator models used here.

The tool used to bring all these ideas into application is the Fourier transform. How each of these ideas relate will be answered in this section. An explanation of the Fourier transform from Fourier sinusoids will reveal the intuitive, geometric interpretation of Fourier mathematics. Whole class map LCLU functions will be introduced as vector inputs into the Fourier transform. And,

the benefit of Fourier analysis for the interpretation of a general LCLU shape will be examined by Fourier theorem and properties.

### 3.4.1 Fourier Series

In 1822 politician, mathematician, and historian Jean Baptiste Joseph Fourier published, "*The Analytical Theory of Heat*" [Fourier, 1822]. Fourier's thesis studied how temperature varied in time after some initial temperature distribution $f[x]$. For the way that heat flows from one part of the body to another part of the body Fourier proposed a governing model.

He began with a heated ring, with some initial temperature $f[x]$, where $x$ is a point on the circle. The initial temperature distribution is assumed to cool down and redistribute itself as a function $u(x, t)$ (*i.e.* the temperature at position $x$ at time $t$).

Periodicity enters the model as periodicity along the ring in space. The temperature at $x$ and $x + \pi \cdot r^2$ are equal when the temperature is periodic as a function of position $x$ on the ring. Mathematically, this is expressed as:

$$f[x] = f[x + T], \qquad (3.18)$$
$$u[x, t] = u[x + T, t]. \qquad (3.19)$$

The initial temperature distribution $f[x]$ is periodic, with period $T$, as a function of $x$. These equations assume observations of any (temperature) distribution $u[x, t]$ at position $x$ for constant time $t$ to have a periodicity, $T$.

Fourier proposed a series of sinusoids to accurately model periodic phenomena. Using a summation of weighted, complex exponentials, he expressed the model as:

$$u[x, t] = \sum_{k=-\infty}^{\infty} C_k[t] e^{i2\pi k x}. \qquad (3.20)$$

The variable temperature distribution $u[x, t]$ is periodic in the spatial variable, so the variable in the periodic complex exponential is $x$. The time dependence is in the coefficient $C_k[t]$.

To solve for the time dependent coefficients, Fourier observed that independent of periodicity or initial temperature distribution heat flow is governed by a partial differential equation related to time. The partial differential heat equation states:

$$u_t = a \cdot u_{xx}, \qquad (3.21)$$

the time-derivative of a temperature $u_t$ is proportional to the second $x$ derivative $u_{xx}$, where $a = \frac{1}{2}$ is a constant.

Using the partial differential equation in Equation 3.21 on $u[x, t]$ in Equation 3.20, the Fourier equation for heat diffusion along a ring is:

$$\sum_{k=-\infty}^{\infty} C_k'[t]e^{\imath 2\pi kx} \quad = \quad \frac{1}{2} \cdot \sum_{k=-\infty}^{\infty} C_k[t](-4\pi^2 k^2)e^{\imath 2\pi kx}$$

from,

$$u_t \quad = \quad \sum_{k=-\infty}^{\infty} C_k'[t]e^{\imath 2\pi kx}, \tag{3.22}$$

$$u_{xx} \quad = \quad \sum_{k=-\infty}^{\infty} C_k[t](\imath 2\pi k)^2 e^{\imath 2\pi kx}$$

$$= \quad \sum_{k=-\infty}^{\infty} C_k[t](-4\pi^2 k^2)e^{\imath 2\pi kx}. \tag{3.23}$$

Equating the coefficients to maintain periodicity,

$$C_k'[t] = (-2\pi^2 k^2) \cdot C_k[t]. \tag{3.24}$$

We can obtain an ordinary differential equation solution for the time-dependent coefficients $C_k[t]$:

$$C_k[t] = C_k[0]e^{-2\pi^2 k^2 t}. \tag{3.25}$$

The initial temperature distribution coefficient $C_k[0]$ at time $t = 0$, can be found using the model assumptions in equation 3.18. By construction, any initial temperature distribution at time $u[x, t = 0]$ is $f[x]$. This means,

$$f[x] \quad = \quad u[x, t = 0] = \sum_{k=-\infty}^{\infty} C_k[t = 0]e^{\imath 2\pi kx},$$

where, by deduction,

$$u[x, t] \quad = \quad \sum_{k=-\infty}^{\infty} \hat{f}[k; t = 0]e^{-2\pi^2 k^2 t}e^{\imath 2\pi kx}. \tag{3.26}$$

The deduction goes as: $f[x]$ as a periodic function, is an expansion of $f[x]$ in terms of the harmonics $e^{\imath 2\pi kx}$, so the coefficients $C_k[t]$ in terms of $f[x]$ must be the Fourier coefficients of $f[x]$. This means, the coefficients are the Fourier coefficients of $f[x]$, $C_k[t = 0] = \hat{f}[k]$. The transform must be able to go from the function to the series $f[x] \to \hat{f}[k]$, but also from the series to the function $\hat{f}[k] \to f[x]$. Given an initial temperature distribution $f[x]$, the temperature of any point $x$ on the ring at any time $t$ is the Fourier series of $f[x]$.

Instead of making observations of a temperature distribution $u[x, t]$ for any time $t$, we are interested in making observations of a LCLU spatial distribution $f[x, t]$ as it changes in time $t$. The analysis of LCLU change in time is found in Fourier's coefficients $C_k[t]$, and these coefficients are interpreted geometrically.

**Fourier Geometry**

Fourier showed that the Fourier Series could be used as an accurate, physically representative model of any periodic phenomena. When solving for the Fourier Coefficients in equation 3.24 the different complex exponentials are said to be completely independent, or orthogonal to each other, and have a magnitude, or length, unit-normalized to 1 over a single period $T$. Mathematically that is called orthonormality and looks like,

$$\int_{t=0}^{T=1} e^{2\pi \imath n t} \cdot e^{-2\pi \imath m t} \partial t = \int_{t=0}^{T=1} e^{2\pi \imath (n-m) t} \partial t = \begin{array}{cc} 0 & n \neq m \\ 1 & n = m \end{array} , \tag{3.27}$$

where the length of a function, or norm of a vector $\tilde{\mathbf{f}}$, is defined by the inner product:

$$< \tilde{\mathbf{f}}, \tilde{\mathbf{f}} > = \tilde{\mathbf{f}} \bullet \tilde{\mathbf{f}}^* = ||\tilde{\mathbf{f}}||^2 = \int_{t=0}^{T=1} |f[t]|^2 \partial t. \tag{3.28}$$

These physical notions of length and orthogonality are extensions of geometry interpreted for Fourier mathematics. The definition and property of length comes from the Pythagorean Theorem: $\tilde{\mathbf{f}}$ *is orthogonal to* $\tilde{\mathbf{g}}$ *if and only if* $||\tilde{\mathbf{f}} + \tilde{\mathbf{g}}||^2 = ||\tilde{\mathbf{f}}||^2 + ||\tilde{\mathbf{g}}||^2$ *if and only if* $< \tilde{\mathbf{f}}, \tilde{\mathbf{g}} > = 0$.

The Pythagorean theorem comes about through vector addition. Where for two vectors $\tilde{\mathbf{u}}$ and $\tilde{\mathbf{v}}$,

$$||\tilde{\mathbf{u}} + \tilde{\mathbf{v}}||^2 = ||\tilde{\mathbf{u}}||^2 + ||\tilde{\mathbf{v}}||^2. \tag{3.29}$$

This geometry holds only when the two vectors are perpendicular to each other (see Figure 3.26).
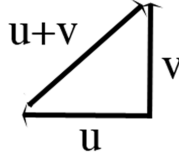


Figure 3.26: The $\tilde{\mathbf{u}}$–$\tilde{\mathbf{v}}$ vector space. Here, $\tilde{\mathbf{u}}$ and $\tilde{\mathbf{v}}$ are perpendicular to each other, and $\tilde{\mathbf{u}} + \tilde{\mathbf{v}}$ is the combination of the two vectors.

Extending Pythagorus' theorem from vectors to functions, and reasoning by analogy, geometric intuition can be used to interpret Fourier math. The Fourier coefficient in equation 3.26 is a geometric projection. We obtain the coefficients through the inner product with the function $\tilde{\mathbf{f}}$ against a complex exponential,

$$< \tilde{\mathbf{f}}, e^{2\pi \imath n t} > = \int_{t=0}^{T=1} f(t) \cdot e^{-2\pi \imath n t} \partial t = \hat{f}[n]. \tag{3.30}$$

The $n^{th}$ Fourier coefficient is exactly the projection of the function against the $n^{th}$ complex exponential:

$$f[t] = \sum_{k=-\infty}^{\infty} \hat{f}[t]e^{2\pi \imath k t} = \sum_{k=-\infty}^{\infty} <\tilde{\mathbf{f}}, e^{2\pi \imath n t}> e^{2\pi \imath k t}, \tag{3.31}$$

and every individual and combination of Fourier coefficients is a vector component of the original function—just like with vectors $\tilde{\mathbf{u}}$ and $\tilde{\mathbf{v}}$ in Figure 3.26. Whole class map LCLU shapes are vector inputs into the Fourier transform, and can be interpreted geometrically by vector space mathematics, as sinusoidal decompositions or reorientations (Section 3.3) into the Fourier domain.

### 3.4.2 Fourier Transform

The generalized Fourier series is the Fourier transform:

$$f[x,y] = \int_{\xi=-\infty}^{\xi=+\infty} \int_{\eta=-\infty}^{\eta=+\infty} F[\xi,\eta]e^{\imath 2\pi(\xi \cdot x + \eta \cdot y)}\partial\xi\partial\eta \tag{3.32}$$

$$F[\xi,\eta] = \int_{x=-\infty}^{x=+\infty} \int_{y=-\infty}^{y=+\infty} f[x,y]e^{-\imath 2\pi(x \cdot \xi + y \cdot \eta)}\partial x\partial y \tag{3.33}$$

where $\xi$ is the horizontal spatial frequency, and $\eta$ is the vertical spatial frequency.

When using the Fourier Transform to model the cosine, only two coefficients are necessary. Equation 3.34 sums these two coefficients and shows how the coefficients are calculated; each unique and predictable [Easton, 2005]. By monitoring the model coefficient values at each sinusoid, Fourier analysis provides additional information about the modeled phenomena. For instance, how any system operation that only resonates with frequencies other than at $|\xi| = 0.16[m^{-1}]$ will never effect the Cosine function:

For

$$y = f[x] \quad = \quad \cos[2\pi.16x],$$

if

$$
\begin{aligned}
f[x] \quad &= \quad \int_{\xi=-\infty}^{\xi=+\infty} \frac{1}{2} \cdot (\delta[\xi - .16] + \delta[\xi + .16]) e^{i2\pi\xi \cdot x} \partial\xi \\
&= \quad 0 \cdot \left(e^{i2\pi x}\right)^{-\infty} + \ldots + 0 \cdot \left(e^{i2\pi x}\right)^{-2} + \ldots + \frac{1}{2} \cdot \left(e^{i2\pi x}\right)^{-.16} + \ldots \\
&\quad + \frac{1}{2} \cdot \left(e^{i2\pi x}\right)^{.16} + \ldots + 0 \cdot \left(e^{i2\pi x}\right)^{2} + \ldots + 0 \cdot \left(e^{i2\pi x}\right)^{\infty} \\
&= \quad \frac{1}{2} \cdot \left(e^{i2\pi x}\right)^{.16} + \frac{1}{2} \cdot \left(e^{i2\pi x}\right)^{-.16} \\
&= \quad \frac{1}{2} \cdot e^{i2\pi.16x} + \frac{1}{2} \cdot e^{-i2\pi.16x} \\
&= \quad \frac{1}{2} \cdot \cos[2\pi.16x] + \frac{1}{2} \cdot i \sin[2\pi.16x] + \frac{1}{2} \cdot \cos[2\pi.16x] - \frac{1}{2} \cdot i \sin[2\pi.16x] \\
&= \quad \cos[2\pi.16x]
\end{aligned}
$$

then,

$$
F[\xi] \quad = \quad \int_{x=-\infty}^{x=+\infty} \cos[2\pi.16x] e^{-i2\pi x \cdot \xi} \partial x = \frac{1}{2} \cdot \delta[\xi - .16] + \frac{1}{2} \cdot \delta[\xi + .16].
$$

(3.34)

Similarly, Fourier analysis provides a quantitative measure of how similar two modeled functions (shapes) are related. This will be reviewed in the Fourier theorem and properties below.

### 3.4.3 Discrete Fourier Transform

The Fourier transform of equation 3.32 is for an infinitely continuous function $f[x, y]$. When the continuous function is sampled and bounded in space, like with an image, the Fourier transform operator becomes the discrete Fourier transform operator. The discrete Fourier transform operator, Equation 3.35, assumes the bounded function $f[x, y]$ is periodic with period $M$ in the $x$-direction and $N$ in the $y$-direction of a $M \times N$ function $f[x, y]$. Periodicity is a governing assumption of Fourier mathematics (see equation 3.18 with corresponding discussion). The periodic assumption is shown in Figure 3.27 for the Lena image.

$$
f[n, m] \quad = \quad \frac{1}{N \cdot M} \sum_{k=0}^{N-1} \sum_{l=0}^{M-1} F[k, l] e^{i2\pi \frac{(k \cdot n + l \cdot m)}{N \cdot M}},
$$

(3.35)

$$
F[k, l] \quad = \quad \frac{1}{N \cdot M} \sum_{n=0}^{N-1} \sum_{m=0}^{M-1} f[n, m] e^{-i2\pi \frac{(n \cdot k + m \cdot l)}{N \cdot M}},
$$

(3.36)

here, $n$ and $m$ are discrete spatial variables analogous to $x$ and $y$, and $k$ and $l$ are discrete spatial frequency variables analogous to $\xi$ and $\eta$.
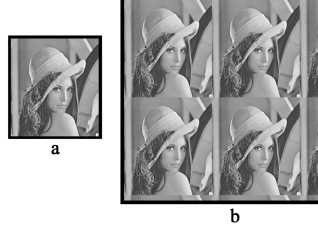
Figure 3.27: The original Lena image **a** is assumed periodic **b** in all directions when using the discrete Fourier transform operator.

As was done for the Cosine in equation 3.34, the discrete Fourier transform of the now observation vector $f[n]$ is also projected onto sinusoidal vectors of increasing frequency $(e^{\frac{i2\pi n}{N}})^k$. The sinusoidal vectors have a square matrix form $(e^{\frac{i2\pi}{N}})^{nk}$, and is used for efficient evaluation of the discrete Fourier transform [Easton, 2005]:

$$F[k] = \sum_{n=0}^{N-1} (e^{\frac{-i2\pi}{N}})^{nk} f[n] \tag{3.37}$$

As an example, the discrete Fourier transform matrix form for the $N = 2$ case is shown in Equation 3.38:

$$
\begin{bmatrix} F[0] \\ F[1] \end{bmatrix} = \begin{bmatrix} A[0,0] & A[0,1] \\ A[1,0] & A[1,1] \end{bmatrix} \begin{bmatrix} f[0] \\ f[1] \end{bmatrix} = \begin{bmatrix} (e^{-\frac{i2\pi 0}{2}})^0 & (e^{-\frac{i2\pi 1}{2}})^0 \\ (e^{-\frac{i2\pi 0}{2}})^1 & (e^{-\frac{i2\pi 1}{2}})^1 \end{bmatrix} \begin{bmatrix} f[0] \\ f[1] \end{bmatrix}
$$
$$
= \begin{bmatrix} +1 & +1 \\ +1 & -1 \end{bmatrix} \begin{bmatrix} f[0] \\ f[1] \end{bmatrix} = \begin{bmatrix} f[0] + f[1] \\ f[1] - f[1] \end{bmatrix} \tag{3.38}
$$

Additionally, the $N = 4$ case is shown in Equation 3.39:

$$
\begin{bmatrix} F[0] \\ F[1] \\ F[2] \\ F[3] \end{bmatrix} = \begin{bmatrix} (e^{-\frac{i2\pi 0}{4}})^0 & (e^{-\frac{i2\pi 1}{4}})^0 & (e^{-\frac{i2\pi 2}{4}})^0 & (e^{-\frac{i2\pi 3}{4}})^0 \\ (e^{-\frac{i2\pi 0}{4}})^1 & (e^{-\frac{i2\pi 1}{4}})^1 & (e^{-\frac{i2\pi 2}{4}})^1 & (e^{-\frac{i2\pi 3}{4}})^1 \\ (e^{-\frac{i2\pi 0}{4}})^2 & (e^{-\frac{i2\pi 1}{4}})^2 & (e^{-\frac{i2\pi 2}{4}})^2 & (e^{-\frac{i2\pi 3}{4}})^2 \\ (e^{-\frac{i2\pi 0}{4}})^3 & (e^{-\frac{i2\pi 1}{4}})^3 & (e^{-\frac{i2\pi 2}{4}})^3 & (e^{-\frac{i2\pi 3}{4}})^3 \end{bmatrix} \begin{bmatrix} f[0] \\ f[1] \\ f[2] \\ f[3] \end{bmatrix}
$$
$$
= \begin{bmatrix} +1 & +1 & +1 & +1 \\ +1 & -i & -1 & +i \\ +1 & -1 & +1 & -1 \\ +1 & +i & -1 & -i \end{bmatrix} \begin{bmatrix} f[0] \\ f[1] \\ f[2] \\ f[3] \end{bmatrix} ; \tag{3.39}
$$

$$
\begin{aligned}
F[0] &= f[0] + f[1] + f[2] + f[3] = (f[0] + f[2]) + (f[1] + f[3]), \\
F[1] &= f[0] - if[1] - f[2] + if[3] = (f[0] - f[2]) - i(f[1] - f[3]), \\
F[2] &= f[0] - f[1] + f[2] - f[3] = (f[0] + f[2]) - (f[1] + f[3]), \\
F[3] &= f[0] + if[1] - f[2] - if[3] = (f[0] - f[2]) + i(f[1] - f[3]).
\end{aligned}
$$

The elements of the 2-pixel and 4-pixel discrete Fourier transform are just sums and differences of the sampled amplitudes. Each of the discrete Fourier transforms are plotted in the Argand diagrams of Figure 3.28. These Argand diagrams can be extended to any size $N$ [Easton, 2005], and represent the Fourier system space that operations are held in. Input vectors $f[x, t]$ can exist along any of the $N$ Argand vector directions.
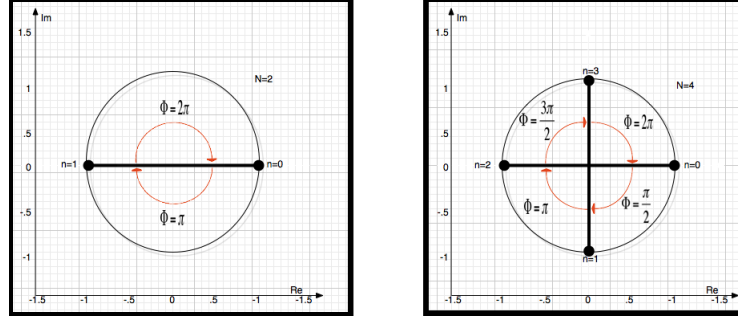


Figure 3.28: Argand diagrams of the complex weights applied in the discrete Fourier transform for a $N = 2$ (left) and $N = 4$ (right) -pixel image.

**Fourier Theorem and Properties**

Fourier mathematics have many well known properties and theorems, but the few that will be referred to most in this thesis can be used to describe a shape's activity. They are the scaling property, translation property, and Parseval's theorem. Each are presented here with spatial variable function $f[x]$ and spatial frequency variable Fourier representation $F[\xi]$.

1. **Scaling Property.** The observed function $f[x]$ may be scaled by a width parameter $b$ as $f[\frac{x}{b}]$, as it grows within a landscape. The scaling theorem shown in Equation 3.40 determines the effect of this paramater $b$ on the LCLU Fourier representation area.

$$\mathfrak{F}_1 \left\{ f \left[ \frac{x}{b} \right] \right\} = |b| \cdot F[b \cdot \xi]. \tag{3.40}$$

2. **Translation Property.** The Fourier transform of a LCLU function $f[x]$ that has been translated by a distance $\pm x_0$ has a Fourier representation:

$$\mathfrak{F}_1 \{ f[x \pm x_0] \} = |F[\xi]| e^{i(\phi\{f[\xi]\} \pm 2\pi\xi x_0)}. \tag{3.41}$$

The Fourier representation of a shifted LCLU function is the transform of the original LCLU function multiplied by a complex sinusoid whose phase is proportional to the distance traveled.

3. **Parseval's Theorem**. The Fourier representation $F[\xi]$ is related to the projection of $f[x]$ onto itself as,

40

$$\int_{-\infty}^{\infty} |f[x]|^2 \partial x = \int_{-\infty}^{\infty} f[x]f^*[x]\partial x = \int_{-\infty}^{\infty} F[\xi]F^*[\xi]\partial \xi = \int_{-\infty}^{\infty} |F[\xi]|^2 \partial \xi. \qquad (3.42)$$

In words, the vector length $\int_{-\infty}^{\infty} |f[x]|^2 \partial x$ of a spatial function $f[x]$ is unchanged when represented by Fourier methods.

## 3.5  Gardner's 1999 Rule: Map Generation and Spatial Analysis Program

A database of progressive LCLU patches in the environment, at appropriate scales, and for a single area would be useful for Fourier analysis of LPM but is not available. Instead the **Rule** multifractal map generation tool can be used to model characteristic pattern change. Robert Gardner created the **Rule** software for null-hypothesis tests of significant LCLU pattern change [O'Neill et al., 1991]. Gardner's null-hypothesis is, "The LCLU change observed is completely random, and ecologically irrelevant." By comparing a randomly generated map to a real LCLU map, and assuming the null-hypothesis is true, Gardner asks, "What is the probability of observing a value for the test statistic that is at least as extreme as the value that was actually observed?" Gardner's null-hypothesis test indicate how much confidence can be had that any LCLU change in pattern has affected the landscape.

After generating a series of maps with a different number of LCLU patches, LCLU patch proportions, and LCLU patch edge fractal dimension the ability of LPM to report these multifractal maps can be recorded. Placing maps in an increasing order of complexity, they could serve as LCLU models for progressive pattern observations and tests for LPM precision.

Simple random maps are created by specifying the number of rows and columns in the map, the number of LCLU classes to be generated, and the probabilities associated with each LCLU class, as is shown in Table 3.2. The Visual Basic code uses a random number generator placed within two nested **do** loops with the variables **irow** and **jcol** defining the number of rows and columns of the map, **in_map**, to be generated. For one class with a probability that any given site in the map will be occupied by the LCLU class of interest **pr**, the code that is sufficient for generating a simple random map with a single LCLU class is [Gardner, 1999]:

```
do i = 2, irow + 1
    do j = 2, jcol + 1
        y = ran1( iseed )
        if ( y .le. pr ) then
            in_map( i, j ) = 1
        else
            in_map( i, j ) = 0
        endif
    enddo
enddo
```

Multifractal maps like in Figure 3.29 are generated by a midpoint displacement algorithm [Saupe, 1988] that creates a map of real numbers by successive division, interpolation, and random

Table 3.2: Log file for a 256 by 256 multifractal random map with: Hurst dimension 1; LCLU probabilities of $r[x] = 0.4$, $s[x] = 0.24$, $t[x] = 0.36$; and generated within one iteration. The actual LCLU probabilities generated were $r[x] = 0.397292$, $s[x] = 0.240794$, and $t[x] = 0.361914$.

```
          Qrule (v 4.1) Landscape Pattern Analysis        11/20/08
          Map choice: M
          Maxlevel     8   H =   1.00000
          Rows x Columns =     256 x     256
          n  Wrap = F
          Random number seed:         -5
          Rule choice is: 2
          Map classes =     2
          The normalized probabilities are:
                    P          CumP
             0    0.4000      0.4000
             1    0.2400      0.6400
             2    0.3600      1.0000
          N_Reps =        1
          Map output choice = G
          Output file for generated map: m8_1n..522.4.24.361g
          Analysis method: RULE


          Resolution:  300.000      meters


                     Mean Association Matrix
          Avg ChiX =   477716.       w/     4 df (FXceed (   9.4480) =    1.0000)
                        0          1          2
            0 0.391728 0.005564 0.000000
            1 0.005564 0.227880 0.007349
            2 0.000000 0.007349 0.354565



          p's  0.397292 0.240794 0.361914

    Time in: [hr 21 m 13 s 47 (ms 612)]
    Time in: [hr 21 m 14 s 29 (ms 846)]
```

perturbation. Two parameters are used by this method: the variance associated with the random perturbations, and $H$, the parameter describing the correlation between points. Values of $H$ range between 0.0 and 1.0. Adjustment of the value of H between 0.0 to 1.0 result in maps that range from extremely fragmented to highly aggregated, like in Figure 3.6. **Rule** converts the grid of real numbers into integers representing the proportion of LCLU classes specified by the input probabilities [Gardner, 1999]

Using version 4.1 of **Rule** takes 9 input parameters:

1. The map type to be analyzed.

2. The size of the map to be generated and Hurst exponent (Hurst exponent, $H$ is $D_{fractal} = D_{real} - H$).

3. The initial value for the pseudorandom number generator.

4. The Neighborhood rule (see section 3.2.4).

5. The number of LCLU classes and the probabilities of occurrence associated with each LCLU class.

6. The number of iterations of maps to be generated and analyzed.

7. Form of output map.

8. The analysis methods and output desired.

9. Resolution along the side of each grid element in meters.

The input parameters for multifractal random maps (see Table 3.2) generated here are:

1. Multifractal map.

2. $256 \times 256$.

3. -5.

4. Nearest-neighbor rule.

5. LCLU maps of two cover types with probabilities
$p[x] \in [.1, .9; \Delta = .1]$;
$q[x] = 1 - p[x]$;

and

LCLU maps of three cover types with probabilities
$t[x] \in [.1, .9; \Delta = .1]$;
$r[x] = (1 - t[x]) \cdot p[x]$;
$s[x] = (1 - t[x]) \cdot q[x]$.

6. One iteration.

7. Generated.

8. No analysis.

9. 300 meters (this value does not effect the results, any value would be fine).
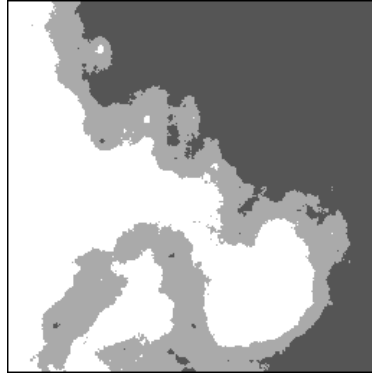
Figure 3.29: Multifractal map generated by **Rule**. The map input parameters are $r[x] = 0.4$, $s[x] = 0.24$, $t[x] = 0.36$, and the log file is shown in Table 3.2.

## 3.6 Interactive Data Language (IDL) Synthetic Noise Models

Each of the **Rule** software LCLU maps generated for analysis are enhanced to model spatial, radiometric, and spectral noise variability (see Section 3.3.2). This section discusses the details of how each map introduces noise variability. Only techniques will be discussed here, not code. While Research Systems Incorporation's (RSI) Interactive Data Language (IDL) was used, each of these noise models are reproducible using any image processing mathematical software.

### 3.6.1 Spatial Model (Spatial Resolution)

A change in spatial resolution for real data is observed as increased pixel area. As shown in Figure 3.30, variable spatial resolution in satellite imagery not only changes the coverage of a pixel but the radiometric value may change as well. Each of these phenomena are captured in the IDL spatial resolution model discussed here.
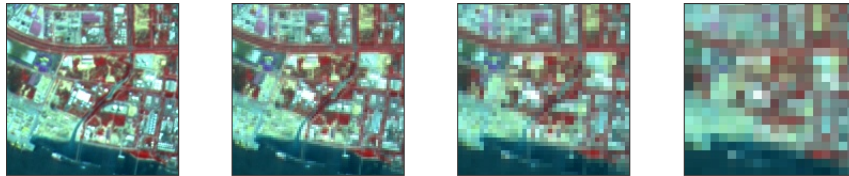


Figure 3.30: The effect of pixel size on the visual appearance of an area. The first image is a SPOT image of $10[m]$ $160 \times 160$ image size derived by merging a SPOT panchromatic image with a SPOT multispectral image. The subsequent images show the effects of digitizing the same area with larger pixel sizes of an $80 \times 80$ scene with $20[m]$ pixels, a $40 \times 40$ scene with $40[m]$ pixels, and a $20 \times 20$ scene with $80[m]$ pixels.

The IDL software first shrinks the $256 \times 256$ **Rule** LCLU map by a factor equal to the modeled pixel size. For instance, assuming the original $256 \times 256$ LCLU map has $1[m]$ pixels, to model a $15[m]$ LCLU map the image is downsampled to a $\frac{256}{15} \times \frac{256}{15} = 17 \times 17$ image size then upsampled to a $256 \times 256$ image size by nearest-neighbor interpolation. The increased pixel area, and LCLU map value are shown in Figure 3.31.



Figure 3.31: The IDL model for spatial resolution variability in LCLU maps. The original $256 \times 256$ LCLU image is downsampled to desired resolution, and then upsampled to the original $256 \times 256$ image frame.

### 3.6.2 Radiometric Model (Detector Noise Error)

A change in individual detector values for real data can mislead LCLU classification decisions. The variable detector noise in satellite imagery modeled here is equally likely across the entire scene (*i.e.* fixed pattern noise), as is shown in Figure 3.32 for SAR data. Variable increases or decreases in individual pixel brightness values make originally unique samples seem equal, and originally equal samples seem unique. Each of these phenomena are captured in the IDL radiometric model used here, where LCLU decisions reveal the expected variable confusion across the scene by uniformly switching LCLU class decisions.

The IDL software does this by increasing fixed pattern noise in a $256 \times 256$ reference scene. This noise has pixel values that vary between 0 and LCLU class map values. An example of this reference fixed pattern noise is shown in Figure 3.33. Scenes like that shown in Figure 3.33 exchange new pixel values with the original LCLU class map. Where pixels are not zero in the reference noise scene the LCLU class pixel at the same position obtains the new value. Conversely, where pixels are zero in the reference noise scene the LCLU class pixel at the same position keeps its current value.

### 3.6.3 Spectral Model (Increased Class Accuracy)

A change in spectral accuracy for real data is observed with better sampling schemes or better algorithm decision models. This increase in class accuracy happens within the areas of mixed pixels, where phenomena confusion occurs. As shown in Figure 3.34, mixed pixels are typically located along the edges of each LCLU class, where class cover may intersect, instead of inside contiguous pure pixel patches. For this reason the spectral model for increased class accuracy uniformly increases pixel variability along LCLU class edge to model the better unmixing of a mixed pixel.

The spectral model uses the same fixed pattern noise technique discussed in Section 3.6.2. This time the reference error map only effects the LCLU class pixels along class edges instead of across
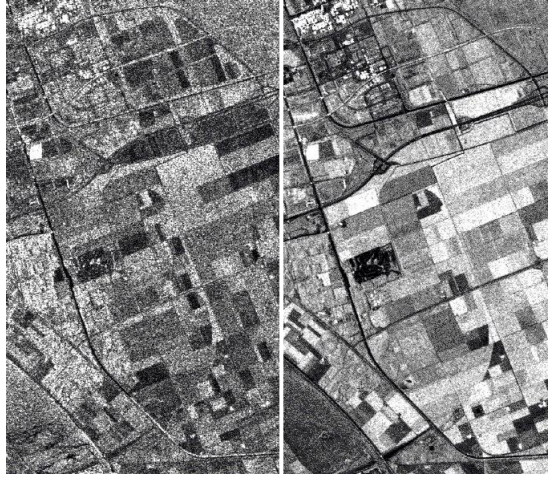
Figure 3.32: Detector noise in a subscene from the Netherlands. The ERS SAR image to the left was captured on 23 May 1993. To the right is a pixel-by-pixel averaged image of 11 superimposed SAR scenes from 1993 (one each month with the exception of July). Detector noise in both scenes is observed as white noise.
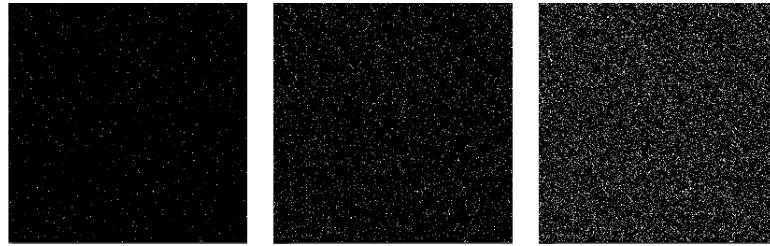


Figure 3.33: Uniformly generated fixed pattern noise error modeled for LCLU likelihood decision confusion. From left to right, these three maps represent $8.2 \times 10^{-3}\%$ (537 out of 65536) noise effected pixels, $46.3 \times 10^{-3}\%$ (3034 out of 65536) noise effected pixels, and $0.19\%$ (1245 out of 65536) noise effected pixels.

the entire scene. Additionally, only LCLU class pixel values between the shared class edges are used in the reference map. The results of the spectral model are shown in Figure 3.35.
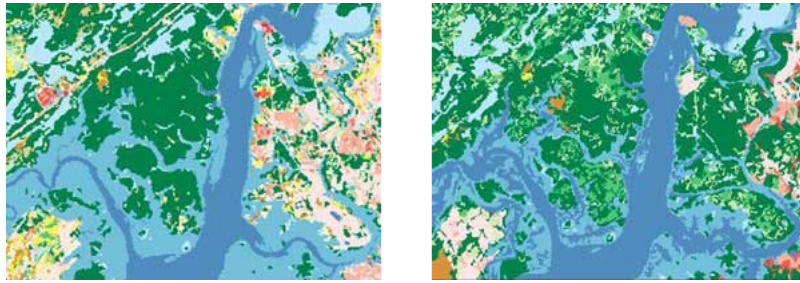
Figure 3.34: Increased LCLU map class accuracy. An increase in spectral model accuracy along the river bed produces scattered assignments of mixed pixels between coastal land and water.
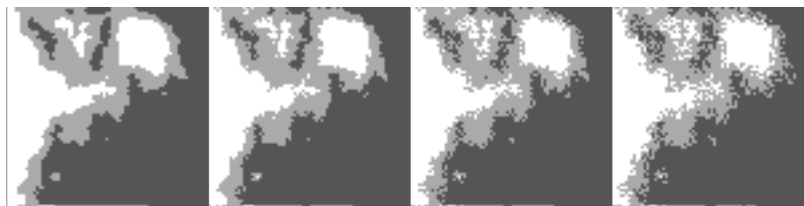


Figure 3.35: LCLU class map spectral model. The model edge spread increases from left to right as ±0 pixels, ±1 pixels, ±2 pixels, and ±3 pixels of modeled unmixed class pixels.

# Chapter 4

# Approach

It was discussed in Chapter 3 Section 3.3.1, how pixel size, or system resolvability in general, is best characterized as the image spatial frequency bandwidth. This spatial frequency bandwidth that can be scaled across resolutions as image power (see Figure 3.21). To capitalize on these spatial frequency properties, Fourier metrics dependent on spatial frequency bandwidth have been developed.

This chapter will present the proposed metrics of LCLU change in Sections 4.1–4.3. Each proposed metric concept and derivation is reviewed, and the performance of these metrics to indicate ecologically relevant LCLU variability is addressed in Section 4.4.

## 4.1 Metric of Landscape Composition

The simplest LPM focus on the *composition* of a landscape (*e.g.* which classes are present and how much of the classes there are), ignoring the spatial arrangement of the classes on the landscape. This section proposes a composition metric that models not only spatial composition correctly, but accounts for the temporal progression of composition as well. The proposed *Fourier Metric of Proportion* ($FMP$) concept and derivation are presented.

### 4.1.1 Fourier Metric of Proportion

The idea is to have a metric that is unit-normalized by landscape coverage of equal LCLU class *Proportion* (see equation 3.2), represented as scalable Fourier spatial frequency that trends exponentially as class proportions change. The final $FMP$ expression in Equation 4.8 is very simple, but a conceptual derivation will help to interpret what is being measured.

To reveal how evenly the *Proportions* of cover types occur, each component LCLU class $f_1[x,y] + f_2[x,y] + f_3[x,y] + \ldots$ is separated from the total LCLU map $f[x,y]$ and their Fourier vector magnitudes are found:

$$
\begin{aligned}
f[x,y] &= f_1[x,y] + f_2[x,y] + f_3[x,y] + \ldots \\
&= \mathcal{F}^{-1}\{|\,F_1[\xi,\eta]\,|^2\,e^{-\imath\phi_{f_1}} + |\,F_2[\xi,\eta]\,|^2\,e^{-\imath\phi_{f_2}} + |\,F_3[\xi,\eta]\,|^2\,e^{-\imath\phi_{f_3}} + \ldots\} \quad (4.1)
\end{aligned}
$$

Each scalar LCLU class spectral density $S_j$, in Equation 4.2, are equal in length if the *Proportions* are the same, and unequal in length otherwise. Example spectral densities for a three class LCLU map would be:

$$
\begin{aligned}
S_1 &= \int_{\xi=-\infty}^{\xi=\infty} \int_{\eta=-\infty}^{\eta=\infty} \mid F_1[\xi,\eta] \mid^2 \partial\xi\partial\eta, \\
S_2 &= \int_{\xi=-\infty}^{\xi=\infty} \int_{\eta=-\infty}^{\eta=\infty} \mid F_2[\xi,\eta] \mid^2 \partial\xi\partial\eta, \\
S_3 &= \int_{\xi=-\infty}^{\xi=\infty} \int_{\eta=-\infty}^{\eta=\infty} \mid F_3[\xi,\eta] \mid^2 \partial\xi\partial\eta
\end{aligned}
\tag{4.2}
$$

The similarity of each class spectral density is revealed by referencing every spectral density by the maximum spectral density *Proportion*. The scalar, three class, maximum spectral density would be:

$$
S_{max} \equiv \mathrm{MAX}(S_1,\ S_2,\ S_3)
\tag{4.3}
$$

These spectral densities can be thought of as radii of a hyperellipsoid referenced against a unit-hypersphere. Here the hyperellipsoid volume is a singular variable representing every possible LCLU spectral density combination. The unit-hypersphere makes reference to every instance where LCLU has the same amount of landscape area. Figure 4.1 shows this concept for the first three dimensions.
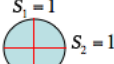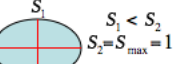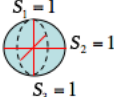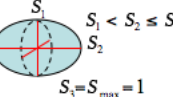


| Dimension (# of proportions) | \| | Volume | \| | Reference Sphere | \| | Proportion Sphere |
|---|---|---|---|---|---|---|
| 1 | | $2S$ | | $S=1$ | | $S=S_{max}=1$ |
| 2 | | $\pi S_j^2$   $j=1,2$ | | $S_1=1$   $S_2=1$ | | $S_1$   $S_1<S_2$   $S_2=S_{max}=1$ |
| 3 | | $\dfrac{4\pi}{3}S_j^3$   $j=1,2,3$ | | $S_1=1$   $S_2=1$   $S_3=1$ | | $S_1$   $S_1<S_2\leq S_3$   $S_2$   $S_3=S_{max}=1$ |

Figure 4.1: The hyperellipsoid concept for $FMP$ derivation. The hyperellipsoid becomes a unit-hypersphere if each class spectral density $S_j$ are equal. Each spectral density $S_j$ is normalized by the maximum class spectral density $S_{max}$, and are radii for the hyperellipsoid. The hyperellipsoid volume will be smaller than a unit-hypersphere volume if the *Proportions* are not equal, so the hyperellipsoid volume is always less than (inside) or equal to the unit-hypersphere volume.

The general volume $V_D(R_1, R_2, \ldots, R_{D-1}, R_D)$ for a hyperellipse with radii $R_j$, and number of radii $D$ is:

$$V_D(R_1, R_2, \ldots, R_{D-1}, R_D) = \frac{\pi^{\frac{D}{2}} R_j^D}{\Gamma\left(\frac{D}{2} + 1\right)} \tag{4.4}$$

$\Gamma(\cdot)$ is the Gamma function.

For the unit-hypersphere volume $\bar{V}_D$, each radius $R_j = 1$. The full equation for the class spectral density hyperellipse volume $V_D(\tilde{S}_1, \tilde{S}_2, \ldots, \tilde{S}_{D-1}, \tilde{S}_D)$ has the radii of normalized class spectral density

$$\bar{S}_j = \frac{\int_{\xi=-\infty}^{\xi=\infty} \int_{\eta=-\infty}^{\eta=\infty} \mid F_j[\xi, \eta] \mid^2 \partial\xi\partial\eta}{\int_{\xi=-\infty}^{\xi=\infty} \int_{\eta=-\infty}^{\eta=\infty} \mid F_{max}[\xi, \eta] \mid^2 \partial\xi\partial\eta} = \frac{S_j}{S_{max}} \tag{4.5}$$

as a series of products:

$$V_D(\tilde{S}_1, \tilde{S}_2, \ldots, \tilde{S}_{D-1}, \tilde{S}_D) = \frac{\pi^{\frac{D}{2}} \cdot \prod_j^D \frac{\int_{\xi=-\infty}^{\xi=\infty} \int_{\eta=-\infty}^{\eta=\infty} |F_j[\xi,\eta]|^2 \partial\xi\partial\eta}{\int_{\xi=-\infty}^{\xi=\infty} \int_{\eta=-\infty}^{\eta=\infty} |F_{max}[\xi,\eta]|^2 \partial\xi\partial\eta}}{\Gamma\left(\frac{D}{2} + 1\right)} \tag{4.6}$$

*Fourier Metric of Proportion* is the fraction of normalized class spectral density hyperellipsoid volume to unit-hypersphere, which can be expressed as:

$$
\begin{aligned}
FMP(\tilde{S}_1, \tilde{S}_2, \ldots, \tilde{S}_{D-1}, \tilde{S}_D) &\equiv V_D(\tilde{S}_1, \tilde{S}_2, \ldots, \tilde{S}_{D-1}, \tilde{S}_D) \cdot \left(\bar{V}_D\right)^{-1} \\
&= \frac{\pi^{\frac{D}{2}} \cdot \prod_j^D \frac{\int_{\xi=-\infty}^{\xi=\infty} \int_{\eta=-\infty}^{\eta=\infty} |F_j[\xi,\eta]|^2 \partial\xi\partial\eta}{\int_{\xi=-\infty}^{\xi=\infty} \int_{\eta=-\infty}^{\eta=\infty} |F_{max}[\xi,\eta]|^2 \partial\xi\partial\eta}}{\Gamma\left(\frac{D}{2} + 1\right)} \cdot \frac{\Gamma\left(\frac{D}{2} + 1\right)}{\pi^{\frac{D}{2}} \cdot 1^D} \\
&= \prod_j^D \frac{\int_{\xi=-\infty}^{\xi=\infty} \int_{\eta=-\infty}^{\eta=\infty} \mid F_j[\xi, \eta] \mid^2 \partial\xi\partial\eta}{\int_{\xi=-\infty}^{\xi=\infty} \int_{\eta=-\infty}^{\eta=\infty} \mid F_{max}[\xi, \eta] \mid^2 \partial\xi\partial\eta}
\end{aligned} \tag{4.7}
$$

This can be simplified by Parseval's theorem:

$$
\begin{aligned}
FMP(\tilde{S}_1, \tilde{S}_2, \ldots, \tilde{S}_{D-1}, \tilde{S}_D) &\equiv \prod_j^D \frac{\int_{x=-\infty}^{x=\infty} \int_{y=-\infty}^{y=\infty} \mid f_j[x, y] \mid^2 \partial x \partial y}{\int_{x=-\infty}^{x=\infty} \int_{y=-\infty}^{y=\infty} \mid f_{max}[x, y] \mid^2 \partial x \partial y} \\
&= \prod_j^D p_j' \\
&= \prod_j^D \frac{\text{total number of pixels in class } j}{\text{total number of pixels in largest class}}
\end{aligned} \tag{4.8}
$$

Equation 4.7 and 4.8 tell us that $FMP$ values can be compared to other $FMP$ values that integrate over the same spatial $\int_{x,y}$, and thereby spatial frequency $\int_{\xi,\eta}$, extent—this means images must be in the same geographic coordinate system before calculation. $FMP$ reports composition

in reference to variable maximum *Proportion* (*i.e.* a proportion with reference to a single area), so the physical landscape location $[x, y]$ of the landscape should remain the same. When reporting $FMP$ values of different landscape locations it should be stated.

Since each spectral density is reported with reference to the largest spectral density (see equation 4.5), multiple (*i.e.* temporal) $FMP$ values can be interpreted with reference to the largest LCLU class. For example, the expectation that any process associated with the largest LCLU class in the landscape scene (say, eutrophication) should become increasingly relevant as that LCLU grows, would be revealed as a direct relationship between temporal $FMP$ values and temporal observations of that process. The further from a direct relationship between $FMP$ and whatever process is an indication of a competing dependency, possibly outside of the satellite image captured landscape extent.
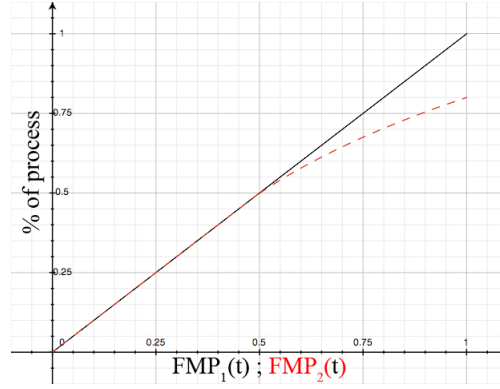


Figure 4.2: Analysis of FMP as a landscape indicator. Correlating the FMP landscape pattern metric to a landscape process dependent on areal coverage, deviation from a linear temporal relationship would indicate a competing influence on the observed process. $FMP_1(t)$ in black, is the expected relationship for $FMP$ and some observed process; and $FMP_2(t)$ in red, is the nonlinear relationship suggesting process influence(s) outside of the currently observed landscape.

Using $FMP$, the influence any LCLU class has on another LCLU class is expressed at a higher rate than *Dominance* by multiplying each proportion $\prod_j^D p'_j$. Still, as was for *Dominance*, $FMP$ is a measure of class diversity ranging from 0 to 1. Values near 1 indicate a landscape dominated by many different cover types of similar proportion, while values near 0 indicate that a single LCLU class is dominant across the landscape.

**FMP Uncertainty**

Uncertainty is introduced into FMP values by using the ROC parameters explained in Section 3.3.2. Upper bound (UB) , lower bound (LB) and observed (OBS) FMP values are expressed as:

$$
\begin{aligned}
FMP_{OBS} &\equiv \prod_{j}^{D} p'_{j,OBS} \quad \begin{matrix} +\prod_{j}^{D} p'_{j,UB} \\ -\prod_{j}^{D} p'_{j,LB} \end{matrix} \\
&= \prod_{j}^{D} p'_{j,TP+\frac{FN}{2}} \quad \begin{matrix} +\prod_{j}^{D} p'_{j,TP} \\ -\prod_{j}^{D} p'_{j,TP+FN} \end{matrix} \quad .
\end{aligned}
\tag{4.9}
$$

## 4.2  Metric of Landscape Configuration

With increased complexity, LPM for LCLU configuration describe the interaction between LCLU classes. Methods to quantify class spatial position and patch influence have been developed to describe landscape configurations that effect LCLU change. However, the measurement of these factors in multiple resolution images have come under considerable error (see Section 3.2.4). In this section the proposed *Fourier Metric of Fragmentation* (*FMF*) concept and derivation are presented, along with a brief review of the theory behind its interpretation for landscape configuration.

### 4.2.1  Fourier Metric of Fragmentation

Attempts to quantify patterns of fragmentation (*i.e.* the incursion of one class onto another) has produced deterministic models and a general theory of class population that follow very close to LCLUC observations. Especially in the field of population dynamics, where Richard Levins' Metapopulation model tracks the succession and recession of local (class) populations from one type to another. The model assumes that across the entire set of LCLU class populations a general measure of species health (*e.g.* survival or extinction) is indicated by an individual class's size and relative distances, and that the class's succession or recession rates of change are logistic-sigmoid with time $t$ (see Equation 4.10). The logistic-sigmoid model in Figure 4.3 initial stage of growth for some set $P$ is approximately exponential; then, as saturation begins, the growth slows, and at maturity, growth stops:

$$
\begin{aligned}
\frac{\partial P(t)}{\partial t} &= P(1-P) \\
P(t) &= \frac{1}{1+e^{-t}}
\end{aligned}
\tag{4.10}
$$

In Equation 4.11, Levin's model for landscape population, $p$ is the fraction of patches occupied at some time. Each occupied patch can become unoccupied with an extinction probability $\varepsilon$, and populated by migration at some constant rate $m$. The fraction of unoccupied patches is $(1-p)$. $(m \cdot p)$ is interpreted as the fraction of unoccupied patch to be colonized, and $(\varepsilon \cdot p)$ is the fraction of occupied patch to recede. For each change in time step $\frac{\partial p}{\partial t}$, the change in the proportion of occupied patches is:

$$
\frac{\partial p}{\partial t} = m \cdot p \cdot (1-p) - \varepsilon \cdot p
\tag{4.11}
$$
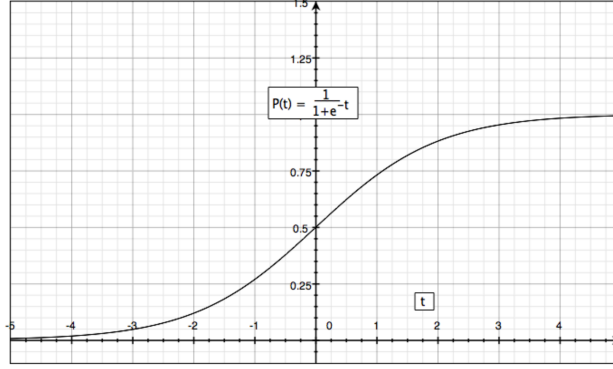
Figure 4.3: Levin's Metapopulation model assumed rate of growth for an individual class. The logistic-sigmoid function's initial stage of growth, before the reference time $t = 0$, for some percent capacity $P(t)$, is approximately exponential. As saturation begins the growth slows, and at maturity growth stops at 100% LCLU capacity.

The Metapopulation model assumes, as an initially exponential and further logistic-sigmoid function of LCLU class growth, that distance to harmful species and relative population sizes are indicators of populous health. And, appropriately models the observed process of fragmentation. *Fourier Metric of Fragmentation* ($FMF$) recognizes each of these assumptions and measures each function with greater sensitivity as LCLU patch growth slows, and at maturity when LCLU patch cover stops.

The $FMF$ metric has two scalar components: $\hat{\Phi}_{f_i,f_k,l}$ phase—a distance measure of spatial similarity between the fragmenting classes; and $\hat{M}_{f_i,f_k}$ spectral density—the normalized spectral density measurement of populated area by the LCLU class being observed. Since the distance between two classes is the same from one class to another, the $\hat{M}_{f_i,f_k}$ parameter determines the direction of fragmentation from $f_i \rightarrow f_k$ or $f_i \leftarrow f_k$. The Fourier fragmentation description used by $FMF$ is compared to *Contagion* in Figure 4.4.

### FMF–Phase

By way of the *phase-only matched* ($POM$) filter [Homer and Gianino, 1984] a measure of physically accurate between-class distance can be derived. The $POM$ filter produces a measure of physically relevant distance by taking advantage of the Fourier shifting theorem seen in Equation 4.12.
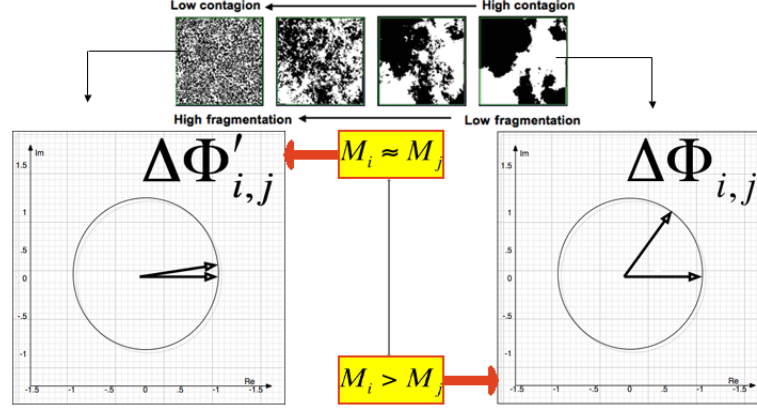
Figure 4.4: Contagion is a measure of the change in phase between two classes $i$ and $j$, and their respective class vector magnitudes during fragmentation. The two classes are $i$, the white LCLU in the binary class map, and a general, all other classification $j$, represented as black in the binary class map. As the LCLU class becomes more fragmented, the phase difference $\Delta\Phi_{i,j}$ between the LCLU of interest $i$ and all other LCLU classes $j$ decrease. Their Fourier magnitudes come closer as $M_i \cong M_j$. Under fragmentation, the LCLU across the landscape becomes increasingly similar.

$$
\begin{aligned}
\mathcal{F}\{f[x \pm x_0, y \pm y_0\} \quad &= \quad \int_{x=-\infty}^{x=\infty} \int_{y=-\infty}^{y=\infty} f[x \pm x_0, y \pm y_0] e^{[-2\pi\imath(\xi \cdot x + \eta \cdot y)]} \partial x \partial y \\
\text{For } u \equiv x \pm x_0 \ , \ v \equiv y \pm y_0 \quad &= \quad \int_{u=-\infty}^{u=\infty} f[u] e^{[-2\pi\imath\xi(u \mp x_0)]} \partial u \int_{v=-\infty}^{v=\infty} f[v] e^{[-2\pi\imath\eta(v \mp y_0)]} \partial v \\
&= \quad e^{[\pm 2\pi\imath\xi x_0]} \cdot e^{[\pm 2\pi\imath\eta y_0]} \cdot F[\xi] \cdot F[\eta] \\
&= \quad e^{[\pm 2\pi\imath(\xi x_0 + \eta y_0)]} F[\xi, \eta] \\
&= \quad \mid F[\xi, \eta] \mid e^{[\imath(\phi\{F[\xi,\eta]\} \pm \imath 2\pi(\tilde{\mathbf{r}}_0 \bullet \tilde{\rho}))]}
\end{aligned}
$$

$$
\text{where} \quad |\tilde{\mathbf{r}}_0| \equiv \sqrt{x_0^2 + y_0^2} \text{ and } |\tilde{\rho}| \equiv \sqrt{\xi^2 + \eta^2} \tag{4.12}
$$

In step four of the Fourier shifting theorem derivation the shifted distance from a defined origin is in the exponential phase term. Using two images $f_1[x, y]$ to $f_2[x, y]$ whose only difference between them is their position $f_2[x, y] = f_1[x \pm x_0, y \pm y_0]$ the $POM$ filter leverages the exponential phase term to find the distance between the two scenes. The $POM$ filter is able to describe radial shifts $\tilde{\mathbf{r}}_0^T = [x_0, y_0]$ between two scenes because it assumes the Fourier spatial frequency vectors $F_1[\xi, \eta]$ and $F_2[\xi, \eta]$ share the same magnitude $\mid F_1[\xi, \eta] \mid = \mid F_2[\xi, \eta] \mid$ and have the same inherent phase $\phi\{F_2[\xi, \eta]\} = \phi\{F_1[\xi, \eta]\}$):

$$POM\{f_1[x,y], f_2[x,y]\} = \mathcal{F}^{-1}\left\{\mid F_2[\xi,\eta]\mid e^{[\imath(\phi\{F_2[\xi,\eta]\}\pm 2\pi(\tilde{\mathbf{r}}_\mathbf{0}\bullet\tilde{\rho}))]} \cdot \mid F_1[\xi,\eta]\mid^{-1} e^{[-\imath\phi\{F_1[\xi,\eta]\}]}\right\}$$

$$= \mathcal{F}^{-1}\left\{\frac{\mid F_2[\xi,\eta]\mid}{\mid F_1[\xi,\eta]\mid}e^{[\imath(\phi\{F_2[\xi,\eta]\}-\phi\{F_1[\xi,\eta]\}\pm 2\pi(\tilde{\mathbf{r}}_\mathbf{0}\bullet\tilde{\rho}))]}\right\}$$

$$= \mathcal{F}^{-1}\left\{e^{[\pm\imath 2\pi(\tilde{\mathbf{r}}_\mathbf{0}\bullet\tilde{\rho}))]}\right\}$$

$$= \delta[\tilde{\mathbf{r}}\pm\tilde{\mathbf{r}}_\mathbf{0}] \qquad (4.13)$$

By the second step of Equation 4.13 it is seen how any shift between $f_1[x,y]$ and $f_2[x,y]$ is revealed as a vector change in slope $\tilde{\mathbf{r}}_0$ of an otherwise linear phase term $\tilde{\rho}$.

In both equations 4.12 and 4.13 the exponential phase term $e^{[\imath\phi]}$ is separated from the magnitude $\mid F[\xi,\eta]\mid$ to find these descriptions of distance. This separation is the first of two steps for the $FMF$ metric. The phase transfer function $\Phi TF_{f_i,f_j}$ for the $FMF$ metric phase can be expressed as:

$$\Phi TF_{f_i,f_j}[\xi,\eta] \equiv \frac{F_i[\xi,\eta]}{\mid F_i[\xi,\eta]\mid}\cdot\frac{F_j^*[\xi,\eta]}{\mid F_j^*[\xi,\eta]\mid} = e^{[\imath(\phi\{F_i[\xi,\eta]\}-\phi\{F_j[\xi,\eta]\})]}$$

$$= e^{[\imath(\phi\{F_i[\xi,\eta]\}-\phi\{F_j[\xi,\eta]\}+2\pi(\tilde{\mathbf{r}}\bullet\tilde{\rho}))]} \qquad (4.14)$$

The $FMF$ metric phase transfer function $\Phi TF_{f_i,f_j}$ measures shape similarity across the landscape, seen between LCLU classes $f_i$ and $f_j$. Under Levins' logistic-sigmoid Metapopulation model assumption (see equation 4.10), $FMF$ has an increased sensitivity to an early indication of fragmentation because of the $\Phi TF_{f_i,f_j}$ exponential shape similarity measurement in Equation 4.14. The transfer function between the observed landscape Metapopulation model in Figure 4.3, and the measured $FMF$ metric can be effectively tuned to provide increasingly early (*i.e.* sensitive) measures of fragmentation detection: $(\Phi TF_{f_i,f_j})^l$. The tuning factor $l$ is interpreted as an increased spatial sensitivity for every $l^{-1}$ units of pixel distance across the landscape. At $l=\frac{1}{2}$, $(\Phi TF_{f_i,f_j})^l$ is twice as sensitive to changes on the landscape; at $l=\frac{1}{3}$, $(\Phi TF_{f_i,f_j})^l$ is three-times as sensitive to changes on the landscape, and so on.

Levins described Metapopulation as a collection of relatively isolated, spatially distributed, local populations bound together by occasional dispersal between populations (see Section 3.1.1). This can be modeled as a landscape with two isolated classes of extreme locality: $\delta[x-x_0, y-y_0]$ and $\delta[x-x_1, y-y_1]$. For this scenario $(\Phi TF_{f_i,f_j})^l = \left(e^{[+2\pi(\tilde{\mathbf{r}}\bullet\tilde{\rho})]}\right)^l$, where the distance between the two classes is $\mid\tilde{\mathbf{r}}\mid = \sqrt{(x_i-x_j)^2+(y_i-y_j)^2}$. The transfer function is shown in Figure 4.5. The LCLU system in Figure 4.5 assume the rates of space and time are directly related $\frac{\delta x}{\delta t}\propto\frac{\delta t}{\delta x}$. This is why the system INputs and OUTputs are a function of unit time/distance.

The $FMF$ transfer functions in Figure 4.5 are generated for a specific case, but LCLU system interpretation is generally applicable. This predator-prey scenario is similar to Figure 3.3 b. The distance between separate objects in the scene model (green ball vs. cyan ball) is still directly proportional to the green object's existence. Still, cyan identifies the predator and green identifies the prey. However now, the distance between the two increases. In response, The green LCLU population increases the further it is away from the cyan LCLU. This is all shown in the *scene model* of Figure 4.5.

Initially, at $t = 0$, the logistic-sigmoid model is set to a 0.67% LCLU prey population, at only 4.32% of the distance away from its LCLU predator population. Finally, at $t = 1$, the logistic-sigmoid model is set to a 99.33% LCLU prey capacity, at 100.00% of the distance away from its LCLU predator population (*i.e.* $FMF = 1$). With sensitivity parameter $l \in [1, 7; \Delta l = .5]$, the transfer function reports increased $FMF$ sensitivity to an early detection of fragmentation for every value. For an individual scene, $l$ effects spatial frequencies by amplifying higher frequencies. This amplification increases $FMF$ sensitivity to individual and contiguous pixel patch pattern, as well as noise. The complete $FMF$ metric phase is a *distance*-normalized scalar $\left( i.e. \ \int_{\xi=-\infty}^{\xi=\infty} \int_{\eta=-\infty}^{\eta=\infty} 2\pi(\tilde{\mathbf{r}}_{max} \bullet \tilde{\rho})\partial\xi\partial\eta \right)$, as shown in Equation 4.15:

$$ 0 < \hat{\Phi}_{f_i, f_j}(\tilde{\mathbf{r}}_{max}, l) \equiv \left( e^{\left[ \left( \frac{\int_{\xi=-\infty}^{\xi=\infty} \int_{\eta=-\infty}^{\eta=\infty} \phi\{F_i[\xi,\eta]\} - \phi\{F_j[\xi,\eta]\} + 2\pi(\tilde{\mathbf{r}} \bullet \tilde{\rho})\partial\xi\partial\eta}{\int_{\xi=-\infty}^{\xi=\infty} \int_{\eta=-\infty}^{\eta=\infty} 2\pi(\tilde{\mathbf{r}}_{max} \bullet \tilde{\rho})\partial\xi\partial\eta} \right) \right]} \right)^l \leq 1 \qquad (4.15) $$

Where, in the phase $\int_{\xi=-\infty}^{\xi=\infty} \int_{\eta=-\infty}^{\eta=\infty} 2\pi(\tilde{\mathbf{r}}_{max} \bullet \tilde{\rho})\partial\xi\partial\eta$ is a summation of the landscape's largest phase. This is a product of the landscape's furthest possible distance $\tilde{\mathbf{r}}_{max}$ between classes $i$ and $j$.
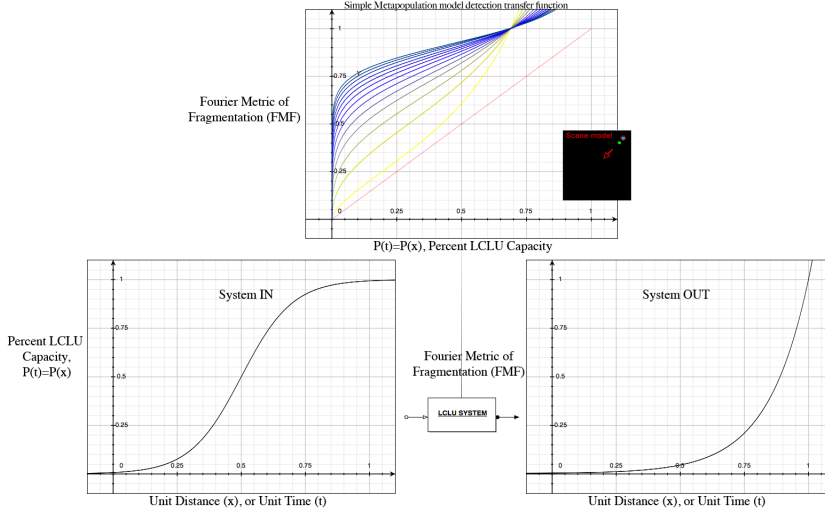


Figure 4.5: The $FMF$ transfer function for LCLU fragmentation, assuming Metapopulation: logistic-sigmoid function of LCLU existence. There are 13 $FMF$ transfer functions for sensitivity parameter $l \in [1, 7; \Delta l = .5]$—the $FMF$ transfer functions are shown as shades of yellow $l = 1$ to dark blue $l = 7$. A direct measure of LCLU fragmentation would be the $1:1$ red line. The *Scene Model* is of two distant delta functions growing further apart along a direct and linear spatial path. The shared transfer function crossing point $TTF = 1$ occurs at 68.91% of the distance away.

**FMF Phase Uncertainty**

Uncertainty is introduced into $\hat{\Phi}_{f_i,f_j}(\tilde{\mathbf{r}}_{max}, l)$ values by error in the phase. In real Fourier imaging applications, the phase has to be unwrapped from only cycling between $\pm\frac{\pi}{2}$[Easton, 2005]. This phase unwrapping introduces phase error $\pm\Delta\phi$. Additionally, the spatial translation in the phase $\tilde{\mathbf{r}}$ can only be as precise as the spatial resolution. The observed position is assumed to be at the center of the pixel, with uncertainty bounded by the extent of the pixel's sides $\pm\Delta\tilde{\mathbf{r}}$. Observed FMF values are expressed as:

$$\hat{\Phi}_{f_i,f_j}(\tilde{\mathbf{r}}_{max}, l) = \left( e^{\left[ \left( \frac{\left( \int_{\xi=-\infty}^{\xi=\infty} \int_{\eta=-\infty}^{\eta=\infty} \phi\{F_i[\xi,\eta]\} - \phi\{F_j[\xi,\eta]\} + 2\pi((\tilde{\mathbf{r}}\pm\Delta\tilde{\mathbf{r}})\bullet\tilde{\rho})\partial\xi\partial\eta \right)\pm\Delta\phi}{\int_{\xi=-\infty}^{\xi=\infty} \int_{\eta=-\infty}^{\eta=\infty} 2\pi(\tilde{\mathbf{r}}_{max}\bullet\tilde{\rho})\partial\xi\partial\eta} \right) \right]} \right)^l \quad (4.16)$$

**FMF–Magnitude**

The scalar magnitude $\hat{M}_{f_j}$ is the *condition*-normalized spectral density of whichever class spectral density is being considered—either the class being observed to increase as it fragments across some landscape, or the class being observed to fragment into extinction, out of some landscape. The chosen class spectral density $S_j$ is normalized for every class spectral density *condition* $S_j + S_k$ being investigated for fragmentation:

$$0 \leq \hat{M}_{f_j,f_k}(S_j, S_k) \equiv \frac{\int_{\xi=-\infty}^{\xi=\infty} \mid F_j[\xi,\eta] \mid^2 \partial\xi\partial\eta}{\int_{\xi=-\infty}^{\xi=\infty} \int_{\eta=-\infty}^{\eta=\infty} \mid F_j[\xi,\eta] \mid^2 \partial\xi\partial\eta + \int_{\xi=-\infty}^{\xi=\infty} \int_{\eta=-\infty}^{\eta=\infty} \mid F_k[\xi,\eta] \mid^2 \partial\xi\partial\eta} \leq 1$$
$$(4.17)$$

Equivalently, by Parseval's theorem

$$\hat{M}_{f_j,f_k}(S_j, S_k) \equiv \frac{S_j}{S_j + S_k} = \frac{\text{total number of pixels in class } j}{\text{total number of pixels in classes } j \text{ and } k} \quad (4.18)$$

Where, $k$ is any combination of the other classes in a LCLU map.

**FMF Magnitude Uncertainty**

Uncertainty is introduced into FMF magnitude values by ROC parameters explained in Section 3.3.2. Upper bound (UB), lower bound (LB), and observed (OBS) FMF magnitude values are expressed as:

$$\begin{aligned}
\hat{M}_{f_j,f_k} &\equiv \prod_j^D \hat{M}_{f_j,f_k,OBS} \quad \begin{array}{l} +\prod_j^D \hat{M}_{f_j,f_k,UB} \\ -\prod_j^D \hat{M}_{f_j,f_k,LB} \end{array} \\
&= \prod_j^D \hat{M}_{f_j,f_k,TP+\frac{FN}{2}} \quad \begin{array}{l} +\prod_j^D \hat{M}_{f_j,f_k,TP} \\ -\prod_j^D \hat{M}_{f_j,f_k,TP+FN} \end{array} \ .
\end{aligned} \quad (4.19)$$

**FMF**

The $FMF$ scalar magnitude $0 \leq \hat{M}_{f_j,f_k} \leq 1$ of Equation 4.18 reveals how relatively large $\hat{M}_{f_j,f_k} \approx 1$, or small $\hat{M}_{f_j,f_k} \approx 0$, class $j$ is within some landscape. The scalar $FMF$ phase $0 < \hat{\Phi}_{f_j,f_k,l} \leq 1$ of equation 4.15 reveals how close $\hat{\Phi}_{f_j,f_k,l} \approx 0$, or far $\hat{\Phi}_{f_j,f_k,l} \approx 1$, class $j$ is from class $k$.

The $FMF$ metric follows fragmentation trends directly. As the class cover increases $\hat{M}_{f_j,f_k} \to 1$ and as between class distance decreases $\hat{\Phi}_{f_j,f_k,l} \to 0$, the potential of class $i$ fragmentation increases. $FMF \approx 0$ is interpreted as low fragmentation, and $FMF \approx 1$ is interpreted as high fragmentation:

$$0 \leq FMF(S_j, S_k, \tilde{\mathbf{r}}_{max}, l) \equiv \hat{M}_{f_j,f_k} \cdot (1 - \hat{\Phi}_{f_j,f_k,l}) < 1 \tag{4.20}$$

**FMF Uncertainty**

Uncertainty is introduced into FMF values by joint FMF magnitude uncertainty and FMF phase uncertainty. These uncertainties are joined by the joint variance expression in equation 3.12.

$$
\begin{aligned}
FMF(S_j, S_k, \tilde{\mathbf{r}}_{max}, l) &\equiv \hat{M}_{f_j,f_k,OBS} \cdot (1 - \hat{\Phi}_{f_j,f_k,l,OBS}) \pm \Delta FMF; \\
\Delta FMF &= \sigma^2_{\hat{\Phi}_{f_i,f_j}} \cdot \hat{M}^2_{f_j,f_k,OBS} + \sigma^2_{\hat{M}_{f_j,f_k}} \cdot (1 - \hat{\Phi}^2_{f_i,f_j,OBS}) + \sigma^2_{\hat{\Phi}_{f_i,f_j}} \cdot \sigma^2_{\hat{M}_{f_j,f_k}}.
\end{aligned}
\tag{4.21}
$$

## 4.3   Metric of Landscape Occupancy

Unlike in the previous sections, there is no proposal of new metric material here. Instead, an introduction to a different type of *Fractal Dimension* estimation for Landscape Ecology LCLU maps is presented. For fractal dimension estimation of statistically self-similar LCLU classification patches (see section 3.2.4), the Yuen et al. [2004] least squares method of the Fourier power spectrum is proposed. After linearizing the Fourier power spectrum, the Hough transform is used to estimate the Hurst dimension $H$ and thereby fractal dimension $D_{fr}$.

The least squares Fourier power spectrum method varies smoothly across resolution, and so maintains accuracy, but decreases precision with increases in pixel size [Brewer and Girolamo, 2006]. To increase $lsFT$ precision the Hough transform, known to be robust to outliers, is adapted for estimation. The least squares Fourier power spectrum method written in a linear form takes advantage of the Hough transform addition.

### 4.3.1   Yuen et al. [2004] Least Squares Fourier Transform Fractal Dimension Estimation

The 2-D Fourier power spectrum $P_{fr}[\xi, \eta]$ for a Fourier fractal signal $F_{fr}[\xi, \eta]$ is statistically equal to the least squares Fourier power spectrum estimator:

$$P_{fr}[\xi, \eta] = |F_{fr}[\xi, \eta]|^2 \equiv \frac{A}{(\xi^2 + \eta^2)^{H+1}}, \text{ where } D_{fr} = 3 - H, \tag{4.22}$$

$A$ is a proportional constant, $D_{fr}$ is the fractal dimension, and $H$ is the Hurst exponent.

The true fractal signal $f_{fr}[x, y]$ and fractal noise $\epsilon[x, y]$, have power spectrum $P_{fr}[\xi, \eta]$ and $\epsilon[\xi, \eta]$, respectively. The composite signal $f[x, y] = f_{fr}[x, y] + \epsilon[x, y]$ has power spectrum $P[\xi, \eta]$:

$$P[\xi, \eta] = P_{fr}[\xi, \eta] + \epsilon[\xi, \eta]. \tag{4.23}$$

Solving for $P_{fr}$ in Equation 4.23, and taking the logarithm of both sides in Equation 4.22 linearizes the least squares Fourier power spectrum equation.

$$
\begin{aligned}
\log\left[P[\xi, \eta] - \epsilon[\xi, \eta]\right] &= \log[A] - (H + 1) \cdot \log\left[\xi^2 + \eta^2\right] \tag{4.24} \\
&\text{So,} \\
\log[A] &= (H + 1) \cdot \log\left[\xi^2 + \eta^2\right] + \log\left[P[\xi, \eta] - \epsilon[\xi, \eta]\right] \\
&\approx (H + 1) \cdot \log\left[\xi^2 + \eta^2\right] + \log\left[P[\xi, \eta]\right]. \tag{4.25}
\end{aligned}
$$

In the last step, fractal noise $\epsilon[x, y]$ is assumed negligible. Here, the least squares Fourier transform method for estimating fractal dimension is best expressed to take advantage of the Hough transform's precision. Each possible linear trend is counted in Hough space, then the most likely linear trend is accepted for derivation of the Hurst parameter $H = 3 - D_{fr}$.

## 4.4 Landscape Pattern Metric Evaluation

It has been shown that each of these metrics can be interpreted spatially, and separately for individual LCLU classes. The $FMP$ conceptual derivation suggested a way to interpret the most significant LCLU process effecting the landscape. The $FMF$ derivation and theory gave proof for its ability to detect the Metapopulation fragmentation process early while using spatially relevant variables. And, the Yuen et al. [2004] least squares Fourier transform method ($lsFT$) increases accuracy and precision of LCLU fractal dimension estimation.

Still, how separable the measures of these landscape pattern metrics are and how much they explain both pattern and process in the landscape has not been answered. The evaluation of LPM LCLU pattern relevance can be done by factor analysis. An approach to LPM factor analysis, taken by Ritters et al. [1995], is be extended for this purpose. As a preliminary experiment to the Ritters et al. landscape pattern structure model the proposed LPM are evaluated for how independent they are to LCLU imaging system pressures (see section 5). A factor analysis of these imaging system spatial, spectral and radiometric inaccuracies in LCLU maps is also examined.

To evaluate the proposed LPM ability to explain landscape process LCLU data would need to coincide with ground truth. So, evaluation of metrics to wetland variability is performed by extending the Smith et al. fecal coliform South Carolina case study, using their data sources. A LPM model for fecal coliform compromised watersheds is trained using 1992 SC sampling data, and the developed LPM model performance is evaluated using 2001 SC sampling data.

### 4.4.1 Ritters et al. [1995] Landscape Pattern and Structure Model

Ritters et al. statistically compared multiple LPM to find how well each metric responds to relevant LCLU map change. Their experiment is repeated here, this time including my proposed LPM and other recently developed LPM from the literature (see Appendix A). Success is interpreted with

regard to how well each metric independently responds to relevant landscape change. The best metrics from this experiment would be the ones whom are clearly not repeats of an existing metric.

Figure 4.6 shows the steps involved. Data values of each observed LPM vector,

$$\mathbf{LPM}^{'} = [\mathbf{LPM}_{\mathbf{1}}^{'}, \mathbf{LPM}_{\mathbf{2}}^{'}, ..., \mathbf{LPM}_{\mathbf{p}}^{'}], \tag{4.26}$$

are used to populate a correlation matrix $\vec{\mathbf{\Sigma}}$ that can reveal the observed metric's ability to explain variable landscapes. Through Principal Components Analysis (PCA) an eigenvector matrix $\vec{\mathbf{E}}$ is produced whose eigenvector columns provide the most general description for LPM ability to explain $t$ variable landscapes. This general description comes by way of the uncorrelated, maximum variance, linear combinations produced through PCA:

$$Y_1 = \mathbf{a}_{\mathbf{1}}^{'}\mathbf{LPM} = a_{11}LPM_1 + a_{12}LPM_2 + \cdots + a_{1(p \cdot t)}LPM_{p \cdot t}$$
$$Y_2 = \mathbf{a}_{\mathbf{2}}^{'}\mathbf{LPM} = a_{21}LPM_1 + a_{22}LPM_2 + \cdots + a_{2(p \cdot t)}LPM_{p \cdot t}$$
$$\vdots$$
$$Y_p = \mathbf{a}_{\mathbf{p}}^{'}\mathbf{LPM} = a_{p1}LPM_1 + a_{p2}LPM_2 + \cdots + a_{p(p \cdot t)}LPM_{p \cdot t}.$$
$$\tag{4.27}$$

These linear combinations are ranked from 1 to $p$ by descending descriptive ability, and are composed of individually weighted $\mathbf{LPM}_{\mathbf{i}}^{'} = [LPM_1, LPM_2, ..., LPM_t]$ from all the $t$ $7.68 \times 7.68$ $[km]$ National Land Cover Data (NLCD) LCLU areas. This $[\sum_t a_{j,t}LPM_t]$ weighted presence of an individual vector $\mathbf{LPM}$ is that LPM's contribution to landscape description. So, the more contribution to independent landscape descriptions $Y_j$ a LPM tends to make, the more uniquely able (*i.e.* independently) to describe (*i.e.* responds with high variance to) a landscape the LPM is.

To obtain this measure for unique, typically descriptive LPM the dot product unit magnitude of individual metric correlation vectors to each eigenvector can be used for the % explanation of an individual metric to relevant landscape variability. The more uncorrelated any metric correlation column vector is to any individual eigenvector column vector, the less of a relationship there is between that metric and the variable landscape condition—this allows us to say to what degree the observed metric and variable landscape are unrelated. Projecting each correlation column vector $\mathbf{Y}_{\mathbf{p}}$, created from every LPM column vector ($\mathbf{FMP}$, $\mathbf{FMF}$, $\mathbf{LsFT}$, etc.), into the original metric space,

$$\widehat{\mathbf{LPM}_{\mathbf{j}}} = \frac{\vec{\mathbf{E}}\mathbf{Y}_{\mathbf{j}}}{|Y_j|}, \tag{4.28}$$

a direct measure of LPM ability to explain the $p$ observed LCLU map changes compared to the full set of metrics, including Appendix A, is obtained. Each element in $\tilde{\mathbf{LPM}}_{\mathbf{j}}$ is the % $LPM_{j,t=k}$ contributed to landscape $k$ explanation. Summing across every $k$ landscape and averaging over the $p$ observed variances, the typically explained variance for the LPM is obtained:

$$\bar{\sigma}_{LPM} = \sum_{j=1}^{p} \frac{\sum_{k=1}^{t} LPM_{j,t}}{p}. \tag{4.29}$$

60

This Factor Analysis is done using the SAS FACTOR analysis statistical software.
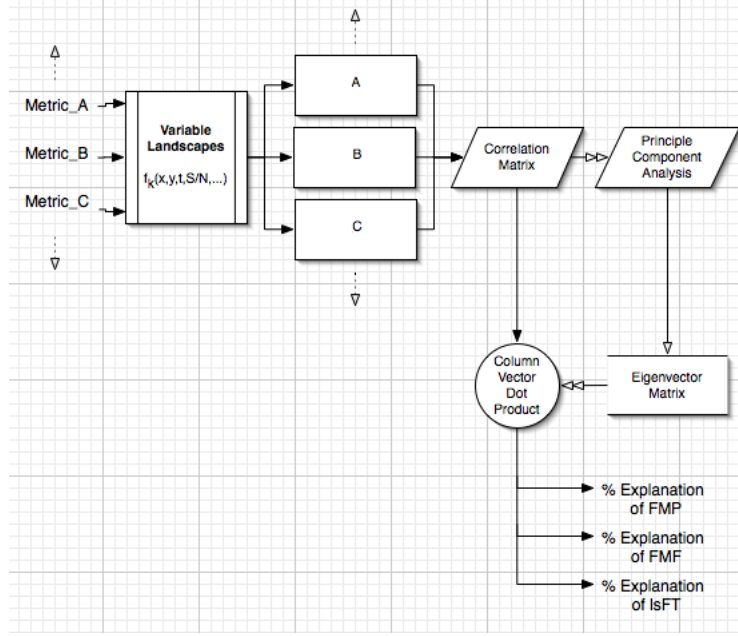


Figure 4.6: The LCLU observation factor analysis flow chart. Vectors for each LPM, from variable landscape values, are produced. With these metric vectors the correlation matrix for observed LPM is populated. Principal Component Analysis eigenvectors that most explain the variable landscapes, are then used to find the % explanation of each proposed metric: $FMP$, $FMF$, and $LsFT$.

Fifty-six maps have been selected from the 1992 National Land Cover Data (NLCD). The selection is intended to represent a rough transect of landscape patterns across physiographic regions of the United States [Hunsaker et al., 1994]. 1992 National Land Cover Data (NLCD) is a 21-category land cover classification scheme (see Table 4.1) that has been applied consistently over the conterminous United States. It is based primarily on the unsupervised classification of Landsat TM (Thematic Mapper) 1992 imagery. Ancillary data sources include topography, census, agricultural statistics, soil characteristics, other land cover maps, and wetlands data. The NLCD 1992 classification is raster data with a spatial resolution of 30 meters. The seamless product is cast to the Albers Equal-Area Conic projection, referenced to the North American Datum of 1983 (NAD83), and divided into $256 \times 256$ GeoTIFF image blocks (see Figure 4.7).

These NLCD maps cover Ecoregions, which are ecosystems of regional extent, in the United States. Four levels of detail are included that encourage unique landscape pattern. The largest ecosystems are *Domains*, or groups of related climates, that are defined based on precipitation and temperature. *Divisions* represent the climates within *Domains* and are differentiated based on precipitation levels and patterns as well as temperature. *Divisions* are subdivided into *Provinces*, which are differentiated based on vegetation or other natural land covers. The finest level of

Table 4.1: Descriptions of LCLU attribute class colors for 1992 NLCD [Anderson et al., 1976].

| LCLU class color | Anderson Level II attribute class description |
|---|---|
| Blue | Open Water |
| Yellow | Low Intensity Residential |
| Orange | High Intensity Residential |
| Red | Commercial, Industrial, Transportation |
| White | Bare Rock, Sand |
| Purple | Quarry, Strip Mine |
| Magenta | Transtional Barren |
| Light Green | Deciduous Forest |
| Dark Green | Evergreen Forest |
| Green | Mixed Forest |
| Lavender | Grassy, Herbaceous |
| Light Tan | Pasture, Hay |
| Brown | Row Crops |
| Tan | Small Grains |
| Gray | Other Grasses |
| Light Blue | Woody Wetlands |
| Very Light Blue | Herbaceous Wetlands |
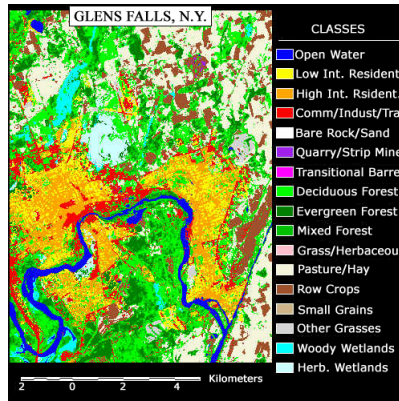


Figure 4.7: A $256 \times 256$ chip of National Land Cover Database (NLCD) Glens Falls, NY land cover.

detail is described by subregions, called *Sections*, which are subdivisions of *Provinces* based on terrain features. Also identified are mountainous areas that exhibit different ecological zones based on elevation. Each of these pattern and process influenced Ecoregions provide ample landscape variability to test these metrics, and are shown in Appendix C. In the Appendix, Table B.1 describes Land Use Data Analysis (LUDA) LCLU attribute class codes used by Ritters et al. for a comparison to Table 4.1.

### 4.4.2   Smith et al. [2001] South Carolina Case Study

States, territories and tribal lands are required to monitor local water quality every two years to comply with section 305 of the Clean Water Act. Part of this assessment includes identification, listing, and prioritization of the water bodies that do not meet water quality standards, referred to as the 303(d) list. After identification States and other jurisdictions develop Total Maximum Daily Loads (TMDL) (*i.e.* pollution budgets) for the water bodies on the 303(d) list, and in doing so create a georeferenced record of polluted locations and amounts.

Smith et al. [2001] reports on LPM for a majority ($\approx 65\%$) of the sites placed on the 303(d) list due to fecal coliform—the bacteria that usually reside in the digestive tract of warm blooded animals, and are used as a surrogate for the presence of pathogens in water bodies. High concentrations of fecal coliform are indicative of pollution that cannot be tracked to a single source discharging into a water body. Exactly the type of process Landscape Ecology provides a description of. For 1998 the LPM of Smith et al. indicated LCLU characteristics of the watershed may be a contributing factor to South Carolina's non-point source fecal coliform problem, particularly for watersheds with large proportions of urban land cover and agriculture on steep slopes ($> 9\%$) [Jennings et al., 2004, Jones et al., 2001, Smith et al., 2001, Vogelmann et al., 2001, Wickham et al., 2000].

Using updated watershed delineations from the National Hydrography Dataset (NHD) [NHD, 2009]; the 303(d) list [SCD] for 1998, 2000 and 2002; and U.S. Multi-Resolution Land Characteristics Consortium (MRLC) National Land Cover Data (NLCD) [MRL], the proposed LPM ability as temporal, ecologically relevant indicators is evaluated. The metrics proposed here are compared to those used by Smith et al. [2001] for their ability to predict presence of fecal coliform. The successful metrics would covary along with fecal coliform measurements from large proportions of urban and agricultural LCLU.

# Chapter 5

# Preliminary Results

The results of this chapter will detail some of the proposed metrics' improvements, capabilities, and application. Several landscapes of different proportions, positions, and complexity have been generated in Interactive Data Language (IDL) and by using Gardner's "Neutral model for testing landscape hypotheses" **Rule** software [Gardner, 2007] (see Sections 3.5 and 3.6). Each of the measured synthetic scene parameters are given for every case.

The independence of each metric to LCLU system noise is found for **Rule** generated LCLU maps of two and three class types. These are the same class map combinations discussed in Section 3.5. For this preliminary metric review eighty-one LCLU maps were generated; each having dimensions $256 \times 256$, and variable parameters:

1. Percent noisy pixels

2. $15[m]$, $30[m]$ and $200[m]$ spatial resolution

3. Edge spread of $\pm 1$ to $\pm 10$ edge pixels

4. LCLU maps of two cover types with probabilities
   $p[x] \in [0.1, 0.9; \Delta = 0.1]$;
   $q[x] = 1 - p[x]$;

   and

   LCLU maps of three cover types with probabilities
   $t[x] \in [0.1, 0.9; \Delta = 0.1]$;
   $r[x] = (1 - t[x]) \cdot p[x]$;
   $s[x] = (1 - t[x]) \cdot q[x]$.

5. Variable Hurst dimension $[0, 1; \Delta H = 0.1]$ for LCLU maps of two cover types.

6. Variable fractal resolution.

This preliminary review is divided into several sections. Each section introduction will review IDL variables and the process being observed in each experimental design. A discussion on each

metric's performance under imaging system spatial, spectral, and radiometric variability then follows. The review begins in Section 5.1 with a simple one-dimensional calculation of the Fourier Metric of Fragmentation ($FMF$), followed by a series of experiments that reveal the ability of $FMF$ to measure the presence of LCLU on a landscape. Section 5.2 compares the proposed metric of landscape composition, Fourier Metric of Proportion ($FMP$), against the current metric of landscape composition, *Dominance*. Additionally, Section 5.2 reveals the independence of $FMF$ and $FMP$, unlike the high correlation between *Contagion* and *Dominance*. Last in this preliminary review, is the Least Squares Fourier Transform Fractal Dimension Estimation ($LsFT$), in Section 5.3. Section 5.3 discusses the performance of $LsFT$ under multiple imaging system conditions (see Section 3.2.4).

## 5.1 Fourier Metric of Fragmentation ($FMF$)

Here, we observe the $FMF$ ability to measure landscape configuration and its performance for $15[m]$, $30[m]$, and $200[m]$ imaging system spatial resolution. Examples used to explain what $FMF$ is measuring in an image are presented with increasing complexity. All of the examples covered in this section are:

**5.1.1 A one-dimensional $FMF$ exercise.** Using the discrete Fourier transform (see equation 3.37), the $FMF$ phase $\hat{\Phi}_{f_j,f_k,l}$ relationship with distance and the application of phase normalization are explored.

**5.1.2 The $FMF$ ability to measure LCLU class existence.** Each of these examples assume the observed LCLU class map has 100% cover, and are measures of $FMF$ in space and time. These observed class maps are line scans of a $1024 \times 192$ scene. Indicative of the base $FMF$ metric precision, the degree of error introduced by Fourier phase unwrapping (see Section 4.2.1) is measured. And, each experimental design reveals these aspects of Island Biogeography concepts (see Section 3.1.1):

- when using multiple sensitivity parameters $l = .5, 2, 4,$ and $6$;
- when a LCLU patch is in motion;
- when a smaller sized LCLU patch is in motion;
- when multiple LCLU patches are in motion;
- when a LCLU patch is growing;
- when two LCLU patches initially have and eventually lose a shared growth and extinction process;
- when the growth and extinction process of two LCLU classes are inextricably linked.

**5.1.3 The $FMF$ performance under variable imaging system spatial resolution.** Examples of $FMF$ on a $512 \times 512$ map are considered:

- when using multiple sensitivity parameters $l = .5, 2, 4,$ and $6$, at $15[m], 30[m],$ and $200[m]$ spatial resolution;
- when at $200[m]$ spatial resolution, and the direction the LCLU patch travels is at $\theta = 30°$, and $60°$ from the horizontal;

65

- when the LCLU pattern has changed;
- when the $P =priori$ (*i.e.* proportion of LCLU) and $AP =a\ priori$ (*i.e.* classification likelihood of LCLU) are
  - $P = 0.95, AP = 1.00;$
  - $P = 0.50, AP = 1.00;$
  - $P = 0.95, AP = 0.50.$

### 5.1.1  A one-dimensional $FMF$ exercise

Consider two LCLU classes with one pixel landscape coverage. These LCLU class maps are $3 \times 1$ and shown in Figure 5.1. Using the discrete Fourier transform (DFT) we can observe the $FMF$ phase operation for this LCLU class map.
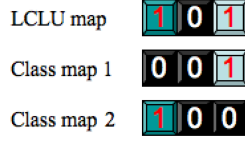


Figure 5.1: Two LCLU class maps. Both cover one pixel in the $3 \times 1$ LCLU map landscape. Black represents no class present, cyan represents class 1 coverage, green represents class 2 coverage, and the scalar value indicating class presence is 1 or no class presence 0.

To prevent any error due to aliasing, we will use zero padded versions of each class map vector. The zero padding extends the $3 \times 1$ class map vectors to $7 \times 1$. Additionally, their corresponding DFT matrix is $7 \times 7$:

$$\begin{bmatrix} F[0] \\ F[1] \\ F[2] \\ F[3] \\ F[4] \\ F[5] \\ F[6] \end{bmatrix} = \begin{bmatrix} (e^{-\frac{i2\pi 0}{7}})^0 & (e^{-\frac{i2\pi 1}{7}})^0 & (e^{-\frac{i2\pi 2}{7}})^0 & (e^{-\frac{i2\pi 3}{7}})^0 & (e^{-\frac{i2\pi 4}{7}})^0 & (e^{-\frac{i2\pi 5}{7}})^0 & (e^{-\frac{i2\pi 6}{7}})^0 \\ (e^{-\frac{i2\pi 0}{7}})^1 & (e^{-\frac{i2\pi 1}{7}})^1 & (e^{-\frac{i2\pi 2}{7}})^1 & (e^{-\frac{i2\pi 3}{7}})^1 & (e^{-\frac{i2\pi 4}{7}})^1 & (e^{-\frac{i2\pi 5}{7}})^1 & (e^{-\frac{i2\pi 6}{7}})^1 \\ (e^{-\frac{i2\pi 0}{7}})^2 & (e^{-\frac{i2\pi 1}{7}})^2 & (e^{-\frac{i2\pi 2}{7}})^2 & (e^{-\frac{i2\pi 3}{7}})^2 & (e^{-\frac{i2\pi 4}{7}})^2 & (e^{-\frac{i2\pi 5}{7}})^2 & (e^{-\frac{i2\pi 6}{7}})^2 \\ (e^{-\frac{i2\pi 0}{7}})^3 & (e^{-\frac{i2\pi 1}{7}})^3 & (e^{-\frac{i2\pi 2}{7}})^3 & (e^{-\frac{i2\pi 3}{7}})^3 & (e^{-\frac{i2\pi 4}{7}})^3 & (e^{-\frac{i2\pi 5}{7}})^3 & (e^{-\frac{i2\pi 6}{7}})^3 \\ (e^{-\frac{i2\pi 0}{7}})^4 & (e^{-\frac{i2\pi 1}{7}})^4 & (e^{-\frac{i2\pi 2}{7}})^4 & (e^{-\frac{i2\pi 3}{7}})^4 & (e^{-\frac{i2\pi 4}{7}})^4 & (e^{-\frac{i2\pi 5}{7}})^4 & (e^{-\frac{i2\pi 6}{7}})^4 \\ (e^{-\frac{i2\pi 0}{7}})^5 & (e^{-\frac{i2\pi 1}{7}})^5 & (e^{-\frac{i2\pi 2}{7}})^5 & (e^{-\frac{i2\pi 3}{7}})^5 & (e^{-\frac{i2\pi 4}{7}})^5 & (e^{-\frac{i2\pi 5}{7}})^5 & (e^{-\frac{i2\pi 6}{7}})^5 \\ (e^{-\frac{i2\pi 0}{7}})^6 & (e^{-\frac{i2\pi 1}{7}})^6 & (e^{-\frac{i2\pi 2}{7}})^6 & (e^{-\frac{i2\pi 3}{7}})^6 & (e^{-\frac{i2\pi 4}{7}})^6 & (e^{-\frac{i2\pi 5}{7}})^6 & (e^{-\frac{i2\pi 6}{7}})^6 \end{bmatrix} \begin{bmatrix} f[0] \\ f[1] \\ f[2] \\ f[3] \\ f[4] \\ f[5] \\ f[6] \end{bmatrix}$$

Where $F[k]$ is the $k^{th}$ element of the Fourier domain vector, and $f[n]$ is the $n^{th}$ element of the spatial domain vector.

To show the vector operation, each class map vector is placed above the DFT transformation vector. Vector multiplication of each class map column vector, against every DFT matrix row vector, can be followed vertically in Equation 5.1. Transforming the zero padded class map vectors into the discrete Fourier domain we have:

$$
\begin{aligned}
&\text{Class map 1 : } \begin{bmatrix} 0 & 0 & 1 & 0 & 0 & 0 & 0 \end{bmatrix} \\
&\text{Class map 2 : } \begin{bmatrix} 1 & 0 & 0 & 0 & 0 & 0 & 0 \end{bmatrix}
\end{aligned}
$$

Class 1 ; Class 2

$$
\begin{bmatrix} e^{-\frac{i2\pi 0}{7}} \\ e^{-\frac{i2\pi 2}{7}} \\ e^{-\frac{i2\pi 4}{7}} \\ e^{-\frac{i2\pi 6}{7}} \\ e^{-\frac{i2\pi 8}{7}} \\ e^{-\frac{i2\pi 10}{7}} \\ e^{-\frac{i2\pi 12}{7}} \end{bmatrix}
\begin{bmatrix} e^{-\frac{i2\pi 0}{7}} \\ e^{-\frac{i2\pi 0}{7}} \\ e^{-\frac{i2\pi 0}{7}} \\ e^{-\frac{i2\pi 0}{7}} \\ e^{-\frac{i2\pi 0}{7}} \\ e^{-\frac{i2\pi 0}{7}} \\ e^{-\frac{i2\pi 0}{7}} \end{bmatrix}
=
\begin{bmatrix}
(e^{-\frac{i2\pi 0}{7}})^0 & (e^{-\frac{i2\pi 1}{7}})^0 & (e^{-\frac{i2\pi 2}{7}})^0 & (e^{-\frac{i2\pi 3}{7}})^0 & (e^{-\frac{i2\pi 4}{7}})^0 & (e^{-\frac{i2\pi 5}{7}})^0 & (e^{-\frac{i2\pi 6}{7}})^0 \\
(e^{-\frac{i2\pi 0}{7}})^1 & (e^{-\frac{i2\pi 1}{7}})^1 & (e^{-\frac{i2\pi 2}{7}})^1 & (e^{-\frac{i2\pi 3}{7}})^1 & (e^{-\frac{i2\pi 4}{7}})^1 & (e^{-\frac{i2\pi 5}{7}})^1 & (e^{-\frac{i2\pi 6}{7}})^1 \\
(e^{-\frac{i2\pi 0}{7}})^2 & (e^{-\frac{i2\pi 1}{7}})^2 & (e^{-\frac{i2\pi 2}{7}})^2 & (e^{-\frac{i2\pi 3}{7}})^2 & (e^{-\frac{i2\pi 4}{7}})^2 & (e^{-\frac{i2\pi 5}{7}})^2 & (e^{-\frac{i2\pi 6}{7}})^2 \\
(e^{-\frac{i2\pi 0}{7}})^3 & (e^{-\frac{i2\pi 1}{7}})^3 & (e^{-\frac{i2\pi 2}{7}})^3 & (e^{-\frac{i2\pi 3}{7}})^3 & (e^{-\frac{i2\pi 4}{7}})^3 & (e^{-\frac{i2\pi 5}{7}})^3 & (e^{-\frac{i2\pi 6}{7}})^3 \\
(e^{-\frac{i2\pi 0}{7}})^4 & (e^{-\frac{i2\pi 1}{7}})^4 & (e^{-\frac{i2\pi 2}{7}})^4 & (e^{-\frac{i2\pi 3}{7}})^4 & (e^{-\frac{i2\pi 4}{7}})^4 & (e^{-\frac{i2\pi 5}{7}})^4 & (e^{-\frac{i2\pi 6}{7}})^4 \\
(e^{-\frac{i2\pi 0}{7}})^5 & (e^{-\frac{i2\pi 1}{7}})^5 & (e^{-\frac{i2\pi 2}{7}})^5 & (e^{-\frac{i2\pi 3}{7}})^5 & (e^{-\frac{i2\pi 4}{7}})^5 & (e^{-\frac{i2\pi 5}{7}})^5 & (e^{-\frac{i2\pi 6}{7}})^5 \\
(e^{-\frac{i2\pi 0}{7}})^6 & (e^{-\frac{i2\pi 1}{7}})^6 & (e^{-\frac{i2\pi 2}{7}})^6 & (e^{-\frac{i2\pi 3}{7}})^6 & (e^{-\frac{i2\pi 4}{7}})^6 & (e^{-\frac{i2\pi 5}{7}})^6 & (e^{-\frac{i2\pi 6}{7}})^6
\end{bmatrix}
$$

$$\tag{5.1}$$

Equation 5.1 creates LCLU class map Fourier domain vectors:

$$
\begin{aligned}
F_1[k] &= 1[k\Delta\xi] \cdot e^{-2\pi\frac{in_1\cdot k}{N}}, \text{ where } n_1 = 0, \tag{5.2}\\
F_2[k] &= 1[k\Delta\xi] \cdot e^{-2\pi\frac{in_2\cdot k}{N}}, \text{ where } n_2 = 2. \tag{5.3}
\end{aligned}
$$

Here, $n_i$ is the pixel element in the spatial domain of class map $i$, and $N = 7$ is the total length of the padded input class map vectors. This relationship is maintained for any length spatial domain vector, and is an example of the Fourier translation property (see equation 3.41).

The steps to obtain $FMF$ phase $\hat{\Phi}_{f_j,f_k,l}$ from these two functions are:

1. - Separate the function into phase only.

$$
\begin{aligned}
e^{i\Delta\Phi_{1,2}} &= \left(1[k\Delta\xi] \cdot e^{-2\pi\frac{in_2\cdot k}{N}}\right) \cdot \left(1[k\Delta\xi] \cdot e^{-2\pi\frac{in_1\cdot k}{N}}\right)^{-1} \\
&= e^{-2\pi\frac{ik}{N}(n_1-n_2)}
\end{aligned}
$$

2. - Unwrap the phase, and take the magnitude.

$$
|\Delta\Phi_{1,2}| = |\Delta\Phi_{2,1}| = \left| -2\pi\frac{k}{N}(n_1-n_2)\right| = 2\pi\frac{k}{N}|n_1-n_2|
$$

3. - Sum the phase.

$$
\begin{aligned}
\sum|\Delta\Phi_{1,2}| &= \sum_{k=1}^{N-1} 2\pi\frac{k}{N}|n_1-n_2| = \frac{2\pi}{N}|n_1-n_2|\sum_{k=1}^{N-1} k \\
&= \frac{2\pi}{N}|n_1-n_2|\left(\frac{N-1+1}{2}(N-1)\right) \\
&= \pi|n_1-n_2|(N-1)
\end{aligned}
$$

4. - Normalize summed phase.

$$
\frac{\Phi}{\Phi_{max}} = \hat{\Phi} = \frac{\pi|n_1-n_2|\cdot(N-1)}{\frac{\pi}{2}(N-2)(N-1)}, 0 \leq \hat{\Phi} \leq 1
$$

5. - Exponentially wrap phase, and scale to 1.

$$
\hat{\Phi}_{FMF} = 1 - e^{\frac{\pi|n_1-n_2|\cdot(N-1)}{\frac{\pi}{2}(N-2)(N-1)}}
$$

6. - Include scale parameter.

$$
\hat{\Phi}_{FMF,l} = 1 - \left(e^{l\cdot\frac{\pi|n_1-n_2|\cdot(N-1)}{\frac{\pi}{2}(N-2)(N-1)}} \cdot e^{-l}\right); 0 \leq \Phi_{FMF,l} \leq l
$$

Where $\Delta\xi = \frac{1}{N\cdot\Delta x}$ in Step 1 is the Fourier vector spatial frequency resolution (see Section 3.3.1).

The differences between positions $|n_1 - n_2|$ is the distance between LCLU class map 1 and LCLU class map 2. This is described by the $FMF$ phase $\hat{\Phi}_{FMF,l}$ in step 6. The $FMF$ magnitude $\hat{M}_{f_1,f_2}(S_1, S_2)$ calculation is trivial and shown in equation 4.18.

## 5.1.2 The $FMF$ ability to measure LCLU class existence

The time-series LCLU map experiments discussed here reveal the ability of $FMF$ to measure the influence one LCLU class has on the colonization and emigration rates of another. The two classes being observed are of a 512 [*units of pixel distance*] line scan covering the red LCLU class and white LCLU class, from within a $512 \times 192$ LCLU map. The Figures shown here will display four observations:

**a.)** on top—the observed LCLU map with a referenced green line scan across red and white LCLU class patches;

**b.)** on the middle-left—a plot of observed $FMF$ values for the two classes when some distance apart;

**c.)** on the middle-right—a plot of the observed unwrapped phase, that leads to a measure of $FMF$ values (see the example in Section 5.1.1;

**d.)** along the bottom—a plot of observed $FMF$ values between the two classes when some distance apart plotted against the error due to phase-unwrapping.

The LCLU map action is varied continuously, and $FMF$ *a priori* and *priori* class likelihood is assumed to be 100% for clarity (*i.e.* this is the only class in the landscape and it is perfectly classified). Each experiment reveals the success of $FMF$ to measure the proximity effects in Island Biogeography activity which are listed in section 5.1.3.

**$FMF$ observed when using multiple sensitivity parameters $l = .5, 2, 4,$ and 6.**

*Aspects of $FMF$ shown in this section are–*

- *The ability of $FMF$ phase to report distance information between two similar LCLU classes using their phase difference:*

Figures 5.2 and 5.3 show $FMF$ values between LCLU red and white class patches that cover 1 pixel and steadily separate from each other. The white LCLU class patch continuously goes from 1 [*units of pixel distance*] away to 512 [*units of pixel distance*] away from the red LCLU class patch, imitating a decreasing influence of the red LCLU class patch on the white LCLU class patch. The different $l$-sensitivity values are in Table 5.1, along with their initial $FMF$ values and color references.

Comparing Figure 5.2 to Figure 5.3, we observe that the area under the unwrapped phase difference between LCLU class 1 and LCLU class 2 increases as the distance between LCLU class 1 and LCLU class 2 increases. Just as was shown in Step 3 of Section 5.1.1, the phase difference is directly related to the distance between LCLU classes.

Table 5.1: Variable Sensitivity Parameter $l$, for a 1 pixel LCLU class patch.

| $l$-value | Plot Color | Initial Value | Value at $x = 300$ | Final Value |
|-----------|-----------|--------------|-------------------|-------------|
| 0.5 | Yellow | 0.39 | 0.19 | 0.00 |
| 2.0 | Blue | 0.86 | 0.56 | 0.00 |
| 4.0 | White | 0.98 | 0.81 | 0.00 |
| 6.0 | Magenta | 1.00 | 0.92 | 0.00 |
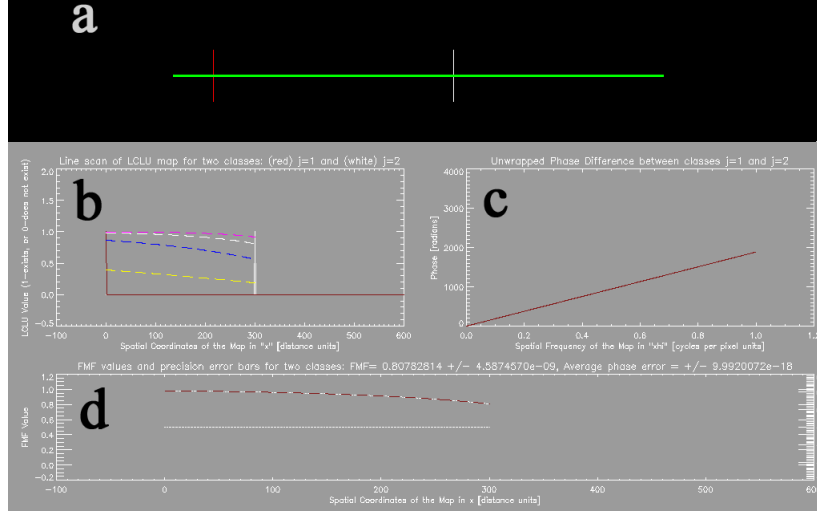


Figure 5.2: $FMF$ values between LCLU red and white class patches that cover 1 pixel at a distance $x = 300$ [*units of pixel distance*]. The white LCLU class patch has continuously moved, by 1 [*units of pixel distance*] away, to 300 [*units of pixel distance*] away from the red LCLU class patch. The green line across the LCLU map in **a** is the area covered by the line scan plot in **b**. The effect on $FMF$ by the different $l$-sensitivity values in plot **b** are referenced in Table 5.1. A plot of the unwrapped phase red-class to white-class phase difference is shown in **c**. All observed $FMF$ values and phase error are plotted in **d**, with the phase error axis displaying values for $0.3 \leq \Delta\Phi \leq -0.3$ (*i.e.* within $\pm$ 30% $FMF$).

- *The direct relationship of $FMF$ phase to patch influence according to Island Biogeography:*

After the summed phase is wrapped into an exponential function and placed into the $FMF$ phase (see Steps 5-6 of Section 5.1.1), plot **c** of both Figures 5.2 and 5.3 show how $FMF$ values decrease with increasing distance. $FMF$ values inversely trend with LCLU class patch distance, but directly trend with potential LCLU class patch influence in accordance with Island Biogeography theory.

- *The adjustable early detection rate $l$, and its effect on reported $FMF$ values:*
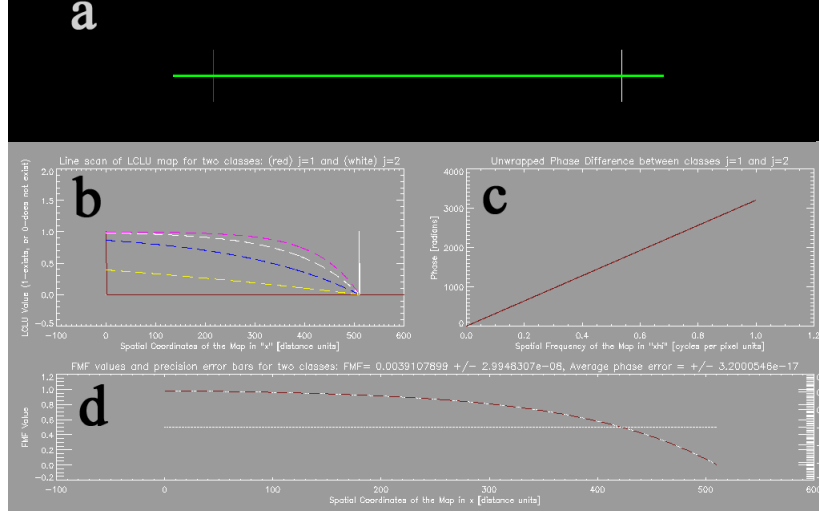
Figure 5.3: $FMF$ values between LCLU red and white class patches that cover 1 pixel. The white LCLU class patch has continuously moved, by 1 [*units of pixel distance*] away, to 512 [*units of pixel distance*] away from the red LCLU class patch. The green line across the LCLU map in **a** is the area covered by the line scan plot in **b**. The effect on $FMF$ by the different $l$-sensitivity values in plot **b** are referenced in Table 5.1. A plot of the unwrapped phase red-class to white-class phase difference is shown in **c**. All observed $FMF$ values and phase error are plotted in **d**, with the phase error axis displaying values for $0.3 \leq \Delta\Phi \leq -0.3$ (*i.e.* within $\pm$ 30% $FMF$).

The multiple $FMF$ sensitivity value plots have increasing early detection rates with increasing sensitivity parameter $l$, and decreasing near detection rates with increasing sensitivity parameter $l$. When LCLU class patches are close to each other, a high sensitivity parameter may not significantly report the difference between small between-class patch movements. For instance for a high $FMF$ sensitivity parameter $l = 6$, one-pixel distance reports $FMF_{f_1,f_2,l=6} = 0.99752125$ while a two-pixel distance reports $FMF_{f_1,f_2,l=6} = 0.99749194$. The difference observed is on the order of the ten-thousandth $1 \times 10^{-4}$ decimal unit.

- *The effects of phase precision and accuracy on reported $FMF$ values:*

The phase error $\pm\Delta\phi$ (see Section 4.2.1) limits $FMF$ precision to only be significant above $\approx \pm 1 \times 10^{-8}$. The observed effects of phase error are far below any significant change in the $1 \times 10^{-4}$ unit pixel distance limit. The inaccuracy introduced by phase error is $\approx 1 \times 10^{-17}$ units of $FMF$, and reported as average phase error in both Figures. The imprecision and inaccuracy due to phase error does not significantly effect $FMF$ values.

**$FMF$ observed when one class patch is in motion.**

*Aspects of $FMF$ shown in this section are–*

Table 5.2: Variable Sensitivity Parameter $l$, for a 200 pixel LCLU class patch.

| $l$-value | Plot Color | Initial Value | Value at $x = 300$ | Final Value |
|-----------|------------|---------------|---------------------|-------------|
| 0.5 | N/A | 0.39 | 0.19 | 0.00 |
| 2.0 | N/A | 0.86 | 0.56 | 0.00 |
| 4.0 | White | 0.98 | 0.81 | 0.00 |
| 6.0 | N/A | 1.00 | 0.92 | 0.00 |

- *The ability of $FMF$ phase to report distance information between two dissimilar LCLU classes;*

- *and the direct relationship of $FMF$ to patch influence according to Island Biogeography:*

Figure 5.4 show $FMF$ values between a red LCLU class that covers 1 pixel, and a white LCLU class that covers 200 pixels. The white LCLU class patch continuously goes from 1 [*units of pixel distance*] away to 312 [*units of pixel distance*] away from the red LCLU class patch, imitating a decreasing influence of the red LCLU class patch on the white LCLU class patch of a different size. The plotted $FMF$ values use sensitivity parameter $l = 4$. The different $l$-sensitivity values are in Table 5.2, along with their $FMF$ values. Though the patch sizes are different, the $FMF$ value relationship to distance is the same as was observed between similar LCLU classes.

Observing the unwrapped phase plot in Figure 5.4, we see that the area under the unwrapped phase difference between LCLU class 1 and LCLU class 2 is the same as the area under the unwrapped phase plot of the previous Figure 5.2, which is also at $x = 300$ [*units of pixel distance*] away. As shown in Step 3 of section 5.1.1, the phase difference is directly related to the distance between LCLU classes.

The summed phase is wrapped into an exponential function and placed into the $FMF$ phase (see Steps 5-6 of Section 5.1.1). When these values are then expressed as $FMF$ they inversely trend with LCLU class patch distance, but directly trend with potential LCLU class patch influence in accordance with Island Biogeography theory.

- *The adjustable early detection rate $l$, and its effect on reported $FMF$ values;*

- *and the effects of phase precision and accuracy on reported $FMF$ values:*

The phase error $\pm\Delta\phi$ (see section 4.2.1) for a 200-pixel LCLU class patch can be seen in plot **c**. The phase error shows up as white phase deviations from the linear red unwrapped phase. This phase error limts a 200-pixel LCLU class patch $FMF$ precision, at a distance $x = 300$ [*units of pixel distance*] and for a sensitivity parameter $l = 4$, to be significant within $\pm 8.26 \times 10^{-6}$ units of $FMF$. The 1-pixel LCLU class patch of Figure 5.2, at a distance $x = 300$ [*units of pixel distance*] and for a sensitivity parameter $l = 4$, has a $FMF$ precision that is siginficant within $\pm 5.36 \times 10^{-9}$. These observed effects of phase error for a 200-pixel LCLU class patch are generally higher across the entire 312 pixel landscape than for a 1-pixel LCLU class patch. Still, they are far below any significant change in the $1 \times 10^{-4}$ unit pixel distance limit (see Section 5.1.2). The inaccuracy introduced by phase error is $\approx 1 \times 10^{-14}$ units of $FMF$ for a 200-pixel LCLU class patch, and is reported as average phase error in Figure 5.4. The imprecision and inaccuracy due to phase error does not significantly effect $FMF$ values.
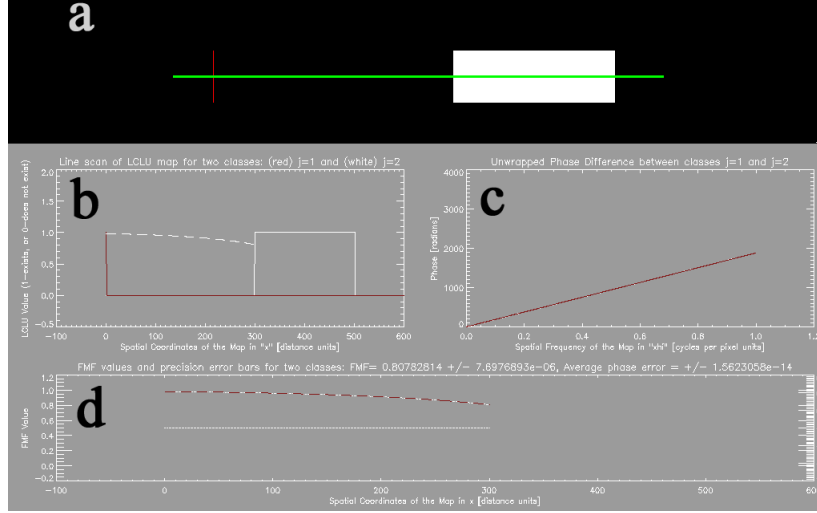
Figure 5.4: $FMF$ values between a red LCLU class that covers 1 pixel, and a white LCLU class that covers 200 pixels at a distance $x = 300$ [*units of pixel distance*] away. The white LCLU class patch has continuously moved, by 1 [*units of pixel distance*] away, to 300 [*units of pixel distance*] away from the red LCLU class patch. The green line across the LCLU map in **a** is the area covered by the line scan plot in **b**. The $FMF$ values are reported with a sensitivity parameter $l = 4$. A plot of the unwrapped phase red-class to white-class phase difference is shown in **c**. All observed $FMF$ values and phase error are plotted in **d**, with the phase error axis displaying values for $0.3 \leq \Delta\Phi \leq -0.3$ (*i.e.* within $\pm 30\% FMF$).

**$FMF$ observed when multiple class patches are in motion.**

*Aspects of $FMF$ shown in this section are–*

- *The adjustable early detection rate $l$, and its effect on reported $FMF$ values;*

- *and the ability of $FMF$ phase to report distance information of complex shaped LCLU classes:*

Figure 5.5 shows $FMF$ values between a red LCLU class that covers 1 pixel, and a patterned white LCLU class cover of two 75 pixel-width patches separated by 50 pixels. This pattern of the white LCLU class patch cover exists over the same 200 pixel area of the previous LCLU class map in Figure 5.5. The white LCLU class patch continuously goes from 1 [*units of pixel distance*] away to 312 [*units of pixel distance*] away from the red LCLU class patch, imitating a decreasing influence of the red LCLU class patch on the white LCLU class patch. The plotted $FMF$ values use sensitivity parameter $l = 4$. The different $l$-sensitivity values are in Table 5.3, along with their $FMF$ values, reporting increasing rates of early change detection with increasing $l$.

Observing the unwrapped phase plot in Figure 5.5, we see that the area under the unwrapped phase difference between LCLU class 1 and LCLU class 2 is different from the area under the unwrapped phase plotted for either of the previous examples in Figure 5.2 and Figure 5.4; which are also at $x = 300$ [*units of pixel distance*] away. This difference is due to an increase in linear

Table 5.3: Variable Sensitivity Parameter $l$, for two 75 pixel LCLU class patches.

| $l$-value | Plot Color | Initial Value | Value at $x = 300$ | Final Value |
|---|---|---|---|---|
| 0.5 | N/A | 0.39 | 0.18 | 0.00 |
| 2.0 | N/A | 0.86 | 0.54 | 0.00 |
| 4.0 | White | 0.98 | 0.79 | 0.00 |
| 6.0 | N/A | 1.00 | 0.91 | 0.00 |
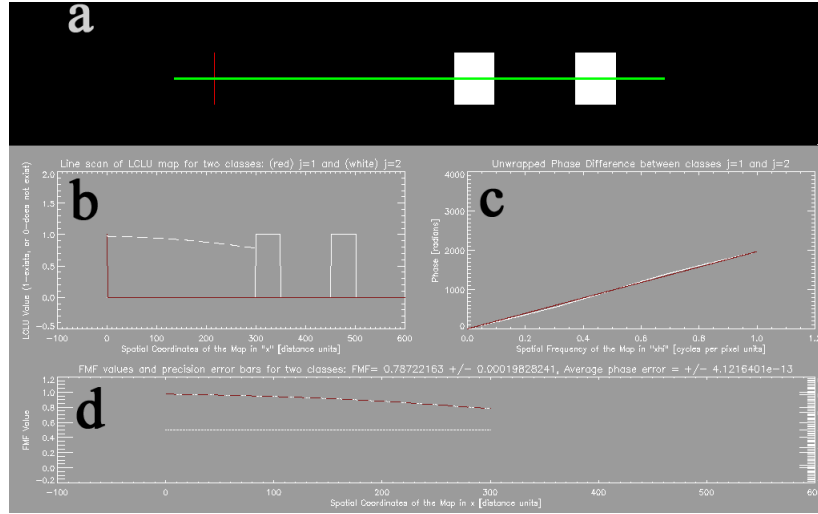


Figure 5.5: $FMF$ values between a red LCLU class that covers 1 pixel, and a white LCLU class that cover 75 pixels each, at a distance of 50 pixels apart. This white LCLU class is at a distance $x = 300$ [*units of pixel distance*] away from the red LCLU class. The white LCLU class patches have continuously moved, by 1 [*units of pixel distance*] away, to 300 [*units of pixel distance*] away from the red LCLU class patch. The green line across the LCLU map **a** is the area covered by the line scan plot **b**. The $FMF$ values are reported with a sensitivity parameter $l = 4$. A plot of the unwrapped phase red-class to white-class phase difference is shown in **c**. All observed $FMF$ values and phase error are plotted in **d**, with the phase error axis displaying values for $0.3 \leq \Delta\Phi \leq -0.3$ (*i.e.* within $\pm$ 30% $FMF$).

phase estimation error. Though, just as was shown in Step 3 of Section 5.1.1, the phase difference continues to be directly related to the distance between LCLU classes and the phase error continues to be negligible (*i.e.* precision on the order of $\pm 1 \times 10^{-8}$ and inaccuracies beyond $\approx 1 \times 10^{-17}$ $FMF$ units).

- *The direct relationship of $FMF$ to patch influence according to Island Biogeography;*

- *and the direct relationship of $FMF$ to landscape fragmentation:*

The summed phase is wrapped into an exponential function and placed into the $FMF$ phase (see Steps 5-6 of Section 5.1.1). When these values are expressed as $FMF$ they inversely trend with LCLU class patch distance, but directly trend with potential LCLU class patch influence in accordance with Island Biogeography theory.

The expected Island Biogeography proximity effects are also shown in the values of table 5.3. All $FMF$ values observed at $x = 300$ [*units of pixel distance*] of Table 5.3 are lower than either of the values in Tables 5.1 and 5.2. $FMF$ values decrease with increased spatial complexity happening in only one LCLU (*i.e.* spatial pattern that is independent of colonization and emigration). This means $FMF$ assumes increased pattern within a *single* LCLU works to prevent colonization, emigration, and fragmentation *between* LCLU.

- *The effects of phase precision and accuracy on reported $FMF$ values:*

The phase error $\pm\Delta\phi$ (see Section 4.2.1) for a patterned LCLU class cover of two 75 pixel-width patches separated by 50 pixels can be seen in plot **c**. The phase error shows up as white phase deviations from the linear red unwrapped phase. This phase error limits a patterned LCLU's $FMF$ precision, at a distance $x = 300$ [*units of pixel distance*] and for a sensitivity parameter $l = 4$, is significant within $\pm 1.98 \times 10^{-4}$ units of $FMF$. The observed effects of phase error for a patterned LCLU class cover of two 75 pixel-width patches separated by 50 pixels is generally higher across the entire 312 pixel landscape, than for any previously observed LCLU class patch experiment. Still, these observed effects of phase error are far below any significant change in the $1 \times 10^{-4}$ unit pixel distance limit (see Section 5.1.2). The inaccuracy introduced by phase error is $\approx 1 \times 10^{-13}$ units of $FMF$ for a patterned LCLU class cover of two 75 pixel-width patches separated by 50 pixels, and is reported as average phase error in Figure 5.5.

**$FMF$ observed when a LCLU class patch is growing.**

*Aspects of $FMF$ shown in this section are–*

- *The adjustable early detection rate l, and its effect on reported $FMF$ values;*

- *and the ability of $FMF$ phase to report distance information between one active and another inactive LCLU class:*

Figures 5.6 and 5.7 show $FMF$ values between a white LCLU class that covers 1 pixel, and a red LCLU class that independently increases its patch cover. The red LCLU class patch growth shrinks the distance between each patch from 512 [*units of pixel distance*] to 1 [*units of pixel distance*]. The plotted $FMF$ values use sensitivity $l = 4$. The different *l*-sensitivity values are in Table 5.4, along with their $FMF$ values, reporting increasing rates of early change detection with increasing $l$.

Comparing Figure 5.6 to Figure 5.7, we observe that the area under the unwrapped phase difference between LCLU class 1 and LCLU class 2 decreases as the distance between LCLU class 1 and LCLU class 2 decreases. Just as was shown in Step 3 of Section 5.1.1, the phase difference is directly related to the distance between LCLU classes.

- *The direct relationship of $FMF$ to patch influence according to Island Biogeography:*

Table 5.4: Variable Sensitivity Parameter $l$, for a growing LCLU class patch.

| $l$-value | Plot Color | Initial Value | Value at $x = 300$ | Final Value |
|---|---|---|---|---|
| 0.5 | N/A | 0.00 | 0.25 | 0.39 |
| 2.0 | N/A | 0.00 | 0.69 | 0.86 |
| 4.0 | White | 0.00 | 0.90 | 0.98 |
| 6.0 | N/A | -0.01 | 0.97 | 1.00 |
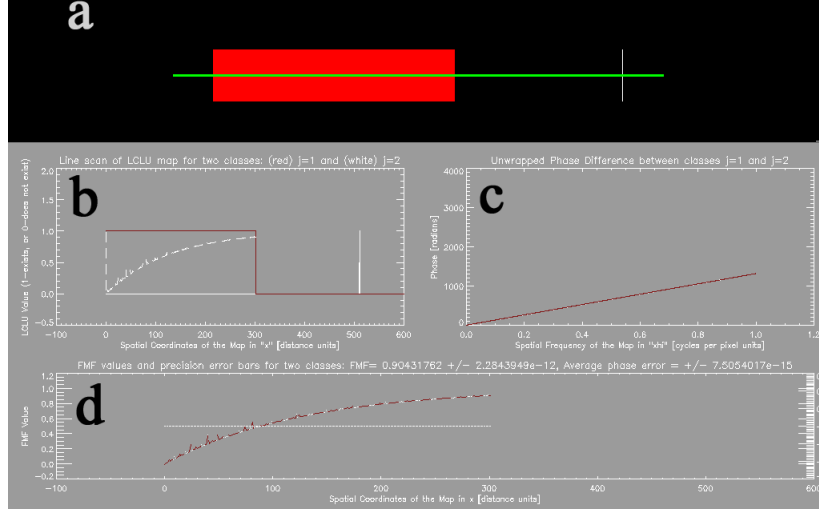


Figure 5.6: $FMF$ values between a white LCLU class that covers 1 pixel, and a red LCLU class that increases its patch cover. This red LCLU class is at a distance $x = 300$ [*units of pixel distance*] away from the white LCLU class. The red LCLU class patch has continuously moved, from 512 [*units of pixel distance*] away, to 1 [*units of pixel distance*] away from the red LCLU class patch. The green line across the LCLU map **a** is the area covered by the line scan plot **b**. The $FMF$ values are reported with a sensitivity parameter $l = 4$. A plot of the unwrapped phase red-class to white-class phase difference is shown in **c**. All observed $FMF$ values and phase error are plotted in **d**, with the phase error axis displaying values for $0.3 \leq \Delta\Phi \leq -0.3$ (*i.e.* within $\pm$ 30% $FMF$).

After the summed phase is wrapped into an exeptional function and placed into the $FMF$ phase (see Steps 5-6 of Section 5.1.1), plot **c** of both Figures 5.6 and 5.7 show how $FMF$ values decrease with increasing distance. $FMF$ values inversely trend with LCLU class patch distance, but directly trend with potential LCLU class patch influence in accordance with Island Biogeography theory.

- *The effects of phase precision and accuracy on reported $FMF$ values:*

The phase error $\pm\Delta\phi$ (see Section 4.2.1) for a growing LCLU class patch, can be seen in plot **c**. The phase error shows up as white phase deviations from the linear red unwrapped phase. This phase error limits a growing LCLU class patch $FMF$ precision, at a distance $x = 300$ [*units of*
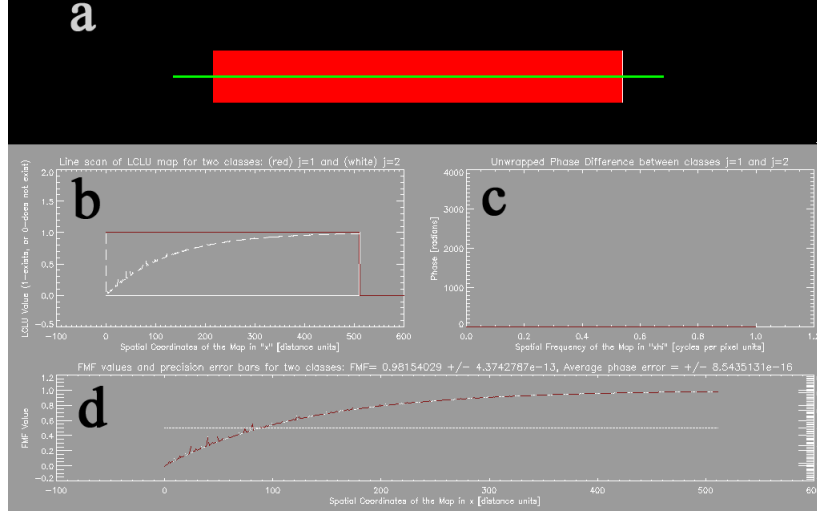
Figure 5.7: $FMF$ values between a white LCLU class that covers 1 pixel, and a red LCLU class that increases its patch cover. The red LCLU class patch has continuously moved, from 512 [*units of pixel distance*] away, to 1 [*units of pixel distance*] away from the red LCLU class patch. The green line across the LCLU map **a** is the area covered by the line scan plot **b**. The $FMF$ values are reported with a sensitivity parameter $l = 4$. A plot of the unwrapped phase red-class to white-class phase difference is shown in **c**. All observed $FMF$ values and phase error are plotted in **d**, with the phase error axis displaying values for $0.3 \leq \Delta\Phi \leq -0.3$ (*i.e.* within $\pm$ 30% $FMF$).

*pixel distance*] and for a sensitivity parameter $l = 4$, to be significant within $\pm 2.28 \times 10^{-12}$ units of $FMF$. The observed effects of phase error for a growing LCLU class patch is generally higher across the entire 512 pixel landscape, than for any previously observed LCLU class patch. Still, these observed effects of phase error are far below any significant change in the $1 \times 10^{-4}$ unit pixel distance limit (see Section 5.1.2). The inaccuracy introduced by phase error is $\approx 3 \times 10^{-14}$ units of $FMF$ for a growing LCLU class patch, and is reported as average phase error in Figure 5.6 and Figure 5.7.

### $FMF$ observed for initially connected LCLU patches.

*Aspects of $FMF$ shown in this section are–*

- *The adjustable early detection rate l, and its effect on reported $FMF$ values;*

- *and the ability of $FMF$ phase to report distance information between two active LCLU classes:*

Figures 5.8, 5.9, and 5.10 show $FMF$ values between a 1-pixel red LCLU class and 112-pixel white LCLU class patches that are separated by 399 [*units of pixel distance*]. The red LCLU class patch continuously goes from 399 [*units of pixel distance*] away to 1 [*units of pixel distance*] away from the white LCLU class patch. For the first 112 [*units of pixel distance*], the red LCLU

Table 5.5: Variable Sensitivity Parameter $l$, for a initially connected LCLU class patches.

| $l$-value | Plot Color | Initial 112 Averaged | Value at $x = 300$ | Final Value |
|---|---|---|---|---|
| 0.5 | N/A | $0.10 \pm 0.79 \times 10^{-3}$ | 0.25 | 0.39 |
| 2.0 | N/A | $0.35 \pm 2.68 \times 10^{-3}$ | 0.69 | 0.86 |
| 4.0 | White | $0.58 \pm 2.05 \times 10^{-3}$ | 0.90 | 0.98 |
| 6.0 | N/A | $0.72 \pm 1.27 \times 10^{-3}$ | 0.97 | 1.00 |

class patch colonization rate is equal to the white LCLU class patch extinction rate. There is no relationship between the two class patches after the first 112 [*units of pixel distance*] movement. The plotted $FMF$ values use sensitivity parameter $l = 4$. The different $l$-sensitivity values are in Table 5.5, along with their $FMF$ values, reporting increasing rates of early change detection with increasing $l$.
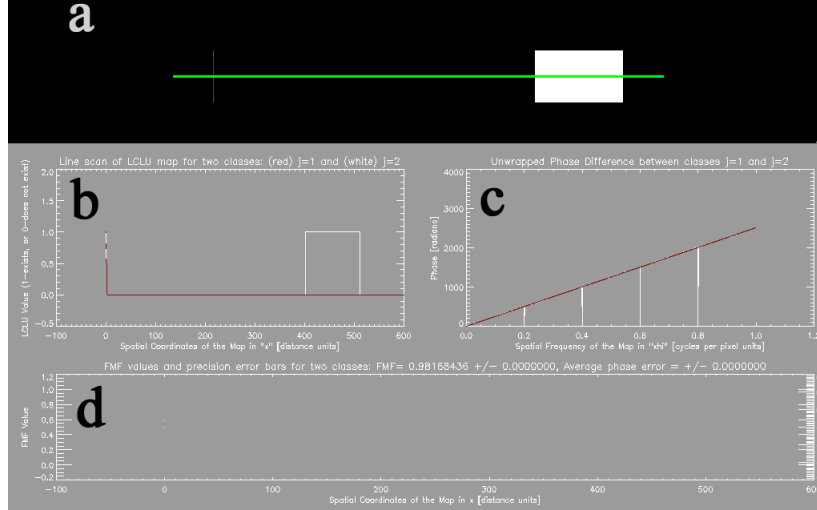


Figure 5.8: $FMF$ values between a white LCLU class that covers 112 pixels, and a red LCLU class that increases its patch cover. This red LCLU class is at a distance $x = 399$ [*units of pixel distance*] away from the white LCLU class. The red LCLU class patch will continuously move, from 399 [*units of pixel distance*] away, to 1 [*units of pixel distance*] away from the red LCLU class patch. The green line across the LCLU map in **a** is the area covered by the line scan plot **b**. The $FMF$ values are reported with a sensitivity parameter $l = 4$. A plot of the unwrapped phase red-class to white- class phase difference is shown in **c**. All observed $FMF$ values and phase error are plotted in **d**, with the phase error axis displaying values for $0.3 \leq \Delta\Phi \leq -0.3$ (*i.e.* within $\pm$ 30% $FMF$).

Comparing Figures 5.8, 5.9, and 5.10, we observe that the area under the unwrapped phase difference between the growing red LCLU class patch and the extinguishing white LCLU class is statistically constant when their respective patch extinction rate and colonization rate are equal. The area under the unwrapped phase difference between the red LCLU class patch and the white
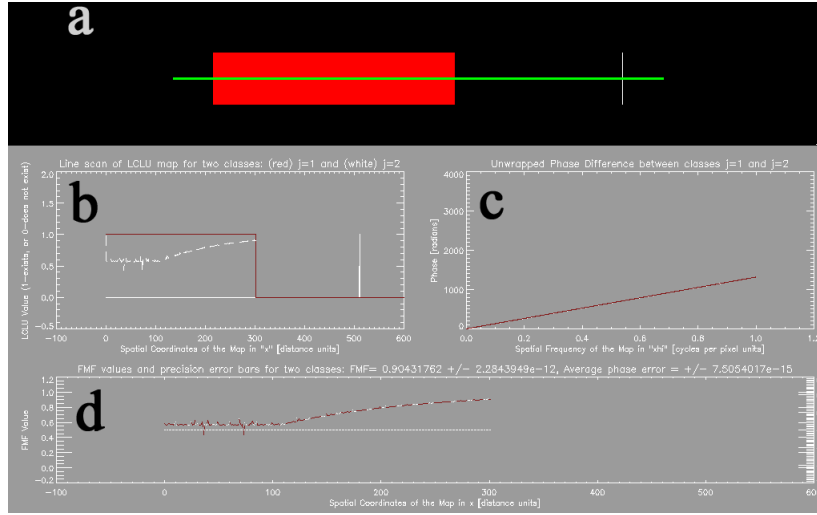
Figure 5.9: $FMF$ values between a white LCLU class that covers 112 pixels, and a red LCLU class that increases its patch cover. This red LCLU class is at a distance $x = 300$ [*units of pixel distance*] away from the white LCLU class. The red LCLU class patch has continuously moved, from 399 [*units of pixel distance*] away, to 1 [*units of pixel distance*] away from the red LCLU class patch. The green line across the LCLU map in **a** is the area covered by the line scan plot **b**. The $FMF$ values are reported with a sensitivity parameter $l = 4$. A plot of the unwrapped phase red-class to white- class phase difference is shown in **c**. All observed $FMF$ values and phase error are plotted in **d**, with the phase error axis displaying values for $0.3 \leq \Delta\Phi \leq -0.3$ (*i.e.* within $\pm$ 30% $FMF$).

LCLU class patch after 112 [*units of pixel distance*] decreases as the distance between the LCLU class patches decreases. As shown in Step 5.1.1, the phase difference used in $FMF$ is directly related to the distance between LCLU classes.

- *The direct relationship of $FMF$ to patch influence according to Island Biogeography:*

After the summed phase is wrapped into an exponential function and placed into the $FMF$ phase (see Steps 5-6 of Section 5.1.1), both Figures show how $FMF$ values increase with decreasing distance. $FMF$ values inversely trend with LCLU class patch distance, but directly trend with potential LCLU class patch influence, as according to Island Biogeography theory.

- *The effects of phase precision and accuracy on reported $FMF$ values:*

The phase error $\pm\Delta\phi$ (see Section 4.2.1) for a growing LCLU class patch, can be seen in plot **c**, the unwrapped phase plot. There, phase error is plotted as white phase deviations from the linear red unwrapped phase. The vertical white lines in plot **c** of Figure 5.8 are errors not included in the phase calculation. This phase error limits a growing LCLU class patch $FMF$ precision, at a distance $x = 300$ [*units of pixel distance*] and for a sensitivity parameter $l = 4$, to be significant
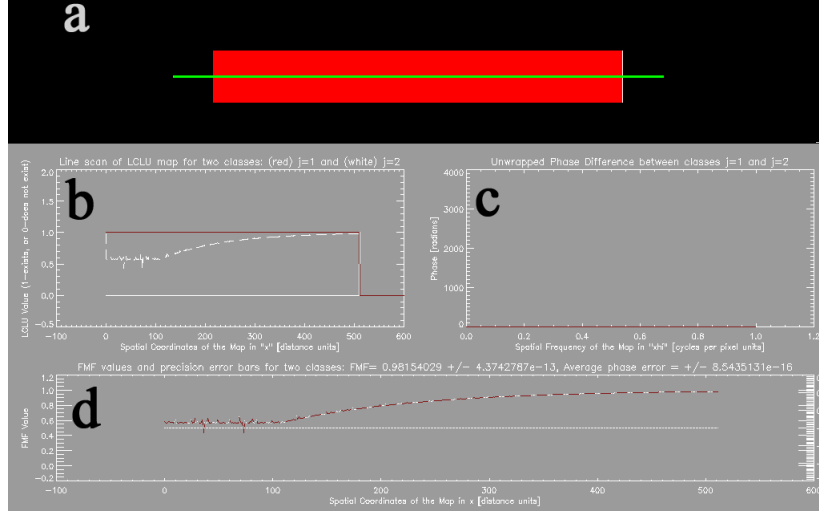
Figure 5.10: $FMF$ values between a white LCLU class that covers 112 pixels, and a red LCLU class that increases its patch cover. The red LCLU class patch has continuously moved, from 399 [*units of pixel distance*] away, to 1 [*units of pixel distance*] away from the red LCLU class patch. The green line across the LCLU map in **a** is the area covered by the line scan plot **b**. The $FMF$ values are reported with a sensitivity parameter $l = 4$. A plot of the unwrapped phase red-class to white-class phase difference is shown in **c**. All observed $FMF$ values and phase error are plotted in **d**, with the phase error axis displaying values for $0.3 \leq \Delta\Phi \leq -0.3$ (*i.e.* within $\pm$ 30% $FMF$).

within $\pm 2.28 \times 10^{-12}$ units of $FMF$. The observed effects of phase error for an initially related, growing LCLU class patch are far below any significant change in the $1 \times 10^{-4}$ unit pixel distance limit (see Section 5.1.2). The inaccuracy introduced by phase error is $\approx 1 \times 10^{-14}$ units of $FMF$ for an initially connected, growing LCLU class patch. This is reported as the average phase error in plot **d** of Figure 5.8, 5.9, and 5.10.

## $FMF$ observed for connected LCLU patches.

*Aspects of $FMF$ shown in this section are–*

- *The adjustable early detection rate $l$, and its effect on reported $FMF$ values;*

- *and the ability of $FMF$ phase to report distance information between two related LCLU classes:*

Figure 5.11 show $FMF$ values between a red LCLU class patch that has an extinction rate that is equal to the colonization rate of a white LCLU class patch. The white LCLU class patch grows from 1 [*units of pixel distance*] to 512 [*units of pixel distance*], while at the same rate the red LCLU class patch extinguishes from 512 [*units of pixel distance*] to 1 [*units of pixel distance*]. The plotted $FMF$ values use sensitivity parameter $l = 4$. The different $l$-sensitivity values are in

Table 5.6: Variable Sensitivity Parameter $l$, for connected LCLU class patches.

| $l$-value | Plot Color | Averaged $FMF$ Values |
|-----------|------------|------------------------|
| 0.5 | N/A | $0.39 \pm 1.44 \times 10^{-5}$ |
| 2.0 | N/A | $0.86 \pm 1.25 \times 10^{-5}$ |
| 4.0 | White | $0.98 \pm 0.10 \times 10^{-5}$ |
| 6.0 | N/A | $1.00 \pm 0.00 \times 10^{-5}$ |

Table 5.6, along with their $FMF$ values, reporting increasing rates of early change detection with increasing $l$. The reported $FMF$ values remain statistically constant.
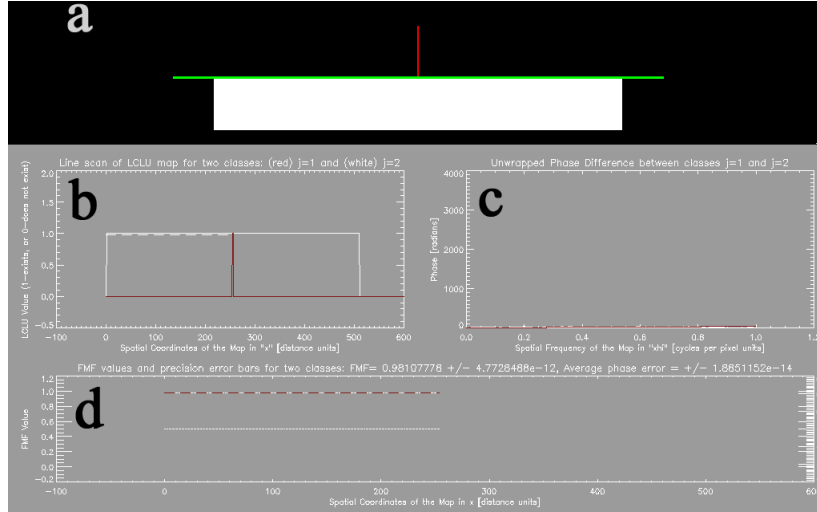


Figure 5.11: $FMF$ values between a white LCLU class that increases its patch cover, and a red LCLU class that decreases its patch cover. This red LCLU class is initially covering 512 [*units of pixel distance*], and the white LCLU class is initially covering 1 [*units of pixel distance*]. This relationship is exchanged as the red LCLU class patch continuously extinguishes and the white LCLU class patch continuously grows. The green line across the LCLU map in **a** is the area covered by the line scan plot **b**. The $FMF$ values are reported with a sensitivity parameter $l = 4$. A plot of the unwrapped phase red-class to white-class phase difference is shown in **c**. All observed $FMF$ values and phase error are plotted in **d**, with the phase error axis displaying values for $0.3 \leq \Delta\Phi \leq -0.3$ (*i.e.* within $\pm$ 30% $FMF$).

- *The direct relationship of $FMF$ to patch influence according to Island Biogeography:*

Observing the $FMF$ values plot in Figure 5.8, we see that the $FMF$ values and error between the red and white LCLU classes are statistically constant. This observed constant relationship for exclusively related LCLU patches is consistent with Island Biogeography theory.

- *The effects of phase precision and accuracy on reported $FMF$ values:*

The phase error $\pm\Delta\phi$ (see section 4.2.1) for continuously connected LCLU patches can be seen in plot **c**, the unwrapped phase plot. There, the phase error is plotted as white phase derivations from the linear red unwrapped phase. This phase error limits description of connected LCLU patches, using a sensitivity parameter $l = 4$, to an average $FMF$ value of $0.98 \pm 0.10 \times 10^{-5}$. The observed effects of phase error for exclusively connected LCLU class patches remains the $1 \times 10^{-4}$ unit pixel distance limit (see Section 5.1.2); and so is negligible error. The observed inaccuracy from phase error for a connected set of LCLU class patches is $\approx 2 \times 10^{-14}$ units of $FMF$. This is reported as average phase error in Figure 5.11 **d**.

### 5.1.3  The $FMF$ in a LCLU map

The time-series LCLU map experiments discussed here reveal the ability of $FMF$ to measure the influence of one LCLU class on another, within a $512 \times 512$ LCLU map. To report $FMF$ values a white LCLU patch is observed in reference to a 1-pixel LCLU class patch located in the lower left-hand corner. This 1-pixel LCLU class patch is necessary since $FMF$ must have a point of reference for calculation. The white LCLU patch being observed moves continuously in one direction across the LCLU map. The Figures shown here will display a plot of observed $FMF$ values reported as the two classes moved some distance away from each other, plotted against the corresponding phase-unwrapping phase error. As the LCLU moves, the $FMF$ *a priori* and *priori* class likelihoods are assumed to be 100%, (*i.e.* this is the only class in the landscape and it is perfectly classified) unless otherwise stated. Each experiment reveals the $FMF$ ability to measure Island Biogeography activity for variable $15[m], 30[m],$ and $200[m]$ spatial resolution. And, each of these maps hold a LCLU class patch that covers a $4[km] \times 4[km]$ area as are shown in Figure 5.12.
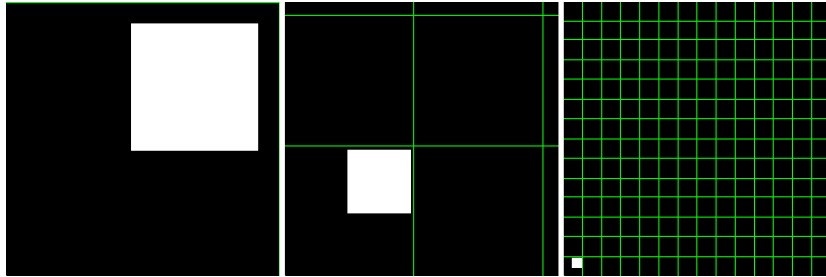


Figure 5.12: $15[m], 30[m],$ and $200[m]$ LCLU maps of a white LCLU patch that covers a $4[km] \times 4[km]$ area. The maps are of: $15[m]$ spatial resolution on the left, $30[m]$ spatial resolution in the center, and $200[m]$ spatial resolution on the right. Each map is gridded into $8[km] \times 8[km]$ areas, by their green bars.

Table 5.7: Variable Sensitivity Parameter $l$, for a $4[km] \times 4[km]$ LCLU patch.

| Resolution | $l$-value | $FMF$ for $x = 0[m]$ | $FMF$ for $x = 5430.58[m]$ |
|---|---|---|---|
| $15[m]$ | | | |
| | 0.5 | $0.394 \pm 0.71 \times 10^{-3}$ | $0.221 \pm 0.91 \times 10^{-3}$ |
| | 2.0 | $0.865 \pm 0.63 \times 10^{-3}$ | $0.632 \, (+1.72/-1.73) \times 10^{-3}$ |
| | 4.0 | $0.982 \pm 0.17 \times 10^{-3}$ | $0.865 \pm 1.27 \times 10^{-3}$ |
| | 6.0 | $0.998 \pm 0.03 \times 10^{-3}$ | $0.950 \pm 0.70 \times 10^{-3}$ |
| $30[m]$ | | | |
| | 0.5 | $0.395 \pm 1.42 \times 10^{-3}$ | $0.222 \pm 1.82 \times 10^{-3}$ |
| | 2.0 | $0.866 \, (+1.25/-1.26) \times 10^{-3}$ | $0.634 \, (+3.41/-3.44) \times 10^{-3}$ |
| | 4.0 | $0.982 \, (+0.33/-0.34) \times 10^{-3}$ | $0.866 \, (+2.50/-2.53) \times 10^{-3}$ |
| | 6.0 | $0.998 \pm 0.07 \times 10^{-3}$ | $0.951 \, (+1.36/-1.40) \times 10^{-3}$ |
| | | | $FMF$ for $x = 4525.48[m]$ |
| $200[m]$ | | | |
| | 0.5 | $0.403 \, (+9.26/-9.40) \times 10^{-3}$ | $0.268 \, (+11.35/-11.53) \times 10^{-3}$ |
| | 2.0 | $0.873 \, (+7.71/-8.20) \times 10^{-3}$ | $0.713 \, (+17.41/-18.53) \times 10^{-3}$ |
| | 4.0 | $0.984 \, (+1.90/-2.16) \times 10^{-3}$ | $0.917 \, (+9.70/-11.00) \times 10^{-3}$ |
| | 6.0 | $0.998 \, (+0.35/-0.42) \times 10^{-3}$ | $0.976 \, (+4.06/-4.89) \times 10^{-3}$ |

**$FMF$ observed when using multiple sensitivity parameters $l = .5, 2, 4,$ and $6$, at $15[m], 30[m]$, and $200[m]$ spatial resolution.**

*Aspects of $FMF$, reported from two-dimensional scenes, shown in this section are–*

- *The adjustable early detection rate $l$, and its effect on reported $FMF$ values for imagery;*

- *and the performance of $FMF$ across multiple sensor scales:*

Figure 5.13 show $FMF$ values for a $15[m], 30[m],$ and $200[m]$ LCLU map that moves in a direction, $\theta = 45°$ up from the horizontal, away from the lower-left corner of a map (see Figure 5.12). $FMF$ values for different $l$ sensitivities are in Table 5.7, along with their respective map spatial resolution, reporting increasing rates of early change detection with increasing $l$.

Observing the initial $FMF$ values in Table 5.7, we see that the previous examples of one-dimensional $FMF$ values are the same values observed here. The imprecision increases with each decrease in $l$-sensitivity value and each decrease in spatial resolution. However, this decrease in precision tends to reliably report above $1 \times 10^{-3}$ units of $FMF$. When imprecision increases above $1 \times 10^{-3}$ units of $FMF$ the reported upper and lower bounds are symmetric, making imprecision statistically negligible (*i.e.* an average can be taken to obtain the true value).

- *The direct relationship of $FMF$ phase to patch influence in imagery, according to Island Biogeography:*

In Figure 5.13 the set of $FMF$ values for each spatial resolution decreases with increasing distance. $FMF$ values inversely trend with LCLU class patch distance, but directly trend with potential LCLU class patch influence in accordance with Island Biogeography theory.
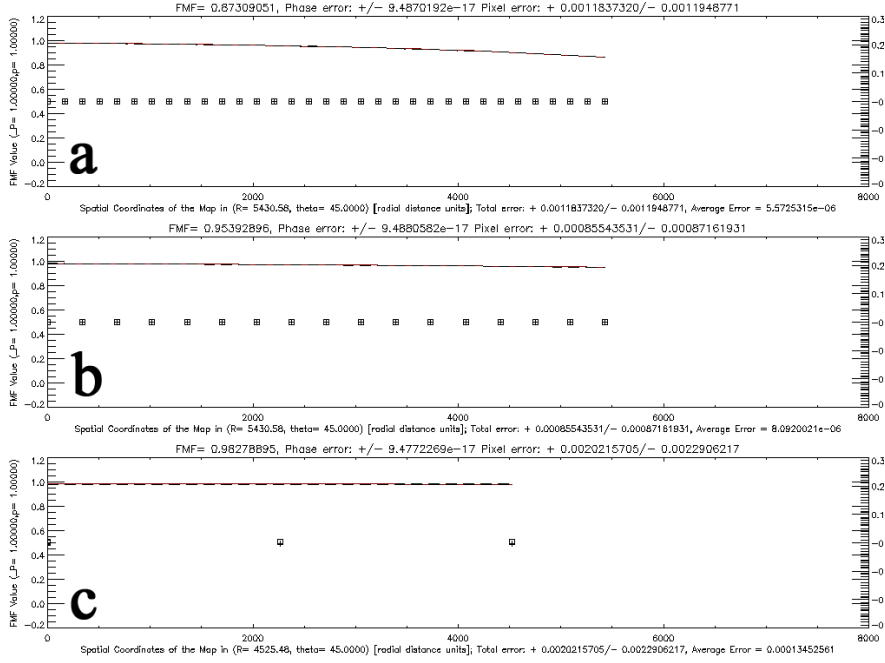
Figure 5.13: $FMF$ values for a white LCLU class patch that covers a $4[km] \times 4[km]$ area, using sensitivity parameter $l = 4$, for separate LCLU map spatial resolution. The plots from **a** to **b** have $15[m], 30[m],$ and $200[m]$ LCLU map spatial resolution. All observed $FMF$ values and total error are plotted with the phase error axis displaying values for $0.3 \leq \Delta\Phi \leq -0.3$ (*i.e.* within $\pm$ 30% $FMF$).

**$FMF$ observed at $200[m]$ spatial resolution, and in the direction $\theta = 30°$, and $60°$ from the horizontal.**

*Aspects of $FMF$, reported from two-dimensional scenes, shown in this section are–*

- *The ability of $FMF$ phase to consistently report distance information along any angular distance:*

$FMF$ values for a $200[m]$ LCLU map that continuously moves $\theta = 30°$, and $60°$ from the horizontal away from the lower-left corner of a map (see Figure 5.12) are exactly the same for $FMF$ values for a $200[m]$ LCLU map that continuously moves $\theta = 45°$ away. $FMF$ values for different $l$-sensitivities and the trend of these values across the landscape are in Table 5.7.

**$FMF$ observed at $15[m]$ spatial resolution, for a complex LCLU pattern.**

*Aspects of $FMF$, reported from two-dimensional scenes, shown in this section are:*

- *The adjustable early detection rate $l$, and its effect on reported $FMF$ values in imagery;*

Table 5.8: Variable Sensitivity Parameter $l$, for a complex $4[km] \times 4[km]$ LCLU patch.

| Resolution | $l$-value | Plot Color | $FMF$ for $x = 0[m]$ | $FMF$ for $x = 5430.58[m]$ |
|---|---|---|---|---|
| $15[m]$ | | | | |
| | 0.5 | N/A | $0.385 \ (+0.72/-0.72) \times 10^{-3}$ | $0.266 \ (+0.86/-0.86) \times 10^{-3}$ |
| | 2.0 | N/A | $0.857 \ (+0.67/-0.67) \times 10^{-3}$ | $0.709 \ (+1.36/-1.36) \times 10^{-3}$ |
| | 4.0 | White | $0.980 \ (+0.19/-0.19) \times 10^{-3}$ | $0.915 \ (+0.80/-0.80) \times 10^{-3}$ |
| | 6.0 | N/A | $0.997 \ (+0.04/-0.04) \times 10^{-3}$ | $0.975 \ (+035/-0.35) \times 10^{-3}$ |

- *The direct relationship of $FMF$ to patch influence according to Island Biogeography;*

- *The ability of $FMF$ phase to report distance information of complex shaped LCLU classes in imagery.*

Figure 5.14 show $FMF$ values for a patterned white LCLU patch on a $15[m]$ spatial resolution LCLU map. $FMF$ values for different $l$-sensitivities are in Table 5.8, along with their respective map spatial resolution, reporting increasing rates of early change detection with increasing $l$.
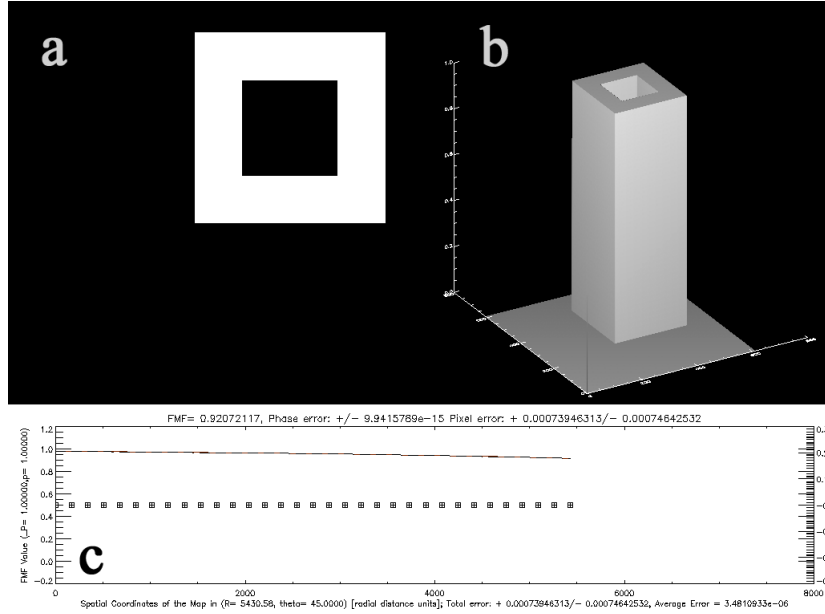


Figure 5.14: $FMF$ values for a complex, white LCLU class patch that covers a $4[km] \times 4[km]$ area outside and is missing a $2[km] \times 2[km]$ inside. The LCLU map has a $15[m]$ resolution. The LCLU map with LCLU patch is shown in **a**. A shaded surface of the LCLU class map is shown in **b**. All observed $FMF$ values and total error are plotted in **c**, with the phase error axis displaying values for $0.3 \leq \Delta\Phi \leq -0.3$ (*i.e.* within $\pm 30\%$ $FMF$).

Table 5.9: Variable Sensitivity Parameter $l$, for a $4[km] \times 4[km]$ LCLU patch and variable patch likelihoods, in a $200[m]$ LCLU map.

| Likelihood | $l$-value | $FMF$ for $x = 0[m]$ | $FMF$ for $x = 4525.38[m]$ |
|---|---|---|---|
| $P = 0.95, AP = 1.00$ | | | |
| | 0.5 | $0.393 \pm 0.013$ | $0.384 \pm 0.013$ |
| | 2.0 | $0.851 \ (+0.025/-0.026)$ | $0.843 \pm 0.026$ |
| | 4.0 | $0.959 \pm 0.025$ | $0.957 \pm 0.025$ |
| | 6.0 | $0.973 \pm 0.024$ | $0.973 \pm 0.024$ |
| $P = 0.50, AP = 1.00$ | | | |
| | 0.5 | $0.302 \ (+0.028/-0.029)$ | $0.295 \ (+0.027/-0.028)$ |
| | 2.0 | $0.655 \pm 0.112$ | $0.648 \pm 0.110$ |
| | 4.0 | $0.738 \pm 0.137$ | $0.736 \pm 0.137$ |
| | 6.0 | $0.748 \pm 0.140$ | $0.748 \pm 0.140$ |
| $P = 0.95, AP = 0.50$ | | | |
| | 0.5 | $0.287 \ (+0.024/-0.025)$ | $0.280 \pm 0.024$ |
| | 2.0 | $0.622 \pm 0.096$ | $0.616 \ (+0.094/-0.095)$ |
| | 4.0 | $0.701 \pm 0.118$ | $0.699 \pm 0.117$ |
| | 6.0 | $0.711 \pm 0.120$ | $0.712 \pm 0.120$ |

Comparing Table 5.7 and 5.8 for the $15[m]$ spatial resolution map, we see that the patterned LCLU patch $FMF$ values are lower. $FMF$ values directly relate to LCLU class patch existence, and so directly relate to potential LCLU class patch influence on one another in accordance with Island Biogeography theory. Also observed is how the imprecision increases as the $l$-sensitivity value decreases. Still, the decrease in precision stays below the reported $1 \times 10^{-3}$ units of $FMF$.

Figure 5.14 is sampled for every pixel within the $8[km] \times 8[km]$ scene, reporting each spatial resolution $FMF$ value decreasing with increasing distance. $FMF$ values inversely trend with LCLU class patch distance, but directly trend with potential LCLU class patch influence in accordance with Island Biogeography theory.

**$FMF$ observed for variable *priori* and *a priori* LCLU class patch likelihoods.**

*Aspects of $FMF$, reported from two-dimensional scenes, shown in this section are–*

- *The adjustable early detection rate $l$, and its effect on reported $FMF$ values for imagery;*

- *The performance of $FMF$ for multiple priori and a priori class likelihoods.*

$FMF$ values for different $l$-sensitivities and class patch likelihoods are in Table 5.9, at a $200[m]$ LCLU map spatial resolution. The characteristic reported $FMF$ trend seen in previous Figures is the same here, but is now reported for variable class patch likelihoods.

Observing the $FMF$ values in Table 5.9, imprecision increases with each decrease in $l$-sensitivity value. A decrease in precision is also observed for the decrease in *priori* class likelihood and considerably so for the decrease in *a priori* class likelihood. This decrease in precision tends to reliably report above $1 \times 10^{-3}$ units of $FMF$. And again, when imprecision increases above

$1 \times 10^{-3}$ units of $FMF$ the reported upper and lower bounds are symmetric, making imprecision statistically negligible (*i.e.* an average can be taken to obtain the true value).

## 5.2 Fourier Metric of Proportion ($FMP$)

Here, we observe the $FMP$ ability to measure landscape composition (*i.e.* LCLU class diversity) for variable imaging system spatial, spectral, and radiometric parameters. Each example operates on $256 \times 256$ LCLU maps generated by Gardner's **Rule** software (see Section 3.5). The error modeled in these maps are produced by IDL software (see Section 3.6). All of the examples covered in this section are for:

**5.2.1 When observing noiseless LCLU maps.** The $FMP$ ability to give a better description of existing class proportion than *Dominance* is explored.

**5.2.2 When observing a** $1[m], 15[m],$ **and** $30[m]$ **spatial resolution LCLU map, under radiometric inaccuracy.** After introducing new pixel classification assignments for increased fixed pattern noise, $FMP$ values are reported for LCLU maps generated by Gardner's **Rule** software (see section 3.6.2). This fixed pattern noise error increasingly effects a range of $2.60 \times 10^{-3}\%$ (170 pixels) to $35.10 \times 10^{-3}\%$ (2300 pixels) in the LCLU maps, by $00.25 \times 10^{-3}\%$ (16 pixel) increments.

**5.2.3 When observed LCLU map spectral classification accuracy has increased.** Spatial detail increases along the edge of each LCLU class to model increased classification accuracy (see section 3.6.3). The increased accuracy is modeled along $\pm 1$ to $\pm 10$ LCLU patch edge pixels.

### 5.2.1 The $FMP$ observed in a noiseless imaging system.

The increased sensitivity to landscape composition for the $FMP$ versus the *Dominance* metric is shown using four generated scenes having six classes. These six classes are ordered from a landscape dominated by one class cover, to a landscape of equally representative class covers. These maps are a model for what would be observed in a landscape over time.

The composition of each synthetic landscape is shown in Table 5.10 and Figure 5.15. Figure 5.16 shows the synthetic scenes and reported measures of $FMP$ and *Dominance*.

Table 5.10: **Rule** Neutral Model synthetic scene class proportions.

|                   | Dominant | Moderately Dominant | Moderately Even | Even |
|-------------------|----------|---------------------|-----------------|------|
| Class 1 (black)   | 0.60     | 0.10                | 0.10            | 0.17 |
| Class 2 (purple)  | 0.08     | 0.40                | 0.40            | 0.17 |
| Class 3 (green)   | 0.08     | 0.30                | 0.20            | 0.17 |
| Class 4 (yellow)  | 0.08     | 0.05                | 0.05            | 0.17 |
| Class 5 (orange)  | 0.08     | 0.15                | 0.10            | 0.17 |
| Class 6 (white)   | 0.08     | 0.10                | 0.15            | 0.17 |

The measures of *Dominance* range from 0.490 to 0.328 as the classes become even in Figure 5.16. Conversely, measures of $FMP$ range from $4.21 \times 10^{-5}$ to 1 as the classes become even. This gives $FMP$ a greater ability to describe composition by having a larger range of values for the same six scenes. Neither of the LPM value trends are linear and $FMP$ has a quickly increasing trend with increasing diversity, as expected from equation 4.8. The reported $FMP$ values are least
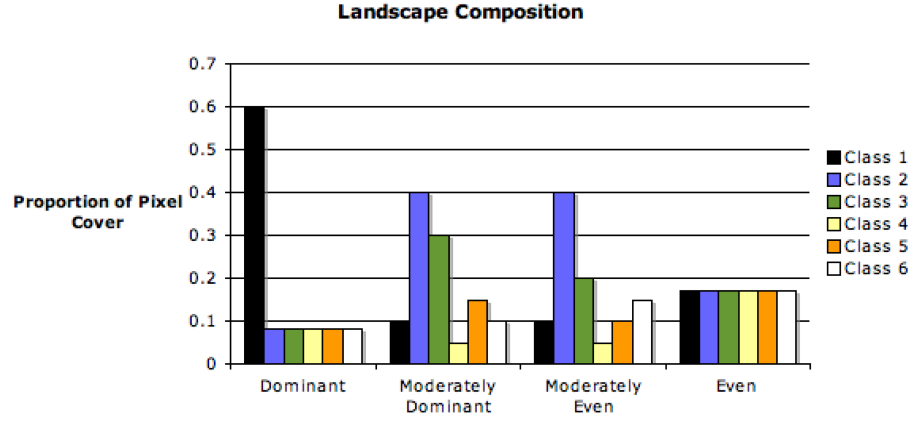
Figure 5.15: Six variable class proportions of the four LCLU maps.
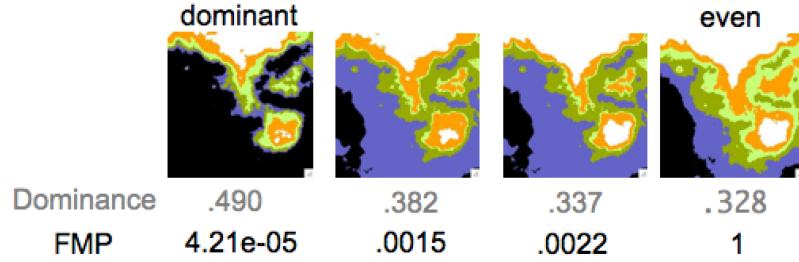


Figure 5.16: Four **Rule** generated LCLU maps. The class cover goes from dominant to even, and their respective *Dominance* and *FMP* values are shown below each map.

sensitive to changes between dominant and moderately dominant class coverage, as are defined in Table 5.10 , while the sensitivity of *Dominance* to any LCLU combination change is the same regardless of what transition of class composition there is.

### Observations of $FMP$, $FMF$, $Contagion$, and $Dominance$

All observations made in this section are qualitative. Discussions concerning the LPM relationships quantitatively follow in later sections. Figure 5.17 shows $256 \times 256$ LCLU maps that each have two classes (*i.e.* class cover and no class cover), with the proportion of total class cover varied between $0.1 \leq p_j \leq 0.9; \Delta p_j = 0.1$.

Figure 5.17 shows how the $FMF$ and $FMP$ LPM do not respond identically to the LCLU maps, unlike the *Contagion* and *Dominance* LPM that respond similarly. The Figure is showing, that for noiseless imagery the proposed Fourier metrics for landscape configuration and composition are independent from one another, unlike the currently applied LPM for landscape configuration and
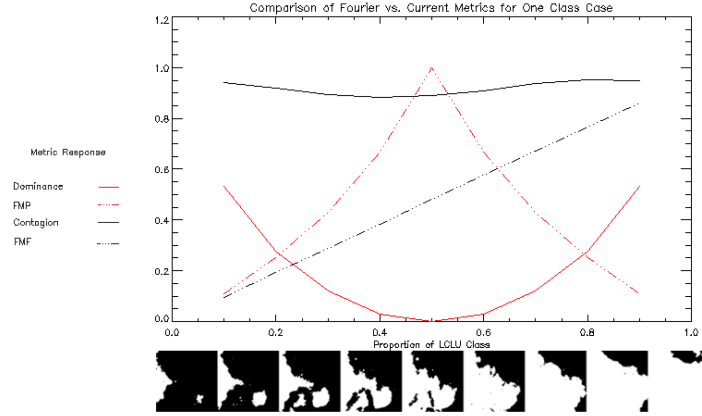
Figure 5.17: The variability of *Dominance*, *FMP*, *Contagion*, and *FMF* for proportions of landscape change ($H = 1, .1 \leq p_{f_j} \leq .9$).

composition (see Figure 3.12).

### 5.2.2 The $FMP$ observed under detector noise.

Figures 5.18 and 5.19 present $1[m], 15[m],$ and $30[m]$ spatial resolution LCLU maps with detector noise. LPM have been taken from a series of nine LCLU maps while increasing the percentage of fixed pattern noise. LPM sensitivity to detector noise correlations are found for each set of LPM observations in Table 5.10 and ranked in Table 5.12 . In both Tables, a value of 0 indicates a high sensitivity to the observed detector noise while a value of 1 indicates a low sensitivity to the observed detector noise. A successful LPM has a correlation value closest to 1 (*i.e.* complete independence from detector noise) and reports the same value for each spatial resolution.

Table 5.11: Landscape Pattern Metric detector noise correlation. Here, the values closer to 0 indicate a high sensitivity to observed detector noise, while the values closer to 1 indicate low sensitivity to observed detector noise.

| Landscape Pattern Metric | $1[m]$ | $15[m]$ | $30[m]$ |
|---|---|---|---|
| $FMF$ (Class 1 vs Class 2) | $7.35 \times 10^{-25}$ | $9.74 \times 10^{-18}$ | $4.97 \times 10^{-14}$ |
| $FMF$ (Class 2 vs Class 3) | $3.55 \times 10^{-25}$ | $2.31 \times 10^{-18}$ | $9.58 \times 10^{-15}$ |
| $FMF$ (Class 1 vs Class 3) | $1.86 \times 10^{-29}$ | $6.51 \times 10^{-21}$ | $1.07 \times 10^{-19}$ |
| $Contagion$ | $1.66 \times 10^{-17}$ | $7.87 \times 10^{-12}$ | $2.99 \times 10^{-9}$ |
| $FMP$ | $5.48 \times 10^{-10}$ | $5.31 \times 10^{-4}$ | $5.74 \times 10^{-4}$ |
| $Dominance$ | $1.13 \times 10^{-13}$ | $3.20 \times 10^{-7}$ | $6.26 \times 10^{-7}$ |

Errors for *Contagion* vary widely in Figures 5.18 and 5.19; a widely variable error that is not statistically negligible. For the initial $1[m]$ spatial resolution, $FMP$ reports the expected change for map proportions $p_j$. This was not true for initial *Dominance* observations, where statistically

89
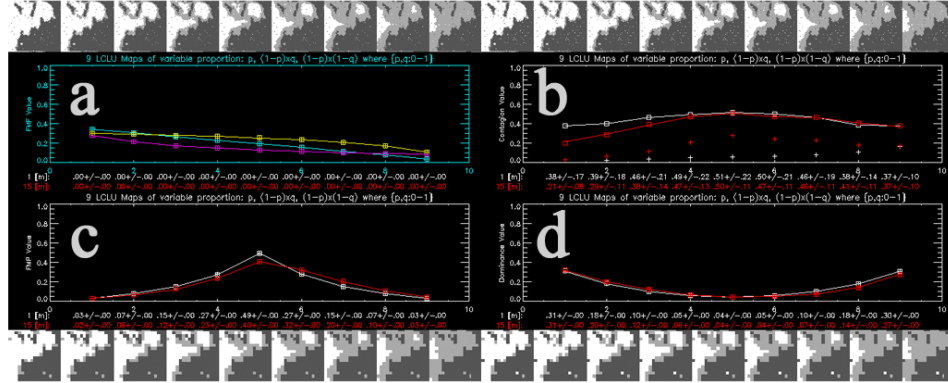
Figure 5.18: $FMP$ values for LCLU maps with detector noise. LCLU maps before detector noise are shown for $1[m]$ spatial resolution in the upper-left, and $15[m]$ spatial resolution in the lower-left. LCLU maps after detector noise are shown for $1[m]$ spatial resolution in the upper-right, and $15[m]$ spatial resolution in the lower-right. In **a**, $FMF$ values are shown above $FMP$ values in **c**. In **b**, *Contagion* values are shown above *Dominance* values in **d**. Landscape pattern metric data for all $1[m]$ LCLU maps are shown in white, and landscape pattern metric data for all $15[m]$ LCLU maps are shown in red. $FMF$ numerical values are not shown.

significant imprecision (*i.e.* asymmetric error bounds) are reported in 4 pairs of the 9 images measured. As spatial resolution increases between Figures 5.18 and 5.19, so does the inaccuracy of $FMP$. The *Dominance* metric becomes inaccurate with increases in spatial resolution as well, but to a lesser degree. $FMP$ is at its most inaccurate in Image 5, where $1[m]$ $FMP = 0.49 \pm 0.00$ versus a $30[m]$ $FMP = 0.30 \pm 0.01$—a 0.19 point difference. *Dominance* is at its most inaccurate in image 9, where $1[m]$ *Dominance* $= 0.30 \pm 0.00$ versus a $30[m]$ *Dominance* $= 0.19 \pm 0.02$—a 0.11 point difference. However, imprecision for both metrics is negligible, being low enough to not effect reported values.

For every spatial resolution in Table 5.11 , each metric shows a high dependence with the generated detector noise. For every spatial resolution in Table 5.12 the rank for most to least fixed pattern noise correlated LPM is the same. However, the $FMP$ metric shows the most independence from detector noise. Also, every metric becomes less dependent on detector noise as pixel resolution decreased (*i.e.* as pixel sizes increased), with the metric most dependent on pixel resolution being $FMF$. The $FMF$ dependence is the most for every class combination and every pixel resolution.

### 5.2.3 The $FMP$ observed under increased data accuracy.

Figures 5.20 and 5.21 compare $1[m], 15[m],$ and $30[m]$ spatial resolution LCLU maps undergoing increased data accuracy. LPM have been taken of the series of nine LCLU maps that increase LCLU patch classification accuracy across $\pm 1$ to $\pm 10$ patch edge pixels (see section 3.6.3). LPM sensitivity to increased classification accuracy correlations are found for each set of LPM observations in Tables 5.13 and 5.14 . In both Tables, a value of 0 indicates a high sensitivity to the observed increase
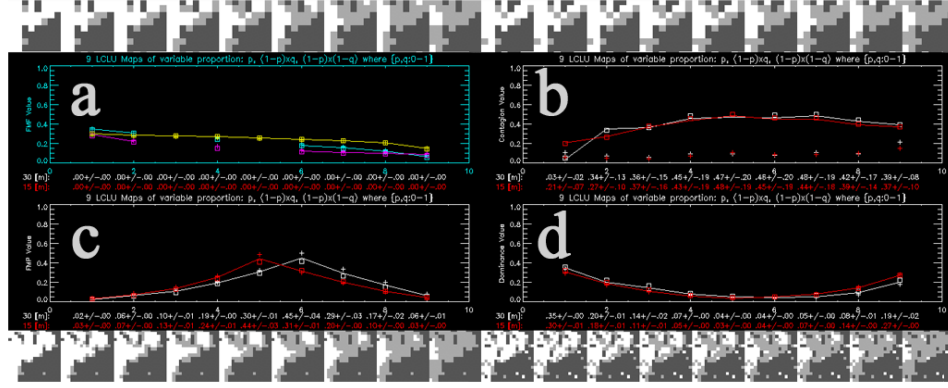
Figure 5.19: $FMP$ values for LCLU maps with detector noise. LCLU maps before detector noise are shown for $30[m]$ spatial resolution in the upper-left, and $15[m]$ spatial resolution in the lower-left. LCLU maps after detector noise are shown for $30[m]$ spatial resolution in the upper-right, and $15[m]$ spatial resolution in the lower-right. In **a**, $FMF$ values are shown above $FMP$ values in **c**. In **b**, $Contagion$ values are shown above $Dominance$ values in **d**. Landscape pattern metric data for all $30[m]$ LCLU maps are shown in white, and landscape pattern metric data for all $15[m]$ LCLU maps are shown in red. $FMF$ numerical values are not shown.

in data accuracy, while a value of 1 indicates a low sensitivity to the observed increase in data accuracy. A successful LPM has a correlation value closest to 1 (*i.e.* complete independence from increased classification accuracy) and reports the same value for each spatial resolution.

Errors for $Contagion$ vary widely in Figures 5.20 and 5.21; a widely variable error that is not statistically negligible. As spatial resolution increases between Figures 5.20 and 5.21, so does the inaccuracy of $FMP$. The $Dominance$ metric becomes inaccurate with increases in spatial resolution as well, but to a lesser degree. $FMP$ is at its most inaccurate in image 5, where $1[m]$ $FMP = 0.48 \pm 0.01$ versus a $30[m]$ $FMP = 0.24 \pm 0.05$—a 0.24 difference. $Dominance$ is at its most inaccurate in image 3, where $1[m]$ $Dominance = 0.11 \pm 0.01$ versus a $30[m]$ $Dominance = 0.18 \pm 0.02$—a 0.07 point difference. However, imprecision for both metrics is negligible, being low enough to not effect reported values.

For every spatial resolution in Table 5.13 , each metric shows a high dependence with the increased data accuracy, but not as high of a dependence as is shown in Section 5.2.2 for fixed pattern noise. For every spatial resolution in Table 5.14  the correlation rank order of every LPM is not the same, this is also different from what is observed for fixed pattern noise in Table 5.11 . In Table 5.14 , the $Dominance$ and $Contagion$ metrics show the most sensitivity to increased data accuracy. And, there is no obvious pattern of increased data accuracy sensitivity as pixel resolution decreases (*i.e.* as pixel sizes increased), but the metric most dependent on pixel resolution is $FMF$. The $FMF$ dependence is the highest for every class combination and every pixel resolution.

Table 5.12: Landscape Pattern Metric detector noise ranked sensitivity. The metrics are ranked from least to most sensitive to observed detector noise.

| 1[m] | 15[m] | 30[m] |
|---|---|---|
| *FMP* | *FMP* | *FMP* |
| *Dominance* | *Dominance* | *Dominance* |
| *Contagion* | *Contagion* | *Contagion* |
| *FMF* (Class 1 vs Class 2) | *FMF* (Class 1 vs Class 2) | *FMF* (Class 1 vs Class 2) |
| *FMF* (Class 2 vs Class 3) | *FMF* (Class 2 vs Class 3) | *FMF* (Class 2 vs Class 3) |
| *FMF* (Class 1 vs Class 3) | *FMF* (Class 1 vs Class 3) | *FMF* (Class 1 vs Class 3) |
| Every Landscape Pattern Metric | | |
| *FMP* (30[m]) | | |
| *FMP* (15[m]) | | |
| *Dominance* (30[m]) | | |
| *Dominance* (15[m]) | | |
| *Contagion* (30[m]) | | |
| *FMP* (1[m]) | | |
| *Contagion* (15[m]) | | |
| *Dominance* (1[m]) | | |
| *FMF* (Class 1 vs Class 2) (30[m]) | | |
| *FMF* (Class 2 vs Class 3) (30[m]) | | |
| *Contagion* (1[m]) | | |
| *FMF* (Class 1 vs Class 2) (15[m]) | | |
| *FMF* (Class 2 vs Class 3) (15[m]) | | |
| *FMF* (Class 1 vs Class 3) (30[m]) | | |
| *FMF* (Class 1 vs Class 3) (15[m]) | | |
| *FMF* (Class 1 vs Class 2) (1[m]) | | |
| *FMF* (Class 2 vs Class 3) (1[m]) | | |
| *FMF* (Class 1 vs Class 3) (1[m]) | | |

## 5.3    Yuen et al. [2004] Fractal Dimension Estimation ($lsFT$).

Here, we observe the $lsFT$ ability to consistently measure landscape occupancy for variable imaging system spatial, spectral, and radiometric parameters. Two currently used LPM based on the *Fractal Dimension* method are presented for comparison: the *Largest Patch Index* (LPI) and *Mean Patch Fractal Dimension* (MPFD) (see Appendix A). How useful these dimension estimators are for LCLU are in their ability to consistently measure some notion of real fractal dimension (see Section 3.2.4). So, this analysis is not concerned with metrics reporting an accurate measure of the real fractal dimension but a consistently precise one—it should be understood that all of these estimators measure some notion of fractal dimension. Each example operates on $512 \times 512$ LCLU maps generated in IDL software, which also produces the error introduced into the maps (see Section 3.6). This system analysis for measuring binary LCLU maps of fractals, using the proposed fractal dimension estimators, include error estimates for:

1. Inherent fractal property
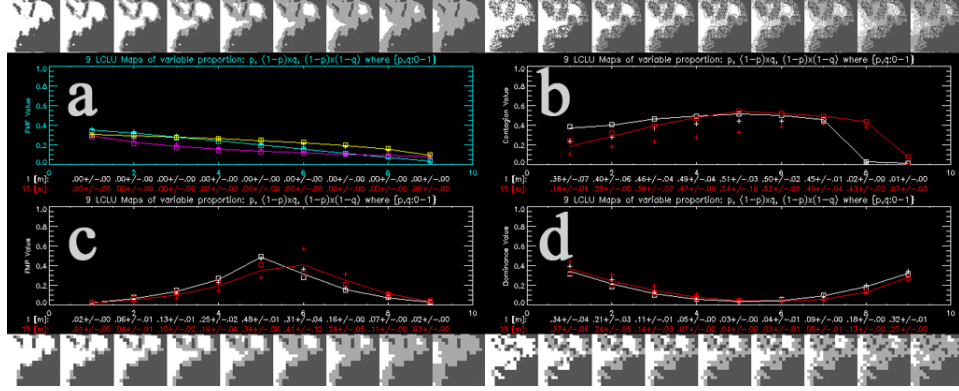
Figure 5.20: $FMP$ values for LCLU maps with increased data accuracy. LCLU maps before the edge spread are shown for $1[m]$ spatial resolution in the upper-left, and $15[m]$ spatial resolution in the lower-left. LCLU maps after the edge spread are shown for $1[m]$ spatial resolution in the upper-right, and $15[m]$ spatial resolution in the lower-right. In **a**, $FMF$ values are shown above $FMP$ values in **c**. In **b**, *Contagion* values are shown above *Dominance* values in **d**. Landscape pattern metric data for all $1[m]$ LCLU maps are shown in white, and landscape pattern metric data for all $15[m]$ LCLU maps are shown in red. $FMF$ numerical values are not shown.

Table 5.13: Landscape Pattern Metric Classification Accuracy Sensitivity.

| Landscape Pattern Metric | $1[m]$ | $15[m]$ | $30[m]$ |
|---|---|---|---|
| $FMF$ (Class 1 vs Class 2) | $1.12 \times 10^{-18}$ | $3.36 \times 10^{-14}$ | $6.51 \times 10^{-12}$ |
| $FMF$ (Class 2 vs Class 3) | $6.37 \times 10^{-18}$ | $2.41 \times 10^{-14}$ | $8.35 \times 10^{-11}$ |
| $FMF$ (Class 1 vs Class 3) | $1.68 \times 10^{-29}$ | $7.04 \times 10^{-15}$ | $7.77 \times 10^{-10}$ |
| *Contagion* | $8.95 \times 10^{-6}$ | $1.36 \times 10^{-4}$ | $7.77 \times 10^{-10}$ |
| $FMP$ | $4.23 \times 10^{-9}$ | $2.57 \times 10^{-6}$ | $4.25 \times 10^{-3}$ |
| *Dominance* | $4.04 \times 10^{-14}$ | $6.13 \times 10^{-6}$ | $4.46 \times 10^{-4}$ |

- fractal resolution

2. Apparent (*i.e.* imaging system) fractal property:

   - noise
   - sampling resolution
   - pixel size

Since the Sierpinski Circle fractal observed here is a complete fractal observed at its characteristic scale, the system sampling resolution is not considered in any of the examples. And lastly, observations of every LPM are presented separately for each set of fractals.
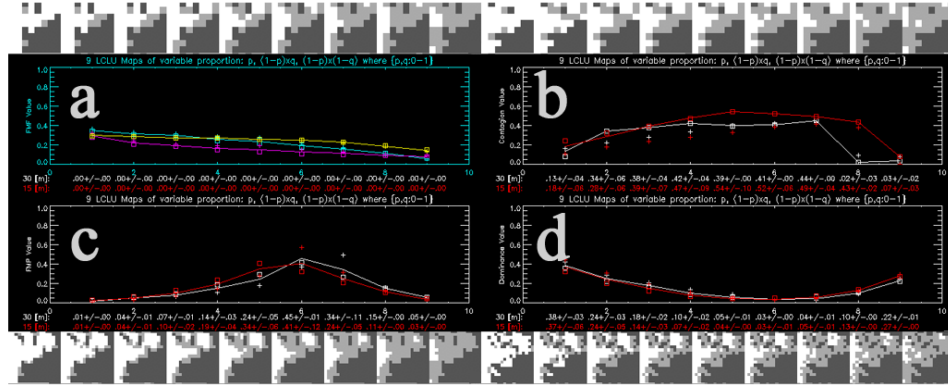
Figure 5.21: $FMP$ values for LCLU maps with increased data accuracy. LCLU maps before the edge spread are shown for $30[m]$ spatial resolution in the upper-left, and $15[m]$ spatial resolution in the lower-left. LCLU maps after the edge spread are shown for $30[m]$ spatial resolution in the upper-right, and $15[m]$ spatial resolution in the lower-right. In **a**, $FMF$ values are shown above $FMP$ values in **c**. In **b**, *Contagion* values are shown above *Dominance* values in **d**. Landscape pattern metric data for all $30[m]$ LCLU maps are shown in white, and landscape pattern metric data for all $15[m]$ LCLU maps are shown in red. $FMF$ numerical values are not shown.

### 5.3.1 Inherent and Apparent Fractal Property for the Sierpinski Circle.

**Inherent Fractal Property**

The values of each metric for increasing inherent fractal resolution are shown in Table 5.15 . Since the observed fractal never changes successful fractal LPM are fractal LPM that report the same value for each inherent fractal resolution generation. The $lsFT$ metric is the most precise for generations of inherent fractal resolution, with an average difference of 0.069. Each of these generations are shown in Figure 5.22.
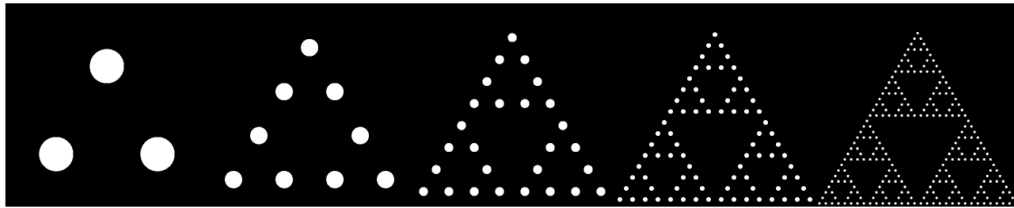


Figure 5.22: From left to right, the second to sixth generation of a Sierpinski circle.

Table 5.14: Landscape Pattern Metric Edge Spread Ranked Sensitivity.

| 1[m] | 15[m] | 30[m] |
|---|---|---|
| *Contagion* | *Contagion* | *FMP* |
| *FMP* | *Dominance* | *Contagion* |
| *Dominance* | *FMP* | *Dominance* |
| *FMF* (Class 2 vs Class 3) | *FMF* (Class 1 vs Class 2) | *FMF* (Class 1 vs Class 3) |
| *FMF* (Class 1 vs Class 2) | *FMF* (Class 2 vs Class 3) | *FMF* (Class 2 vs Class 3) |
| *FMF* (Class 1 vs Class 3) | *FMF* (Class 1 vs Class 3) | *FMF* (Class 1 vs Class 2) |

| Every Landscape Pattern Metric |
|---|
| *FMP* (30[m]) |
| *Contagion* (30[m]) |
| *Dominance* (30[m]) |
| *Contagion* (15[m]) |
| *Contagion* (1[m]) |
| *Dominance* (15[m]) |
| *FMP* (15[m]) |
| *FMP* (1[m]) |
| *FMF* (Class 1 vs Class 3) (30[m]) |
| *FMF* (Class 2 vs Class 3) (30[m]) |
| *FMF* (Class 1 vs Class 2) (30[m]) |
| *Dominance* (1[m]) |
| *FMF* (Class 1 vs Class 2) (15[m]) |
| *FMF* (Class 2 vs Class 3) (15[m]) |
| *FMF* (Class 1 vs Class 3) (15[m]) |
| *FMF* (Class 2 vs Class 3) (1[m]) |
| *FMF* (Class 1 vs Class 2) (1[m]) |
| *FMF* (Class 1 vs Class 3) (1[m]) |

Table 5.15: Dimension Estimates for Variable Inherent Fractal Resolution.

| | LPI | MPFD | lsFT |
|---|---|---|---|
| Generation 2 | -0.01288 | 1.44112 | 1.24337 |
| Generation 3 | 0.31663 | 1.57617 | 1.30779 |
| Generation 4 | 0.55846 | 1.72033 | 1.37099 |
| Generation 5 | 0.78951 | 1.93329 | 1.45045 |
| Generation 6 | 0.00000 | 2.21478 | 1.51978 |
| Average Difference | 0.39797 | 0.19342 | 0.06910 |

**Apparent Fractal Property**

Error bounds on each metric are shown in Table 5.16 for an increase in fixed pattern noise. The values are for fractals with an increasing percentage of noise across the entire fractal, having pixel errors of $1.22 \times 10^{-3}\%$ (320 pixels), $2.44 \times 10^{-3}\%$ (640 pixels), $4.88 \times 10^{-3}\%$ (1280 pixels), and

$8.54 \times 10^{-3}\%$ (2240 pixels). Figure 5.23 show the generations of fixed pattern noise across the fractal.

Table 5.16: Dimension Estimates for Variable Fractal Detector Noise.

| $\%Noise \times 10^{-3}$ | LPI | MPFD | lsFT |
|---|---|---|---|
| 1.22% | 0.00000 | 1.504 (+0.862/ − 0.154) | 1.529 (+0.689/ − 0.005) |
| 2.44% | 0.00000 | 1.510 (+0.602/ − 0.100) | 1.524 (+0.691/ − 0.002) |
| 4.88% | 0.00000 | 1.627 (+0.375/ − 0.210) | 1.522 (+0.692/ − 0.001) |
| 8.54% | 0.00000 | 1.849 (+0.219/ − 0.144) | 1.521 (+0.692/ − 0.001) |
| 1.22% | 0.00000 | 2.044 (+0.091/ − 0.077) | 1.520 (+0.693/ − 0.000) |
| Average Value | 0.00000 | 1.707 ± 0.235 | 1.524 ± 0.004 |
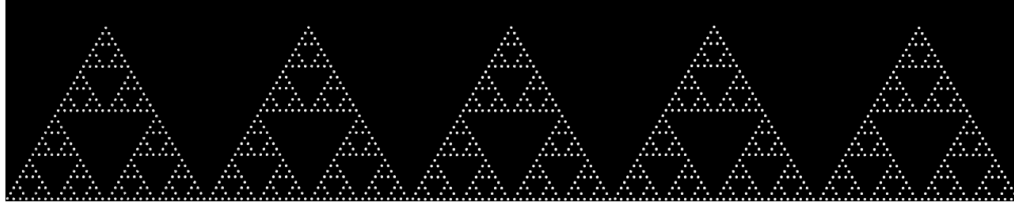


Figure 5.23: From left to right, increasingly effected fixed pattern noise generations of a Sierpinski circle.

Error bounds on each metric are shown for increased data accuracy in Table 5.17 . These values are for fractals with an increasing complexity across fractal edges over ±2, ±4, and ±6 edge pixels. Figure 5.24 shows each generation of increased data accuracy along the fractal edge. And, again $lsFT$ is the most precise LPM.

Table 5.17: Dimension Estimates for Increased Fractal Data Accuracy

| Edge Pixels | LPI | MPFD | lsFT |
|---|---|---|---|
| ±2 | 0.00000 | 1.127 (+1.086/ − 0.003) | 1.530 (+0.683/ − 0.005) |
| ±4 | 0.00000 | 1.519 (+0.693/ − 0.831) | 1.538 (+0.674/ − 0.006) |
| ±6 | 0.00000 | 1.519 (+0.693/ − 0.831) | 1.538 (+0.674/ − 0.006) |
| Average Value | 0.00000 | 1.388 ± 0.618 | 1.535 ± 0.131 |

The metric performances for a fractal at $1[m]$, $15[m]$, and $30[m]$ spatial resolution are shown in Figure 5.25. Each metric performs poorly, with $MPFD$ reporting most precisely with a variance of $\pm 4.05 \times 10^{-2}$ while $LPI$ and $lsFT$ have respective variances $\pm 4.996 \times 10^{-2}$ and $\pm 0.0269$.
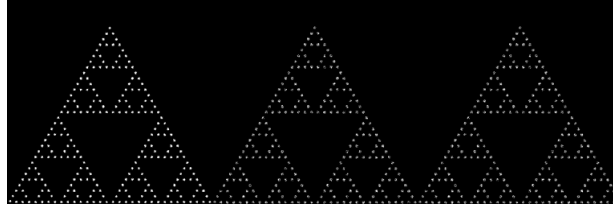
Figure 5.24: From left to right, the increased LCLU accuracy generations for a Sierpinski circle.
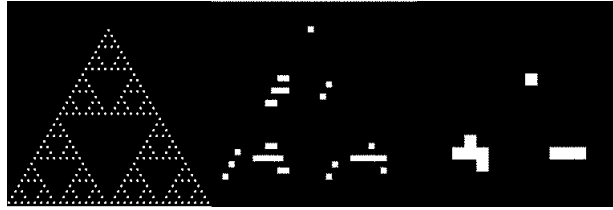


Figure 5.25: From left to right, the generations of a Sierpinski circle under decreased spatial resolution $1[m]$, $15[m]$, and $30[m]$. The respective metric values are: $LPI$-0, $MPFD$-1.130, $lsFT$-1.525 for $1[m]$; $LPI$-0.527, $MPFD$-1.621, $lsFT$-1.249 for $15[m]$; and $LPI$-0.135, $MPFD$-1.416, $lsFT$-1.136 for $30[m]$.

## 5.4 Summary of Preliminary Results

These preliminary results discussed improvements of each proposed Fourier LPM against imaging system errors and for increased accuracy to interpret the existence of landscape configuration, landscape composition, and landscape occupancy. This ability of LPM to report on landscape existence is the ability for LPM to describe the colonization and emigration relationships within and between LCLU. For this reason eleven experiments were presented for analysis of the $FMF$ LPM, three experiments were presented for analysis of the $FMP$ LPM along with a comparison of current versus proposed metric performance under imaging system pressures, and four experiments were presented for analysis of the $lsFT$ LPM under imaging system pressures while being compared to currently used fractal dimension LPM.

The eleven experiments used to analyze the $FMF$ ability to record landscape configuration were: 5.1.2 *FMF observed when using multiple sensitivity parameters $l = .5, 2, 4,$ and 6*, 5.1.2 *FMF observed when one class patch is in motion*, 5.1.2 *FMF observed when multiple class patches are in motion*, 5.1.2 *FMF observed when a LCLU class patch is growing*, 5.1.2 *FMF observed for initially connected LCLU patches*, 5.1.2 *FMF observed for connected LCLU patches*, 5.1.3 *FMF observed when using multiple sensitivity parameters $l = .5, 2, 4,$ and 6, at $15[m], 30[m],$ and $200[m]$ spatial resolution*, 5.1.3 *FMF observed at $200[m]$ spatial resolution, and in the direction $\theta = 30°$, and $60°$ from the horizontal*, 5.1.3 *FMF observed at $15[m]$ spatial resolution, for a complex LCLU pattern*, and 5.1.3 *FMF observed for variable priori and a priori LCLU class patch likelihoods*.

In each $FMF$ existence of landscape configuration experiment the metric always correctly imitated patterns of Island Biogeography influence across the landscape. Whether for variable

97

$l$-sensitivities, different colonization and emigration rates, or patterned LCLU relationships influential distances were consistently reported by $FMF$. When reporting influential distances with early rates of detection, by using high $l = 6$ sensitivity, precision increased up from lower $l$-sensitivities to $\pm 0.03 \times 10^{-3}$ units of $FMF$. However, the ability to see pixel-position differences for near LCLU (*i.e.* late detection conditions) decreased. With a $1 \times 10^{-4}$ unit pixel distance limit (see Section 5.1.2) the increased $l = 6$ precision was greater than the reported $FMF$ value. When using this high $l = 6$ sensitivity, a change in $FMF$ values along LCLU edges could not be seen until the third or fourth pixel distance difference $|n_1 - n_2| > 4$.

With increased pattern, independent growth, or separated single LCLU patches $FMF$ values reported lower than for contiguous, actively related, compact LCLU patches. This observation means $FMF$ assumes increased pattern, independent, and separate patches within a *single* LCLU works to prevent colonization, emigration, and fragmentation *between* LCLU. These experimental results prove that the definition of fragmentation interpreted as $FMF$ through Fourier phase is correct (see Figure 4.4).

The three experiments used to analyze the $FMP$ ability to record landscape composition when under imaging system pressures were: 5.2.1 *the FMP observed in a noiseless imaging system*, 5.2.2 *the FMP observed under detector noise*, and 5.2.3 *the FMP observed under increased data accuracy*.

The $FMP$ existence of landscape composition experiments recorded increased sensitivity for LCLU combination change, especially for when no imaging system errors effected values of $FMP$ (see Figure 5.17). The LPM is least sensitive to changes between dominant and moderately dominant class coverage and most sensitive to large spatial resolution (*i.e.* $30[m]$) fixed pattern noise. Only a 0.04 units of $FMP$ difference is reported between dominant and moderately dominant $30[m]$ class coverage, while for that same type of class coverage low $30[m]$ spatial resolution fixed pattern noise report statistically negligible $\pm 0.01$ - $\pm 0.04$ units of $FMP$ (see Figure 5.19). When compared to the currently used *Dominance* LPM for landscape composition the $FMP$ imprecision and inaccuracy is increased, however, even with these errors the tendency to report earlier patterns of composition is maintained.

The four experiments used to analyze the $lsFT$ ability to record landscape occupancy when under imaging system pressures were: conditions of fractal resolution in 5.3.1 *Inherent Fractal Property*, and imaging system conditions of fixed pattern noise, increased classification accuracy and variable spatial resolution in 5.3.1 *Apparent Fractal Property*.

In every LPM experiment for landscape occupancy the $lsFT$ metric performed better than either currently used fractal dimension measure, except for the low spatial resolution imagery case. The least error being seen for interpreting fractal dimension in fixed pattern noise ($\pm 0.004$), and most error for interpreting fractal dimension in low spatial resolution imagery ($\pm 0.0269$).

This preliminary record has shown that every proposed LPM is capable, even when under imaging system effects, to reliably report independent measures and trends of landscape pattern.

# Chapter 6

# Uniqueness of Fourier Landscape Pattern Metrics

## 6.1 Introduction

However reliable (*i.e.* accuracy and precision from Chapter 5) the reported Fourier Landscape Pattern Metrics are, they are useless if they report similar or exactly the same values as currently used LPM. For this reason this chapter discusses the uniqueness of the proposed Fourier metrics, measured as degree of correlation to other LPM, and ability to generally describe a landscape. Data values from 56 landscape pattern metrics (see Appendix A), including the proposed Fourier metrics, were used to populate a correlation matrix. This correlation matrix quantifies the ability of landscape pattern metrics to explain seamless USGS 1992 Land Cover Land Use (LCLU) across the conterminous United States.

Through Principal Components Analysis (PCA) an eigenvector matrix was produced: from which the first 3 Principal Components (PC's) explain 92.2% of the variation from the 59 metrics, the first 2 PC's explained 86.28% of the variation from the 59 metrics, and the first PC explained 74.24% of the variation from the 59 metrics. Three of the entire fifty-nine PC's explained most of the landscape pattern variability measured, suggesting that many of these LPM are measuring similar landscape pattern.

The metrics that contributed most to explained variability were Jackson's *Contagion* statistic ($P005$) typically contributing to 97% of the explained variability, the Fourier Metric of Fragmentation ($FMF$) typically contributing to 65% of the explained variability, and *average LCLU class lacunarity* ($TLAC$) typically contributing to 62% of the explained variability. Explained variability is defined as the variability, or landscape LPM LCLU information, that is most distinct (*i.e.* independently varies from other types of landscape information)—this is mathematically described in each Principal Component. The three assumptions made to analyze this work are that:

1. the 59 LPM values were directly related to LCLU information, making every metric is equally reliable and results comparable;

2. the chosen 59 metrics produced a representative sample of LCLU information, so the correlation metric analyzed is the *true* seamless USGS 1992 LCLU correlation matrix;

3. and that all LPM information are relevant, meaning every Principal Component should be included for analysis.

The proposed Fourier LPM $FMF$, the Least Squares Fourier Transform Fractal Dimension Estimation ($LsFT$), and the Fourier Metric of Proportion ($FMP$) respectively contributed 65%, 50%, and 12% to the explained variability. The values reported by each of the proposed Fourier metrics are revealed to be distinct among commonly used LPM by having a low correlation to the other 58 LPM. Due to the second and third assumption, these reported values have also shown themselves to be capable to explain general landscape pattern variability by contributing to the explained landscape variability in each Principal Component.

Ritters et al. statistically compared multiple LPM to find how well each metric responded to relevant LCLU map change. Their experiment is repeated here. This time including the proposed Fourier LPM and other LPM considered as most developed in the literature (see Appendix A). Results are interpreted with regard to how well each metric independently responds to relevant landscape change.

This evaluation is an extension for LPM that have shown their potential to be used as Landscape Indicators (LI) when correlated with landscape level ecology. The most robust metric for measuring ecological processes emerging as landscape pattern would resist inaccuracies caused by image data, and clearly reveal what ecology drives their measured pattern. The utility when using a combination of these robust metrics are in their independence from one another, and ability to explain many types of pattern. These statistical characteristics of independence and ubiquity increase their joint ability to best describe relevant variable pattern.

This statistical evaluation proves the proposed Fourier LPM to be both independent against commonly used LPM, and generally applicable for landscape pattern interpretation. This conclusion is especially for the conterminous United States Ecoregions, where a diversity of landscape pattern can be seen across each of the Environmental Protection Agency (EPA) *Provinces*.

## 6.2 Methods

The proposed Fourier LPM and frequently used LPM are found for $7.68 \times 7.68$ [$km$] NLCD LCLU areas. As previously discussed and shown in chapter 5, the proposed Fourier LPM are applied to each LCLU class then reported as an average. These proposed metrics are evaluated along with each metric in Appendix A for PCA factor analysis. Each of the metric references and algorithm details are also shown in Appendix A. The NLCD data used and the factor analysis details used in this chapter can be reviewed in Section 4.4.1.

## 6.3 Analysis

Interpreting a landscape's ecology when using landscape pattern is best done with a combination of robust LPM. The utility when using a combination of these robust metrics are in their independence from one another, and ability to explain many types of pattern. These statistical characteristics of independence and ubiquity increase their joint ability to best describe relevant variable pattern, which are quantitatively described and discussed in this section.

This statistical evaluation proves the proposed Fourier LPM to be both independent against commonly used LPM, and generally applicable for landscape pattern interpretation. Separated

into two subsections, these conclusions are revealed for the conterminous United States Ecoregions, where a diversity of landscape pattern can be seen across each of the Environmental Protection Agency (EPA) *Provinces*. The two subsections are *Independence of Fourier LPM* measured by the degree of correlation to commonly used LPM and *Ubiquity of Fourier LPM* measured by the typical amount contributed to explained landscape variability in each Principal Component.

## 6.3.1   Independence of Fourier LPM

The scree plot in Figure 6.1 trails off significantly by the third Principal Component (PC) Factor, with the combination of these first three Factors explaining 92% of the landscape pattern variability. It would be a mistake to interpret this as meaning that most of the observed landscape pattern variability can be revealed using only three LPM parameters. Since the PC only reveal how much information (*i.e.* explained variability) the landscape holds, and not which equation best parses that information for interpretation, it can only be said that the 59 LPM values are generally reporting redundant (*i.e.* highly correlated) values.
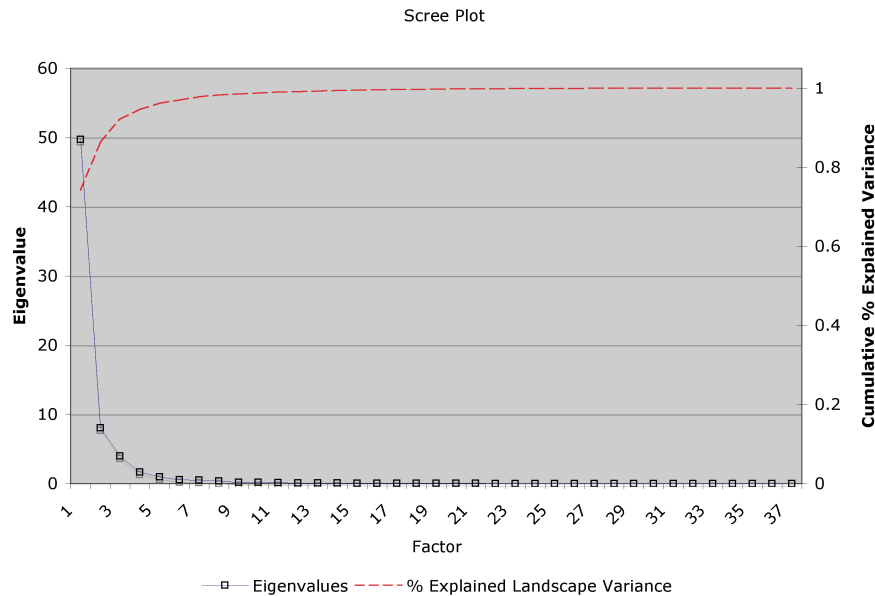


Figure 6.1: A Scree plot of Eigenvalues and cumulative % explained variance when observing NLCD 1992 LCLU data.

For more specific analysis, correlation values for each LPM in the $59 \times 59$ correlation matrix is shown in Appendix D. Also, the most related LPM for greater than .95, .97, and .98 correlation are shown in Figure 6.2, Figure 6.3, and Figure 6.4 respectively. These figures also show the most independent metrics, those metrics that report actual or near 0 correlation values. These most independent metrics are underlined in Table 6.2. While the ability of these most independent metrics to generally explain landscape variability is discussed in Section 6.3.2, their reliability, relevance and interpretation are not understood.

Figure 6.2: The number of LPM correlated greater than .95 points. Fourier metrics $LsFT$, $FMP$, and $FMF$ are correlated to 9, 5, and 12 other LPM respectively.

The least frequently correlated Fourier metric is $LsFT$. This small amount of between metric correlation is not observed in every *Fractal Dimension* LPM, like those seen in Appendix A.5, A.8, and A.9. This makes the values reported by $LsFT$ the most independent Fourier description of landscape occupancy pattern. The most correlated Fourier metric is $FMF$. These $FMF$ reported values were the least independent description of landscape pattern. The four highest correlated LPM to the Fourier metrics are shown in Table 6.1.

The four leading metrics in Table 6.1 seem to report redundant Fourier landscape pattern information, though none of them have as physical a description of pattern and processes as their Fourier relatives. For instance, though $FMP$ values are very related to $SHCO$, $n-Q$, $PSCV$, and $LOAX$ only $FMP$ is directly related to and interprets itself along the physical migration and extinction rates between LCLU patches. Meanwhile, the Contagion $SHCO$ method has shown itself to be unreliable in Section 5.2; $n-Q$ is an inter-quartile abundance that has only a mathematical, no physical, interpretation; and both $PSCV$ and $LOAX$ measure of how different patch sizes are within a landscape, using the $nearest-neighbor$ patch definition (see Section 3.2.4 for a discussion on the errors in this approach).

## 6.3.2 Ubiquity of Fourier LPM

To see how well each LPM performed using their individual definitions for relevant pattern variability we can observe the amount of explained variability each metric contributes to these PC

Figure 6.3: The number of LPM correlated greater than .97 points. Fourier metrics $LsFT$, $FMP$, and $FMF$ are correlated to 3, 5, and 12 other LPM respectively.

Table 6.1: The top four LPM most correlated to Fourier metrics when observing seamless conterminous United States NLCD 1992 LCLU.

| LsFT | FMP | FMF |
|------|------|------|
| PORO | SHCO | DLFD |
| TEDG | n-Q | NASQ |
| IEDG | PSCV | LOAX |
| KT-Q | LOAX | PSCV |

Factors. The ranking for all PC Factors is shown in Table 6.2. The metrics that contributed most to explained variability were Jackson's *Contagion* statistic ($P005$) typically contributing to 97% of the explained variability, the Fourier Metric of Fragmentation ($FMF$) typically contributing to 65% of the explained variability, the *average LCLU class lacunarity* ($TLAC$) typically contributing to 62% of the explained variability, and the Least Squares Fourier Transform Fractal Dimension Estimation ($LsFT$) typically contributing to 50% of the explained variability—the Fourier Metric of Proportion ($FMP$) typically contributed to about 12% of the explained variability. While LPM like $P005$, and $TLAC$ define landscape pattern that explain landscape pattern variability well, they both fall short of the criteria to measure physical variables while $P005$ also uses the error limited *nearest-neighbor* method (see Section 3.2.4).

103

Table 6.2: The LPM ranked by most expected contribution to the explanation of seamless conterminous United States NLCD 1992 LCLU. This ranking reveals how well each metric generally relates to landscape variability, ignoring any ability to reliably or relevantly interpret that variability. Highly independent metrics are underlined, and the Fourier Metrics are in bold.

| LPM | Expected Correlation Contribution | LPM | Expected Correlation Contribution |
|---|---|---|---|
| P005 | 97.46% | | |
| **FMF** | 64.76% | SIHO | 7.75% |
| TLAC | 61.54% | PD | 7.39% |
| **LsFT** | 50.06% | OCFC | 7.01% |
| ABRA | 38.76% | RGYR | 6.52% |
| BETL | 33.04% | SICO | 6.45% |
| OIFC | 32.05% | n-Q | 6.28% |
| SqP | 30.93% | PA-1 | 6.19% |
| PVAR | 28.35% | TVAR | 6.09% |
| MPFD | 27.32% | NYTP | 6.06% |
| PSSD | 26.52% | DLFD | 5.96% |
| OIFT | 25.11% | AWMSI | 5.89% |
| PLAC | 24.80% | BRRA | 5.88% |
| OEFT | 18.72% | NFTD | 5.88% |
| OPER | 18.59% | KT-Q | 5.70% |
| NASQ | 18.35% | MCDI | 5.67% |
| PENT | 17.72% | OEDG | 5.06% |
| PMAS | 17.72% | AWMPFD | 4.83% |
| PSIZ | 17.72% | CCRA | 4.80% |
| SHDI | 15.98% | PA-2 | 4.34% |
| SHHO | 15.46% | IEDG | 4.22% |
| TMAS | 15.42% | TEDG | 4.22% |
| SUMD | 13.55% | PORO | 4.22% |
| ABFT | 13.15% | TENT | 2.84% |
| NACI | 11.94% | PSCV | 2.65% |
| **FMP** | 11.81% | LOAX | 2.54% |
| P050 | 11.67% | P500 | 2.14% |
| LSI | 10.48% | OEFC | 2.14% |
| DSTA | 10.42% | SHCO | 2.07% |
| SIDI | 9.67% | SHEV | 2.03% |
| MSI | 9.31% | OCFT | 1.11% |
| SIEV | 9.07% | TE | .95% |
| PSI | 8.82% | LPI | .61% |
| MCEV | 7.79% | NPAT | .23% |

Figure 6.4: The number of LPM correlated greater than .99 points. For Fourier metrics $LsFT$, $FMP$, and $FMF$ are correlated to 0, 5, and 12 other LPM respectively.

## 6.4 Summary of Uniqueness of Fourier Landscape Pattern Metrics

The values reported by each of the proposed Fourier metrics have been shown to be independent from commonly used LPM by having a low correlation to the other 56 LPM—with the lowest correlated Fourier LPM being $LsFT$, and the highest correlated Fourier LPM being $FMF$. The high correlation of other landscape pattern metrics to the $FMF$ is expected, as other LPM approximate physical distance by flawed LPM edge and *nearest-neighbor* measures.

These reported Fourier pattern metric values have also shown themselves to be capable to explain general landscape pattern variability by contributing to the explained landscape variability in each Principal Component, again with exceptional results from $LsFT$ and $FMF$ respectively contributing 50.06% and 64.76% to explained pattern variability. This Fourier explained pattern variability is reported consistently against imaging system error. In the following Chapter 7 the relevance of these reliable and unique Fourier LPM for connecting an ecological process to landscape pattern and interpreting the cause is observed.

# Chapter 7

# Relevance of Fourier Landscape Pattern Indicators to predict Fecal Coliform

## 7.1  Introduction

Now being assured of the reliability (*i.e.* accuracy and precision from chapter 5) and uniqueness (*i.e.* the independence and ubiquity shown in chapter 6) of these Fourier metrics, their relevance for pollutant load prediction can be determined. Extending the results in Smith et al. [2001], a model valid for decadal studies targeting fecal coliform compromised South Carolina watersheds was developed. Introducing landscape pattern metrics (LPM) more sophisticated than the previously applied *proportion* LPM, this model attempts to identify the maximum number of compromised watersheds within the SC border. The model parameters were land-cover land-use (LCLU), % slope, and streamline relevant *proportion*, Fourier Metric of Fragmentation ($FMF$), Fourier Metric of Proportion ($FMP$), and Least Squares Fourier Transform Fractal Dimension Estimation ($LsFT$) when observing 1992 National Land Cover Data (NLCD) LCLU within fecal coliform compromised watersheds. This model was then validated using 2001 NLCD LCLU to identify fecal coliform compromised watersheds.

The most significant model parameters were along stream bare rock $LsFT$ (with 99.33% typical contribution to explained variance), $FMF$ between urban/recreational grasses and evergreen forests (with 99.32% typical contribution to explained variance), and $FMF$ between deciduous forests and high density residential areas (with 98.66% typical contribution to explained variance). These metrics contribute significantly more than the best *proportion* descriptor: proportion of urban/recreational grasses (with 45.12% typical contribution to explained variance).

In training the proposed model correctly identified 92% of the compromised watersheds, however, using the Smith et al. [2001] Beaulac and Reckhow [1982] *proportion* LPM only model, 94% of the compromised watersheds were correctly identified. The results of this study point to the significance of the proposed Fourier metrics to the interpretation of landscape level ecological processes and the necessity for more appropriate models to take advantage of sophisticated landscape

level tools.

The land-use appropriation of States, territories and tribal lands have altered hydrologic connectivity between landscapes, groundwater, and streams. This has led to more efficient delivery of contaminants to receiving waters through nonpoint source pollutants. Loss of natural headwater streams and floodplain wetlands associated with LCLU change decreases retention capacity, increases erosion, and may further contribute to nonpoint source contaminants downstream [Kaushal et al., 2010].

In part to prevent aggressive loads of nonpoint source pollutants into local waters, environmental assessments of waters are obtained on a biennial schedule under section 305 of the Clean Water Act (CWA). Part of this assessment includes identification, listing and prioritization of the water bodies that do not meet water quality standards, referred to as the 303(d) list. Under the Clean Water Act States and other jurisdictions are required to develop Total Maximum Daily Loads (TMDL) (*i.e.* pollution budgets) for the water bodies on the 303(d) list, toward the prevention of these water bodies being compromised.

Smith et al. [2001] reports on LPM for a majority ($\approx 65\%$) of the sites placed on the 303(d) list due to fecal coliform—the bacteria that usually reside in the digestive tract of warm blooded animals, and are used as a surrogate for the presence of pathogens in water bodies. High concentrations of fecal coliform are indicative of pollution that cannot be tracked to effluent emanating from a pipe discharging into a water body. Exactly the type of process Landscape Ecology provides a description of. For 1998, the LPM of Smith et al. indicated LCLU characteristics of the watershed may be a contributing factor to South Carolina's non-point source fecal coliform problem, particularly for watersheds with large proportions of urban land-cover and agriculture on steep slopes ($> 9\%$) [Jennings et al., 2004, Jones et al., 2001, Smith et al., 2001, Vogelmann et al., 2001, Wickham et al., 2000], but their work did not identify which watersheds suffered from these LCLU characteristics. In part, the analysis shown here extends the Smith et al. work to not only identify likely causes of Fecal Coliform loadings, but uses that information to predict which watersheds may be compromised in the future.

Using updated watershed delineations from the National Hydrography Dataset (NHD) [NHD, 2009], the 303(d) list [SCD] for 1992 and 2001, and U.S. Multi-Resolution Land Characteristics Consortium (MRLC) National Land Cover Data (NLCD) [MRL] the proposed Fourier metrics' abilities as temporal and ecologically relevant indicators are evaluated. Along with the Smith et al. landscape pattern indicators the proposed Fourier LPI ecological relevance are interpreted through factor analysis, extending the Smith et al. analysis of likely causes of Fecal Coliform loads to indications of Fecal Coliform sources (*i.e.* watersheds). An additional extension to the Smith et al. analysis done here is to use LPI determined as relevant to predict future Fecal Coliform compromised watersheds.

## 7.2 Methods

Multiple geographic information system (GIS) data layers were used to identify and create landscape pattern metrics (LPM) cognizant of geographical and sociological variability. Land-cover land-use products compiled with the CWA fecal coliform census and recent 14-digit NHD stream and watershed delineations are the base component map this LPM model is built upon. Each of these datasets aggregate into a product where nonpoint source fecal coliform transport potential can be surmised. This surmisal is done by proxy using historical nitrogen load export coefficients,

since fecal coliform export coefficients have not been developed. The equivalence of nitrogen export coefficients to fecal coliform export coefficients is explained further in section 7.2.4.

## 7.2.1 National Land Cover Data

1992 and 2001 National Land Cover Data (NLCD) are a 21-category LCLU classification scheme (see Table 7.1) and a 19-category LCLU classification scheme (see Table 7.2). Outside of the 21-to-19-category difference it is equivalent to the NLCD 1992 data, and the details of their component parts and characteristics can be found in the discussion of Section 4.4.1.

An example of the NLCD LCLU products for Columbia, SC 1992 and 2001 are shown in Figure 7.1. Class descriptions and codes for NLCD 1992 and NLCD 2001 were derived from components of Anderson Level I and II [Anderson et al., 1976] and National Oceanic and Atmospheric Administration (NOAA) Coastal Change and Analysis Program (C-CAP) land-cover classes MRL [2010]. The accuracy between 2001 and 1992 data have not been settled, however the increased 2001 NLCD LCLU detail is most obvious along streams, like in Figure 7.1.

Table 7.1: Descriptions of LCLU attribute class codes for 1992 NLCD [Anderson et al., 1976].

| LCLU class code | Anderson Level II attribute class description |
| --- | --- |
| 11 | Open Water |
| 12 | Perennial Ice/Snow |
| 21 | Low Intensity Residential |
| 22 | High Intensity Residential |
| 23 | Commercial, Industrial, Transportation |
| 31 | Bare Rock, Sand |
| 32 | Quarry, Strip Mine, Gravel Pits |
| 33 | Transtional Barren |
| 41 | Deciduous Forest |
| 42 | Evergreen Forest |
| 43 | Mixed Forest |
| 51 | Shrubland |
| 61 | Orchards, Vineyards, Other |
| 71 | Grassy, Herbaceous |
| 81 | Pasture, Hay |
| 82 | Row Crops |
| 83 | Small Grains |
| 84 | Fallow |
| 85 | Urban, Recreational Grasses |
| 91 | Woody Wetlands |
| 92 | Emergent Herbaceous Wetlands |

To maintain LPM model precision between 1992 and 2001, all datasets are registered to the same general LCLU code used by Smith et al. [2001]. The LCLU code includes: urban (11, 21, 22, 23, 31, 32, 33), natural vegetation (41, 42, 43, 52, 71, 90, 91, 92, 95), and agriculture (81, 82, 85). To be clear, statistical analysis and interpretation is done for the full 1992 LCLU code in Table

Table 7.2: Descriptions of LCLU attribute class codes for 2001 NLCD [Anderson et al., 1976], and 1992 replaced codes.

| LCLU class code (*1992 retrofit*) | Anderson Level II attribute class description |
| --- | --- |
| 11 | Open Water |
| 12 | Perennial Ice/Snow |
| 21 (*85*) | Developed, Open Space |
| 22 | Developed, Low Intesnity |
| 23 | Developed, Medium Intensity |
| 24 | Developed, High Intensity |
| 31 (*32, 33*) | Barren Land, Rock, Sand, Clay |
| 32 | Unconsolidated Shore in Coastal Areas |
| 41 | Deciduous Forest |
| 42 | Evergreen Forest |
| 43 | Mixed Forest |
| 52 (*51*) | Shrub, Scrub |
| 71 | Grassy, Herbaceous |
| 81 | Pasture, Hay |
| 82 (*83,84*) | Cultivated Crops |
| 90 (*91*) | Woody Wetlands |
| 91 | Palustrine Forested Wetland in Coastal Areas Only |
| 92 | Palustrine Scrub/Shrub Wetland in Coastal Areas Only |
| 95 (*92*) | Emergent Herbaceous Wetlands |

7.1. It is only when LPM are incorporated into the model that the general urban, vegetation, and agriculture codes from Smith et al. are used.

### 7.2.2   National Hydrography Dataset

Digital coverage of the 2001 14-digit hydrologic unit code (HUC) S.C. watersheds were obtained from the South Carolina Department of Health and Environmental Control (DHEC). They are 1,032 watersheds that range in size from 4.5 to 226 $[km^2]$. These watersheds were clipped to South Carolina's border, with those watersheds on the South Carolina-North Carolina border not delineated by interfluves removed. The 14-digit HUC NHD is cast to the Albers Equal-Area Conic projection, referenced to the North American Datum of 1983 (NAD83), and rasterized using a cell size of 30 $[m]$.

### 7.2.3   The 1992 and 2001 SC 303(d) list

Which watersheds were compromised by fecal coliform in 1992 and 2001 were obtained from the South Carolina Department of Health and Environmental Control (DHEC) archived 303(d) lists. Two basic sampling strategies were employed in gathering the water quality data. Primary test points, which are established near high-use waters, are tested every month throughout the year; while secondary points, located near areas with a history of impairment problems, are tested for six months of the year during the summer.
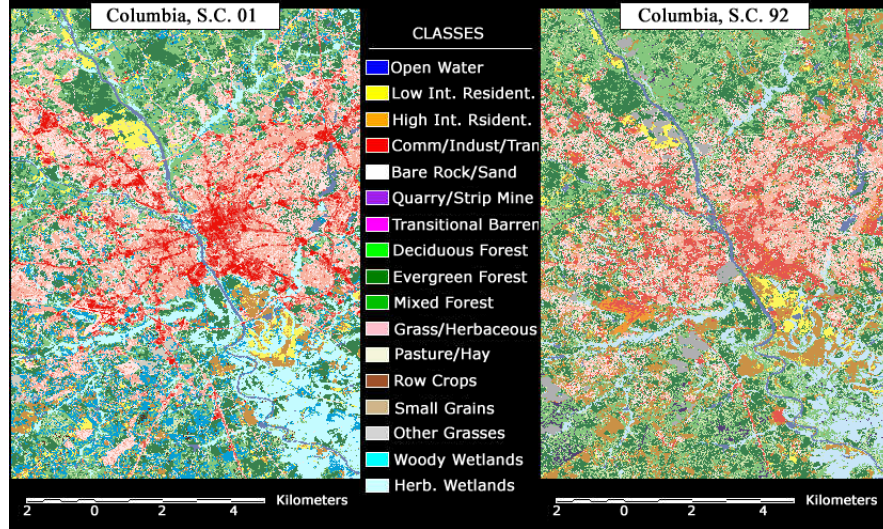
Figure 7.1: A chip of the National Land Cover Database (NLCD) Columbia, SC 1992 and 2001 land-cover.

A map of the 2001 303(d) list fecal coliform compromised watersheds is shown in Figure 7.2. Out of the total 1,032 watersheds, 471 (46%) were compromised in 1992 and 436 (42%) in 2001.

## 7.2.4 Modified Beaulac and Reckhow [1982] LPM Model

Nutrient export coefficients are numbers multiplied by the amount (area) of a given LCLU type to estimate the amount of nutrients received by waters from that type. When modeling the likelihood of increased nutrient loads as a result of differences in land-cover composition, broad LCLU categories (*i.e.* urban, natural vegetation, and agriculture) can be estimated reliably across watersheds [Vogelmann et al., 1998a,b, Zhu et al., 2000].

The modified Beaulac and Reckhow [1982] LPM model developed here identifies potentially compromised watersheds due to increased fecal coliform nutrient loads. Using parameters of LCLU composition within a watershed, Beaulac and Reckhow [1982] modeled nitrogen and phosphorus loads as:

$$N, P = \sum_{i}^{n} c_i \cdot A_i. \qquad (7.1)$$

$N$ and $P$ loads are estimated as the product of the area $A$ of LCLU type $i$ and its export coefficient $c_i$ summed across all LCLU types in the watershed. This equation can be used in two ways. If areal estimates are known for the different LCLU types, Equation 7.1 provides a weighted average estimate of nutrient load. In this case units would be in kilograms per year $[\frac{Kg}{yr}]$. Or, LCLU types could be considered as *proportion* of different LCLU types like in Equation 7.2. Equation
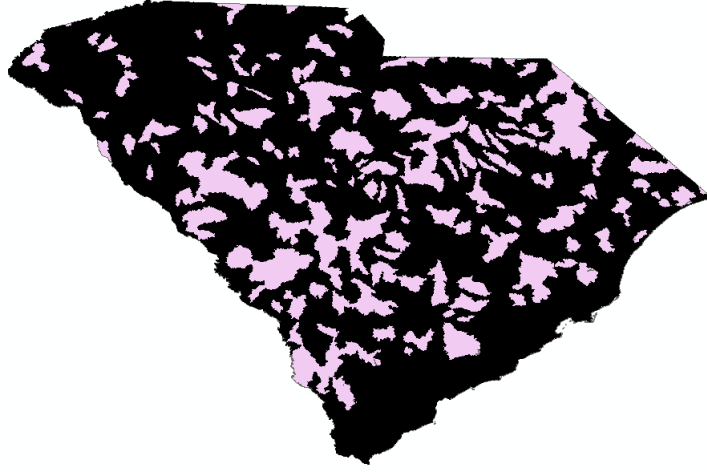
Figure 7.2: A map of S.C. watersheds that were compromised in 2001. The watersheds compromised are shown as black, while areas not effected by inordinate fecal coliform loadings are shown as pink.

7.2 provides a weighted average estimate of a nutrient export coefficient. Its units are in kilograms per hectare per year $[\frac{Kg}{ha \cdot yr}]$:

$$\hat{c}_N, \hat{c}_P = \sum_i^n c_i \cdot A \cdot p_i. \tag{7.2}$$

Equation 7.2 was used in the Smith et al. analysis of likely causes of Fecal Coliform loads.

### Average-Based Model

Modifying equation 7.2, connectivity of LCLU within watersheds can be incorporated into this LCLU composition model. Taking the average of the $j$ proposed LCLU Fourier composition and connectivity metrics $FMP$, $FMF$, and $LsFT$, and modulating the *proportion* metric by $m_i$, Equation 7.3 completes the increased nutrient load likelihood model:

$$c_N, c_P = \sum_i^n c_i \cdot A \cdot p_i \cdot m_i = \sum_i^n c_i \cdot A \cdot p_i \cdot \frac{\sum_j^M m_{ij}}{M}. \tag{7.3}$$

This model applies equal emphasis on each type of watershed sub-basin LCLU connectivity (*i.e.* pattern) by averaging the proposed connectivity LPM into a connectivity modulation $m_{ij}$.

**Vector-Based Model**

Instead of using Equation 7.3, assuming any connected cover describes nutrient transport in general for a modulation factor $m_{ij}$, we can use models that emphasize other types of connected LCLU relationships. This can be done by way of vector products between a unit vector $\tilde{\mathbf{u}}$ whose values are all 1, and the LPM vector $\tilde{\mathbf{v}} \equiv [m_{ij}]$ whose values are every $j$ watershed sub-basin landscape indicator for one of the $i = 3$ watershed sub-basin's urban, natural vegetation or agricultural aggregate LCLU:

$$|\tilde{\mathbf{v}} \times \tilde{\mathbf{u}}|^2 = |\tilde{\mathbf{v}}|^2|\tilde{\mathbf{u}}|^2 - (\tilde{\mathbf{v}} \cdot \tilde{\mathbf{u}})^2. \tag{7.4}$$

Equation 7.4 is a LCLU *simmilarity based* model. The unit reference vector and the LPM vector are the same if the LPM vector is composed of all ones. This vector would be the LPM response for a landscape that is compact from $FMF = 1$, well connected from $FMP = 1$, and evenly grouped from $LsFT = 1$. Comparing the LPM unit vector for how similar it is to this LCLU extreme is mathematically expressed as the similarity between the two vectors, or the vector dot product:

$$\cos[\theta] = \frac{(\tilde{\mathbf{v}} \cdot \tilde{\mathbf{u}})}{|\tilde{\mathbf{v}}||\tilde{\mathbf{u}}|}. \tag{7.5}$$

Conversely, comparing the LPM unit vector to how dissimilar it is to this LCLU extreme is mathematically expressed as the dissimilarity between the two vectors, or the vector cross product:

$$\sin[\theta] = \frac{|\tilde{\mathbf{v}} \times \tilde{\mathbf{u}}|}{|\tilde{\mathbf{v}}||\tilde{\mathbf{u}}|} = \frac{\sqrt{|\tilde{\mathbf{v}} \times \tilde{\mathbf{u}}|^2}}{|\tilde{\mathbf{v}}||\tilde{\mathbf{u}}|} = \frac{\sqrt{|\tilde{\mathbf{v}}|^2|\tilde{\mathbf{u}}|^2 - (\tilde{\mathbf{v}} \cdot \tilde{\mathbf{u}})^2}}{|\tilde{\mathbf{v}}||\tilde{\mathbf{u}}|}. \tag{7.6}$$

Equation 7.6 is a LCLU *dissimilarity based* model. A high measure of dissimilarity from Equation 7.6 would indicate a landscape cover that is sparse, not very diverse and that lay in no structured pattern. Using the original model parameters from Equation 7.3, expressions for LCLU similarity and dissimilarity look very similar to the average based model:

$$\cos[\theta] = \frac{\sum_j^M m_{ij}}{\sqrt{m_{ij}M}} \Rightarrow c_N, c_P = \sum_i^n c_i \cdot A \cdot p_i \cdot \frac{\sum_j^M m_{ij}}{\sqrt{m_{ij}M}}; \tag{7.7}$$

$$\sin[\theta] = \frac{\sum_j^M \sqrt{m_{ij}M - m_{ij}^2}}{\sqrt{m_{ij}M}} \Rightarrow c_N, c_P = \sum_i^n c_i \cdot A \cdot p_i \cdot \frac{\sum_j^M \sqrt{m_{ij}M - m_{ij}^2}}{\sqrt{m_{ij}M}}. \tag{7.8}$$

**Model Interpretation**

The best of these three models for $m_i$ would modulate the existing LCLU $p_i$ to more accurately predict potentially compromised watersheds. The LCLU $m_i$ that increases accuracies also provides the conditions additional to proportion of LCLU that are related to non-point source fecal coliform. Those additional conditions, tested here, being: any connection between LCLU describes nutrient transport in general (*ref.* the average-based Equation 7.3); LCLU must be compact, well connected, and evenly grouped to best describe nutrient transport (*ref.* the similarity-based Equation 7.7); or LCLU must be sparse, not very diverse, and lay in no structured pattern to best describe nutrient transport (*ref.* the dissimilarity-based Equation 7.8).

For use in a decadal model of fecal coliform compromised watersheds, export coefficients $c_i$ for fecal coliform nutrient transport are necessary. However, significant differences in nutrient export coefficients across urban, natural vegetation, and agriculture LCLU have not been developed for fecal coliform. Nutrient export coefficients are well-documented for nitrogen loadings, which relate to fecal coliform.

**Fecal Coliform Export Coefficients**

Fecal coliform is the bacteria that usually reside in the digestive tract of warm blooded animals, and are used as a surrogate for the presence of pathogens in water bodies. Sources of anthropogenic nitrogen to streams include sewage, animal wastes, fertilisers, and natural sources such as organic matter. This means, levels of nitrogen can be used to indicate the impact of human settlements and land use on the natural environment, provided "natural" sources are assumed negligible. The importance of this measure may increase as nitrate contamination of groundwater, such as that around some rural-residential areas, increases [Sta, 2010]. Due to increased activity, this condition is satisfied in fecal coliform compromised S.C. watersheds: likely dominant anthropogenic sources of nitrogen. It is assumed that fecal coliform export coefficients covary with nitrogen export coefficients in these compromised watersheds since their anthropogenic sources are nearly identical. Nitrogen export coefficients are treated as a suitable substitute of fecal coliform export coefficients.

The export coefficients used here are shown in Table 7.3. These export coefficients indicate the potential LCLU annual nitrogen load in kilograms, across 1 hectare. When used as areal loads in the LPM model (see equation 7.3), the three LCLU aggregates are taken as relevant export coefficient LCLU code averages: urban ($450[\frac{kg}{ha \cdot yr}]$), natural vegetation ($173.4[\frac{kg}{ha \cdot yr}]$), and agriculture ($610[\frac{kg}{ha \cdot yr}]$).

Table 7.3: Descriptions of LCLU nitrogen export coefficients [Jeje, 2006].

| 2001 LCLU class code | Description | Nitrogen export coefficient $[\frac{Kg}{ha \cdot yr}]$ |
|---|---|---|
| 21 | Urban | 5.50 [Reckhow et al.] |
| 22 | Urban, Residential | 6.15 [Reckhow et al.] |
| 23 (24) | Industrial | 2.25 [Reckhow et al.] |
| 31 | Subalpine | 3.75 [Bondelid et al., 2001] |
| 32 | Strip mines/barren land | 8.60 Group [1998] |
| 33 | Mostly urban | 0.79 [USEPA, 2002] |
| 41 | Forest | 2.50 [USEPA, 1976] |
| 42 | Forest | 2.50 [USEPA, 1976] |
| 43 (52,71) | Forest | 2.46 [Reckhow et al.] |
| 81 | Pasture | 5.10 [of Environmental Quality, 2001] |
| 82 | Row Crops | 8.20 [of Environmental Quality, 2001] |
| 85 | Urban | 5.00 [USEPA, 1976] |
| 91 (90) | Watershed wetlands | 0.55 [Group, 1998] |
| 92 (95) | Watershed agricultural basin | 0.60 [Associates, 1999] |

The allowed S.C. DHEC watershed nitrogen load is $\frac{200}{100}[\frac{cfu}{ml}]$–where the units $[\frac{cfu}{ml}]$ are colony forming units per milliliter [of Health and Control, 2008]. Using S.C. DHEC suggested, typical

watershed, gallons per minute flow rate this $\frac{200}{100}[\frac{cfu}{ml}]$ limit can be expressed as $2986[\frac{Kg}{yr}]$. An allowed limit in $[\frac{Kg}{yr}]$ is comparable to the predicted LPM model potential loads in $[\frac{Kg}{yr}]$, and is the threshold used to determine whether a watershed is, or is not, modeled as compromised.

### 7.2.5 Factor Analysis

The approach to factor analysis is the same as was discussed in Section 4.4.1. However, here the correlation matrix $\vec{\Sigma}$ is populated with LPM values from each of the $t$ watersheds, that reveal the observed metric's ability to explain compromised watersheds. The $[\sum_t a_{j,t} LPM_t]$ weighted presence of an individual vector **LPM** is now the LPM's potential to predict fecal coliform loadings. So, the more contribution to independent fecal coliform descriptions $Y_j$ a LPM tends to make, the more uniquely able (*i.e.* independently) to describe (*i.e.* responds with high variance to) fecal coliform the LPM is—this allows us to say to what degree the observed metric and fecal coliform are unrelated.

In this factor analysis a direct measure of LPM ability to explain the $p$ observed LCLU watershed changes compared to the full set of metrics (*i.e.* % slope, and streamline relevant *proportion*, $FMF$, $FMP$, and $LsFT$) is obtained. Each element in **LPM$_j$** is the % $LPM_{j,t=k}$ contributed to the $k^{th}$ compromised watershed fecal coliform explanation. Summing across every $k$ compromised watershed and averaging over the $p$ observed LPM responses, the typically explained fecal coliform loading for the LPM is obtained:

$$\bar{\sigma}_{LPM}[F.C.] = \sum_{j=1}^{p} \frac{\sum_{k=1}^{t} LPM_{j,t}}{p}. \tag{7.9}$$

Only the most relevant 1992 LPM, and LPM coefficients, were included in the models for indication of compromised watersheds. The condition of LPM relevance and detailed descriptions are discussed in the Section 7.3.

After the LPM model parameters have been trained on the S.C. 1992 LCLU watersheds, how effective the model is to predict compromised watersheds is determined by applying the model to S.C. 2001 LCLU watersheds. The measure of success is the 1992 trained model's ability to identify 2001's fecal coliform compromised watersheds.

## 7.3 Analysis

304 parameters were used in the 1992 LPM training model, of which only 19 typically contributed to greater than 50% of the explained compromised watershed LCLU variability. Only these 19 LPM and their contribution are considered as relevant, having contributed to greater than 50% of the 1992 explained compromised watershed LCLU variability, and are shown in Figure 7.3. Each of the model parameters determined to be relevant at a $> 50\%$ significance level were proposed Fourier metrics. The *proportion* LPM used by Smith et al. [2001] typical contributions are shown in Figure 7.4, which correspond to the *proportion* LPM published in their general prediction results. However, these *proportion* LPM are generally less significant than the proposed Fourier metrics.

Using the average-based Beaulac and Reckhow [1982] model in equation 7.3, and the generalized LCLU code export coefficients, the 1992 model is trained to a 91.72% accuracy. The 1992 average-based LPM model identified 432 out of 471 fecal coliform compromised watersheds. Using the
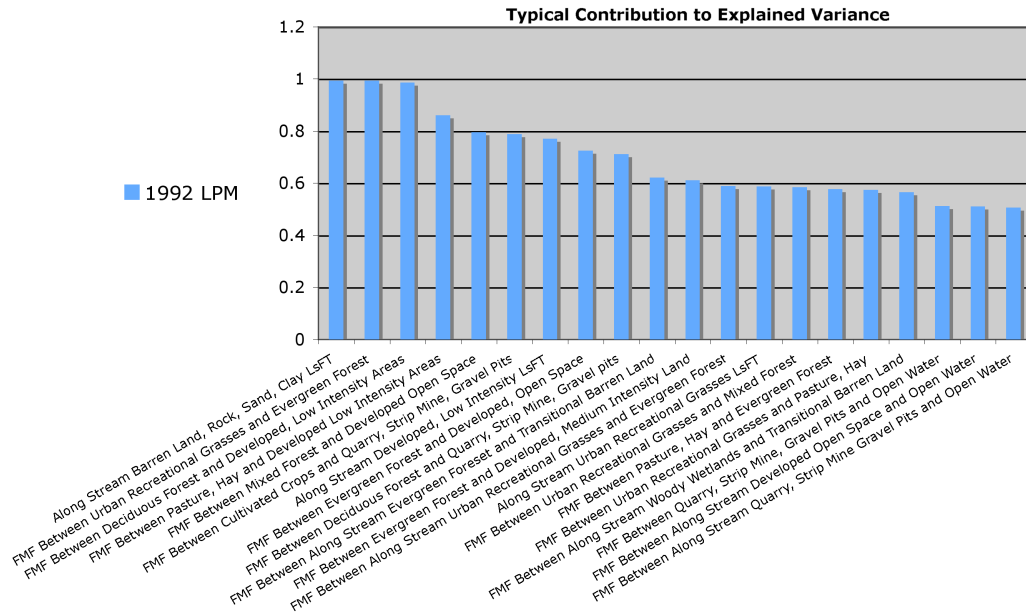
Figure 7.3: LPM model parameters that typically contribute greater than 50% to the explained compromised watershed LCLU variability. These LPM parameters are all Fourier based and ranked from left-to-right as most-to-least significant.

original Beaulac and Reckhow [1982] model, as was used by Smith et al. [2001] (see equation 7.2), the 1992 LCLU prediction accuracy increases to 93.63%—identifying 441 out of the 471 fecal coliform compromised watersheds. When applied to the 436 compromised watersheds in 2001 the average-based LPM model identified 81.42% (355 out of 436) of the fecal coliform compromised watersheds. Both of the vector-based models performed near the same level or better than the original Beaulac and Reckhow [1982] model, in training and testing data results. A summary of these model performances and the other modified model predictions is shown in Table 7.4.

Table 7.4: Landscape Indicator Model Fecal Coliform Load Prediction.

|  | 1992 Training Data Results | 2001 Testing Data Results |
| --- | --- | --- |
| Smith et al. [2001] Model | 93.63% | 91.51% |
| Average-Based Model | 91.72% | 81.42% |
| Similarity-Based Model | 93.64% | 89.22% |
| Dissimilarity-Based Model | 99.36% | 98.62% |
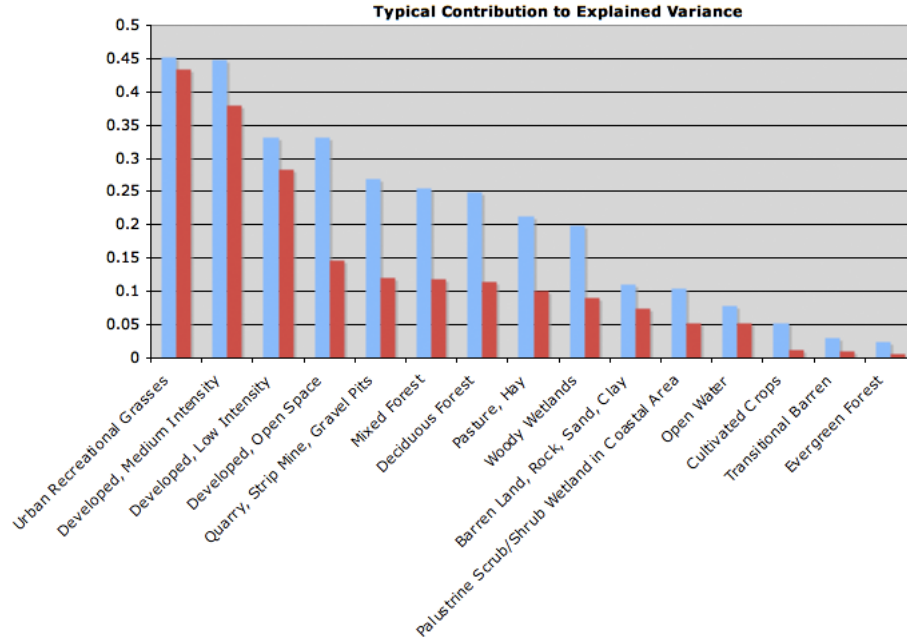
Figure 7.4: LPM model parameters of Smith et al. [2001] *proportion*. These LPM parameters are separated between within watershed (blue) and along stream (red) within watershed *proportion*. They are also based and ranked from left-to-right as most-to-least significant.

## 7.4 Summary of the Relevance of Fourier Landscape Pattern Indicators to predict Fecal Coliform

The predicted loads for each compromised watershed in 2001 by two models are shown in Figure 7.5, separated by model predictions. From left to right, the first loads are those where the models disagreed, and the later loads are those where the models agreed—the difference between these two is clearly marked by the spiked increase in potential annual nitrogen load. The effects of modulating the Smith et al. [2001] model by $m_i$ in equation 7.3 are seen as only decreasing the potential annual load prediction. This was the effect seen in each vector-based method as well. No effective variability was introduced by using either of these model modifications, though detection accuracy was increased for the vector-based methods—particularly for the dissimilarity- based method. The dissimiliarty-based model's exceptional performance leads to the interpretation that the type of LCLU connectivity that best explains watershed level, non-point source, fecal coliform transport is sparse, not very diverse, and lay in no structured pattern.

Those *proportion* parameters deemed by Smith et al. to be significant explained the watershed level landscape variability relatively less than the connectivity LPM, though the order of importance was the same (see Figure 7.4). These parameters' ability to explain more variability suggests their increased ability to predict nutrient loads. Because the connectivity LPM modified models only decreased predicted loads from the *proportion* LPM model, the prediction advantage

suggested by the connectivity LPM % explained variability may have not been fully exploited by the models developed here.
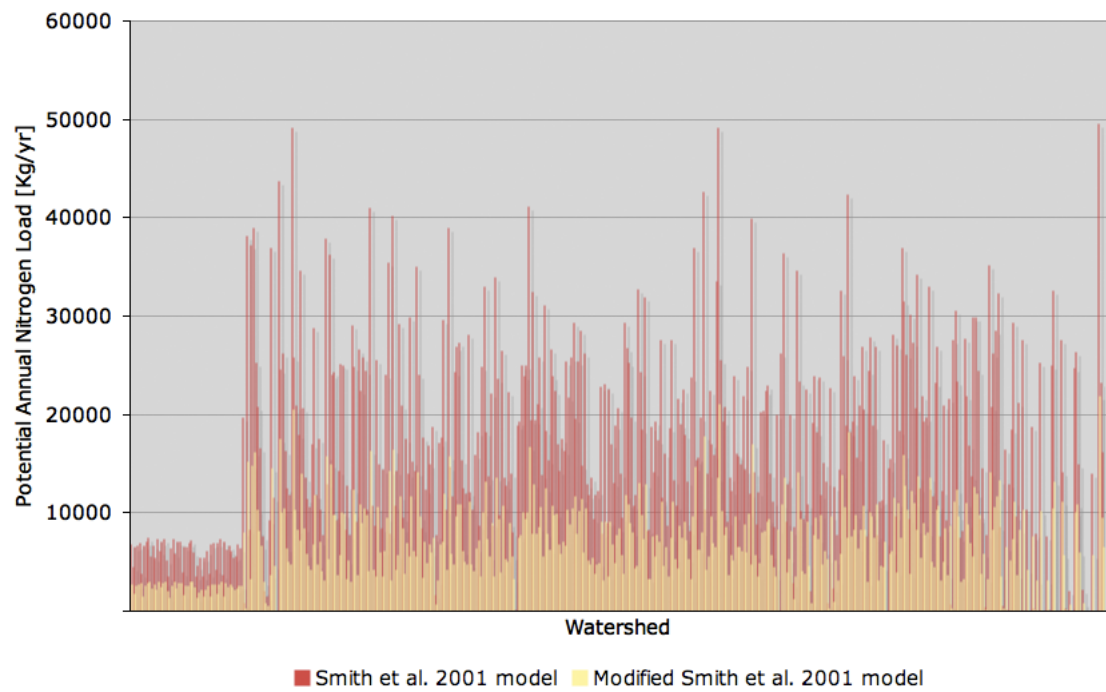


Figure 7.5: Potential nitrogen load predictions of the Smith et al. [2001] model and the modified *average* model presented here.

# Chapter 8

# Summary

Three metrics of landscape pattern were proposed: the *Fourier Metric of Fragmentation* ($FMF$) as a metric of landscape configuration, the *Fourier Metric of Proportion* ($FMP$) as a metric of landscape composition, and the Least Squares Fourier Transform Fractal Dimension Estimation ($LsFT$) as a metric of landscape complexity. Each metric was derived in the Fourier domain to take advantage of scalable spectral energy across imaging system resolution.

A general review of theory and current Landscape Ecology metrics were presented in Chapter 3. Limitations of currently used metrics, and proposed solutions were explored theoretically in Chapter 4 and experimentally in Chapter 5. In Chapter 4, each current and proposed landscape metric concept and derivation were reviewed. Chapter 4 also discussed the proposed method of study in Section 4.4, to reveal how separable the measures of these Landscape Pattern Metrics are, and how much they explain both pattern and phenomena in the landscape. The preliminary landscape pattern metric examples in Chapter 5 present the $FMF$ spatial interpretation (Section 5.1), the $FMP$ increased sensitivity to landscape composition (Section 5.2), the $lsFT$ metric's ability to consistently measure landscape patch dimension (Section 5.3), and each of their performances under system radiometric, spectral, and spatial effects (see Section 3.6 for the methods used). The analysis of LCLU map system effects on the proposed Fourier methods was done by varying pixel values characteristics to find lower and upper bounds of each metric (see Section 3.3.2 for details). Through it all, as shown through the imaging system stressors of Chapter 5, the landscape factor analysis in Chapter 6, and the model prediction results in Chapter 7; these proposed metrics have shown themselves to be reliable, unique, and relevant as Landscape Indicators for Landscape Ecology.

**Fourier Landscape Pattern Metric Reliability**

$FMF$ showed no significant dependence on phase unwrapping error, and maintained errors within $\pm 0.3$ units of $FMF$ due to pixel size. Even for the largest pixel size of $200[m]$, at a distance $x = 4,225.48[m]$ away, only $\pm 0.002$ units of $FMF$ were observed—that is $\pm 0.002\%$ error. The performance of $FMF$ for progressive LCLU maps under variable system effects was much better than the current *Contagion* metric. *Contagion* error bounds were not symmetric, nor did the values consistently report a measure of configuration. Additionally, preliminary results revealed the known correlation between landscape pattern metrics *Contagion*, and *Dominance* (see Figure

3.12). Under the same conditions, there was no observable correlation for the proposed metrics $FMF$ and $FMP$.

The $FMF$ metric corresponded to Island Biogeography spatial interpretations, was consistently accurate and precise under variable system effects and for progressive LCLU maps, and acted as a measure of pattern independent from all others (maintaining very low error bounds)—none of which can be said about the *Contagion* metric $FMF$ is related to.

$FMP$ showed an increased sensitivity to measuring landscape composition over the current *Dominance* landscape pattern metric. Both the current and proposed metrics were comparable and maintained tight upper and lower error bounds during radiometric noise and under variable spatial resolution, but *Dominance* was more independent to an increased spectral accuracy. For both metrics a decrease in spatial resolution resulted in a decrease in dependence on system effects—this is expected. While slightly more inaccurate, and insignificantly less precise, the $FMP$ metric maintained its increased sensitivity to real landscape composition variability while witnessing system effects.

$lsFT$ performed well, and consistently so, for both the inherent and apparent fractal variability. While fractal resolution changed its resolution but not its fractal dimension, the $lsFT$ metric maintained the most accurate measure of dimension compared to traditional LPM *Largest Patch Index LPI* and *Mean Patch Fractal Dimension MPFD*. Over 6 generations of fractal resolution, the $lsFT$ inaccuracy remained within 0.069 units, while $LPI$ and $MPFD$ reported inaccuracies within 0.340 units and 0.193 units respectively. Under system detector noise, increased LCLU patch accuracy, and for variable spatial resolution $lsFT$ continued to report more accurate and precise measures of dimension than traditional LPM.

The proposed metrics are reliable to report relevant values under radiometric, spectral, and spatial imaging system effects. This research included two additional examinations. How unique the measures of these LPM are, and how much they explain relevant pattern in a landscape by factor analysis was also evaluated in Chapter 6 (see Section 4.4.1 for method details). To evaluate the proposed LPM ability to explain landscape phenomena in Chapter 7, these metrics were applied to LCLU data that coincide with ground truth (see Section 4.4.2 for method details). Metrics were evaluated for wetland nutrient variability as a time-series analysis extension of the Smith et al. fecal coliform South Carolina case study. Having understood their abilities under system effects, and after understanding how broadly these metrics can interpret spatial pattern (*i.e.* independence and ubiquity) and how closely they relate to a landscape process (*i.e.* SC wetland fecal coliform dependence), the utility of these metrics as accurate and precise, unique, relevant landscape pattern metrics is known.

**Fourier Landscape Pattern Metric Uniqueness**

LCLU pattern variability across the conterminous United States *Provinces* were observed through 59 LPM. These LPM included the proposed Fourier metrics. Using the correlation matrix it was revealed how unique these proposed Fourier metrics are to commonly used LPM. Additionally, how capable these Fourier metrics are to report relevant information was shown through PCA factor analysis.

When observing LCLU pattern the Fourier metrics consistently reported high contributions to typically explained variability, especially the Fourier Metric of Fragmentation. $FMF$ was found to typically contribute to 65% of the typically explained LCLU variability. The Least Squares Fourier Transform Fractal Dimension Estimation consistently reported high contributions to typically ex-

plained variability as well, 50% as much. The *LsFT* Fourier metric was also the most independent of the other LPM. The Fourier Metric of Proportion consistently varied with LPM $n - Q$, $PSCV$, $LOAX$, and $SHCO$ as shown in Figures 6.2 to 6.4, but none of these metrics contributed as much to the explained LCLU variability observed. *FMP* typically contributed 12% to the explained LCLU variability observed while LPM $n - Q$, $PSCV$, $LOAX$, and $SHCO$ respectively typically contributed 6.28%, 2.65%, 2.54%, and 2.07% to the explained LCLU variability observed. Again, the interpretive power of the Fourier metrics underscore their utility as LPM, besides seeming to have such strong relationships with other currently used LPM. Other currently used LPM that, certainly for the Jackson's *Contagion* statistic (*P005*), have not shown themselves to be reliable measures of image properties.

These observations were made across unique and varied *Provinces*, so the LPM results observed here can be extended for the general interpretation of LCLU pattern. The Fourier metrics, having already shown their reliability against system effects in Chapter 5, have shown themselves to be unique amongst commonly used LPM and relevant when interpreting LCLU variability under multiple environmental scenarios.

### Fourier Landscape Pattern Metric Relevance

A decadal LPM model for potential watershed fecal coliform loads was developed using the Smith et al. [2001] *proportion* parameter LPM model and three other modified *proportion*-connectivity parameter LPM models. Model performance between the original *proportion*-based LPM model and t he modified average-based, similarity-based, and dissimilarity-based models showed a general decrease in detection accuracy. For instance, the average-based modified model performed with 92% accuracy on the 1992 training data while the Smith et al. [2001] model performed with 94% accuracy. The only model exception being the dissimilarity-based model performing with 99.36% accuracy on the 1992 training data and 98.62% prediction accuracy on the 2001 testing data. This leads to the interpretation that the type of LCLU connectivity that best explains watershed level, non-point source, fecal coliform transport is sparse, not very diverse, and lay in no structured pattern.

This decreased LPM model performance when including Fourier connectivity LPM is due to a poor incorporation of these metrics into the model. Each Fourier metric consistently and significantly expressed more information about LCLU pattern within compromised watersheds, but this was not capitalized on in the modified model. The results of this study point to the significance of the proposed Fourier metrics to the interpretation of landscape level ecological processes and the necessity for more appropriate models to take advantage of sophisticated landscape level tools.

### Future Research for Applications of Landscape Pattern Metrics

One of the more simple tasks for the direction of this work would include producing and optimizing current LPM for analysis of precise and accurate records when using image data. A database of the precision and accuracy limits for every relevant LPM would be a valuable resource in determining the necessary satellite sensor designs and classification accuracies needed to make LPM increasingly reliable as relevant Landscape Indicators.

As mentioned before, a better understanding of process and connectivity needs to be had before models that could take full advantage of the high interpretive power of connectivity LPM can be developed. At least one of the simple models discussed here performed better in their

prediction performance, and provided a likely analysis of what types of LCLU may effect nutrient transport most. Going back to gain an appreciation for how much more interpretive variability was introduced by the dissimilarity-based model over the original Smith et al. [2001] model would point to how predictions were made with increased accuracy, and whether even better predictions could be made.

One approach to solving these questions would be to do a transfer curve analysis between each model's results. Highlighting the similarities between the models, and the type and degree of dissimilarity. This transfer function curve analysis would point to how to improve the incorporation of connectivity LPM into *proportion* based landscape indicator models, or even how to produce better Landscape Indicator models using only connectivity LPM.

Identifying the physical factors that appeal most to connectivity LPM and their relation to social dynamics will be the mainstay of research for Landscape Pattern Metrics. What is most exciting about this direction of research is that the current research in Urban Science and Ecosystems theory have began to seriously develope these links [Bettencourt et al., 2007, Brown et al., 2004]. Much like the current *proportion* Landscape Indicator models consistently explaining 65% to 86% of the total variation in nitrogen yields to streams and 73% to 79% of the total variability in dissolved phosphorus and suspended sediment [Jones et al., 2001], Bettencourt et al. [2007] are finding 72% to 99% explanation of total variation in social variables of a city using only city size. These social variables include human needs (job, house, household water consumption), economies of scale associated with infrastructure, and social currencies, such as information, innovation or wealth, associated with the intrinsically social nature of cities [Bettencourt et al., 2007]. The sought after link between pattern, process, cause and society may be brought a step closer by not only understanding these landscapes in terms of their immediate cover, but also the connections between them.

# Chapter 9

# Bibliography

Atmospheric correction for flat and rugged terrain, January 2007. URL http://www.op.dlr.de/atcor/at2$_sp_2$20495.$jpg$.

Globio: Mapping human impacs on the biosphere, 2001. URL http://www.globio.info/.

Stream Biodiversity; The Ghost of Land Use Past, volume 95, 1998.

2007. URL http://www.landscape-ecology.org/.

URL http://www.epa.gov/mrlc/.

July 2010. URL http://www.mrlc.gov/faq.php.

February 2009. URL http://nhd.usgs.gov/.

URL http://www.scdhec.gov/environment/water/tmdl/.

July 2010. URL http://www.envcomm.act.gov.au/soe/soe2004/Ind/surfacewaterquality.htm.

Environmental Protection Agency. Landscape Monitoring and Assessment Research Plan. Office of research and Development, Washington, D.C., epa 620/r-94/009 edition, 1994.

Environmental Protection Agency. Mid-Atlantic Landscape Indicators Project Plan. Office of Research and Development, Washington, D.C., epa 620/draft edition, 1996.

H.R. Akcakaya, Mark A. Burgman, and Lev R. Ginzburg. Applied Population Ecology: Principles and Computer Exercises Using Ramas Ecolab 2.0. Sinauer Associates, 2 edition, 1999. URL http://www.amazon.com/Applied-Population-Ecology-Principles-Exercises/dp/0878930280.

J. R. Anderson, E. E. Hardy, J. T. Roach, and R. E. Witmer. A land use and land cover classification system for use with remote sensor data. Geological survey professional paper 964, U.S. Geological Survey, Washington, D.C., 1976.

C. L. Arnold and C. J. Gibbons. Impervious surface coverage: The emergence of a key environmental indicator. American Planners Association Journal, 62:243–258, 1996.

Golder Associates, 1999.

W. L Baker and Y. Cai. The r.le programs for multiscale analysis of landscape structure using the grass geographical information system. Landscape Ecology, 7:291–302, 1992.

M.F. Barnsley. Fractals Everywhere. Academic Press, 1988.

Michael N. Beaulac and Kenneth H. Reckhow. An examination of land use - nutrient export relationships. Water Resources Bulletin, 18(6):1023–1024, December 1982.

Luis M.A. Bettencourt, Jose Lobo, Dirk Helbing, Christian Kuhnert, and Geoffrey B. West. Growth, innovation, scaling, and the pace of life in cities. Proceedings of the National Academy of Sciences, 104(17):7301–7306, April 2007.

T. Bondelid, B. Murray, S. Pattanayak, D. Lawrence, Yang, Jui-Chen., B. McCail, and Gilling. Water benefits and co-benefits of greenhouse gas reduction incentives in agriculture and forestry. Contract 68-01-001, EPA, 2001.

D. B. Booth and C. R. Jackson. Urbanization of aquatic systems: Degradation thresholds, stormwater detection, and the limits of mitigation. Journal of America Water Resources Association, 33: 1077–1090, 1997.

Joe Brewer and Larry Di Girolamo. Limitations of fractal dimension estimation algorithms with implications for cloud studies. Atmospheric Research, 82:433–454, December 2006.

J.H. Brown, J.F. Gilooly, A.P. Allen, V. M. Savage, and G.B. West. Toward a metabolic theory of ecology. Ecology, 85(7):1771–1789, 2004.

Françoise Burel and Jacques Baury. Landscape Ecology: Concepts Methods and Applications, chapter Return to Scale Dependence: Contribution of Fractal Geometry, pages 105–114. Science Publishers, 2003.

C. Castelnovo, A. Podesta, P. Piseri, and P. Milani. Fractal analysis of sampled profiles: systematic study. Physical Review, E(65):021601–1–021601–11, 2002.

M. S. Cresser, R. Smart, M. F. Billett, G. Soulsby, C. Neal, A. Wade, S. Langan, and A. C. Edwards. Modelling water chemistry for a major scottish river from catchment attributes. Journal of Applied Technology, 37:171–184, 2000.

K. A. Crews-Meyer. Temporal extensions of landscape ecology theory and practice: Examples from the peruvian amazon. The Professional Geographer, 58(4):421–435, 2006.

L. De Cola. Fractal analysis of a classified landsat scene. Photogrammetric Engineering and Remote Sensing, 55:601–610, 1989.

N. Detenbeck, C. A. Johnston, and G. Niemi. Wetland effects on lake water quality in the minneapolis/st. paul metropoitan area. Landscape Ecology, 8:39–61, 1993.

W. E. Dramstad. Landscape Ecology Principles in Landscape Architecture and Land-Use Planning. American Society of Landscape Architechts. Island Press, Washington, D.C., 1996.

T. Dunne and L. B. Leopold. Water in Environmental Planning. Freeman, 1978.

Roger Jr. Easton. Basic principles of imaging science ii. The Diffraction Integral, February 2005.

T. Fawcett. Roc graphs: Notes and practical considerations for researchers. Technical report, HP Laboratories, Palo Alto, USA, 2004.

Jean Baptiste Joseph Fourier. Théorie analytique de la chaleur. Chez Firmin Didot, père et fils, 1822.

R. Frohn. Remote Sensing for Landscape Ecology: New Metric Indicators for Monitoring, Modeling and Assessment of Ecosystems. CRC-Lewis Publishers, Boca Raton, USA, 1998.

O.E. Gaggiotti and I. Hanski. Mechanisms of Population Extinction. Ecology, Genetics, and Evolution of Metapopulations. Elsevier Academc Press, San Diego, USA, 2004.

R. H. Gardner. Nuetral models for testing landscape hypothesis. Landscape Ecology, 22:15–29, 2007.

Robert H. Gardner. Landscape Ecological Analysis: Issues and Applications, chapter RULE: Map Generation and Spatial Analysis Program, pages 281–289. Springer, New York, 1999.

J. D. Gaskill. Linear Systems, Fourier Transforms, and Optics. Wiley Series in Pure and Applied Optics. Wiley-Interscience, 1978.

S. E. Gergel, M. G. Turner, and K. T. Kratz. Scale-dependent landscape effects on north temperate lakes and rivers. Ecological Applications, 9:1377–1390, 1999.

Sarah E. Gergel and Monica G. Turner. Learning Landscape Ecology. Springer, 2003.

Sarah E. Gergel, Monica G. Turner, James R. Miller, John M. Melack, and Emily H. Stanley. Landscape indicators of human impacts to riverine systems. Aquatic Sciences, 64:118–128, 2002.

R. L. Graham, C. T. Hunsaker, R. V. O'Neill, and B. Jackson. Ecological risk assessment at the regional scale. Ecological Application, 1:196–206, 1991.

The Camdus Group. Watershed assessment: Reading, pennsylvania. Contract 68-C5-0061, U.S. Environmental Protection Agency, 1998.

E. J. Gustafson and G. R. Parker. Relationships between landcover proportion and indices of landscape spatial pattern. Landscape Ecology, 7:101–110, 1992.

R. Haines-Young and M. Chopping. Quantifying landscape structure: A review of landscape indices and their applicaiton to forested landscapes. Progress in Physical Geography, 20:418–445, 1996.

I. Hanski. Spatially Realistic Models of Metapopulation Dynamics and their Implications for Ecological, Genetic and Evolutionary Processes. Integrating Ecology and Evolution in a Spatial Context. Blackwell Science, 2002.

I. Hanski, J. J. Hellmann, C. L. Boggs, and J.F. McLaughlin. Checkerspots as a Model System in Population Biology. On The Wings of Checkerspots: A Model System for Population Biology. Oxford University Press, Oxford, 2004.

Eugene Hecht. Optics. Addison-Wesley, 2 edition, 1987.

J.L. Homer and P.D. Gianino. Phase-only matched filtering. Applied Optics, 23:812–816, 1984.

Q. Huang, J.R. Lorch, and R.C. Dubes. Can the fractal dimension of images be measured? Pattern Recognition, 27:339–349, 1994.

Carolyn T. Hunsaker, Robert V. O'Neill, Barbara L. Jackson, S. P. Timmins, Daniel A. Levine, and Douglas J. Norton. Sampling to characterize landscape pattern. Landscape Ecology, 9(3): 207–226, September 1994.

V. Ingegnoli. Landscape Ecology: A Widening Foundation. Springer, New York, 2002.

Yetunde Jeje. Export Coefficients for Total Phosphorus, Total Nitrogen and Total Suspended Solids in the Southern Alberta Region: A Literature Review. Regional Environmental Management, Alberta Environment, 3rd Floor, Deerfoot Square, 2938 - 11 Street N. E. Calgary, Alberta T2E 7L7, 2006.

D. B. Jennings, S. T. Jarnigan, and D. W. Ebert. A modeling approach for estimating watershed impervious surface area from national land cover data. Photogrammetric Engineering and Remote Sensing, 70(11):1295–1307, 2004.

P. Johnes, B. Moss, and G. Phillips. The determination of total nitrogen and total phosphorous concentrations in freshwaters from land use, stock headage and population data: Testing a model for use in conservation and water quality management. Freshwater Biology, 36:451–473, 1996.

W. C. Johnson, C. Richards, G. E. Host, and J. W. Arthur. Landscape influence on water chemistry in midwestern stream ecosystems. Freshwater Biology, 37(1):193–218, 1997.

E. D. B. Jones, G. S. Helfman, Harper J.O., and P. V. Bolstad. Effects of riparian forest removal on fish assemblages in soutern appalachain streams. Conservation Biology, 13(6):1454–1465, 1999.

K. B. Jones, A. C. Neale, M. S. Nash, R. D. Van Remortel, J. D. Wickham, K. H. Ritters, and R. V. O'Neill. Predicting nutrient and sediment loadings to streams from landscape metrics: A multiple watershed study from the united states mid-atlantic region. Landscape Ecology, 16: 301–312, 2001.

S. S. Kaushal, M. L. Pace, P. M. Groffman, L. E. Band, K. T. Belt, P. M. Mayer, and C. Welty. Land use and climate variability amplify contaminant pulses. Eos, Transactions, American Geohphysical Union, 91(25):221–222, July 2010.

R. D. Klein. Urbanization and stream quality impairment. Water Resources Bulletin, 15:948–963, 1979.

J. Kolibal and J. Monde. Fractal image error analysis. Computation Geoscience, 24:785–795, 1998.

J. R. Krummel, R. H. Gardner, G. Sugihara, R. V. O'Neill, and P. R. Coleman. Landscape patterns in disturbed environment. Oikos, 48:321–324, 1987.

A. Leduc, Y. T. Prairie, and Y. Bergeron. Fracal dimension estimates of a fragmented landscape: sources of variability. Landscape Ecology, 9:279–286, 1994.

R. Levins. Some demographic and genetic consequences of environmental heterogeneity for biological control. Bulletin of The Entomology Society of America, 71:237–240, 1969.

H. Li and J. F. Reynolds. A new contagion index to quantify spatial patterns of landscapes. Landscape Ecology, 8:155–162, 1993.

Larry S. Liebovitch. Fractals and Chaos Simplified for the Life Sciences. Oxford University Press, Center for Complex Systems, Florida Atlantic University, 1998.

Amy J. Liu and Guy N. Cameron. Analysis of landscape patterns in coastal wetlands of gavelston bay, texas (usa). Lndscape Ecology, 16(7):581–595, October 2001.

S. Lovejoy. Area-perimeter relation for rain and cloud areas. Science, 216:185–187, 1982.

Robert H. MacArthur and Edward O. Wilson. The Theory of Island Biogeography. Princeton University Press, 1967. ISBN 0-691-08836-5. URL http://press.princeton.edu/titles/7051.html.

I. Maddock. The importance of physical habitat assessment for evaluating river health. Freshwater Biology, 41:373–391, 1993.

A. E. Magurran. Ecological Diversity and its Measurement. Princeton University Press, Princeton, NJ, 1988.

B. B. Mandelbrot. Fractals, Form, Chance and Dimension. Freeman, San Francisco, 1977.

K. McGarigal and B. J. Marks. Fragstats: Spatial pattern analysis program for quantifying landscape structure, version 2.0. Oregon State University, Corvallis, 1994.

B. T. Milne. The utility of fractal geometry in landscape design. Landscape and Urban Planning, 21:81–90, 1991a.

B. T. Milne. Quantitative Methods of Landscape Ecology, volume 82, chapter Lessons from applying fractal models to landscape patterns, pages 199–239. Springer-Verlag, New York, 1991b.

B. T. Milne. Ecological Indicators, volume 2, chapter Indication of landscape condition at many scales, pages 883–895. Elsevier Applied Science, 1992.

B. T. Milne. Wildlife and Landscape Ecology: Effects of Pattern and Scale, chapter Applications of Fractal Geometry in Wildlife Biology, pages 32–69. Springer, 1997.

D. R. Morse, J. H. Larson, M. M. Dodson, and M. H. Williamson. Fractal dimension of anthropod body lengths. Nature, 315:731–733, 1985.

Montana Department of Environmental Quality. Draft nutrient management plan to total maximum daily load for flathead lake, montana. Technical report, 2001.

S.C. Department of Health and Environmental Control. R.61-68, Water Classifications Standards. Bureau of Water, 2600 Bull Street, April 2008.

R. V. O'Neill, C. T. Hunsaker, S. P. Timmins, B. L. Jackson, K. H. Ritters, and J. D. Wickham. Quantifying landscape status and trends at regional scale. Manuscript.

R. V. O'Neill, J. R. krummel, R. H. Gardner, G. Sugihara, B. Jackson, D. L. DeAngelis, B. T. Milne, Monica G. Turner, B. Zygmut, S. W. Christensen, V. H. Dale, and R. L. Graham. Indices of landscape pattern. Landscape Ecology, 11:169–180, 1988.

R. V. O'Neill, R. H. Gardner, B. T. Milne, Monica G. Turner, and B. Jackson. Heterogeneity and Spatial Hierarchies, chapter Ecological Heterogeneity, pages 85–96. Springer-Verlag, New York, 1991.

Robert V. O'Neill, K. H. Riitters, J. D. Wickham, and K. Bruce Jones. Landscape pattern metrics and regional assessment. Ecosystem Health, 5(4):226–233, December 1999.

L. L. Osborne and M. J. Wiley. Empirical relationships between land use/land cover and stream water quality in an agricultural watershed. Journal of Environmental Management, 26:9–27, 1988.

O. Ovaskainen and I. Hanski. Metapopulation Dynamics in Highly Fragmented Landscapes. Ecology, Genetics, and Evolution of Metapopulations. Elsevier Academc Press, San Diego, USA, 2004.

Haldun M. Ozaktas, Zeev Zalevsky, and Alper M. Kutay. The Fractional Fourier Transform with Applications in Optics and Signal Processing. Pure and Applied Optics. John Wiley, 2001.

C. A. Pickover. Computers, Pattern, Chaos and Beauty, Graphics from an Unseen World. St. Martin's Press, New York, NY, 1990.

K. H. Reckhow, M.N. Beaulac, and Simpson. Modeling Phosphorus loading and lake response under uncertainty: A manual compilation of export coefficients. EPA, 440/5-80-011 edition.

D. Richards, Johnson L.B., and Host G. Landscape-scale influences on stream habitats and biota. Canadian Journal of Fisheries and Aquatic Sciences, 53(Suppl. 1):295–311, 1996.

K. H. Ritters. Fractal dimension from partial perimeters. Manuscript.

K. H. Ritters, R. V. O'Neill, J. D. Wickham, and K. B. Jones. A note on contagion metrics of landscape analysis. Manuscript.

K. H. Ritters, R. V. O'Neill, C. T. Hunsaker, J. D. Wickham, D. H. Yankee, S. P. Timmins, K. B. Jones, and B. L. Jackson. A factor analysis of landscape pattern and structure metrics. Landscape Ecology, 10:23–39, 1995.

W. H. Romme and D. H. Knight. Landscape diversity: The concept applied to yellowstone park. BioScience, 32:664–670, 2004.

T. Rychener, M. Dixon, and J. Stromberg. Interaction between landscape pattern and disturbance: The response of a southwest riparian forest to fire. 19th Annual Symposium of the United States Regional Association of the International Association for Landscape Ecology, March 2004.

C. Saloma and G. Narisma. Modeling spatially extended complex systems from experimental data: sensitivity to sampling intervals. Journal of Applied Physics, 77:1374–1377, 1995.

D. Saupe. The Science of Fractal Images, chapter Algorithms for random fractals, page 101. Springer-Verlag, 1988.

John R. Schott. Remote Sensing: The Image Chain Approach, chapter 5, 6, 13, pages 180–258, 557–616. Oxford University Press, 2 edition, 2007.

T. R. Schueler and J. Galli. Environmental Impacts of Stormwater Ponds. Watershed Restoration Source Book, Washington, D.C., Metropolis. Washington Council Government, 1992.

B. Shorrocks, J. Marsters, I. Ward, and P. J Evennett. The fractal dimensions of lichens and the distribution of anthropod body lengths. Functional Ecology, 5:457–460, 1991.

M. C. Singer and I. Hanski. Dispersal Behavior and Evolutionary Metapopulation Dynamics. On The Wings of Checkerspots: A Model System for Population Biology. Oxford University Press, Oxford, 2004.

J. H. Smith, J. D. Wickham, D. J. Norton, T. G. Wade, and K. B. Jones. Utilization of landscape indicators to model potential pathogen impaired waters. Journal of the American Water Resources Association, 37:1–10, 2001.

R.A. Sponseller, Benfield E.F., and H.M. Valett. Relationships between land use, spatial scale and stream macroinvertebrate communities. Freshwater Biology, 46(10):1409–1424, 2001.

Carl Troll. Luftbildplan und ökologische bodenforschung (aerial photography and ecological studies of the earth). Zeitschrift der Gesellschaft für Erdkunde, pages 241–298, 1939.

Monica G. Turner. Landscape ecology: The effect of pattern on process. Annual Review of Ecology and Systematics, 20:171–197, 1989.

Monica G. Turner. Spatial and temporal analysis of landscape pattern. Landscape Ecology, 3: 153–162, 1990a.

Monica G. Turner. Landscape changes in nine rural counties of georgia. Photogrammetric Engineering and Remote Sensing, 56:379–386, 1990b.

Monica G. Turner and R. H. Gardner, editors. Quantitative Methods of Landscape Ecology. Springer-Verlag, New York, NY, USA, 2001.

Monica G. Turner and C. L. Ruscher. Changes in landscape patterns in georgia, usa. Landscape Ecology, 1:241–245, 1988.

Monica G. Turner, r. Costanza, and F. H. Sklar. Methods to compare spatial patterns for landscape modeling and analysis. Ecological Modeling, 48:1–18, 1989.

USEPA. Polluted runoff (nonpoint source pollution). National Management Measures to Control Nonpoint Source Pollution from Agriculture, page 314, 2002.

USEPA. Areawide assessment procedures. Technical Report EPA-600/9-76-014, Municipal Environmental Research Laboratory, 1976.

Charles Vassallo. Notion of fractal dimension, 2007. URL http://perso.orange.fr/charles.vassallo/en/art/dimension.html.

J. E. Vogelmann, T. Sohl, P.V. Campbell, and D.M. Shaw. Regional land cover characterization using landsat thematic mapper data and anciliary data sources. Environmental Monitoring and Assessment, 51:415–428, 1998a.

J. E. Vogelmann, T. Sohl, and Howard S.M. Regional characterization of land cover using multiple sources of data. Photogrammetric Engineering and Remote Sensing, 64(1):45–47, 1998b.

J. E. Vogelmann, Howard SM., L. Yang, C. R. Larson, B. K. Wylie, and N. Van Driel. Completion of the 1990s national land cover data set for the conterminous united states from landsat thematic mapper data and ancillary data sources. Photogrammetric Engineering and Remote Sensing, 67:650–662, 2001.

R. F. Voss. Fractals in Nature, chapter From Characterization to Simulation, pages 21–70. The Science of Fractal Images. Springer-Verlag, New York, NY, 1988.

N. Wahlberg, P. R. Ehrlich, C. L. Boggs, and I. Hanski. Bay Checkerspot and Glanville Fritillary Compared with other Species. On The Wings of Checkerspots: A Model System for Population Biology. Oxford University Press, Oxford, 2004.

L. Wang, J. Lyons, P. Kanehl, and R. Gatti. Influences of watershed land use on habitat quality and biotic integrity of wisconsin streams. Fisheries, 22:6–12, 1998.

J. A. Weins and B. T. Milne. Scaling of 'landscapes' in landscape ecology, or, landscape ecology from a beetle's perspective. Landscape Ecology, 3:87–96, 1989.

D. E. Weller, Jordan T. E., and D. L. Correll. Heuristic models for material discharge from landscapes with riparian buffers. Ecological Applications, 8:1156–1169, 1998.

J. D. Wickham and D. J. Norton. Mapping and analyzing landscape patterns. Landscape Ecology, 9:7–23, 1994.

J. D. Wickham and K. H. Ritters. Sensitivity of landscape metrics to pixel size. International Journal of Remtoe Sensing, 16(18):3585–3594, 1995.

J. D. Wickham, K. H. Ritters, R. V. O'Neill, K. H. Reckhow, T. G. Wade, and K. B. Jones. Land cover as a framework for assessing risk of water pollution. Journal of American Water Resources Association, 36(6):1–6, 2000.

T. Wiegand, F. Jeltsch, I. Hanski, and V. Grimm. Using pattern-oriented modeling for revealing hidden information: A key for reconciling ecological theory and application. Oikos, 100:209–222, 2003.

M. R. Williams and John M Melack. Solute export from forested and partially deforested catchments in the central amazon. Biogeochemistry, 38:67–102, 1997.

M. R. Williams, T. R. Fisher, and John M Melack. Solute dynamics in soil water and groundwater in central amazon catchment undergoing deforestation. Biogeochemistry, 38(3):303–335, 1997.

J. Wu. Effects of changing scale on landscape pattern analysis: Scaling relations. Landscape Ecology, 19:125–138, 2004.

J. Wu, W Shen, W Sun, and P. T. Tueller. Empirical patterns of the effects of changing scale on landscape metrics. Landscape Ecology, 17:761–782, 2002.

Shiu Yin Yuen, Chun Ki Fong, Kwok Leung Chan, and Yiu Wah Leung. Fractal dimension estimation and noise filtering using hough transform. <u>Signal Processing</u>, 84:907–917, January 2004.

Z. Zhu, L. Yang, S. Stehman, and R. Czaplewski. Designing an accuracy assessment for usgs regional land cover mapping program. <u>Photogrammetric Engineering and Remote Sensing</u>, 66 (12):1425–1435, December 2000.

# Appendix A

# Landscape Pattern Metrics

Every Landscape Pattern Metric is taken from Ritters et al. [1995], unless otherwise referenced. Every independent landscape pattern metric is numbered. The indented metrics are highly correlated to their numerated header.

1. Number of LCLU classes

   - $NTYP$ (Total number of LCLU classes)
     - $NTYP = S$

2. Shannon evenness of LCLU classes

   - $SIDI$ (Simpson diversity of LCLU classes)
     - $SIDI = 1 - \sum_{j=1}^{S} p_j^2$

       Here, $S$ is the number of LCLU classes, and $p_j$ is the proportion of each LCLU class $j$.
   - $SIEV$ (Simpson evenness of LCLU classes)
     - $SIEV = \frac{SIDI}{1 - \frac{1}{S}}$

       Here, $S$ is the number of LCLU classes. See *Shannon evenness of LCLU classes* for $SIDI$.
   - $SHDI$ (Shannon diversity of attribute classes)
     - $SHDI = -\sum_{j=1}^{S} p_j \ln[p_j]$

       Here, $S$ is the number of LCLU classes, and $p_j$ is the proportion of LCLU class $j$.
   - $SHEV$ (Shannon evenness of LCLU classes)
     - $SHEV = \frac{SHDI}{\ln[S]}$

       Here, $S$ is the number of LCLU classes.
   - $MCDI$ (McIntosh diversity of attribute classes [Magurran, 1988])

- $MCDI = \dfrac{N - \sqrt{\sum_{j=1}^{S} n_j^2}}{N - \sqrt{N}}$

  Here, $S$ is the number of LCLU classes, $N$ is the total number of pixels in the landscape, and $n_j$ is the total number of pixels in LCLU class $j$.

- *MCEV* (McIntosh evenness of attribute classes)

  - $MCEV = \dfrac{N - \sqrt{\sum_{j=1}^{S} n_j^2}}{N - \frac{N}{\sqrt{S}}}$

    Here, $S$ is the number of LCLU classes, $N$ is the total number of pixels in the landscape, and $n_j$ is the total number of pixels in LCLU class $j$.

- *SHHO* (Shannon homogeneity of the adjacency matrix)

  - 

$$
\begin{aligned}
SHHO \;&=\; -\sum_{i=1}^{S}\sum_{j=1}^{S} p_j \cdot q_{i,j} \ln\left[p_j \cdot q_{i,j}\right] \\
&=\; -\sum_{i=1}^{S}\sum_{j=1}^{S} \frac{n_{i,j}[E_{hor}, E_{vert}]}{N} \ln\left[\frac{n_{i,j}[E_{hor}, E_{vert}]}{N}\right]
\end{aligned}
$$

    Here, $S$ is the number of LCLU classes, $N$ is the total number of pixels in the landscape, and $n_{i,j}[E_{hor}, E_{vert}]$ the total number of horizontal and vertical edge pixels shared by LCLU classes $i$ and $j$.

- *SIHO* (Simpson homogeneity of adjacency matrix [Ritters et al.])

  - $SIHO = 1 - \sum_{i=1}^{S}\sum_{j=1}^{S} \left(\frac{n_{i,j}[E_{hor}, E_{vert}]}{N}\right)^2$

    Here, $S$ is the number of LCLU classes, $N$ is the total number of pixels in the landscape, and $n_{i,j}[E_{hor}, E_{vert}]$ the total number of horizontal and vertical edge pixels shared by LCLU classes $i$ and $j$.

3. Kempton-Taylor Q-statistic

   - $KT - Q$ (The inter-quartile slope of the cumulative LCLU abundance curve [Magurran, 1988])

     - $KT - Q = \dfrac{\frac{n_{Q_1}}{2} + \frac{n_{Q_2}}{2} + \sum_{Q=Q_1+1}^{Q_2-1} n_Q}{\ln\left[\frac{Q_2}{Q_1}\right]},$

       where $n_Q$ is the number of LCLU classes with abundance $Q$, $Q_1$; $Q_2$ are the $25^{th}$ and $75^{th}$ quartiles:

       i. $n_{Q_1} = n_j$ the number of pixels in the LCLU class where $Q_1$ falls—the $1^{st} - 25^{th}$ percentile number of pixels     ii. $n_{Q_2} = n_j$ the number of pixels in the LCLU class where $Q_2$ falls—the $75^{th} - 100^{th}$ percentile number of pixels

       The quartiles are chosen such that,

       $\sum_{Q=1}^{Q_1-1} n_Q < \frac{S}{4} \leq \sum_{Q=1}^{Q_1} n_Q,$

     and

$$\sum_{Q=1}^{Q_2-1} n_Q < \frac{3 \cdot S}{4} \leq \sum_{Q=1}^{Q_2} n_Q.$$

where $S$ is the number of LCLU classes.

4. Shannon *Contagion*

- *PMAX* (The maximum LCLU class proportion)
  - $p_{max} = \frac{n_{max}}{N}$

    Here, $N$ is the total number of pixels in the landscape, and $n_{max}$ is the maximum number of pixels in a LCLU class.

- *SHCO* (Shannon *Contagion*)
  - $SHCO = 1 - \frac{SHHO}{2 \cdot \ln[S]} = Contagion$

    Here, $S$ is the number of LCLU classes. See *Shannon evenness of LCLU classes* for *SHHO*.

- *SICO* (Simpson *Contagion*)
  - $SICO = \frac{SIHO}{1 - \frac{1}{S^2}}$

    Here, $S$ is the number of LCLU classes. See *Shannon evenness of LCLU classes* for *SIHO*.

5. Sum of LCLU adjacencies

- *SUMD* (Sum of adjacencies for one LCLU class [Wickham and Ritters, 1995])
  - $SUMD = \sum_{j=1}^{S} n_j[E_h, E_v]$

    Here, $S$ is the number of LCLU classes, and $n_j[E_h, E_v]$ are the total horizontal and vertical edges of LCLU class $j$.

- *TENT* (Average fractal estimator of LCLU class configurational entropy from the scaling of LCLU class density to the size of the neighborhood of an arbitrary pixel in the class)
  - $P_t[L; n_j]$ is the probability of finding $t$ other pixels of the same LCLU class, in an $L \times L$ kernel, centered on an arbitrarily chosen pixel.

    $$P_t[L; n_j] = \frac{s_{t,L}[j]}{n_j}$$

    where $s_{t,L}[j]$ is the number of $L \times L$ kernels that had $t$ pixels of the same LCLU class $j$, and $n_j$ is the number of pixels in LCLU class $j$.

    Letting $n_j[L]$ be the maximum number of pixels, of the same LCLU class $j$, observed in any $L \times L$ kernel:

    $$M^0[P_t[L; n_j]] = \sum_{t=1}^{n_j[L]} \ln[t] \cdot P_t[L; n_j]$$

    From each LCLU class with $> 400$ pixels, a random sample of at least 400 pixels are selected. Square kernels of size $L$=5, 15, 25, 35, and 45 are placed around each sampled pixel and the occurrence of pixels of the same LCLU class are counted for each kernel size. Letting $\beta_{10j}$ be the estimated slope from the regression of $M^0[P_t[L; n_j]]$ on $\ln[L]$ for the $j^{th}$ LCLU class, the fractal estimator is:

133

$$TENT = \sum_{j=1}^{S} \frac{n_j}{N} \beta_{10j}$$

Here, $S$ is the number of LCLU classes, $N$ is the total number of pixels in the landscape, and $n_j$ is the total number of pixels in LCLU class $j$.

- $TMAS$ (Fractal estimator of LCLU class mass from the scaling of LCLU class density to the size of a neighborhood of an arbitrary pixel in the class.)

  - $P_t[L; n_j]$ is the probability of finding $t$ other pixels of the same LCLU class, in an $L \times L$ kernel, centered on an arbitrarily chosen pixel.

    $$P_t[L; n_j] = \frac{s_{t,L}[j]}{n_j}$$

    where $s_{t,L}[j]$ is the number of $L \times L$ kernels that had $t$ pixels of the same LCLU class $j$, and $n_j$ is the number of pixels in LCLU class $j$.

    Letting $n_j[L]$ be the maximum number of pixels, of the same LCLU class $j$, observed in any $L \times L$ kernel:

    $$M^1[P_t[L; n_j]] = \sum_{t=1}^{n_j[L]} t \cdot P_t[L; n_j]$$

    From each LCLU class with $> 400$ pixels, a random sample of at least 400 pixels are selected. Square kernels of size $L$=5, 15, 25, 35, and 45 are placed around each sampled pixel and the occurrence of pixels of the same LCLU class are counted for each kernel size. Letting $\beta_{11j}$ be the estimated slope from the regression of $\ln \left[ M^1[P_t[L; n_j]] \right]$ on $\ln[L]$ for the $j^{th}$ LCLU class. The fractal estimator is:

    $$TMAS = \sum_{j=1}^{S} \frac{n_j}{N} \beta_{11j}$$

    Here, $S$ is the number of LCLU classes, $N$ is the total number of pixels in the landscape, and $n_j$ is the total number of pixels in LCLU class $j$.

- $TVAR$ (Fractal estimator of LCLU class variance from the scaling of LCLU class density to the size of the neighborhood of an arbitrary pixel in the class)

  - $P_t[L; n_j]$ is the probability of finding $t$ other pixels of the same LCLU class, in an $L \times L$ kernel, centered on an arbitrarily chosen pixel.

    $$P_t[L; n_j] = \frac{s_{t,L}[j]}{n_j}$$

    where $s_{t,L}[j]$ is the number of $L \times L$ kernels that had $t$ pixels of the same LCLU class $j$, and $n_j$ is the number of pixels in LCLU class $j$.

    Letting $n_j[L]$ be the maximum number of pixels, of the same LCLU class $j$, observed in any $L \times L$ kernel:

    $$M^2[P_t[L; n_j]] = \sum_{t=1}^{n_j[L]} t^2 P_t[L; n_j]$$

    From each LCLU class with $> 400$ pixels, a random sample of at least 400 pixels are selected. Square kernels of size $L$=5, 15, 25, 35, and 45 are placed around each sampled pixel and the occurrence of pixels of the same LCLU class are counted for each kernel size. Letting $\beta_{12j}$ be the estimated slope from the regression of $\ln \left[ M^2[P_t[L; n_j]] \right]$ on $\ln(L)$ for the $j^{th}$ LCLU class. The fractal estimator is:

    $$TVAR = \sum_{j=1}^{S} \frac{n_j}{N} \beta_{12j}$$

    Here, $S$ is the number of LCLU classes, $N$ is the total number of pixels in the

landscape, and $n_j$ is the total number of pixels in LCLU class $j$.

- $P050$ (Weighted average proportion of pixels contained in patches with area > 50 pixels)

  - $P050 = \sum_{j=1}^{S} \frac{n_j}{N} \frac{\sum_{\tau=1}^{\psi_j} n_\tau^*}{\sum_{\tau=1}^{\psi_j} n_\tau}$

    where $S$ is the number of LCLU classes, $N$ is the total number of pixels in the landscape, $n_j$ is the total number of pixels in the LCLU class $j$, $\psi_j$ is the total number of nearest-neighbor patches of LCLU class $j$, and $n_\tau$ is the total number of pixels in patch $\tau$.

    $$n_\tau^* = \begin{cases} 0 \text{ if } n_\tau < 51, \\ n_\tau \text{ otherwise.} \end{cases}$$

- $P500$ (Weighted average proportion of pixels contained in patches with area > 500 pixels)

  - $P500 = \sum_{j=1}^{S} \frac{n_j}{N} \frac{\sum_{\tau=1}^{\psi_j} n_\tau^*}{\sum_{\tau}^{\psi_j} n_\tau}$

    where $S$ is the number of LCLU classes, $N$ is the total number of pixels in the landscape, $n_j$ is the total number of pixels in the LCLU class $j$, $\psi_j$ is the total number of nearest-neighbor patches of LCLU class $j$, and $n_\tau$ is the total number of pixels in patch $\tau$.

    $$n_\tau^* = \begin{cases} 0 \text{ if } n_\tau < 501, \\ n_\tau \text{ otherwise.} \end{cases}$$

6. Average LCLU class lacunarity

   - $TLAC$ (Average LCLU class lacunarity from the scaling of class density with kernel size)

     - $TLAC = TVAR - TENT$

       See, *Sum of LCLU adjacencies*

7. Average proportion of area in patches larger than 5 pixels

   - $P005$ (Weighted average proportion of pixels contained in patches with area > 5 pixels— Jackson's *Contagion* statistic [O'Neill et al.])

     - $P005 = \sum_{j=1}^{S} \frac{n_j}{N} \frac{\sum_{\tau=1}^{\psi_j} n_\tau^*}{\sum_{\tau}^{\psi_j} n_\tau}$

       where $S$ is the number of LCLU classes, $N$ is the total number of pixels in the landscape, $n_j$ is the total number of pixels in the LCLU class $j$, $\psi_j$ is the total number of nearest-neighbor patches of LCLU class $j$, and $n_\tau$ is the total number of pixels in patch $\tau$.

       $$n_\tau^* = \begin{cases} 0 \text{ if } n_\tau < 6, \\ n_\tau \text{ otherwise.} \end{cases}$$

8. Perimeter-area scaling, patch perimeter complexity

   - $OEFC$ (Fractal estimator of patch perimeter complexity from perimeter-area scaling enclosing edges basis [Lovejoy, 1982])

– $OEFC = 2 \cdot \beta_1$

where $\beta_1$ is the estimated slope from the regression of the natural log of left-diagonal and right-diagonal patch edge pixels, $\ln[n_\tau[E_{left}, E_{right}]]$, on the natural logarithm of the total number of pixels in LCLU patch $\tau$, $\ln[n_\tau]$, for all nearest-neighbor patches greater than 3 pixels, $n_\tau > 3$, that do not touch the border of the LCLU map.

- $OIFC$ (Fractal estimator of patch perimeter complexity from perimeter-area scaling, all edges basis)

– $OIFC = 2 \cdot \beta_3$

where $\beta_3$ is the estimated slope from the regression of left-diagonal, right-diagonal, horizontal, and vertical patch edge pixels, $\ln[n_\tau[E_{left}, E_{right}, E_{hor}, E_{vert}]]$, on the natural logarithm of the total number of pixels in LCLU patch $\tau$, $\ln[n_\tau]$, for all nearest-neighbor patches greater than 3 pixels, $n_\tau > 3$, that do not touch the border of the LCLU map.

- $OCFC$ (Fractal estimator of patch perimeter complexity from perimeter-area scaling, enclosing pixels basis)

– $OCFC = 2 \cdot \beta_2$

where $\beta_2$ is the estimated slope from the regression of the left-diagonal, right-diagonal, horizontal, and vertical patch edge pixels complement,

$$\ln[n_\tau - n_\tau[E_{left}, E_{right}, E_{hor}, E_{vert}]] = \ln[n_\tau^{\complement}]$$

on the natural logarithm of the total number of pixels in LCLU patch $\tau$, $\ln[n_\tau]$, for all nearest-neighbor patches greater than 3 pixels, $n_\tau > 3$, that do not touch the border of the LCLU maps.

9. Perimeter-area scaling, patch topology transformation, enclosing pixel basis

- $OEFT$ Fractal estimator of patch topology from perimeter-area scaling, enclosing edges basis [Ritters]

– $OEFT = \frac{1}{\beta_1}$

where $\beta_1$ is the estimated slope from the regression of the natural log of left-diagonal and right-diagonal patch edge pixels, $\ln[n_\tau[E_{left}, E_{right}]]$, on the natural logarithm of the total number of pixels in LCLU patch $\tau$, $\ln[n_\tau]$, for all nearest-neighbor patches greater than 3 pixels, $n_\tau > 3$, that do not touch the border of the LCLU map.

- $OIFT$ Fractal estimator of patch topology from perimeter-area scaling, all edges basis.

– $OIFT = \frac{1}{\beta_3}$

where $\beta_3$ is the estimated slope from the regression of left-diagonal, right-diagonal, horizontal, and vertical patch edge pixels, $\ln[n_\tau[E_{left}, E_{right}, E_{hor}, E_{vert}]]$, on the natural logarithm of the total number of pixels in LCLU patch $\tau$, $\ln[n_\tau]$, for all nearest-neighbor patches greater than 3 pixels, $n_\tau > 3$, that do not touch the border of the LCLU map.

- $OCFT$ Fractal estimator of patch topology from perimeter-area scaling, enclosing pixels basis.
    - $OCFT = \frac{1}{\beta_2}$

      where $\beta_2$ is the estimated slope from the regression of the left-diagonal, right-diagonal, horizontal, and vertical patch edge pixels complement,

      $$\ln[n_\tau - n_\tau[E_{left}, E_{right}, E_{hor}, E_{vert}]] = \ln[n_\tau^{\complement}]$$

      on the natural logarithm of the total number of pixels in LCLU patch $\tau$, $\ln[n_\tau]$, for all nearest-neighbor patches greater than 3 pixels, $n_\tau > 3$, that do not touch the border of the LCLU maps.

10. Patch area-bounding circle scaling

- $ABFT$ (Fractal estimator of patch topology from area-bounding rectangular kernel scaling)
    - $ABFT = \beta_4$

      where $\beta_4$ is the estimated slope from the regression of the natural logarithm of the total number of pixels in the LCLU patch $\tau$, $\ln(n_\tau)$, on the natural logarithm of the largest rectangular kernel side length difference $Y_\tau$ from a box bounding a patch $\tau$ is:

      $$Y_\tau = \ln\left[\mathrm{MAX}\left(L_{hor,\tau}, L_{vert,\tau}\right)\right]$$

      Here, $L_{hor,\tau} \times L_{vert,\tau}$ is the rectangular kernel size that fits over patch $\tau$. This is for all nearest-neighbor patches greater than 3 pixels, $n_\tau > 3$, that do not touch the border of the LCLU maps.

- $BCFT$ (Fractal estimator of patch topology from area-bounding circular kernel scaling)
    - $BCFT = \beta_5$

      where $\beta_5$ is the estimated slope from the regression of the natural logarithm of the total number of pixels in the LCLU patch $\tau$, $\ln(n_\tau)$, on the natural logarithm of an area-bounding circular kernel radius $L_{hor}$ that would cover patch $\tau$, $\ln\left[\frac{L_{hor,\tau}}{2}\right]$, for all nearest-neighbor patches greater than 3 pixels, $n_\tau > 3$, that do not touch the border of the LCLU maps.

11. Patch perimeter complexity from the scaling of Euclidean distance to actual distance along large patch perimeters

- $BETL$ (Fractal estimator of perimeter complexity from scaling the average patch edge to variable square kernel size [Weins and Milne, 1989])
    - $BETL = \frac{1}{\hat{\psi}} \sum_{\hat{\tau}=1}^{\hat{\psi}} \frac{1}{\beta_{6\hat{\tau}}}$

      where $\beta_{6\hat{\tau}}$ is the estimated box-counting fractal dimension of the $\hat{\tau}^{th}$ patch—only for patches with area $n_\tau > 400$—using the average Euclidean distance $\bar{r}_{\hat{\tau}}$ from patch $\hat{\tau}$ centroid $(\bar{x}_{\hat{\tau}}, \bar{y}_{\hat{\tau}})$ to a $L \times L$ patch bounding-box, or patch perimeter (whichever comes first) regression, $\ln[\bar{r}_{\hat{\tau}}]$ on the natural logarithm of bounding-box perimeter,

$perimeter = 4 \cdot L$, or patch $\hat{\tau}$, $perimeter = n_{\hat{\tau}}[E_{left}, E_{right}, E_{hor}, E_{vert}]$, perimeter $\ln[perimeter]$.

Ritters describes the procedures as follows. For each patch meeting the minimum 400 pixel area ($n_{\hat{\tau}} > 400$) constraint, the average Euclidean distance $\bar{r}_{\tau}$ along the perimeter is found for actual distances $L = 4, 8, 16, 32, 64, 128$, and 512 bounding-box pixels. The proportions of patch perimeters that touched the map border are excluded.

The expression for average patch centroid Euclidean distance is:

$$\bar{r}_{\hat{\tau}} = \tfrac{1}{n_{\hat{\tau}}} \sum_{\hat{\tau}=1}^{\hat{\psi}} r_{\hat{\tau}}$$

where the patch $\hat{\tau}$ distances $r_{\hat{\tau}}$ are for all $\hat{\tau} = 1, 2, 3 \ldots \hat{\psi}$ pixels, and are normalized by the $\hat{\tau}$ patch area $n_{\hat{\tau}}$.

Within patch distances are expressed as:

$$r_{\hat{\tau}} = \sqrt{\sum_u \sum_v (x_u - \bar{x}_{\hat{\tau}})^2 + (y_v - \bar{y}_{\hat{\tau}})^2}$$

for every pixel $u = v = 1, 2, 3, 4 \ldots n_{\hat{\tau}}$ within patch $\hat{\tau}$, for the total number of nearest-neighbor patches $\hat{\psi}$ patches.

12. Metric of large-patch 'mass' from the scaling of patch density with neighborhood size

- $PD$ (Patch density. The number of patches (units: $km^{-2}$) [McGarigal and Marks, 1994])
  - $PD = \frac{\psi}{N_s(km^2)}$

    where $\psi$ is the total number of nearest-neighbor patches, and $N_s$ is the total number of pixels in a square landscape (units: $km^2$).

- $PENT$ (Fractal estimator of patch configurational entropy from the scaling of patch density to the size of a neighborhood of an arbitrary pixel in the patch [Voss, 1988])
  - $P_t[L; n_{\tau}^*]$ is the probability of finding $t$ other pixels of the same LCLU class, in an $L \times L$ kernel, centered on an arbitrarily chosen pixel. For example, $P_2[L = 5; n_{\tau}^*]$ is the probability of finding two more pixels of a patch in a $5 \times 5$ square centered on an arbitrary pixel in the patch. In general,

    $$P_t[L; n_{\tau}^*] = \frac{s_{t,L}}{n_{\tau}^*}$$

    where $s_{t,L}$ is the number of $L \times L$ kernels that had $t$ pixels of the same LCLU class, and $n_j$ is the number of pixels in LCLU class $j$.

    Letting $n_j[L]$ be the maximum number of pixels of the same LCLU class $j$, observed in any $L \times L$ kernel:

    $$M^0[P_t[L; n_{\tau}^*]] = \sum_{t=1}^{n_j[L]} \ln[t] \cdot P_t[L; n_{\tau}^*]$$

    From each patch with size > 400 pixels, a random sample of at least 400 pixels was selected.

    $$n_{\tau}^* = \begin{cases} 0 \text{ if } n_{\tau} < 401, \\ n_{\tau} \text{ otherwise.} \end{cases}$$

Square kernels of size $L = 5$, 15, 25, 35, and 45 are placed around each sampled pixel, and the occurrences of pixels of the same patch were counted for each kernel size. The values of $P_t[L; n_\tau^*]$ and $M^0[P_t[L; n_\tau^*]]$ were calculated after the counts are accumulated for all sampled pixels. Letting $\beta_{7\hat{\tau}}$ be the estimated slope from the regression of $M^0[P_t[L; n_\tau^*]]$ on $\ln[L]$ for the $\hat{\tau}^{th}$ patch. The fractal estimator is:

$$PENT = \frac{1}{\hat{\psi}} \sum_{\hat{\tau}=1}^{\hat{\psi}} \beta_{7\hat{\tau}}$$

where, $\hat{\psi}$ is the total number of nearest-neighbor patches.

- $PMAS$ (Fractal estimator of patch mass from the scaling of patch density to the size of a neighborhood of an arbitrary cell in the patch [**?**])

  - $P_t[L; n_\tau^*]$ is the probability of finding $t$ other pixels of the same LCLU class, in an $L \times L$ kernel, centered on an arbitrarily chosen pixel. For example, $P_2[L = 5; n_\tau^*]$ is the probability of finding two more pixels of a patch in a $5 \times 5$ square centered on an arbitrary pixel in the patch. In general,

    $$P_t[L; n_\tau^*] = \frac{s_{t,L}}{n_\tau^*}$$

    where $s_{t,L}$ is the number of $L \times L$ kernels that had $t$ pixels of the same LCLU class, and $n_j$ is the number of pixels in LCLU class $j$.

    Letting $n_j[L]$ be the maximum number of pixels of the same LCLU class $j$, observed in any $L \times L$ kernel:

    $$M^1[P_t[L; n_\tau^*]] = \sum_{t=1}^{n_j[L]} t \cdot P_t[L; n_\tau^*]$$

    From each patch with size $> 400$ pixels, a random sample of at least 400 pixels was selected.

    $$n_\tau^* = \left\{ \begin{array}{l} 0 \text{ if } n_\tau < 401, \\ n_\tau \text{ otherwise.} \end{array} \right.$$

    Square kernels of size $L = 5$, 15, 25, 35, and 45 are placed around each sampled pixel, and the occurrences of pixels of the same patch were counted for each kernel size. The values of $P_t[L; n_\tau^*]$ and $M^1[P_t[L; n_\tau^*]]$ were calculated after the counts are accumulated for all sampled pixels. Letting $\beta_{8\hat{\tau}}$ be the estimated slope from the regression of $M^1[P_t[L; n_\tau^*]]$ on $\ln[L]$ for the $\hat{\tau}^{th}$ patch. The fractal estimator is:

    $$PMAS = \frac{1}{\hat{\psi}} \sum_{\hat{\tau}=1}^{\hat{\psi}} \beta_{8\hat{\tau}}$$

    where, $\hat{\psi}$ is the total number of nearest-neighbor patches.

- $PVAR$ (Fractal estimator of patch variance from the scaling of patch density to the size of a neighborhood of an arbitrary pixel in the patch [**?**])

  - $P_t[L; n_\tau^*]$ is the probability of finding $t$ other pixels of the same LCLU class, in an $L \times L$ kernel, centered on an arbitrarily chosen pixel. For example, $P_2[L = 5; n_\tau^*]$ is the probability of finding two more pixels of a patch in a $5 \times 5$ square centered on an arbitrary pixel in the patch. In general,

    $$P_t[L; n_\tau^*] = \frac{s_{t,L}}{n_\tau^*}$$

    where $s_{t,L}$ is the number of $L \times L$ kernels that had $t$ pixels of the same LCLU class, and $n_j$ is the number of pixels in LCLU class $j$.

Letting $n_j[L]$ be the maximum number of pixels of the same LCLU class $j$, observed in any $L \times L$ kernel:

$$M^2[P_t[L; n_\tau^*]] = \sum_{t=1}^{n_j[L]} t^2 \cdot P_t[L; n_\tau^*]$$

From each patch with size $> 400$ pixels, a random sample of at least $400$ pixels was selected.

$$n_\tau^* = \begin{cases} 0 \text{ if } n_\tau < 401, \\ n_\tau \text{ otherwise.} \end{cases}$$

Square kernels of size $L = 5,15, 25, 35,$ and $45$ are placed around each sampled pixel, and the occurrences of pixels of the same patch were counted for each kernel size. The values of $P_t[L; n_\tau^*]$ and $M^2[P_t[L; n_\tau^*]]$ were calculated after the counts are accumulated for all sampled pixels. Letting $\beta_{9\hat{\tau}}$ be the estimated slope from the regression of $M^2[P_t[L; n_\tau^*]]$ on $\ln[L]$ for the $\hat{\tau}^{th}$ patch. The fractal estimator is:

$$PENT = \frac{1}{\hat{\psi}} \sum_{\hat{\tau}=1}^{\hat{\psi}} \beta_{9\hat{\tau}}$$

where, $\hat{\psi}$ is the total number of nearest-neighbor patches.

13. Average large-patch lancunarity from the scaling from the scaling of patch density with neighborhood size

- $PLAC$ (Average large-patch lancunarity)
  - $PLAC = PVAR - PENT$

    See *Metric of large-patch 'mass' from the scaling of patch density with neighborhood size.*

14. Number of patches

- $NPAT$ (Number of patches [McGarigal and Marks, 1994])
  - $NPAT = \psi$

    where $\psi$ is the number of nearest-neighbor patches in the LCLU map.

15. Largest patch index

- $LPI$ (The ratio of area of the largest patch to the total area of the landscape (unit: %) [McGarigal and Marks, 1994])
  - $LPI = \frac{\text{MAX}[n_\tau]}{N}$

    where $N$ is the total number of pixels in the landscape, and $n_\tau$ is the total number of pixels in nearest-neighbor patch $\tau$.

16. Average patch size or area

- $PSIZ$ (Average patch size or area [McGarigal and Marks, 1994])
  - $PSIZ = \frac{1}{\psi} \sum_{\tau=1}^{\psi} n_\tau$

    where $\psi$ is the total number of nearest-neighbor patches, and $n_\tau$ is the total area of patch $\tau$.

17. Patch size standard deviation

   - $PSSD$ (The standard deviation of patch size in the entire landscape (unit: ha) [McGarigal and Marks, 1994])

     - $PSSD = \frac{1}{\psi-1} \sum_{\tau=1}^{\psi} (n_\tau - PSIZ)$

       where $\psi$ is the total number of nearest-neighbor patches, $n_\tau$ is the total area of patch $\tau$, and $PSIZ$ is the average patch size or area.

18. Patch size coefficient of variation

   - $PSCV$ (The standard deviation of patch size divided by mean patch size for the entire landscape (unit:%))

     - $PSCV = \frac{PSSD}{PSIZ}$

       See *Average patch size or area* for $PSIZ$ and *Patch size standard deviation* for $PSSD$.

19. Total edge

   - $TE$ (The sum of the lengths of all edge segments (unit: m) [McGarigal and Marks, 1994])

     - $TE = E_{left} + E_{right} + E_{hor} + E_{vert}$

       Here, the left-diagonal, right-diagonal, horizontal, and vertical LCLU map edge pixels are $E_{left}$, $E_{right}$, $E_{hor}$, and $E_{vert}$ respectively.

20. Average patch radius of gyration

   - $OEDG$ (Average number of edges enclosing a patch—'outside edges')

     - $OEDG = \frac{1}{\psi} \sum_{\tau=1}^{\psi} n_\tau [E_{left}, E_{right}]$

       where $\psi$ is the total number of nearest-neighbor patches, and $n_\tau [E_{left}, E_{right}]$ are left-diagonal and right-diagonal patch $\tau$ edge pixels.

   - $TEDG$ (Average total number of perimeter edges, or 'perimeter length', per patch)

     - $TEDG = IEDG + OEDG$

       See *Average number of inside edges per patch* for $IEDG$ and *Average patch radius of gyration* for $OEDG$.

   - $OPER$ (Average number of pixels enclosing a patch—'outside pixels')

     - $OPER = \frac{1}{\psi} \sum_{\tau=1}^{\psi} n_\tau^{\complement}$

       where $\psi$ is the total number of nearest neighbor patches, and all patch $\tau$ nearest-neighbor pixels that are not left-diagonal, right- diagonal, horizontal, or vertical edge pixels are $n_\tau^{\complement} = (n_\tau - n_\tau[E_{left}, E_{right}, E_{hor}, E_{vert}])$.

   - $RGYR$ (Average radius of gyration [Pickover, 1990])

- $RGYR = \frac{1}{\psi} \sum_{\tau=1}^{\psi} r_\tau$

  The patch centroid $(\bar{x}_\tau, \bar{y}_\tau)$ is used to find the radius of gyration $r_\tau$ of patch $\tau$:
  $$r_\tau = \sqrt{\sum_u \sum_v (x_u - \bar{x}_\tau)^2 + (y_v - \bar{y}_\tau)^2}$$
  for every pixel $u + v = 2, 3, 4 \ldots n_\tau$ within nearest-neighbor patch $\tau$, for the total number of nearest-neighbor patches $\psi$.

- *LOAX* (Average length of long axis)

  - $LOAX = \frac{1}{\psi} \sum_{\tau=1}^{\psi} L_{hor,\tau}$

    where $\psi$ is the total number of nearest-neighbor patches, and $L_{hor,\tau}$ is the longest horizontal diameter of patch $\tau$.

21. Average number of inside edges per patch

   - *IEDG* (Average number of edges between a patch and its inclusions—'inside edges')

     - $IEDG = \frac{1}{\psi} \sum_{\tau=1}^{\psi} n_\tau [E_{hor}, E_{vert}]$

       where $\psi$ is the total number of nearest-neighbor patches, and $n_\tau[E_{hor}, E_{vert}]$ are horizontal and vertical patch $\tau$ edge pixels.

22. Landscape shape index

   - *LSI* (A modified perimeter-area ratio)

     - $LSI = \frac{0.25 \cdot n_\tau[TE]}{\sqrt{N}}$

       where $N$ is the total number of pixels in the landscape, and $n_\tau[TE]$ is the total number of nearest-neighbor patch edges (unitless). See *Average patch radius of gyration* for $TE$.

23. Mean patch shape index

   - *MSI* (A patch-level shape index averaged over all patches in the landscape)

     - $MSI = \frac{1}{\psi} \sum_{\tau=1}^{\psi} \frac{0.25 \cdot n_\tau[TE]}{\sqrt{n_\tau}}$

       where $\psi$ is the total number of nearest-neighbor patches, $n_\tau$ is the total area of patch $\tau$, and $n_\tau[TE]$ is the total number of patch edges (unitless). See *Average patch radius of gyration* for $TE$.

24. Area-Weighted mean patch shape index

   - *AWMSI* (Mean patch shape index weighted by relative patch size)

     - $AWMSI = \sum_{\tau=1}^{\psi} \frac{0.25 \cdot n_\tau[TE]}{\sqrt{n_\tau}} \cdot \frac{n_\tau}{N}$

       where $N$ is the total number of pixels in the landscape, $\psi$ is the total number of nearest-neighbor patches, $n_\tau$ is the total area of patch $\tau$, and $n_\tau[TE]$ is the total number of patch edges (unitless). See *Average patch radius of gyration* for $TE$.

25. Double-Log fractal dimension

- $DLFD$ (The fractal dimension of the entire landscape)
  - Twice the inverse regression line slope between the logarithm of patch area and the logarithm of patch perimeter:
  $$DLFD = 2 \cdot \left( \frac{\psi \cdot \sum_{\tau=1}^{\psi} \ln[n_\tau[TE]] \ln[n_\tau] - \sum_{\tau=1}^{\psi} \ln[n_\tau]}{\psi \cdot \sum_{\tau=1}^{\psi} \ln[n_\tau[TE]^2] - \left( \sum_{\tau=1}^{\psi} \ln[n_\tau[TE]^2] \right)} \right)^{-1}$$
  where $\psi$ is the total number of nearest-neighbor patches, $n_\tau$ is the total area of patch $\tau$, and $n_\tau[TE]$ is the total number of patch edges (unitless). See *Average patch radius of gyration* for $TE$.

26. Mean patch fractal dimension

- $MPFD$ (The average fractal dimension of individual patches in the landscape)
  - The summation of fractal dimension for all patches divided by the total number of patches in the landscape:
  $$MPFD = \frac{1}{\psi} \sum_{\tau=1}^{\psi} \frac{2 \cdot \ln[0.25 \cdot n_\tau[TE]]}{\ln[n_\tau]}$$
  where $\psi$ is the total number of nearest-neighbor patches, $n_\tau$ is the total area of patch $\tau$, and $n_\tau[TE]$ is the total number of patch edges (unitless). See *Average patch radius of gyration* for $TE$.

27. Area-weighted mean patch fractal dimension

- $AWMPFD$ (The patch fractal dimension weighted by relative patch area)
  - $AWMPFD = \sum_{\tau=1}^{\psi} \frac{2 \cdot \ln[0.25 \cdot n_\tau[TE]]}{\ln[n_\tau]} \cdot \frac{n_\tau}{N}$

  where $N$ is the total number of pixels in the landscape, $\psi$ is the total number of nearest-neighbor patches, $n_\tau$ is the total area of patch $\tau$, and $n_\tau[TE]$ is the total number of patch edges (unitless). See *Average patch radius of gyration* for $TE$.

28. Square pixel index

- $SqP$ (A normalized perimeter-area ratio [Frohn, 1998])
  - $SqP = 1 - \frac{4\sqrt{N}}{(TE)}$
  where $N$ is the total number of pixels in the landscape, and $TE$ are all left-diagonal, right-diagonal, horizontal, and vertical edge pixels in the landscape (unitless). See *Average patch radius of gyration* for $TE$.

29. Average patch perimeter-area ratio

- $PA - 1$ (Average nearest-neighbor perimeter-area ratio)
  - $PA - 1 = \frac{1}{\psi} \sum_{\tau=1}^{\psi} \frac{n_\tau[E_{left}, E_{right}]}{n_\tau}$
  where $\psi$ is the total number of nearest-neighbor patches, $n_\tau$ is the total area of patch $\tau$, and $n_\tau[E_{left}, E_{right}]$ are left-diagonal and right-diagonal patch $\tau$ edge pixels.

30. Average patch adjusted perimeter-area ratio

- $PA - 2$ (Average adjusted perimeter-area ratio [Baker and Cai, 1992])

- $PA - 2 = \frac{1}{\psi} \sum_{\tau=1}^{\psi} \frac{0.282 \cdot n_\tau [E_{left}, E_{right}]}{\sqrt{n_\tau}}$

  where $\psi$ is the total number of nearest-neighbor patches, $n_\tau$ is the total area of patch $\tau$, and $n_\tau [E_{left}, E_{right}]$ are left-diagonal and right-diagonal patch $\tau$ edge pixels.

31. Average patch normalized area, square model

  - *NACI* (Average normalized area, circular model)
    - $NACI = \frac{1}{\psi} \sum_{\tau=1}^{\psi} \frac{4\pi \cdot n_\tau}{n_\tau [E_{left}, E_{right}]^2}$

      where $\psi$ is the total number of nearest-neighbor patches, $n_\tau$ is the total area of patch $\tau$, and $n_\tau [E_{left}, E_{right}]$ are left-diagonal and right-diagonal patch $\tau$ edge pixels.

  - *NASQ* (Average normalized area, square model)
    - $NASQ = \frac{1}{\psi} \sum_{\tau=1}^{\psi} \frac{16 \cdot n_\tau}{n_\tau [E_{left}, E_{right}]^2}$

      where $\psi$ is the total number of nearest-neighbor patches, $n_\tau$ is the total area of patch $\tau$, and $n_\tau [E_{left}, E_{right}]$ are left-diagonal and right-diagonal patch $\tau$ edge pixels.

  - *BRRA* (Average bounding rectangle ratio)
    - $BRRA = \frac{1}{\psi} \sum_{\tau=1}^{\psi} \frac{n_\tau}{\chi_\tau}$

      where

      $$\chi_\tau = L_{hor,\tau} \times L_{vert,\tau}$$

      Here, $\psi$ is the total number of nearest-neighbor patches, $n_\tau$ is the total area of patch $\tau$, $L_{hor,\tau}$ and $L_{vert,\tau}$ are respectively the rectangular kernel horizontal and vertical sides that fit over patch $\tau$.

32. Average patch topology ratio

  - *NFTD* (Average topology ratio)
    - $NFTD = \frac{1}{\psi} \sum_{\tau=1}^{\psi} 2 - \frac{\left(n_\tau^C - 4\sqrt{n_\tau}\right)}{(2 \cdot n_\tau + 2 - 4\sqrt{n_\tau})}$

      where $\psi$ is the total number of nearest-neighbor patches, and $n_\tau$ is the total area of patch $\tau$

33. Average patch ratio of number of inside edges of area

  - *PORO* (Average ratio of number of inside edges to area)
    - $PORO = \frac{1}{\psi} \sum_{\tau=1}^{\psi} \frac{n_\tau [E_{hor}, E_{vert}]}{n_\tau}$

      where $\psi$ is the total number of nearest-neighbor patches, $n_\tau$ is the total area of patch $\tau$, and $n_\tau [E_{hor}, E_{vert}]$ are horizontal and vertical patch $\tau$ edge pixels.

34. Average patch adjusted perimeter-area ratio

  - *DSTA* (Average adjusted area-perimeter ratio—Gardner's D-statistic)
    - $DSTA = \frac{1}{\psi} \sum_{\tau=1}^{\psi} \frac{4 \cdot n_\tau}{\ln[n_\tau [E_{left}, E_{right}]]}$

      where $\psi$ is the total number of nearest-neighbor patches, $n_\tau$ is the total area of patch $\tau$, and $n_\tau [E_{left}, E_{right}]$ are left-diagonal and right-diagonal patch $\tau$ edge pixels.

- *ABRA* (Average ratio of area to largest bounding rectangle dimension)
  - $ABRA = \frac{1}{\psi} \sum_{\tau=1}^{\psi} \frac{\ln(n_\tau)}{Y_\tau}$

    Here, $\psi$ is the total number of nearest-neighbor patches, $n_\tau$ is the total area of patch $\tau$, and the largest and smallest rectangular kernel side length differences $Y_\tau$ that would cover a patch $\tau$ is:

    $$Y_\tau = \ln\left[\text{MAX}\left(L_{hor,\tau}, L_{vert,\tau}\right)\right].$$

35. Average ratio of patch area to area of the circumscribing circle

- *CCRA* (Average ratio of area to the area of a circumscribing circle [Baker and Cai, 1992]
  - $CCRA = \frac{1}{\psi} \sum_{\tau=1}^{\psi} \frac{n_\tau}{\pi\left(\frac{L_{hor,\tau}}{2}\right)^2}$

    where $\psi$ is the total number of nearest-neighbor patches, $n_\tau$ is the total area of patch $\tau$, and $L_{hor,\tau}$ is the longest horizontal diameter of patch $\tau$.

36. Average ratio of patch radius of gyration to long axis length

- *RGLA* (Average ratio of nearest-neighbor patch radius of gyration to long axis length)
  - $RGLA = \frac{1}{\psi} \sum_{\tau=1}^{\psi} \frac{r_\tau}{L_{hor,\tau}}$

    where $\psi$ is the total number of nearest-neighbor patches, and $L_{hor,\tau}$ is the longest horizontal diameter of patch $\tau$.

    The patch centroid $(\bar{x}_\tau, \bar{y}_\tau)$ is used to find the radius of gyration $r_\tau$ of patch $\tau$:
    $$r_\tau = \sqrt{\sum_u \sum_v (x_u - \bar{x}_\tau)^2 + (y_v - \bar{y}_\tau)^2}$$
    for every pixel $u + v = 2, 3, 4 \ldots n_\tau$ within nearest-neighbor patch $\tau$.

- *LARA* (Average ratio of area to long axis length)
  - $LARA = \frac{1}{\psi} \sum_{\tau=1}^{\psi} \frac{n_\tau}{\ln[L_{hor,\tau}]}$

    where $\psi$ is the total number of nearest-neighbor patches, $n_\tau$ is the total area of patch $\tau$, and $L_{hor,\tau}$ is the longest horizontal diameter of patch $\tau$.

37. Average patch ratio of perimeter pixels to perimeter edges

- *OPOE* (Average ratio of perimeter pixels to perimeter edges)
  - $OPOE = \frac{1}{\psi} \sum_{\tau=1}^{\psi} \frac{n_\tau^{\complement}}{n_\tau[E_{left}, E_{right}]}$

    where $\psi$ is the total number of nearest neighbor patches, $n_\tau[E_{left}, E_{right}]$ are left-diagonal and right-diagonal patch $\tau$ edge pixels, and all patch $\tau$ nearest-neighbor pixels that are not left-diagonal, right-diagonal, horizontal, or vertical edge pixels are $n_\tau^{\complement} = (n_\tau - n_\tau[E_{left}, E_{right}, E_{hor}, E_{vert}])$.

# Appendix B

# Anderson Level II Attribute Class Description

Table B.1: Descriptions of LUDA LCLU attribute class codes [Anderson et al., 1976].

| LUDA class code | Anderson Level II attribute class description |
| --- | --- |
| 11 | Residential |
| 12 | Commercial, service, institutional |
| 13 | Industrial |
| 14 | Transportation |
| 15 | Industrial and commercial complex |
| 16 | Mixed urban and built-up |
| 17 | Other urban or built-up |
| 21 | Cropland and pasture |
| 22 | Orchards, vineyards, and nurseries |
| 23 | Confined feeding operations |
| 24 | Other agricultural lands |
| 31 | Herbaceous rangeland |
| 32 | Shrub-brush rangeland |
| 33 | Mixed rangeland types |
| 41 | Deciduous forest |
| 42 | Evergreen forest |
| 43 | Mixed forest types |
| 51 | Streams and canals |
| 52 | Natural lakes |
| 53 | Reservoirs |
| 54 | Bays and estuaries |
| 61 | Forested wetlands |
| 62 | Non-forested wetlands |
| 71 | Dry salt flats |
| 72 | Beach |
| 73 | Non-beach sandy area |
| 74 | Bare exposed rock |
| 75 | Strip mine, quarry, and borrow areas |
| 76 | Transitional (disturbed, little cover, not agricultural) |
| 77 | Mixed barren lands |
| 81 | Shrub-brush tundra |
| 82 | Herbaceous tundra |
| 83 | Bare ground tundra |
| 84 | Wet tundra |
| 85 | Mixed tundra |
| 91 | Perennial snowfield |
| 92 | Glacier |

# Appendix C

# Ecoregions of the United States
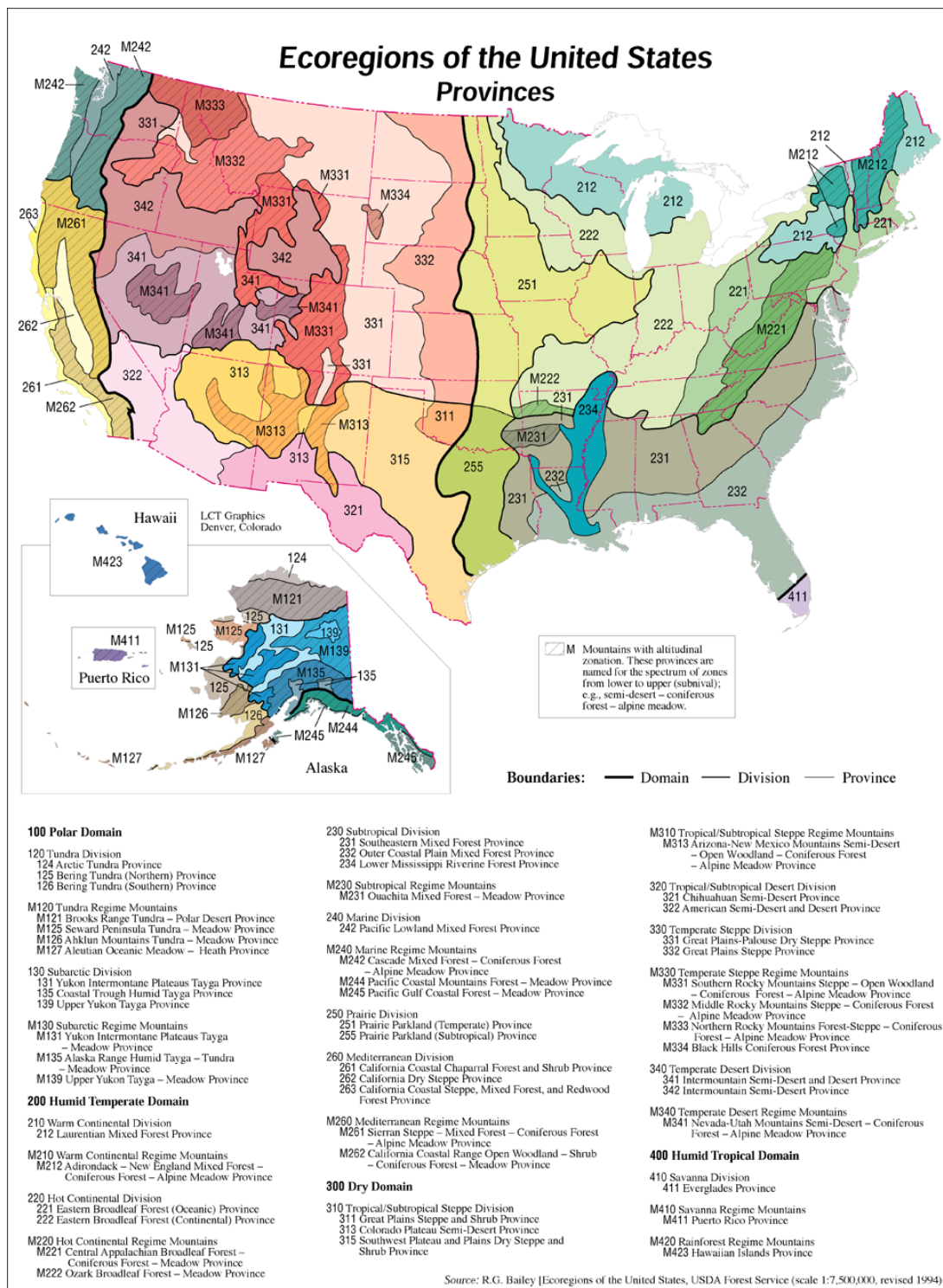
Figure C.1: This data set shows ecoregions, which are ecosystems of regional extent, in the United States, Puerto Rico, and the U.S. Virgin Islands.

# Appendix D

# LPM Correlation matrix when observing seamless conterminous United States NLCD 1992 LCLU

| | LsFT | NYTP | SIDI | SIEV | SHDI | SHEV | MCDI | MCEV |
|------|------|------|------|------|------|------|------|------|
| LsFT | 1 | | | | | | | |
| NYTP | -0.8428121 | 1 | | | | | | |
| SIDI | -0.8600067 | 0.87435162 | 1 | | | | | |
| SIEV | -0.8797156 | 0.8219824 | 0.98483284 | 1 | | | | |
| SHDI | -0.851098 | 0.90867904 | 0.99100983 | 0.96215139 | 1 | | | |
| SHEV | -0.8966064 | 0.78132103 | 0.95257355 | 0.98852186 | 0.92853981 | 1 | | |
| MCDI | -0.8377683 | 0.86338947 | 0.9977126 | 0.97893521 | 0.99147354 | 0.94377119 | 1 | |
| MCEV | -0.8624947 | 0.77587154 | 0.96765729 | 0.99564963 | 0.93921271 | 0.99215771 | 0.96374237 | 1 |
| SHHO | -0.7688752 | 0.92486297 | 0.90911923 | 0.85479251 | 0.94838965 | 0.81792125 | 0.91122732 | 0.8190189 |
| SIHO | 0.49316072 | -0.5491835 | -0.6477521 | -0.6198931 | -0.6389257 | -0.5890818 | -0.6440988 | -0.5997161 |
| n_Q | 0.9059623 | -0.9280297 | -0.8767352 | -0.8482787 | -0.8836719 | -0.8245683 | -0.856319 | -0.8098461 |
| KT_Q | 0.96140244 | -0.8984472 | -0.8733111 | -0.8625009 | -0.8744894 | -0.8576869 | -0.8509312 | -0.8303453 |
| FMP | 0.90237923 | -0.9481348 | -0.8715212 | -0.8416413 | -0.884584 | -0.8182703 | -0.8509074 | -0.8015917 |
| SHCO | 0.92627295 | -0.9313371 | -0.8807865 | -0.8564996 | -0.8876567 | -0.8377332 | -0.8596579 | -0.8190938 |
| SICO | 0.81961716 | -0.8279009 | -0.9895995 | -0.9780111 | -0.9740328 | -0.9420078 | -0.9939524 | -0.96907 |
| SUMD | -0.8150182 | 0.53604597 | 0.500377 | 0.55566702 | 0.45736633 | 0.59168743 | 0.46060641 | 0.54696489 |
| TENT | -0.7682429 | 0.56893317 | 0.50108759 | 0.54381687 | 0.49731089 | 0.58643058 | 0.47558985 | 0.53697522 |
| TMAS | -0.6967675 | 0.81157677 | 0.86124763 | 0.81559627 | 0.87794957 | 0.7788533 | 0.86011851 | 0.78433383 |
| TVAR | -0.7283402 | 0.87696381 | 0.90750749 | 0.85497756 | 0.93963707 | 0.81459815 | 0.91379806 | 0.82427999 |
| POS0 | -0.7278514 | 0.8738895 | 0.9085202 | 0.85638967 | 0.93969905 | 0.81612993 | 0.91475154 | 0.82596628 |
| POS0 | -0.7268741 | 0.86937452 | 0.90926254 | 0.85769612 | 0.93913856 | 0.81760774 | 0.91537125 | 0.82762091 |
| P500 | -0.7676244 | -0.7676244 | -0.7167248 | -0.7167248 | -0.7720266 | -0.6923181 | -0.7416385 | -0.6791903 |
| TLAC | 0.65911866 | -0.7552589 | -0.7613855 | -0.7613855 | -0.8240524 | -0.7288277 | -0.7976931 | -0.7253266 |
| POO5 | 0.67921754 | -0.8022108 | -0.8055228 | -0.8055228 | -0.7613855 | -0.7288277 | -0.7416385 | -0.7253266 |
| OEFC | -0.7268482 | 0.86928105 | 0.90926864 | 0.85771327 | 0.9391201 | 0.81762856 | 0.91537532 | 0.82764515 |
| OIFC | 0.64437626 | -0.7536229 | -0.7287634 | -0.6918689 | -0.7448217 | -0.6690164 | -0.7130998 | -0.6535837 |
| OCFC | -0.8452132 | 0.89152727 | 0.85501042 | 0.81557932 | 0.86715168 | 0.78890737 | 0.83622251 | 0.77282986 |
| OEFT | -0.8477123 | 0.89854984 | 0.85923747 | 0.8169581 | 0.87114804 | 0.78619673 | 0.84118415 | 0.77359299 |
| OIFT | -0.9388563 | 0.78294704 | 0.76372996 | 0.76737544 | 0.75753841 | 0.78079715 | 0.73725698 | 0.73884231 |
| OCFT | -0.7353814 | 0.70797613 | 0.62931091 | 0.60217646 | 0.63661909 | 0.58491827 | 0.61281918 | 0.56992994 |
| ABFT | -0.8576225 | 0.84615778 | 0.76863964 | 0.73461523 | 0.77689959 | 0.71100139 | 0.74925343 | 0.69533546 |
| FMF | -0.9081273 | 0.93655744 | 0.89949646 | 0.86407032 | 0.91439184 | 0.8413417 | 0.88336294 | 0.82396831 |
| PSI | -0.9378831 | 0.86749294 | 0.83864667 | 0.82090657 | 0.84300392 | 0.81587007 | 0.81676863 | 0.78470418 |
| BETL | -0.8302011 | 0.8469063 | 0.78739617 | 0.75109883 | 0.79960593 | 0.72712462 | 0.76923243 | 0.71138291 |
| PD | 0.84467852 | -0.9101152 | -0.844897 | -0.7984072 | -0.8574371 | -0.7630902 | -0.8261791 | -0.7529545 |

| | | | | | | | | |
|---|---|---|---|---|---|---|---|---|
| PENT | -0.6740589 | 0.81881133 | 0.84278345 | 0.79305753 | 0.8703518 | 0.7570546 | 0.84461989 | 0.76129818 |
| PMAS | -0.6740589 | 0.81881133 | 0.84278345 | 0.79305753 | 0.8703518 | 0.7570546 | 0.84461989 | 0.76129818 |
| PVAR | -0.9538334 | 0.91066189 | 0.89457067 | 0.89491502 | 0.87577427 | 0.87322689 | 0.85281301 | |
| PLAC | -0.9544417 | 0.91016531 | 0.88389726 | 0.89470983 | 0.87606664 | 0.87309166 | 0.85300494 | |
| NPAT | -0.9552316 | 0.90947581 | 0.89429597 | 0.88404011 | 0.87647288 | 0.87291378 | 0.85327694 | |
| LPI | -0.9552459 | 0.90946282 | 0.89429263 | 0.8844279 | 0.87647986 | 0.87291005 | 0.85328144 | |
| PSIZ | -0.6740589 | 0.81881133 | 0.84278345 | 0.79305753 | 0.8703518 | 0.7570546 | 0.84461989 | 0.76129818 |
| PSSD | 0.78634304 | -0.8218208 | -0.967228 | -0.9477993 | -0.9546504 | -0.9067598 | -0.9725586 | -0.935907 |
| PSCV | 0.93888767 | -0.9113753 | -0.8807648 | -0.8628597 | -0.8836933 | -0.8506704 | -0.8590509 | -0.8281756 |
| TE | 0.39352728 | 0.00541912 | -0.1624211 | -0.303433 | -0.1135009 | -0.4110459 | -0.1481329 | -0.3582053 |
| OEDG | 0.40091049 | 0.00142984 | -0.1662448 | -0.3074815 | -0.1169073 | -0.4151883 | -0.1516859 | -0.3621616 |
| OPER | -0.6945551 | 0.81088652 | 0.86166327 | 0.81564333 | 0.878272 | 0.86086788 | 0.78448892 | |
| RGYR | -0.5023366 | 0.14241519 | 0.3335869 | 0.4827286 | 0.27375508 | 0.31597662 | 0.5401244 | |
| LOAX | 0.94048703 | -0.9107009 | -0.8813837 | -0.86449 | -0.8839215 | -0.8529784 | -0.8595924 | -0.8302416 |
| IEDG | 0.97166334 | -0.8848532 | -0.8799628 | -0.8835439 | -0.8754336 | -0.8566928 | -0.8566928 | -0.8579708 |
| TEDG | <u>0.97166334</u> | -0.8848532 | -0.8799628 | -0.8835439 | -0.8876851 | -0.8566928 | -0.8566928 | -0.8579708 |
| LSI | -0.4598921 | 0.10629407 | 0.29722456 | 0.44874044 | 0.23825958 | 0.55067744 | 0.28031149 | 0.50762336 |
| MSI | -0.4742161 | 0.11737961 | 0.3091211 | 0.46052243 | 0.24967152 | 0.56192815 | 0.29193649 | 0.51919404 |
| AWMSI | -0.6896879 | 0.81037259 | 0.85979986 | 0.8132408 | 0.87774604 | 0.85966188 | 0.78226347 | |
| DLFD | -0.9373042 | 0.91867178 | 0.89211984 | 0.87444811 | 0.89577839 | 0.87115249 | 0.84039886 | |
| MPFD | -0.6301646 | 0.66972643 | 0.68615333 | 0.66286192 | 0.68145597 | 0.6634623 | 0.62740051 | |
| AWMPFD | -0.8125001 | 0.87842478 | 0.78998453 | 0.74648286 | 0.80714912 | 0.77265964 | 0.70311065 | |
| SqP | -0.9538867 | 0.90185022 | 0.89456023 | 0.88686496 | 0.89356644 | 0.881582 | 0.85744999 | |
| PA_1 | -0.9313718 | 0.89984365 | 0.91121375 | 0.90204169 | 0.91010407 | 0.89446718 | 0.87336416 | 0.8729283 |
| PA_2 | -0.6333422 | 0.62611058 | 0.63186239 | 0.62890471 | 0.6303792 | 0.62673766 | 0.61588101 | 0.6085426 |
| NACI | -0.801401 | 0.919158 | 0.86191608 | 0.82198491 | 0.87267537 | 0.79281492 | 0.84230091 | 0.77848332 |
| NASQ | -0.9384264 | 0.91372266 | 0.8907471 | 0.87244056 | 0.89335219 | 0.85898304 | 0.86971959 | 0.83822094 |
| BRRA | -0.6571476 | 0.33137275 | 0.37343432 | 0.42941607 | 0.36005388 | 0.49384711 | 0.35609157 | 0.43511022 |
| NFTD | -0.6571473 | 0.33137235 | 0.37343394 | 0.42941572 | 0.3600535 | 0.49384679 | 0.35609119 | 0.4351099 |
| PORO | 0.97166334 | -0.8848532 | -0.8799628 | -0.8835439 | -0.8754336 | -0.8876851 | -0.8566928 | -0.8579708 |
| DSTA | -0.8645682 | 0.9193849 | 0.8681403 | 0.82446275 | 0.88043514 | 0.79154327 | 0.85110953 | 0.78116813 |
| ABRA | -0.8753658 | 0.92179148 | 0.85850509 | 0.81809969 | 0.87139517 | 0.78936347 | 0.83934704 | 0.77457565 |
| CCRA | -0.4099495 | 0.00233106 | 0.16240255 | 0.29888258 | 0.11539397 | 0.40558847 | 0.14777871 | 0.35079594 |

|  | SHHO | SIHO | n_Q | KT_Q | FMP | SHCO | SICO | SUMD |
| --- | --- | --- | --- | --- | --- | --- | --- | --- |
| LsFT | -0.7688752 | 0.49316072 | 0.9059623 | 0.96140244 | 0.90237923 | 0.92627295 | 0.81961716 | -0.8150182 |
| NYTP | 0.92486297 | -0.5491835 | -0.9280297 | -0.8984472 | -0.9481348 | -0.9313371 | -0.8279009 | 0.53604597 |
| SIDI | 0.90911923 | -0.6477521 | -0.8767352 | -0.8733111 | -0.8715212 | -0.8807865 | -0.9895995 | 0.500377 |
| SIEV | 0.85479251 | -0.6198931 | -0.8482787 | -0.8625009 | -0.8416413 | -0.8564996 | -0.9780111 | 0.55566702 |
| SHDI | 0.94838965 | -0.6389257 | -0.8836719 | -0.8744894 | -0.884584 | -0.8876567 | -0.9740328 | 0.45736633 |
| SHEV | 0.81792125 | -0.5890818 | -0.8245683 | -0.8576869 | -0.8182703 | -0.8377332 | -0.9420078 | 0.59168743 |
| MCDI | 0.91122732 | -0.6440988 | -0.856319 | -0.8509312 | -0.8509074 | -0.8596579 | -0.9939524 | 0.46060641 |
| MCEV | 0.8190189 | -0.5997161 | -0.8098461 | -0.8303453 | -0.8015917 | -0.8190938 | -0.96907 | 0.54696489 |
| SHHO | 1 | -0.6474406 | -0.8634784 | -0.8382752 | -0.8735042 | -0.8651644 | -0.8769936 | 0.31872691 |
| SIHO | -0.6474406 | 1 | 0.60593271 | 0.5925241 | 0.58967197 | 0.60286192 | -0.2437498 | -0.2437498 |
| n_Q | -0.8634784 | 0.60593271 | 1 | 0.97267858 | 0.99089821 | 0.99765471 | 0.82856263 | -0.6975965 |
| KT_Q | -0.8382752 | 0.5925241 | 0.97267858 | 1 | 0.96294633 | 0.98454696 | 0.82426951 | -0.7696003 |
| FMP | -0.8735042 | 0.58967197 | 0.99089821 | 0.96294633 | 1 | 0.99253505 | 0.82018455 | -0.6814007 |
| SHCO | -0.8651644 | 0.60286192 | 0.99765471 | 0.98454696 | 0.99253505 | 1 | 0.82018455 | -0.717932 |
| SICO | -0.8769936 | -0.2437498 | 0.82856263 | 0.82426951 | 0.82018455 | 0.82018455 | 1 | -0.4574472 |
| SUMD | 0.31872691 | -0.2437498 | -0.6975965 | -0.7696003 | -0.6814007 | -0.717932 | -0.4574472 | 1 |
| TENT | 0.42137346 | 0.14641588 | -0.6226221 | -0.693793 | -0.6247497 | -0.64645 | -0.4614795 | 0.76757129 |
| TMAS | 0.91841084 | -0.8891383 | -0.8154146 | -0.7939356 | -0.8107102 | -0.81434441 | -0.8334186 | 0.30100324 |
| TVAR | 0.98163639 | -0.698521 | -0.8198595 | -0.796419 | -0.8257168 | -0.8207429 | -0.8848481 | 0.26264777 |
| P050 | 0.9801308 | -0.7100765 | -0.8200375 | -0.7968829 | -0.8252841 | -0.820857 | -0.8860532 | 0.26355321 |
| P500 | 0.97750697 | -0.724516 | -0.8198919 | -0.7971309 | -0.824306 | -0.8206224 | -0.8870071 | 0.26481392 |
| TLAC | -0.8492389 | 0.87474742 | 0.79609609 | 0.77574538 | 0.79250111 | 0.79544696 | 0.70713027 | -0.3314766 |
| P005 | -0.8856645 | 0.86461303 | 0.80429008 | 0.78203161 | 0.802609 | 0.80363363 | 0.76605532 | -0.3140973 |
| OEFC | 0.9744907 | -0.7247844 | -0.8198808 | -0.7971274 | -0.8242794 | -0.8206097 | -0.8870179 | 0.26483343 |
| OIFC | -0.829958 | 0.85103137 | 0.7894325 | 0.76792243 | 0.7862511 | 0.78852347 | 0.67816331 | -0.3397117 |
| OCFC | 0.87179216 | -0.6599805 | -0.9428092 | -0.9322221 | -0.9347671 | -0.9447632 | -0.8031753 | 0.58658441 |
| OEFT | 0.86900881 | -0.646945 | -0.9497288 | -0.933573 | -0.9416522 | -0.9502406 | -0.8094145 | 0.59304793 |
| OIFT | 0.70031469 | -0.4868156 | -0.8753358 | -0.9451066 | -0.8627372 | -0.8971602 | -0.7101782 | 0.82491869 |
| OCFT | 0.6131865 | -0.399534 | -0.7925566 | -0.790541 | -0.7883007 | -0.7966124 | -0.5925785 | 0.65810975 |
| ABFT | 0.75940432 | -0.5118615 | -0.9214445 | -0.9298377 | -0.9121691 | -0.9280173 | -0.7232857 | 0.72625518 |
| FMF | 0.90963104 | -0.6508415 | -0.9664796 | -0.9715178 | -0.9640668 | -0.9740646 | -0.8500155 | 0.63116383 |
| BETL | 0.80220481 | -0.5517844 | -0.9268626 | -0.9646351 | -0.9190396 | -0.9416337 | -0.7860441 | 0.74333121 |
| PSI | 0.78533695 | -0.550891 | -0.9093096 | -0.9009535 | -0.9058042 | -0.9126722 | -0.7394089 | 0.64753478 |
| PD | -0.855913 | 0.61108119 | 0.97289807 | 0.94634465 | 0.96402322 | 0.97061911 | 0.79537867 | -0.6311489 |

| | | | | | | | | |
|---|---|---|---|---|---|---|---|---|
| PENT | 0.93489913 | -0.8355739 | -0.7972966 | -0.7729706 | -0.7986131 | -0.7967342 | -0.8151819 | 0.25715179 |
| PMAS | 0.93489913 | -0.8355739 | -0.7972966 | -0.7729706 | -0.7986131 | -0.7967342 | -0.8151819 | 0.25715179 |
| PVAR | 0.85430621 | -0.6015083 | -0.9759467 | -0.993024 | -0.9858793 | | -0.8480911 | 0.7420728 |
| PLAC | 0.85378472 | -0.6011501 | -0.9755307 | -0.9931099 | -0.985589 | | -0.8479902 | 0.74296836 |
| NPAT | 0.85308067 | -0.6006624 | -0.974958 | -0.9931997 | -0.9851824 | | -0.8478609 | 0.74413091 |
| LPI | 0.85306729 | -0.6006532 | -0.974947 | -0.9932011 | -0.9851746 | | -0.847858 | 0.74415234 |
| PSIZ | 0.93489913 | -0.8355739 | -0.7972966 | -0.7729706 | -0.9684888 | -0.7967342 | -0.8151819 | 0.25715179 |
| PSSD | -0.8792956 | -0.7972966 | -0.7729706 | -0.7986131 | -0.9684888 | -0.7967342 | -0.8151819 | -0.41338 |
| PSCV | -0.8539003 | 0.604832 | 0.98100164 | 0.99247642 | 0.97366296 | 0.9892626 | 0.83214011 | -0.7331859 |
| TE | 0.01449955 | -0.0254491 | 0.0365945 | 0.18492378 | 0.04486663 | 0.0782685 | 0.17049891 | -0.4339698 |
| OEDG | 0.01269828 | -0.0251068 | 0.04276876 | 0.19237364 | 0.05059632 | 0.084723 | 0.1740748 | -0.4448995 |
| OPER | 0.91734865 | -0.8912824 | -0.8130013 | -0.7913309 | -0.8084682 | -0.8119025 | -0.8344416 | 0.29856705 |
| RGYR | 0.12484555 | -0.0801773 | -0.2141653 | -0.3197721 | -0.2199444 | -0.2451345 | -0.3441863 | 0.5180847 |
| LOAX | -0.8533133 | 0.60428654 | 0.98066212 | 0.99279128 | 0.97337922 | 0.98910786 | 0.83290793 | -0.7352161 |
| IEDG | -0.8271684 | 0.58331011 | 0.9592961 | 0.99278526 | 0.95326783 | 0.97357029 | 0.8338967 | -0.7790758 |
| TEDG | -0.8271684 | 0.58331011 | 0.9592961 | 0.99278526 | 0.95326783 | 0.97357029 | 0.8338967 | -0.7790758 |
| LSI | 0.09340728 | -0.0552446 | -0.1730295 | -0.2751665 | -0.1802315 | -0.2031145 | -0.3085093 | 0.47649714 |
| MSI | 0.10305912 | -0.0628262 | -0.1858554 | -0.2894135 | -0.1926649 | -0.2163183 | -0.320247 | 0.49063228 |
| AWMSI | 0.91882565 | -0.8896404 | -0.8085395 | -0.7864816 | -0.8047519 | -0.8074787 | -0.8331154 | 0.29044848 |
| DLFD | 0.86668932 | -0.6149374 | -0.9812477 | -0.9904661 | -0.9752211 | -0.9892132 | -0.844566 | 0.7170317 |
| MPFD | 0.72401679 | -0.8259278 | -0.7607781 | -0.7481643 | -0.7470436 | -0.7595936 | -0.6326791 | 0.40543458 |
| AWMPFD | 0.82171369 | -0.5093677 | -0.9279633 | -0.9072368 | -0.918215 | -0.9267176 | -0.7431506 | 0.61132974 |
| SqP | 0.85434421 | -0.6158302 | -0.9677627 | -0.9897205 | -0.9619243 | -0.9790695 | -0.8497902 | 0.7340755 |
| PA_1 | 0.88642067 | -0.6843396 | -0.962873 | -0.9799471 | -0.9552908 | -0.9244411 | -0.8664628 | 0.67585149 |
| PA_2 | 0.60156196 | -0.426872 | -0.628812 | -0.6436959 | -0.6515515 | -0.6424653 | -0.5987319 | 0.42080237 |
| NACI | 0.86540066 | -0.6132187 | -0.9800964 | -0.9683844 | -0.9720803 | -0.9820193 | -0.8117043 | 0.66325333 |
| NASQ | 0.8609077 | -0.6175106 | -0.9790712 | -0.9896682 | -0.9721754 | -0.9871873 | -0.8433617 | 0.72108044 |
| BRRA | 0.28798751 | -0.1896539 | -0.3683642 | -0.5333777 | -0.3680003 | -0.414817 | -0.3461933 | 0.62835445 |
| NFTD | 0.28798712 | -0.1896535 | -0.3683637 | -0.5333773 | -0.3679999 | -0.4148166 | -0.346193 | 0.62835425 |
| PORO | -0.8271684 | 0.5992961 | 0.9592961 | 0.99278526 | 0.95326783 | 0.97357029 | 0.8338967 | -0.7790758 |
| DSTA | 0.87632122 | -0.6250113 | -0.9684176 | -0.9543787 | -0.9619246 | -0.9699912 | -0.8222074 | 0.62442586 |
| ABRA | 0.86850559 | -0.6053815 | -0.9767927 | -0.9648362 | -0.9698191 | -0.9788686 | -0.8082604 | 0.65553154 |
| CCRA | -0.011537 | 0.02483161 | -0.0450723 | -0.2020297 | -0.0522359 | -0.0888471 | -0.1679856 | 0.45608109 |

| | TENT | TMAS | TVAR | P050 | P500 | TLAC | P005 | OEFC |
|---|---|---|---|---|---|---|---|---|
| LsFT | -0.782429 | -0.6967675 | -0.7283402 | -0.7278514 | -0.7268741 | 0.65911866 | 0.67921754 | -0.7268482 |
| NYTP | 0.56893317 | 0.8115767 | 0.87696381 | 0.8738895 | 0.86937452 | -0.7676244 | -0.8022108 | 0.86928105 |
| SIDI | 0.50108759 | 0.86124763 | 0.90750749 | 0.9085202 | 0.90926254 | -0.7552589 | -0.8055228 | 0.90926864 |
| SIEV | 0.54381687 | 0.81559627 | 0.85497756 | 0.85638967 | 0.85769612 | -0.7167248 | -0.7613855 | 0.85771327 |
| SHDI | 0.49731089 | 0.87794957 | 0.93963707 | 0.93969905 | 0.93913856 | -0.7720266 | -0.8240524 | 0.93912201 |
| SHEV | 0.58643058 | 0.7788533 | 0.81459815 | 0.81612993 | 0.81760774 | -0.6923181 | -0.7288277 | 0.81762856 |
| MCDI | 0.47558985 | 0.86011851 | 0.91379806 | 0.91475154 | 0.91537125 | -0.7416385 | -0.7976931 | 0.91537532 |
| MCEV | 0.53697522 | 0.78433383 | 0.82427999 | 0.82596628 | 0.82762091 | -0.6791903 | -0.7253266 | 0.82764515 |
| SHHO | 0.42137346 | 0.91841084 | 0.98163639 | 0.9801308 | 0.97750697 | -0.8492389 | -0.8856645 | 0.97744907 |
| SIHO | 0.14641588 | -0.8891383 | -0.698521 | -0.7100765 | -0.724516 | 0.87474742 | 0.86461303 | -0.7247844 |
| n_Q | -0.6226221 | -0.8154146 | -0.8198595 | -0.8200375 | -0.8198919 | 0.79609609 | 0.80429008 | -0.8198808 |
| KT_Q | -0.693793 | -0.7939356 | -0.796419 | -0.7968829 | -0.7971309 | 0.77574538 | 0.78203161 | -0.7971274 |
| FMP | -0.6247497 | -0.8107102 | -0.8257168 | -0.8252841 | -0.824306 | 0.79250111 | 0.802609 | -0.8242794 |
| SHCO | -0.64645 | -0.8143441 | -0.8207429 | -0.820857 | -0.8206224 | 0.79544696 | 0.80363363 | -0.8206097 |
| SICO | -0.4614795 | -0.8334186 | -0.8848481 | -0.8860532 | -0.8870071 | 0.70713027 | 0.76605532 | -0.8870179 |
| SUMD | 0.76757129 | 0.30100324 | 0.26264777 | 0.26355321 | 0.26481392 | -0.3314766 | -0.3140973 | 0.26483343 |
| TENT | 1 | 0.17279911 | 0.3331864 | 0.32441864 | 0.31310344 | -0.1630972 | -0.1773772 | 0.31288387 |
| TMAS | 0.17279911 | 1 | 0.93537329 | 0.94076924 | 0.94712871 | -0.9583866 | -0.9682627 | 0.94724144 |
| TVAR | 0.3331864 | 0.93537329 | 1 | 0.99975406 | 0.99870989 | -0.8581656 | -0.9062271 | 0.99868211 |
| P050 | 0.32441864 | 0.94076924 | 0.99975406 | 1 | 0.99958929 | -0.8639031 | -0.9113126 | 0.99957356 |
| P500 | 0.31310344 | 0.94712871 | 0.99870989 | 0.99958929 | 1 | -0.8708627 | -0.917381 | 0.99999985 |
| TLAC | -0.1630972 | -0.9583866 | -0.8581656 | -0.8639031 | -0.8708627 | 1 | 0.97262531 | -0.8709866 |
| P005 | -0.1773772 | -0.9682627 | -0.9062271 | -0.9113126 | -0.917381 | 0.97262531 | 1 | -0.9174877 |
| OEFC | 0.31288387 | 0.94724144 | 0.99868211 | 0.99957356 | 0.99999985 | -0.8709866 | -0.9174877 | 1 |
| OIFC | -0.1733464 | -0.9385841 | -0.8284731 | -0.8338316 | -0.8403846 | 0.98731877 | 0.94068385 | -0.8405005 |
| OCFC | 0.52120824 | 0.85336663 | 0.8363231 | 0.83781495 | 0.83936216 | -0.8439471 | -0.8426168 | 0.839383 |
| OEFT | 0.52945255 | 0.84313524 | 0.83380618 | 0.83500062 | 0.83615937 | -0.8265449 | -0.8333507 | 0.8361729 |
| OIFT | 0.7306177 | 0.65812099 | 0.6518016 | 0.65195782 | 0.65190808 | -0.6504046 | -0.6432194 | 0.65190012 |
| OCFT | 0.57689682 | 0.55869154 | 0.56880554 | 0.56829358 | 0.56739035 | -0.5403906 | -0.5518009 | 0.56736726 |
| ABFT | 0.64654593 | 0.70422605 | 0.71067746 | 0.71032419 | 0.7095681 | -0.6897963 | -0.6952918 | 0.7095463 |
| FMF | 0.58653542 | 0.866419 | 0.87961152 | 0.88032552 | 0.88082242 | -0.8368492 | -0.860369 | 0.88082309 |
| BETL | 0.67746046 | 0.74984265 | 0.76225262 | 0.7623533 | 0.76215022 | -0.7256038 | -0.7410109 | 0.76213847 |
| PSI | 0.57492823 | 0.7408222 | 0.74591444 | 0.74623202 | 0.74631 | -0.7222799 | -0.7367679 | 0.74630381 |
| PD | -0.565675 | -0.8151935 | -0.812048 | -0.8124797 | -0.812676 | 0.80047457 | 0.80488649 | -0.8126714 |

| | | | | | | |
|---|---|---|---|---|---|---|
| PENT | 0.19028014 | 0.98165782 | 0.93748658 | 0.94568516 | -0.938962 | 0.9457598 |
| PMAS | 0.19028014 | 0.98165781 | 0.9413541 | 0.94568516 | -0.938962 | 0.9457598 |
| PVAR | 0.67691625 | 0.80722704 | 0.81584638 | 0.81647792 | -0.7830017 | 0.81647328 |
| PLAC | 0.67764747 | 0.80672434 | 0.81535439 | 0.8159961 | -0.782432 | 0.81599158 |
| NPAT | 0.67861114 | 0.80604721 | 0.81469024 | 0.81534653 | -0.7816588 | 0.81534217 |
| LPI | 0.67862875 | 0.80603434 | 0.81467762 | 0.81533417 | -0.7816442 | 0.81532981 |
| PSIZ | 0.19028014 | 0.98165782 | 0.93748658 | 0.94568516 | -0.938962 | 0.9457598 |
| PSSD | -0.3894751 | -0.8584287 | -0.9036322 | -0.906692 | 0.73821913 | -0.9067121 |
| PSCV | -0.6637792 | -0.8097878 | -0.8114704 | -0.8121748 | 0.79187335 | -0.8121171 |
| TE | -0.4204177 | 0.0252855 | 0.00999815 | 0.00932958 | -0.034089 | 0.00932228 |
| OEDG | -0.4291044 | 0.02421816 | 0.00840667 | 0.00803845 | -0.0328972 | 0.00803148 |
| OPER | 0.16775225 | 0.99971579 | 0.93593433 | 0.9479244 | -0.9571824 | 0.94803964 |
| RGYR | 0.49329797 | 0.11052237 | 0.12740875 | 0.1281432 | -0.0969523 | 0.12815568 |
| LOAX | -0.6658053 | -0.809089 | -0.8108745 | -0.8115854 | 0.79111932 | -0.8115817 |
| IEDG | -0.7090454 | -0.7824552 | -0.7864277 | -0.787202 | 0.76377669 | -0.7871993 |
| TEDG | -0.7090454 | -0.7824552 | -0.7864277 | -0.787202 | 0.76377669 | -0.7871993 |
| LSI | 0.46216828 | 0.07948086 | 0.09564305 | 0.09612989 | -0.0669992 | 0.09674688 |
| MSI | 0.4731576 | 0.0889615 | 0.10574518 | 0.10639192 | -0.0761099 | 0.10640295 |
| AWMSI | 0.16324226 | 0.99910769 | 0.93567439 | 0.94762033 | -0.9553742 | 0.94773509 |
| DLFD | 0.65398768 | 0.82187844 | 0.82475192 | 0.82559089 | -0.8016806 | 0.82558834 |
| MPFD | 0.1792853 | 0.8720942 | 0.73181878 | 0.74784386 | -0.9312325 | 0.74800512 |
| AWMPFD | 0.6100673 | 0.74423013 | 0.76109164 | 0.75950052 | -0.725705 | 0.75710321 |
| SqP | 0.66498351 | 0.81519421 | 0.81903851 | 0.81979522 | -0.80468 | 0.81980145 |
| PA_1 | 0.59686028 | 0.87403517 | 0.86136448 | 0.86467464 | -0.8571616 | 0.86469803 |
| PA_2 | 0.40856028 | 0.57094567 | 0.5729979 | 0.57362173 | -0.557607 | 0.5736204 |
| NACI | 0.60067615 | 0.82191878 | 0.8210104 | 0.82131839 | -0.8060761 | 0.82131022 |
| NASQ | 0.65026127 | 0.81994359 | 0.82281442 | 0.82415211 | -0.799708 | 0.82415493 |
| BRRA | 0.56943625 | 0.26252252 | 0.26920391 | 0.26951783 | -0.259801 | 0.26951743 |
| NFTD | 0.56943613 | 0.26252209 | 0.26920353 | 0.26951744 | -0.2529797 | 0.26951703 |
| PORO | -0.7090454 | -0.7824552 | -0.7864277 | -0.787202 | 0.76377669 | -0.7871993 |
| DSTA | 0.5726178 | 0.83353774 | 0.83674572 | 0.83749248 | -0.8140276 | 0.83748878 |
| ABRA | 0.60294687 | 0.81901569 | 0.81973302 | 0.81936945 | -0.8027032 | 0.81935405 |
| CCRA | 0.43636832 | -0.0235344 | -0.0083396 | -0.0080847 | 0.03204449 | -0.0077317 |

| | OIFC | OCFC | OEFT | OIFT | OCFT | ABFT | FMF | BETL |
|---|---|---|---|---|---|---|---|---|
| **LsFT** | 0.64437626 | -0.8452132 | -0.8477123 | -0.9388563 | -0.7353814 | -0.8576225 | -0.9081273 | -0.9378831 |
| NYTP | -0.756229 | 0.89152727 | 0.89854984 | 0.78294704 | 0.70797613 | 0.84615778 | 0.93655744 | 0.86749294 |
| SIDI | -0.7287634 | 0.85501042 | 0.85923747 | 0.76372996 | 0.62931091 | 0.76863964 | 0.89949646 | 0.83864667 |
| SIEV | -0.6918689 | 0.81557932 | 0.8169581 | 0.76737544 | 0.60217646 | 0.73461523 | 0.86407032 | 0.82090657 |
| SHDI | -0.7448217 | 0.86715168 | 0.87114804 | 0.75753841 | 0.63661909 | 0.77689959 | 0.91439184 | 0.84300392 |
| SHEV | -0.6690164 | 0.78890737 | 0.78619673 | 0.78079715 | 0.58491827 | 0.71100139 | 0.8413417 | 0.81587007 |
| MCDI | -0.7130998 | 0.83622251 | 0.84118415 | 0.73725698 | 0.61281918 | 0.74925343 | 0.88336294 | 0.81676863 |
| MCEV | -0.6535837 | 0.77282986 | 0.77359299 | 0.73884231 | 0.56992994 | 0.69533546 | 0.82396831 | 0.78470418 |
| SHHO | -0.829958 | 0.87179216 | 0.86900881 | 0.70031469 | 0.6131865 | 0.75940432 | 0.90963104 | 0.80220481 |
| SIHO | 0.85103137 | -0.6599805 | -0.646945 | -0.4868156 | -0.399534 | -0.5118615 | -0.6508415 | -0.5517844 |
| n_Q | 0.7894325 | -0.9428092 | -0.9497288 | -0.8753358 | -0.7925566 | -0.9214445 | -0.9664796 | -0.9268626 |
| KT_Q | 0.76792243 | -0.9322221 | -0.933573 | -0.9451066 | -0.790541 | -0.9298377 | -0.9715178 | -0.9646351 |
| **FMP** | 0.7862511 | -0.9347671 | -0.9416522 | -0.8627372 | -0.7883007 | -0.9121691 | -0.9640668 | -0.9190396 |
| SHCO | 0.78852347 | -0.9447632 | -0.9502406 | -0.8971602 | -0.7966124 | -0.9280173 | -0.9740646 | -0.9416337 |
| SICO | 0.67816331 | -0.8031753 | -0.8094145 | -0.7101782 | -0.5925785 | -0.7232857 | -0.8500155 | -0.7860441 |
| SUMD | -0.3397117 | 0.58658441 | 0.59304793 | 0.82491869 | 0.65810975 | 0.72625518 | 0.63116383 | 0.74333121 |
| TENT | -0.1733464 | 0.52120824 | 0.52945255 | 0.73061773 | 0.57689682 | 0.64654593 | 0.58653542 | 0.67746046 |
| TMAS | -0.9385841 | 0.85336663 | 0.84313524 | 0.65812099 | 0.55869154 | 0.70422605 | 0.866419 | 0.74984265 |
| TVAR | -0.8284731 | 0.8363231 | 0.83380618 | 0.6518016 | 0.56880554 | 0.71067746 | 0.87961152 | 0.76225262 |
| P0SO | -0.8338316 | 0.83781495 | 0.83500062 | 0.65195782 | 0.56829358 | 0.71032419 | 0.88032552 | 0.7623533 |
| P500 | -0.8403846 | 0.83936216 | 0.83615937 | 0.65190808 | 0.56739035 | 0.7095681 | 0.88082242 | 0.76215022 |
| P050 | -0.98731877 | -0.8439471 | -0.8265449 | -0.6504046 | -0.5403906 | -0.6897963 | -0.8368492 | -0.7256038 |
| TLAC | 0.94068385 | -0.8426168 | -0.8333507 | -0.6432194 | -0.5518009 | -0.6952918 | -0.860369 | -0.7410109 |
| P005 | -0.8405005 | 0.8361729 | 0.8361729 | 0.65190012 | 0.56736726 | 0.7095463 | 0.88082309 | 0.76213847 |
| OEFC | 0.839383 | 0.8361729 | 0.8361729 | -0.65123 | -0.5339016 | -0.6852877 | -0.8186915 | -0.7132311 |
| OIFC | 1 | -0.8371361 | -0.8154097 | -0.65123 | -0.5339016 | -0.6852877 | -0.8186915 | -0.7132311 |
| OCFC | -0.8371361 | 1 | 0.95395107 | 0.83998013 | 0.71546221 | 0.90666044 | 0.94976382 | 0.89511607 |
| OEFT | -0.8154097 | 0.95395107 | 1 | 0.83697642 | 0.74576992 | 0.91111934 | 0.95174493 | 0.89704056 |
| OIFT | -0.65123 | 0.83998013 | 0.83697642 | 1 | 0.75156041 | 0.87881503 | 0.88426556 | 0.95429356 |
| OCFT | -0.5339016 | 0.71546221 | 0.74576992 | 0.75156041 | 1 | 0.8483442 | 0.76765081 | 0.77263735 |
| ABFT | -0.6852877 | 0.90666044 | 0.91111934 | 0.87881503 | 0.8483442 | 1 | 0.91026784 | 0.8950543 |
| **FMF** | -0.8186915 | 0.94976382 | 0.95174493 | 0.88426556 | 0.76765081 | 0.91026784 | 1 | 0.94382962 |
| BETL | -0.7132311 | 0.89511607 | 0.89704056 | 0.95429356 | 0.77263735 | 0.8950543 | 0.94382962 | 1 |
| PSI | -0.7098038 | 0.86738874 | 0.88887432 | 0.83179672 | 0.84681125 | 0.89788026 | 0.89826129 | 0.87507823 |
| PD | 0.7292905 | -0.953849 | -0.961854 | -0.851637 | -0.8123708 | -0.9433194 | -0.9594594 | -0.9123376 |

157

| | C1 | C2 | C3 | C4 | C5 | C6 | C7 | C8 |
|---|---|---|---|---|---|---|---|---|
| PENT | -0.9343371 | 0.83217906 | 0.81870792 | 0.63791915 | 0.54511183 | 0.69086447 | 0.84660852 | 0.72660106 |
| PMAS | -0.9343371 | 0.83217906 | 0.81870792 | 0.63791915 | 0.54511183 | 0.69086447 | 0.84660852 | 0.72660106 |
| PVAR | -0.7715357 | 0.94005541 | 0.92830139 | | 0.79201399 | 0.93108108 | 0.97697228 | 0.95769292 |
| PLAC | -0.709587 | 0.9443402 | 0.92880268 | | 0.79163379 | 0.93094351 | 0.97674076 | 0.95762783 |
| NPAT | -0.701806 | 0.93903062 | 0.92944248 | | 0.79111469 | 0.93071439 | 0.97641346 | 0.95753504 |
| LPI | -0.7001659 | 0.93901932 | 0.92945412 | | 0.79110479 | 0.93071006 | 0.97640708 | 0.95753292 |
| PSIZ | -0.9343371 | 0.83217906 | 0.81870792 | 0.63791915 | 0.54511183 | 0.69086447 | 0.84660852 | 0.72660106 |
| PSSD | 0.70143048 | -0.7966586 | -0.803273 | -0.6830211 | | -0.7048372 | -0.8435896 | -0.7705391 |
| PSCV | 0.78377146 | -0.9486892 | -0.9528203 | -0.926676 | | -0.9433915 | -0.9787937 | -0.9583702 |
| TE | -0.0335041 | 0.02394094 | 0.05014287 | -0.2890203 | 0.03757546 | 0.017446668 | -0.0651733 | -0.1734809 |
| OEDG | -0.0325346 | 0.01868338 | 0.04463815 | -0.2982331 | 0.02694615 | 0.00667308 | -0.0707832 | -0.1810969 |
| OPER | -0.9349652 | 0.85059306 | 0.84087464 | 0.65472666 | 0.55722656 | 0.701925 | 0.86518255 | 0.74799518 |
| RGYR | -0.092841 | 0.14107997 | 0.12014968 | 0.35650627 | 0.10679341 | 0.14000962 | 0.20170534 | 0.26059119 |
| LOAX | 0.78301192 | -0.947883 | -0.9518899 | -0.9273726 | -0.804375 | -0.942543 | -0.9783782 | -0.9584566 |
| IEDG | 0.75596025 | -0.918694 | -0.918898 | -0.9448715 | -0.7789375 | -0.9161527 | -0.9612201 | -0.9580397 |
| TEDG | 0.75596025 | -0.9186974 | -0.918898 | -0.9448715 | -0.7789375 | -0.9161527 | -0.9612201 | -0.9580397 |
| LSI | -0.064741 | 0.09098425 | 0.07415261 | 0.32027346 | 0.06945843 | 0.08043298 | 0.16095366 | 0.23850398 |
| MSI | -0.0732954 | 0.10613995 | 0.08803195 | 0.33222102 | 0.08075995 | 0.09834939 | 0.17361929 | 0.24595475 |
| AWMSI | -0.934662 | 0.84622053 | 0.83604765 | 0.64984335 | 0.55301879 | 0.69754833 | 0.86068539 | 0.74288785 |
| DLFD | -0.7913986 | 0.95202675 | 0.95585817 | 0.91748299 | 0.79266984 | 0.93444818 | 0.9808424 | 0.95335432 |
| MPFD | -0.9431762 | 0.81156649 | 0.79230894 | 0.64957934 | 0.51777655 | 0.66097699 | 0.79915367 | 0.69367496 |
| AWMPFD | -0.7394392 | 0.90176686 | 0.90602115 | 0.83029367 | 0.7505596 | 0.89400695 | 0.90981396 | 0.87312491 |
| SqP | -0.779603 | 0.93699719 | 0.93871637 | 0.92598769 | 0.77897033 | 0.91800776 | 0.97313454 | 0.95454464 |
| PA_1 | -0.8478858 | 0.94800496 | 0.94435378 | 0.90267539 | 0.74226061 | 0.89080187 | 0.97627257 | 0.93965943 |
| PA_2 | -0.5518342 | 0.66375816 | 0.66417302 | 0.6560125 | 0.55085619 | 0.64706325 | 0.68687712 | 0.67561537 |
| NACI | -0.8008866 | 0.95842328 | 0.96579368 | 0.8843241 | 0.80527605 | 0.94630871 | 0.97415047 | 0.93464703 |
| NASQ | -0.785541 | 0.95195454 | 0.95617492 | 0.91739331 | 0.79483477 | 0.93659026 | 0.97971194 | 0.95056446 |
| BRRA | -0.2522529 | 0.30774406 | 0.30275134 | 0.65490171 | 0.29829778 | 0.36570894 | 0.44047481 | 0.56094414 |
| NFTD | -0.2522524 | 0.30774361 | 0.30275089 | 0.65490141 | 0.29829749 | 0.36570856 | 0.44047439 | 0.56094378 |
| PORO | 0.7596025 | -0.9186974 | -0.918898 | -0.9448715 | -0.7789375 | -0.9161527 | -0.9612201 | -0.9580397 |
| DSTA | -0.8023287 | 0.95367576 | 0.96063202 | 0.86258623 | 0.78555628 | 0.9299546 | 0.96863026 | 0.92080869 |
| ABRA | -0.8010859 | 0.95541891 | 0.96176912 | 0.88033176 | 0.79827778 | 0.94310658 | 0.97093732 | 0.93027018 |
| CCRA | 0.03175195 | -0.0154481 | -0.0408055 | 0.31840434 | -0.0169413 | 0.00421972 | 0.07976665 | 0.19869083 |

| | PSI | PD | PENT | PMAS | PVAR | PLAC | NPAT | LPI |
|---|---|---|---|---|---|---|---|---|
| **LsFT** | **-0.8302011** | **0.84467852** | **-0.6740589** | **-0.6740589** | **-0.9538334** | **-0.9544417** | **-0.9552316** | **-0.9552459** |
| NYTP | 0.8469063 | -0.9101152 | 0.81881133 | 0.81881133 | 0.91066189 | 0.91016531 | 0.90947581 | 0.90946282 |
| SIDI | 0.78739617 | -0.844897 | 0.84278345 | 0.84278345 | 0.89457067 | 0.89445218 | 0.89429597 | 0.89429263 |
| SIEV | 0.75109883 | -0.7984072 | 0.79305753 | 0.79305753 | 0.88379852 | 0.88389726 | 0.88404011 | 0.88404224 |
| SHDI | 0.79960593 | -0.8574371 | 0.8703518 | 0.8703518 | 0.89491502 | 0.89470983 | 0.89443342 | 0.8944279 |
| SHEV | 0.72712462 | -0.7630902 | 0.7570546 | 0.7570546 | 0.87577427 | 0.87606664 | 0.87647288 | 0.87647986 |
| MCDI | 0.76923243 | -0.8261791 | 0.84461989 | 0.84461989 | 0.87322689 | 0.87309166 | 0.87291378 | 0.87291005 |
| MCEV | 0.71138291 | -0.7529545 | 0.76129818 | 0.76129818 | 0.85281301 | 0.85300494 | 0.85327694 | 0.85328144 |
| SHHO | 0.78533695 | -0.855913 | 0.93489913 | 0.93489913 | 0.85430621 | 0.85378472 | 0.85308067 | 0.85306729 |
| SIHO | -0.550891 | 0.61108119 | -0.8355739 | -0.8355739 | -0.6015083 | -0.6011501 | -0.6006624 | -0.6006532 |
| n_Q | -0.9093096 | 0.97289807 | -0.7972966 | -0.7972966 | -0.9759467 | -0.9755307 | -0.974958 | -0.974947 |
| KT_Q | -0.9009535 | 0.94634465 | -0.7729706 | -0.7729706 | -0.993024 | -0.9931099 | -0.9931997 | -0.9932011 |
| **FMP** | **-0.9058042** | **0.96402322** | **-0.7986131** | **-0.7986131** | **-0.9695375** | **-0.9691001** | **-0.9685003** | **-0.9684888** |
| SHCO | -0.9126722 | 0.97061911 | -0.7967342 | -0.7967342 | -0.9858793 | -0.985589 | -0.9851824 | -0.9851746 |
| SICO | -0.7394089 | 0.79537867 | -0.8151819 | -0.8151819 | -0.8480911 | -0.8479902 | -0.8478609 | -0.847858 |
| SUMD | 0.64753478 | -0.6311489 | 0.25715179 | 0.25715179 | 0.7420728 | 0.74296836 | 0.74413091 | 0.74415234 |
| TENT | 0.57492823 | -0.565675 | 0.19028014 | 0.19028014 | 0.67691625 | 0.67764747 | 0.67861114 | 0.67862875 |
| TMAS | 0.7408222 | -0.8151935 | 0.98165782 | 0.98165781 | 0.80722704 | 0.80672434 | 0.80604721 | 0.80603434 |
| TVAR | 0.74591444 | -0.812048 | 0.93748658 | 0.93748659 | 0.81584638 | 0.81535439 | 0.81469024 | 0.81467762 |
| P0S0 | 0.74623202 | -0.8124797 | 0.9413541 | 0.9413541 | 0.81628049 | 0.81579274 | 0.81513462 | 0.81512211 |
| P0S0 | 0.74631 | -0.812676 | 0.94568516 | 0.94568516 | 0.81647792 | 0.81599961 | 0.81534653 | 0.81533417 |
| P500 | -0.7222799 | 0.80047457 | -0.938962 | -0.938962 | -0.7830017 | -0.782432 | -0.7816588 | -0.7816442 |
| TLAC | -0.7367679 | 0.80488649 | -0.9403929 | -0.9403929 | -0.7974628 | -0.7969395 | -0.7962257 | -0.7962122 |
| P005 | 0.74630381 | -0.8126714 | 0.9457598 | 0.9457598 | 0.81647328 | 0.81599158 | 0.81534217 | 0.81532981 |
| OEFC | -0.7098038 | 0.79292905 | -0.9343371 | -0.9343371 | -0.7715357 | -0.7709587 | -0.7701806 | -0.7701659 |
| OIFC | 0.86738874 | -0.953849 | 0.83217906 | 0.83217906 | 0.94005541 | 0.93962854 | 0.93903062 | 0.93901932 |
| OCFC | 0.8887432 | -0.961854 | 0.81870792 | 0.81870792 | 0.94478703 | 0.9443402 | 0.94371085 | 0.94369901 |
| OEFT | 0.83179672 | -0.851637 | 0.63791915 | 0.63791915 | 0.92830139 | 0.92880268 | 0.92944248 | 0.92945412 |
| OIFT | 0.84681125 | -0.8123708 | 0.54511183 | 0.54511183 | 0.79201399 | 0.79163379 | 0.79111469 | 0.79110479 |
| OCFT | 0.89788026 | -0.9433194 | 0.69086447 | 0.69086447 | 0.93108108 | 0.93094351 | 0.93071439 | 0.93071006 |
| ABFT | 0.89826129 | | | | | | | |
| **FMF** | **0.89826129** | **-0.9594594** | **0.84660852** | **0.84660852** | **0.9697228** | **0.97674076** | **0.97641346** | **0.97640708** |
| BETL | 0.8507823 | -0.9123376 | 0.72660106 | 0.72660106 | 0.95769292 | 0.95762783 | 0.95753504 | 0.95753292 |
| PSI | 1 | -0.9237451 | 0.72192864 | 0.72192864 | 0.95725099 | 0.90684699 | 0.90627839 | 0.90626766 |
| PD | -0.9237451 | 1 | -0.7966809 | -0.7966809 | -0.9577282 | -0.9569232 | -0.955832 | -0.9558114 |

| | | | | | | | |
|---|---|---|---|---|---|---|---|
| PENT | 0.7192864 | -0.7966809 | 1 | 1 | 0.7829744 | 0.78243507 | 0.78169705 |
| PMAS | 0.7192864 | -0.7966809 | 1 | 1 | 0.7829744 | 0.78243507 | 0.78169705 |
| PVAR | 0.90725099 | -0.9577282 | 0.7829744 | 0.7829744 | 1 | 0.9999915 | 0.9999545 |
| PLAC | 0.90684699 | -0.9569232 | 0.78243507 | 0.78243507 | 0.9999915 | 1 | 0.9999545 |
| NPAT | 0.90627839 | -0.955832 | 0.7817108 | 0.7817108 | 0.9999545 | 0.9999545 | 0.99998585 |
| LPI | 0.90626766 | -0.9558114 | 0.78169705 | 0.78169705 | 0.9999545 | 0.9999545 | 0.99998532 |
| PSIZ | 0.7192864 | -0.7966809 | 1 | 1 | 0.7829744 | 0.78243507 | 0.78169705 |
| PSSD | -0.7288408 | 0.78403902 | -0.8295041 | -0.8295041 | -0.8295043 | -0.8293122 | -0.8290507 |
| PSCV | -0.9175132 | 0.97284071 | -0.7888985 | -0.7888985 | -0.9970251 | -0.9968604 | -0.9966185 |
| TE | 0.03887784 | -0.1162849 | 0.03356964 | 0.03356964 | -0.1630246 | -0.1652403 | -0.1682181 |
| OEDG | 0.02997485 | -0.1089369 | 0.03266188 | 0.03266188 | -0.1704448 | -0.1726862 | -0.1756952 |
| OPER | 0.73905272 | -0.8126824 | 0.98044737 | 0.98044737 | 0.80506138 | 0.80456451 | 0.80389407 |
| RGYR | 0.12308619 | -0.0712528 | 0.09263339 | 0.09263339 | 0.32282008 | 0.32459942 | 0.32698894 |
| LOAX | -0.9166734 | 0.97159565 | -0.7881292 | -0.7881292 | -0.9973532 | -0.9971983 | -0.9969698 |
| IEDG | -0.8873089 | 0.92907464 | -0.760908 | -0.760908 | -0.9939465 | -0.9941225 | -0.9943381 |
| TEDG | -0.8873089 | 0.92907464 | -0.760908 | -0.760908 | -0.9939465 | -0.9941225 | -0.9943381 |
| LSI | 0.08050881 | -0.0329877 | 0.06446122 | 0.06446122 | 0.27832619 | 0.27966742 | 0.28151553 |
| MSI | 0.09340227 | -0.0444228 | 0.07303579 | 0.07303579 | 0.29255237 | 0.29402826 | 0.29604352 |
| AWMSI | 0.73453121 | -0.8080498 | 0.98505149 | 0.98505149 | 0.79987785 | 0.7993772 | 0.79870183 |
| DLFD | 0.9191174 | -0.9716122 | 0.8010345 | 0.8010345 | 0.99708656 | 0.9968409 | 0.99661668 |
| MPFD | 0.68575968 | -0.7667077 | 0.82827101 | 0.82827101 | 0.75066994 | 0.75016924 | 0.74949794 |
| AWMPFD | 0.85633207 | -0.9414498 | 0.74936255 | 0.74936255 | 0.91084191 | 0.91016898 | 0.90926387 |
| SqP | 0.89727615 | -0.948161 | 0.78938347 | 0.78938347 | 0.99387255 | 0.99386018 | 0.99382309 |
| PA_1 | 0.88184855 | -0.9417144 | 0.84892864 | 0.84892864 | 0.9857744 | 0.9856985 | 0.98558233 |
| PA_2 | 0.63384235 | -0.6718658 | 0.55561039 | 0.55561039 | 0.70456318 | 0.70451611 | 0.70444346 |
| NACI | 0.92219968 | -0.9946846 | 0.8046399 | 0.8046399 | 0.97566115 | 0.97508477 | 0.97429788 |
| NASQ | 0.91431236 | -0.9683287 | 0.79416188 | 0.79416188 | 0.99677778 | 0.99675567 | 0.99668954 |
| BRRA | 0.33414109 | -0.2683156 | 0.25265228 | 0.25265228 | 0.48754544 | 0.48981932 | 0.49281682 |
| NFTD | 0.33414072 | -0.2683151 | 0.25265189 | 0.25265189 | 0.48754504 | 0.48981892 | 0.49281642 |
| PORO | -0.8873089 | 0.92907464 | -0.760908 | -0.760908 | -0.9939465 | -0.9941225 | -0.9943381 |
| DSTA | 0.90890712 | -0.9868732 | 0.81553767 | 0.81553767 | 0.96284233 | 0.96220237 | 0.96133058 |
| ABRA | 0.91500535 | -0.9918263 | 0.80807312 | 0.80807312 | 0.97145867 | 0.97083533 | 0.96999007 |
| CCRA | -0.0212634 | 0.10440543 | -0.0318379 | -0.0318379 | 0.17614777 | 0.17848319 | 0.18166936 |

| | PSIZ | PSSD | PSCV | TE | OEDG | OPER | RGYR | LOAX |
|---|---|---|---|---|---|---|---|---|
| LsFT | -0.6740589 | 0.78634304 | 0.93888767 | 0.39352728 | 0.4091049 | -0.6945551 | -0.5023366 | 0.94048703 |
| NYTP | 0.8188133 | -0.8218208 | -0.9113753 | 0.00541912 | 0.00142984 | 0.81088652 | 0.14241519 | -0.9107009 |
| SIDI | 0.84278345 | -0.967228 | -0.8807648 | -0.1624211 | -0.1662448 | 0.86166327 | 0.3335869 | -0.8813837 |
| SIEV | 0.79305753 | -0.9477993 | -0.8628597 | -0.303433 | -0.3074815 | 0.81564333 | 0.4827286 | -0.866449 |
| SHDI | 0.8703518 | -0.9546504 | -0.8836933 | -0.1135009 | -0.1169073 | 0.878272 | 0.27375508 | -0.8839215 |
| SHEV | 0.7570546 | -0.9067598 | -0.8506704 | -0.4110459 | -0.4151883 | 0.77825104 | 0.58153119 | -0.8529784 |
| MCDI | 0.84461989 | -0.9725586 | -0.8590509 | -0.1481329 | -0.1516859 | 0.86086788 | 0.31597662 | -0.8595924 |
| MCEV | 0.76129818 | -0.935907 | -0.8281756 | -0.3582053 | -0.3621616 | 0.78448892 | 0.5401244 | -0.8302416 |
| SHHO | 0.93489913 | -0.8792956 | -0.8539903 | 0.01449955 | 0.01269828 | 0.91734865 | 0.12484555 | -0.8533133 |
| SIHO | -0.8355739 | 0.68112062 | 0.604832 | -0.0254491 | -0.0251068 | -0.8912824 | -0.0801773 | 0.60428654 |
| n_Q | -0.7972966 | 0.81304765 | 0.98100164 | 0.0365945 | 0.04276876 | -0.8130013 | -0.2141653 | 0.98066212 |
| KT_Q | -0.7729706 | 0.80412132 | 0.99247642 | 0.18492378 | 0.19237364 | -0.7913309 | -0.3197721 | 0.99279128 |
| FMP | -0.7986131 | 0.80515302 | 0.97366296 | 0.04486663 | 0.05059632 | -0.8084682 | -0.2199444 | 0.97337922 |
| SHCO | -0.7967342 | 0.81456488 | 0.9892626 | 0.0782685 | 0.084723 | -0.8119025 | -0.2451345 | 0.98910786 |
| SICO | -0.8151819 | 0.97707802 | 0.83214011 | 0.17049891 | 0.1740748 | -0.8344416 | -0.3441863 | 0.83290793 |
| SUMD | 0.25715179 | -0.41338 | -0.7331859 | -0.4339698 | -0.4448995 | 0.29856705 | 0.5180847 | -0.73521161 |
| TENT | 0.19028014 | -0.3894751 | -0.6637792 | -0.4204177 | -0.4291044 | 0.16775525 | 0.49329797 | -0.66580853 |
| TMAS | 0.98165782 | -0.8584287 | -0.8097878 | 0.0252855 | 0.02421816 | 0.99971579 | 0.11052237 | -0.809089 |
| TVAR | 0.93748658 | -0.9036322 | -0.8114704 | 0.0099815 | 0.00867851 | 0.93593433 | 0.1268113 | -0.8108745 |
| PO50 | 0.9413541 | -0.9052366 | -0.8119343 | 0.00971361 | 0.00840667 | 0.94143778 | 0.12740875 | -0.8113411 |
| PO50 | 0.94568516 | -0.906692 | -0.8121748 | 0.00932958 | 0.00803845 | 0.9479244 | 0.1281432 | -0.8115854 |
| P500 | -0.938962 | 0.73821913 | 0.79187335 | -0.0338495 | -0.0328636 | -0.9571824 | -0.0969523 | 0.79111932 |
| TLAC | -0.9403929 | 0.81089704 | 0.79808198 | -0.034089 | -0.0328972 | -0.9699384 | -0.1013781 | 0.79733687 |
| PO05 | 0.9457598 | -0.9067121 | -0.812171 | 0.00932228 | 0.00803148 | 0.94803964 | 0.12815568 | -0.8115817 |
| OEFC | -0.9343371 | 0.70143048 | 0.78377146 | -0.0335041 | -0.0325346 | -0.9349652 | -0.092841 | 0.78301192 |
| OIFC | 0.83217906 | -0.7966586 | -0.9486892 | 0.02394094 | 0.01868338 | 0.85059306 | 0.14107997 | -0.947883 |
| OCFC | 0.81870792 | -0.803273 | -0.9528203 | 0.05014287 | 0.04463815 | 0.84087464 | 0.12014968 | -0.9518899 |
| OEFT | 0.63791915 | -0.6830211 | -0.926676 | -0.2890203 | -0.2982331 | 0.65472666 | 0.35650627 | -0.9273726 |
| OIFT | 0.54511183 | -0.5757191 | -0.8051197 | 0.03757546 | 0.02694615 | 0.55722656 | 0.10679341 | -0.804375 |
| OCFT | 0.69086447 | -0.7048372 | -0.9433915 | 0.01744668 | 0.00667308 | 0.701925 | 0.14000962 | -0.942543 |
| FMF | 0.84660852 | -0.8435896 | -0.9787937 | -0.051733 | -0.0707832 | 0.86518255 | 0.20170534 | -0.9783782 |
| BETL | 0.72660106 | -0.7705391 | -0.9583702 | -0.1734809 | -0.1810969 | 0.74799518 | 0.26059119 | -0.9584566 |
| PSI | 0.72192864 | -0.7288408 | -0.9175132 | 0.03887784 | 0.02997485 | 0.73905272 | 0.12308619 | -0.9166734 |
| PD | -0.7966809 | 0.78403902 | 0.97284071 | -0.1162849 | -0.1089369 | -0.8126824 | -0.0712528 | 0.97159565 |

| | | | | | | | | |
|---|---|---|---|---|---|---|---|---|
| PENT | 1 | -0.8295041 | -0.7888985 | 0.03356964 | 0.03266188 | 0.98044737 | 0.09263339 | -0.7881292 |
| PMAS | 1 | -0.8295041 | -0.7888985 | 0.03356964 | 0.03266188 | 0.98044737 | 0.09263339 | -0.7881292 |
| PVAR | 0.7829744 | -0.8295043 | -0.9970251 | -0.1630246 | -0.1704448 | 0.80506138 | 0.32282008 | -0.9973532 |
| PLAC | 0.78243507 | -0.8293122 | -0.9968604 | -0.1652403 | -0.1726862 | 0.80456451 | 0.32459942 | -0.9971983 |
| NPAT | 0.7817108 | -0.8290507 | -0.9966185 | -0.1682181 | -0.1756952 | 0.80389407 | 0.32698894 | -0.9969698 |
| LPI | 0.78169705 | -0.8290455 | -0.9966137 | -0.168273 | -0.1757506 | 0.80388133 | 0.32703291 | -0.9969653 |
| PSIZ | 1 | -0.8295041 | -0.7888985 | 0.03356964 | 0.03266188 | 0.98044737 | 0.09263339 | -0.7881292 |
| PSSD | -0.8295041 | 1 | 0.81329878 | 0.13134029 | 0.13435454 | -0.8611042 | -0.2976217 | 0.81379431 |
| PSCV | -0.7888985 | 0.81329878 | 1 | 0.1108945 | 0.11837716 | -0.8071754 | -0.2696648 | 0.99998013 |
| TE | 0.03356964 | 0.13134029 | 0.1108945 | 1 | 0.02633109 | -0.9251242 | -0.9274066 | 0.11672286 |
| OEDG | 0.03266188 | 0.13435454 | 0.11837716 | 0.02633109 | 1 | 0.02525466 | 0.1094192 | 0.12420293 |
| OPER | 0.98044737 | -0.8611042 | -0.8071754 | -0.9251242 | 0.02525466 | 1 | 0.1094192 | -0.80647721 |
| RGYR | 0.09263339 | -0.2976217 | -0.2696648 | -0.9274066 | 0.1094192 | 0.1094192 | 1 | -0.2756732 |
| LOAX | -0.7881292 | 0.81379431 | 0.99998013 | 0.11672286 | 0.12420293 | -0.80647721 | -0.2756732 | 1 |
| IEDG | -0.760908 | 0.80964371 | 0.98912898 | 0.25569488 | 0.26307245 | -0.7797678 | -0.3994393 | 0.9899724 |
| TEDG | -0.760908 | 0.80964371 | 0.98912898 | 0.25569488 | 0.26307245 | -0.7797678 | -0.3994393 | 0.9899724 |
| LSI | 0.06446122 | -0.2622824 | -0.2258791 | -0.9191484 | -0.9201965 | 0.07806373 | -0.2320062 | -0.23200062 |
| MSI | 0.07303579 | -0.2737412 | -0.2396928 | -0.9244753 | -0.9258922 | 0.08763166 | -0.24580086 | -0.24580086 |
| AWMSI | 0.98505149 | -0.8585263 | -0.8022897 | 0.02710135 | -0.02608296 | 0.99943561 | 0.10703787 | -0.8015809 |
| DLFD | 0.8010345 | -0.8262023 | -0.9987181 | -0.1135319 | -0.1203665 | 0.81948373 | 0.27679659 | -0.9987539 |
| MPFD | 0.82827101 | -0.6349483 | -0.762473 | 0.00957226 | 0.00834035 | 0.86659252 | 0.12130949 | -0.7619271 |
| AWMPFD | 0.74936255 | -0.7259107 | 0.06478519 | 0.05932145 | 0.05932145 | 0.73972102 | 0.08560512 | -0.9260325 |
| SqP | 0.78938347 | -0.8314795 | -0.9270912 | -0.184285 | -0.1910903 | 0.81360131 | 0.33724086 | -0.9922892 |
| PA_1 | 0.84892864 | -0.8555706 | -0.9832276 | -0.1792996 | -0.1848712 | 0.87143609 | 0.33363659 | -0.9836634 |
| PA_2 | 0.55561039 | -0.5831768 | -0.7029865 | -0.1364835 | -0.1411483 | 0.56902396 | 0.249399 | -0.703373 |
| NACI | 0.8046399 | -0.7981758 | -0.9872603 | 0.03945342 | -0.03270077 | 0.81907047 | 0.12710473 | -0.9863451 |
| NASQ | 0.79416188 | -0.8273682 | -0.9971319 | -0.1133681 | -0.1207996 | 0.81814836 | 0.27846294 | -0.9971425 |
| BRRA | 0.25265228 | -0.3227057 | -0.4598858 | -0.736065 | -0.7408707 | 0.26090717 | 0.57806509 | -0.4628036 |
| NFTD | 0.25265189 | -0.3227053 | -0.4598853 | -0.7360651 | -0.7408708 | 0.26090675 | 0.57806513 | -0.4628032 |
| PORO | -0.760908 | 0.80964371 | 0.98912898 | 0.25569488 | 0.26307245 | -0.7797678 | -0.3994393 | 0.9899724 |
| DSTA | 0.8155767 | -0.8123262 | -0.9747022 | 0.06047546 | 0.05423883 | 0.83194164 | 0.10681646 | -0.9736768 |
| ABRA | 0.80807312 | -0.7925918 | -0.9838532 | 0.03996834 | 0.03355865 | 0.81573505 | 0.12344297 | -0.9829292 |
| CCRA | -0.0318379 | -0.1294999 | -0.1251398 | -0.996856 | -0.9976235 | -0.0245291 | 0.90578582 | -0.1308088 |

| | IEDG | TEDG | LSI | MSI | AWMSI | DLFD | MPFD | AWMPFD |
|---|---|---|---|---|---|---|---|---|
| **LsFT** | 0.97166334 | 0.97166334 | -0.4598921 | -0.4742161 | -0.6896879 | -0.9373042 | -0.6301646 | -0.8125001 |
| NYTP | -0.8848532 | -0.8848532 | 0.10629407 | 0.11737961 | 0.81037259 | 0.9186718 | 0.66972643 | 0.87842478 |
| SIDI | -0.8799628 | -0.8799628 | 0.29722456 | 0.3091211 | 0.85979986 | 0.89211984 | 0.68615333 | 0.78998453 |
| SIEV | -0.8835439 | -0.8835439 | 0.44874044 | 0.4605243 | 0.8132408 | 0.87444811 | 0.66286192 | 0.74648286 |
| SHDI | -0.8754336 | -0.8754336 | 0.23825958 | 0.24967152 | 0.87774604 | 0.89577839 | 0.68145597 | 0.80714912 |
| SHEV | -0.8876851 | -0.8876851 | 0.55067744 | 0.56192815 | 0.7757762 | 0.86185806 | 0.64475128 | 0.71675651 |
| MCDI | -0.8566928 | -0.8566928 | 0.28031149 | 0.29193649 | 0.85966188 | 0.87115249 | 0.6634623 | 0.77265964 |
| MCEV | -0.8579708 | -0.8579708 | 0.50762336 | 0.51919404 | 0.78226347 | 0.84039886 | 0.62740051 | 0.70311065 |
| SHHO | -0.8271684 | -0.8271684 | 0.09340728 | 0.10305912 | 0.91882565 | 0.86668932 | 0.72401679 | 0.82171369 |
| SIHO | 0.58331011 | 0.58331011 | -0.0552446 | -0.0628262 | -0.8896404 | -0.6149374 | -0.8259278 | -0.5093677 |
| n_Q | 0.9592961 | 0.9592961 | -0.1730295 | -0.1858554 | -0.8085395 | -0.9812477 | -0.7607781 | -0.9279633 |
| KT_Q | 0.99278526 | 0.99278526 | -0.2751665 | -0.2894135 | -0.7864816 | -0.9904661 | -0.7481643 | -0.9072368 |
| **FMP** | 0.95326783 | 0.95326783 | -0.1802315 | -0.1926649 | -0.8047519 | -0.9752211 | -0.7470436 | -0.918215 |
| SHCO | 0.97357029 | 0.97357029 | -0.2031145 | -0.2163183 | -0.8074787 | -0.9892132 | -0.7595936 | -0.9267176 |
| SICO | 0.8338967 | 0.8338967 | -0.3085093 | -0.320247 | -0.8331154 | -0.844566 | -0.6326791 | -0.7431506 |
| SUMD | -0.7790758 | -0.7790758 | 0.47649714 | 0.49063228 | 0.29044848 | 0.7170317 | 0.40543458 | 0.61132974 |
| TENT | -0.7090454 | -0.7090454 | 0.46216828 | 0.47315762 | 0.16324226 | 0.65398768 | 0.17792853 | 0.6100673 |
| TMAS | -0.7824552 | -0.7824552 | 0.07948086 | 0.0889615 | 0.99910769 | 0.82187844 | 0.8720942 | 0.74423013 |
| TVAR | -0.7864277 | -0.7864277 | 0.09564305 | 0.10522372 | 0.93567439 | 0.82475192 | 0.73181878 | 0.76109164 |
| P050 | -0.7869164 | -0.7869164 | 0.09612989 | 0.10574518 | 0.94116479 | 0.82528525 | 0.73886453 | 0.75950052 |
| P500 | -0.787202 | -0.787202 | 0.09673651 | 0.10639192 | 0.94762033 | 0.82559089 | 0.74784386 | 0.75715596 |
| TLAC | 0.76377669 | 0.76377669 | -0.0669992 | -0.0761099 | -0.9553742 | -0.8016806 | -0.9312325 | -0.725705 |
| P005 | 0.76982758 | 0.76982758 | -0.0692194 | -0.0789904 | -0.9677688 | -0.8100614 | -0.8665276 | -0.7254114 |
| OEFC | -0.7871993 | -0.7871993 | 0.09674688 | 0.10640295 | 0.94773509 | 0.82588834 | 0.74800512 | 0.75710321 |
| OIFC | 0.75596025 | 0.75596025 | -0.064741 | -0.0732954 | -0.934662 | -0.7913986 | -0.9431762 | -0.7394392 |
| OCFC | -0.9186974 | -0.9186974 | 0.09098425 | 0.10613995 | 0.84622053 | 0.95202675 | 0.81156649 | 0.90176686 |
| OEFT | -0.918898 | -0.918898 | 0.07415261 | 0.08803195 | 0.83604765 | 0.95585817 | 0.79230894 | 0.90602115 |
| OIFT | -0.9448715 | -0.9448715 | 0.32027346 | 0.33222102 | 0.64984335 | 0.91748299 | 0.64957934 | 0.83029367 |
| OCFT | -0.7789375 | -0.7789375 | 0.06945843 | 0.08075995 | 0.55301879 | 0.79266984 | 0.51777655 | 0.7505596 |
| ABFT | -0.9161527 | -0.9161527 | 0.08043298 | 0.09834939 | 0.69754833 | 0.93444818 | 0.66097699 | 0.89400695 |
| **FMF** | -0.9612201 | -0.9612201 | 0.16095366 | 0.17361929 | 0.86068539 | 0.9808424 | 0.77915367 | 0.90981396 |
| BETL | -0.9580397 | -0.9580397 | 0.23850398 | 0.24595475 | 0.74288785 | 0.95335432 | 0.69367496 | 0.87312491 |
| PSI | -0.8873089 | -0.8873089 | 0.08050881 | 0.09340227 | 0.73453121 | 0.91191174 | 0.68575968 | 0.85633207 |
| PD | 0.92907464 | 0.92907464 | -0.0329877 | -0.0444228 | -0.8080498 | -0.9716122 | -0.7667077 | -0.9414498 |

| | | | | | | | |
|---|---|---|---|---|---|---|---|
| PENT | -0.760908 | -0.760908 | 0.06446122 | 0.07303579 | 0.8010345 | 0.82827101 | 0.74936255 |
| PMAS | -0.760908 | -0.760908 | 0.06446122 | 0.07303579 | 0.98505149 | 0.8010345 | 0.74936255 |
| PVAR | -0.9939465 | -0.9939465 | 0.27832619 | 0.29255237 | 0.99708656 | 0.75066994 | 0.91084191 |
| PLAC | -0.9941225 | -0.9941225 | 0.27966742 | 0.29402826 | 0.9989372 | 0.75016924 | 0.91016898 |
| NPAT | -0.9943381 | -0.9943381 | 0.28151553 | 0.29604352 | 0.99870183 | 0.74949794 | 0.90926387 |
| LPI | -0.9943418 | -0.9943418 | 0.28154915 | 0.2960803 | 0.99661668 | 0.74948517 | 0.90924674 |
| PSIZ | -0.760908 | -0.760908 | 0.07303579 | 0.798689 | 0.99661123 | 0.82827101 | 0.74936255 |
| PSSD | 0.80964371 | 0.80964371 | -0.2622824 | 0.98505149 | 0.8010345 | -0.6349483 | -0.7259107 |
| PSCV | 0.98912898 | 0.98912898 | -0.2258791 | -0.2396928 | -0.8262023 | -0.762473 | -0.9270912 |
| TE | 0.25569488 | 0.25569488 | -0.9191484 | -0.9244753 | -0.1135319 | 0.00957226 | 0.06478519 |
| OEDG | 0.26307245 | 0.26307245 | -0.9201965 | -0.9258922 | -0.1203665 | 0.00834035 | 0.05932145 |
| OPER | -0.7797678 | -0.7797678 | 0.07806373 | 0.08763166 | 0.819483773 | 0.86659252 | 0.73972102 |
| RGYR | -0.3994393 | -0.3994393 | 0.98145557 | 0.99073786 | 0.27679659 | 0.12130949 | 0.08560512 |
| LOAX | 0.9899724 | 0.9899724 | -0.2320062 | -0.2458086 | -0.9987539 | -0.7619271 | -0.9260325 |
| IEDG | 1 | 1 | -0.3556949 | -0.3699994 | -0.9880837 | -0.7389137 | -0.8917469 |
| TEDG | 1 | 1 | -0.3556949 | -0.3699994 | -0.7748949 | -0.8917469 | -0.8917469 |
| LSI | -0.3556949 | -0.3556949 | -0.3556949 | 1 | 0.23455718 | 0.0920071 | 0.05185138 |
| MSI | -0.3699994 | -0.3699994 | -0.3699994 | -0.3699994 | 0.24794759 | 0.10102237 | 0.06202644 |
| AWMSI | -0.7748949 | -0.7748949 | 0.07619543 | 0.08560452 | 1 | 0.85977986 | 0.73798282 |
| DLFD | -0.9880837 | -0.9880837 | 0.23455718 | 0.24794759 | 0.8149319 | 0.76686421 | 0.92536307 |
| MPFD | -0.7389137 | -0.7389137 | 0.0920071 | 0.10102237 | 0.76686421 | 1 | 0.68446375 |
| AWMPFD | -0.8917469 | -0.8917469 | 0.05185138 | 0.06202644 | 0.92536307 | 0.68446375 | 1 |
| SqP | -0.9918969 | -0.9918969 | 0.29353727 | 0.30758885 | 0.99329997 | 0.76014051 | 0.89483444 |
| PA_1 | -0.9824197 | -0.9824197 | 0.29249668 | 0.30578667 | 0.98625818 | 0.82769206 | 0.89560039 |
| PA_2 | -0.7038386 | -0.7038386 | 0.22089034 | 0.23017039 | 0.70360155 | 0.53837385 | 0.64288952 |
| NACI | -0.9542749 | -0.9542749 | 0.08634547 | 0.09872429 | 0.98645684 | 0.77463623 | 0.9490037 |
| NASQ | -0.9866968 | -0.9866968 | 0.22784927 | 0.24368827 | 0.99765025 | 0.7651954 | 0.91378406 |
| BRRA | -0.5567838 | -0.5567838 | 0.5507859 | 0.56098076 | 0.44864077 | 0.25584104 | 0.30799817 |
| NFTD | -0.5567834 | -0.5567834 | 0.55078596 | 0.56098081 | 0.25878371 | 0.25584056 | 0.30799774 |
| PORO | 1 | 1 | -0.3556949 | -0.3699994 | -0.9880837 | -0.7389137 | -0.8917469 |
| DSTA | -0.9388201 | -0.9388201 | 0.06653783 | 0.07869788 | 0.97657814 | 0.770586 | 0.93027386 |
| ABRA | -0.9507904 | -0.9507904 | 0.08479384 | 0.09654311 | 0.98379536 | 0.76803307 | 0.95520687 |
| CCRA | -0.2693585 | -0.2693585 | 0.89744526 | 0.90338685 | 0.12536169 | -0.0081231 | -0.0538666 |

| | SqP | PA_1 | PA_2 | NACI | NASQ | BRRA | NFTD | PORO |
|---|---|---|---|---|---|---|---|---|
| **LsFT** | -0.9538867 | -0.9313718 | -0.6333422 | -0.8801401 | -0.9384264 | -0.6571476 | -0.6571473 | 0.97166334 |
| NYTP | 0.90185022 | 0.89984365 | 0.62611058 | 0.919158 | 0.91372266 | 0.33137275 | 0.33137235 | -0.8848532 |
| SIDI | 0.89456023 | 0.91121375 | 0.63186239 | 0.86191608 | 0.8907471 | 0.37343432 | 0.37343394 | -0.8799628 |
| SIEV | 0.88686496 | 0.90204169 | 0.62890471 | 0.82198491 | 0.87244056 | 0.42941607 | 0.42941572 | -0.8835439 |
| SHDI | 0.89356644 | 0.9101047 | 0.6303792 | 0.87267537 | 0.89335219 | 0.36005388 | 0.3600535 | -0.87544336 |
| SHEV | 0.881582 | 0.89446718 | 0.62673766 | 0.7928492 | 0.85898304 | 0.49384711 | 0.49384679 | -0.88768851 |
| MCDI | 0.87336416 | 0.89141208 | 0.61588101 | 0.84230091 | 0.86971959 | 0.35609157 | 0.3560919 | -0.8566928 |
| MCEV | 0.85744999 | 0.8729283 | 0.6085426 | 0.77848332 | 0.83822094 | 0.43511022 | 0.4351099 | -0.8579708 |
| SHHO | 0.85434421 | 0.88642067 | 0.60156196 | 0.86540066 | 0.8609071 | 0.28798751 | 0.28798712 | -0.82716684 |
| SIHO | -0.6158302 | -0.6843396 | -0.426872 | -0.6132187 | -0.6175106 | -0.1896539 | -0.1896535 | 0.58331011 |
| n_Q | -0.977627 | -0.962873 | -0.628812 | -0.9800964 | -0.9790712 | -0.3683642 | -0.3683637 | 0.9592961 |
| KT_Q | -0.9897205 | -0.9799471 | -0.6436959 | -0.9683844 | -0.9896682 | -0.5333777 | -0.5333773 | 0.99278526 |
| **FMP** | -0.9619243 | -0.9552908 | -0.6515515 | -0.9720803 | -0.9721754 | -0.3680003 | -0.3679999 | 0.95326783 |
| SHCO | -0.9790695 | -0.9724411 | -0.6424653 | -0.9820193 | -0.9871873 | -0.414817 | -0.4148166 | 0.97357029 |
| SICO | -0.8497902 | -0.8664628 | -0.5987319 | -0.8117043 | -0.8433617 | -0.3461933 | -0.346193 | 0.8338967 |
| SUMD | 0.7340755 | 0.67585149 | 0.42080237 | 0.66325533 | 0.72108044 | 0.62835445 | 0.62835425 | -0.7790758 |
| TENT | 0.66498351 | 0.59686028 | 0.40856028 | 0.60067615 | 0.65026127 | 0.56943625 | 0.56943613 | -0.7090454 |
| TMAS | 0.81519421 | 0.87403517 | 0.57094567 | 0.82191878 | 0.81994359 | 0.26252252 | 0.26252209 | -0.7824552 |
| TVAR | 0.81814436 | 0.86136448 | 0.5729979 | 0.8210104 | 0.82281442 | 0.26920391 | 0.26920353 | -0.7864277 |
| POSO | 0.81903851 | 0.86297523 | 0.57338113 | 0.82130038 | 0.82356775 | 0.26938501 | 0.26938462 | -0.7869164 |
| P500 | 0.8197522 | 0.86467464 | 0.57362173 | 0.82131839 | 0.82415211 | 0.26951783 | 0.26951744 | -0.787202 |
| TLAC | -0.7950259 | -0.8571616 | -0.557607 | -0.8060761 | -0.799708 | -0.2529801 | -0.2529797 | 0.76377669 |
| POO5 | -0.80468 | -0.8605447 | -0.5618765 | -0.8097922 | -0.8112067 | -0.2542497 | -0.2542493 | 0.76982758 |
| OEFC | 0.81980145 | 0.86469803 | 0.5736204 | 0.82131022 | 0.82415493 | 0.26951743 | 0.26951703 | -0.7871993 |
| OIFC | -0.779603 | -0.8478858 | -0.5518342 | -0.8008866 | -0.7855541 | -0.2522529 | -0.2522524 | 0.75596025 |
| OCFC | 0.93699719 | 0.94800496 | 0.66375816 | 0.95842328 | 0.95195454 | 0.30774406 | 0.30774361 | -0.9186974 |
| OEFT | 0.93871637 | 0.94435378 | 0.66417302 | 0.96579368 | 0.95617492 | 0.30275134 | 0.30275089 | -0.918898 |
| OIFT | 0.92598769 | 0.90267539 | 0.6560125 | 0.8843241 | 0.91739331 | 0.65490171 | 0.65490141 | -0.9448715 |
| OCFT | 0.77897033 | 0.74226061 | 0.55085619 | 0.80527605 | 0.79483477 | 0.29829778 | 0.29829749 | -0.7789375 |
| ABFT | 0.91800776 | 0.89080187 | 0.64706325 | 0.94630871 | 0.93659026 | 0.36570894 | 0.36570856 | -0.9161527 |
| **FMF** | 0.9731345 | 0.97627257 | 0.68687712 | 0.97415047 | 0.97971194 | 0.44047481 | 0.44047439 | -0.9612201 |
| BETL | 0.95454464 | 0.93965943 | 0.67561537 | 0.93464703 | 0.95056446 | 0.56094414 | 0.56094378 | -0.9580397 |
| PSI | 0.89727615 | 0.88184855 | 0.63384235 | 0.92219968 | 0.91431236 | 0.33414109 | 0.33414072 | -0.8873089 |
| PD | -0.948161 | -0.9417144 | -0.6718658 | -0.9946846 | -0.9683287 | -0.2683156 | -0.2683151 | 0.92907464 |

165

| | | | | | | |
|---|---|---|---|---|---|---|
| PENT | 0.78938347 | 0.84892864 | 0.55561039 | 0.8046399 | 0.25265228 | -0.760908 |
| PMAS | 0.78938347 | 0.84892864 | 0.55561039 | 0.8046399 | 0.25265228 | -0.760908 |
| PVAR | 0.99387255 | 0.9857744 | 0.97566115 | 0.99677778 | 0.48754544 | -0.9939465 |
| PLAC | 0.99386018 | 0.9856985 | 0.97508477 | 0.99675567 | 0.48981932 | -0.9941225 |
| NPAT | 0.99382309 | 0.98558233 | 0.97429788 | 0.99668954 | 0.49281682 | -0.9943381 |
| LPI | 0.99382209 | 0.98557983 | 0.97428299 | 0.99668813 | 0.49287238 | -0.9943418 |
| PSIZ | 0.78938347 | 0.84892864 | 0.55561039 | 0.79416188 | 0.25265228 | -0.760908 |
| PSSD | -0.8314795 | -0.8555706 | -0.7981758 | -0.8273682 | -0.3227057 | 0.80964371 |
| PSCV | -0.9918553 | -0.9832276 | -0.9872603 | -0.9971319 | -0.4598858 | -0.98912898 |
| TE | -0.184285 | -0.1792996 | 0.03945342 | -0.1133681 | -0.736065 | 0.25569488 |
| OEDG | -0.1910903 | -0.1848712 | 0.03270077 | -0.1207996 | -0.7408707 | 0.26307245 |
| OPER | 0.81360131 | 0.87143609 | 0.81907047 | 0.81814836 | 0.26090717 | -0.7797678 |
| RGYR | 0.33724086 | 0.249399 | 0.12710473 | 0.27846294 | 0.57806509 | -0.3994393 |
| LOAX | -0.9922892 | -0.703373 | -0.9863451 | -0.9971425 | -0.4628036 | -0.3994393 |
| IEDG | -0.9918969 | -0.9836634 | -0.9542749 | -0.9866968 | -0.5567838 | 0.9899724 |
| TEDG | -0.9918969 | -0.9824197 | -0.9542749 | -0.9542749 | -0.5567838 | 1 |
| LSI | 0.29353727 | 0.22089034 | 0.08634547 | 0.22784927 | 0.5507859 | -0.3556949 |
| MSI | 0.30758885 | 0.23017039 | 0.09872429 | 0.24368827 | 0.56098076 | -0.3699994 |
| AWMSI | 0.8085701 | 0.56559273 | 0.81458065 | 0.81285309 | 0.25878413 | -0.7748949 |
| DLFD | 0.99329997 | 0.70360155 | 0.98645684 | 0.99765025 | 0.44864077 | -0.9880837 |
| MPFD | 0.76014051 | 0.53837385 | 0.77463623 | 0.7651954 | 0.25584104 | -0.7389137 |
| AWMPFD | 0.89483444 | 0.89560039 | 0.64288952 | 0.91378406 | 0.30799817 | -0.8917469 |
| SqP | 0.98666498 | 0.9490037 | 0.9490037 | 0.99371698 | 0.49990002 | -0.9918969 |
| PA_1 | 1 | 0.69895091 | 0.96706301 | 0.99371698 | 0.48131367 | -0.9824197 |
| PA_2 | 0.70287842 | 1 | 0.96245505 | 0.70179229 | 0.34752269 | -0.7038386 |
| NACI | 0.96706301 | 0.96245505 | 1 | 0.9822683 | 0.34860369 | -0.9542749 |
| NASQ | 0.99371698 | 0.98449625 | 0.9822683 | 1 | 0.45398197 | -0.9866968 |
| BRRA | 0.4999002 | 0.34752269 | 0.34860413 | 0.45398156 | 1 | -0.5567838 |
| NFTD | 0.49989962 | 0.34860369 | 0.34860369 | 0.45398156 | 0.45398156 | 1 |
| PORO | -0.9918969 | -0.9542749 | -0.9866968 | -0.9866968 | -0.5567838 | -0.9866968 |
| DSTA | 0.96640128 | 0.67682958 | 0.97667662 | 0.97375026 | 0.32298134 | -0.9388201 |
| ABRA | 0.96149712 | 0.68345126 | 0.9985154 | 0.97667662 | 0.34618141 | -0.9507904 |
| CCRA | 0.19662973 | 0.18842176 | 0.14364288 | 0.12680183 | 0.7786201 | -0.2693585 |

| | DSTA | ABRA | CCRA |
|---|---|---|---|
| LsFT | -0.8645682 | -0.8753658 | -0.4099495 |
| NYTP | 0.9193849 | 0.92179148 | 0.00233106 |
| SIDI | 0.8681403 | 0.85850509 | 0.16240255 |
| SIEV | 0.82446275 | 0.81809969 | 0.29888258 |
| SHDI | 0.88043514 | 0.87139517 | 0.11539397 |
| SHEV | 0.79154327 | 0.78936347 | 0.40558847 |
| MCDI | 0.85110953 | 0.83934704 | 0.14777871 |
| MCEV | 0.78116813 | 0.77457565 | 0.35079594 |
| SHHO | 0.87632122 | 0.86850559 | -0.011537 |
| SIHO | -0.6250113 | -0.6053815 | 0.02483161 |
| n_Q | -0.9684176 | -0.9767927 | -0.0450723 |
| KT_Q | -0.9543787 | -0.9648362 | -0.2020297 |
| FMP | -0.9619246 | -0.9698191 | -0.0522359 |
| SHCO | -0.9699912 | -0.9788686 | -0.0888471 |
| SICO | -0.8222074 | -0.8082604 | -0.1679856 |
| SUMD | 0.62442586 | 0.65553154 | 0.45608109 |
| TENT | 0.57026178 | 0.60294687 | 0.43636832 |
| TMAS | 0.83353774 | 0.81901569 | -0.0235344 |
| TVAR | 0.83674572 | 0.81973859 | -0.0083396 |
| P050 | 0.83724981 | 0.81973302 | -0.0080847 |
| P500 | 0.83749248 | 0.81936945 | -0.0077383 |
| TLAC | -0.8140276 | -0.8027032 | 0.03204449 |
| P005 | -0.8224048 | -0.8044985 | 0.03184929 |
| OEFC | 0.83748878 | 0.81935405 | -0.0077317 |
| OIFC | -0.8023287 | -0.8010859 | 0.03175195 |
| OCFC | 0.95367576 | 0.95541891 | -0.0154481 |
| OEFT | 0.96063202 | 0.96176912 | -0.0408055 |
| OIFT | 0.86258623 | 0.88033176 | 0.31840434 |
| OCFT | 0.78555628 | 0.79827778 | -0.0169413 |
| ABFT | 0.9299546 | 0.94310658 | 0.00421972 |
| FMF | 0.96863026 | 0.97093732 | 0.07976665 |
| BETL | 0.92080869 | 0.93027018 | 0.19869083 |
| PSI | 0.90890712 | 0.91500535 | -0.0212634 |
| PD | -0.9868732 | -0.9918263 | 0.10440543 |

| | | | |
|---|---|---|---|
| PENT | 0.81553767 | 0.80807312 | -0.0318379 |
| PMAS | 0.81553767 | 0.80807312 | -0.0318379 |
| PVAR | 0.96284233 | 0.97145867 | 0.17614777 |
| PLAC | 0.96220237 | 0.97083533 | 0.17848319 |
| NPAT | 0.96133058 | 0.96999007 | 0.18161162 |
| LPI | 0.96131412 | 0.96997407 | 0.18166936 |
| PSIZ | 0.81553767 | 0.80807312 | -0.0318379 |
| PSSD | -0.8123262 | -0.7925918 | -0.1294999 |
| PSCV | -0.9747022 | -0.9838532 | -0.1251398 |
| TE | 0.06047546 | 0.03996834 | -0.996856 |
| OEDG | 0.05423883 | 0.03355865 | -0.9976235 |
| OPER | 0.83194164 | 0.81573505 | -0.0245291 |
| RGYR | 0.10681646 | 0.12344297 | 0.90578582 |
| LOAX | -0.9736768 | -0.9829292 | -0.1308088 |
| IEDG | -0.9388201 | -0.9507904 | -0.2693585 |
| TEDG | -0.9388201 | -0.9507904 | -0.2693585 |
| LSI | 0.06653783 | 0.08479384 | 0.89744526 |
| MSI | 0.07869788 | 0.09654311 | 0.90338685 |
| AWMSI | 0.82787026 | 0.81225264 | -0.0253793 |
| DLFD | 0.97657814 | 0.98379536 | 0.12536169 |
| MPFD | 0.770586 | 0.76803307 | -0.0081231 |
| AWMPFD | 0.93027386 | 0.95520687 | -0.0538666 |
| SqP | 0.96640128 | 0.96149712 | 0.19662973 |
| PA_1 | 0.95400059 | 0.95843995 | 0.18842176 |
| PA_2 | 0.67682958 | 0.68345126 | 0.14364288 |
| NACI | 0.99986537 | 0.9985154 | -0.026117 |
| NASQ | 0.97375026 | 0.97667662 | 0.12680183 |
| BRRA | 0.32298134 | 0.34618141 | 0.77861995 |
| NFTD | 0.32298091 | 0.34618097 | 0.7786201 |
| PORO | -0.9388201 | -0.9507904 | -0.2693585 |
| DSTA | 0.98706577 | 0.98706577 | -0.048273 |
| ABRA | 1 | 1 | -0.0273013 |
| CCRA | -0.048273 | -0.0273013 | 1 |